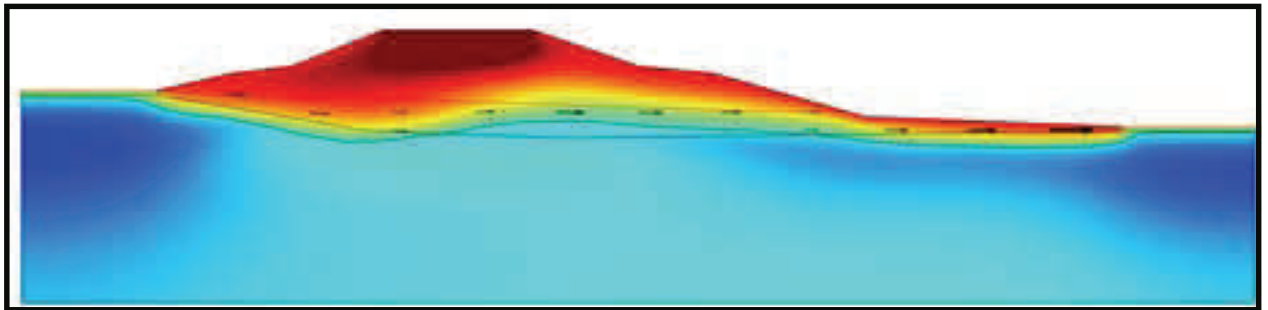# Impact of Groundwater Flow on Permafrost Degradation and Transportation Infrastructure Stability

UAF:
Margaret M. Darrow, Ph.D
Ronald P. Daanen, Ph.D
Jason T. Zottola,
        M.S. Candidate

UdeM:
Daniel Fortier, Ph.D
Isabelle de Grandpre, M.Sc.
Sabine Veuille, M.Sc.
Michel Sliger,
        M.Sc. Candidate

February 2013

Prepared By:

1. AGENCY USE ONLY (LEAVE BLANK)	2. REPORT DATE	3. REPORT TYPE AND DATES COVERED
FHWA-AK-RD-	February 2013	Final Report (April 2011-December 2012)

4. TITLE AND SUBTITLE	5. FUNDING NUMBERS
Impact of Groundwater Flow on Permafrost Degradation and Transportation Infrastructure Stability	AUTC#510011 DTRT06-G-0011

6. AUTHOR(S)

Margaret M. Darrow, Ronald P. Daanen, Jason T. Zottola (UAF)
Daniel Fortier, Isabelle de Grandpre, Sabine Veuille, Michel Sliger (UdeM)

7. PERFORMING ORGANIZATION NAME(S) AND ADDRESS(ES)	8. PERFORMING ORGANIZATION REPORT NUMBER
Alaska University Transportation Center P.O. Box 755900, Fairbanks, AK 99775-5900 Universite de Montreal C.P. 6128, Succursale Centre-ville Montreal (Quebec), Canada	INE/AUTC 13.08

9. SPONSORING/MONITORING AGENCY NAME(S) AND ADDRESS(ES)	10. SPONSORING/MONITORING AGENCY REPORT NUMBER
Research and Innovative Technology Administration (RITA), U.S. Dept. of Transportation (USDOT) 1200 New Jersey Ave, SE, Washington, DC 20950 Transport Canada 330 Sparks Street, Ottawa, ON K1A 0N5	FHWA-AK-RD-

11. SUPPLENMENTARY NOTES

12a. DISTRIBUTION / AVAILABILITY STATEMENT	12b. DISTRIBUTION CODE
No restrictions	

13. ABSTRACT (Maximum 200 words)

A warming climate has been identified as unequivocal by the Intergovernmental Panel on Climate Change with greater and faster temperature increase demonstrated at northern latitudes, and with an overall increase in precipitation. Analysis of field data collected throughout the arctic and subarctic corroborates with these findings, demonstrating an overall warming of permafrost temperatures. As indicated by thermal modeling, the stability of permafrost below roadway embankments is greatly affected by surface temperatures; thus, as climate warms, permafrost degradation represents a major issue for the design and maintenance of embankments. While the thermal stability of embankments in a warming climate has been investigated, the impact of groundwater and the effect of advective heat transfer on permafrost degradation below embankments has been overlooked. Recent studies indicate that groundwater flow along the permafrost table will cause permafrost degradation to occur one to several orders of magnitude faster than atmospheric warming alone. Thus, it is imperative for the long-term stability of infrastructure in permafrost regions that we better understand the complex interaction among groundwater, permafrost, and overlying embankments. The overall goal of this research is to develop a relationship among groundwater flow, permafrost degradation, and embankment stability. The completion of this study requires collaboration between researchers from the University of Alaska Fairbanks (UAF) and from the Université de Montréal (UdeM).

14- KEYWORDS: Groundwater flow, embankment, COMSOL modeling, Alaska Highway, permafrost	15. NUMBER OF PAGES 142
	16. PRICE CODE N/A

17. SECURITY CLASSIFICATION OF REPORT	18. SECURITY CLASSIFICATION OF THIS PAGE	19. SECURITY CLASSIFICATION OF ABSTRACT	20. LIMITATION OF ABSTRACT
Unclassified	Unclassified	Unclassified	N/A

SI* (MODERN METRIC) CONVERSION FACTORS

APPROXIMATE CONVERSIONS TO SI UNITS

Symbol	When You Know	Multiply By	To Find	Symbol
LENGTH				
in	inches	25.4	millimeters	mm
ft	feet	0.305	meters	m
yd	yards	0.914	meters	m
mi	miles	1.61	kilometers	km
AREA				
in^2	square inches	645.2	square millimeters	mm^2
ft^2	square feet	0.093	square meters	m^2
yd^2	square yard	0.836	square meters	m^2
ac	acres	0.405	hectares	ha
mi^2	square miles	2.59	square kilometers	km^2
VOLUME				
fl oz	fluid ounces	29.57	milliliters	mL
gal	gallons	3.785	liters	L
ft^3	cubic feet	0.028	cubic meters	m^3
yd^3	cubic yards	0.765	cubic meters	m^3
NOTE: volumes greater than 1000 L shall be shown in m^3				
MASS				
oz	ounces	28.35	grams	g
lb	pounds	0.454	kilograms	kg
T	short tons (2000 lb)	0.907	megagrams (or "metric ton")	Mg (or "t")
TEMPERATURE (exact degrees)				
^oF	Fahrenheit	5 (F-32)/9 or (F-32)/1.8	Celsius	^oC
ILLUMINATION				
fc	foot-candles	10.76	lux	lx
fl	foot-Lamberts	3.426	candela/m^2	cd/m^2
FORCE and PRESSURE or STRESS				
lbf	poundforce	4.45	newtons	N
lbf/in^2	poundforce per square inch	6.89	kilopascals	kPa

APPROXIMATE CONVERSIONS FROM SI UNITS

Symbol	When You Know	Multiply By	To Find	Symbol
LENGTH				
mm	millimeters	0.039	inches	in
m	meters	3.28	feet	ft
m	meters	1.09	yards	yd
km	kilometers	0.621	miles	mi
AREA				
mm^2	square millimeters	0.0016	square inches	in^2
m^2	square meters	10.764	square feet	ft^2
m^2	square meters	1.195	square yards	yd^2
ha	hectares	2.47	acres	ac
km^2	square kilometers	0.386	square miles	mi^2
VOLUME				
mL	milliliters	0.034	fluid ounces	fl oz
L	liters	0.264	gallons	gal
m^3	cubic meters	35.314	cubic feet	ft^3
m^3	cubic meters	1.307	cubic yards	yd^3
MASS				
g	grams	0.035	ounces	oz
kg	kilograms	2.202	pounds	lb
Mg (or "t")	megagrams (or "metric ton")	1.103	short tons (2000 lb)	T
TEMPERATURE (exact degrees)				
^oC	Celsius	1.8C+32	Fahrenheit	^oF
ILLUMINATION				
lx	lux	0.0929	foot-candles	fc
cd/m^2	candela/m^2	0.2919	foot-Lamberts	fl
FORCE and PRESSURE or STRESS				
N	newtons	0.225	poundforce	lbf
kPa	kilopascals	0.145	poundforce per square inch	lbf/in^2

*SI is the symbol for the International System of Units. Appropriate rounding should be made to comply with Section 4 of ASTM E380.
(Revised March 2003)

EXECUTIVE SUMMARY

A major issue with infrastructure stability in northern regions is thermal degradation of the underlying permafrost. Thermal modeling using conductive heat transfer has indicated that permafrost stability below roadway embankments is greatly affected by the surface temperatures; thus, as climate warms permafrost degradation represents a major issue for the design and maintenance of embankments. Previous research projects have produced innovative designs to stabilize embankments over degrading permafrost, many of which have demonstrated long-term success. These studies, however, did not include the detrimental effects of groundwater interaction with the embankment and underlying soil.

The overall goal of this research was to develop a relationship among groundwater flow, permafrost degradation, and embankment stability. To achieve this goal, we investigated the Alaska Highway test section (AHTS) near Beaver Creek, Yukon, Canada, as this site is well-known for the ongoing thermal degradation of the permafrost below the embankment, demonstrates significant groundwater flow, and is heavily instrumented from previous work. Our research included two summers of field work and laboratory testing, from which we determined the necessary input parameters for numerical simulations. We produced a fully-coupled model that included both conductive heat flow and heat advection that simulated groundwater flow measured in the field. The model results indicate that groundwater flow creates significant thermal effects that are not present in the more traditional conduction-only model. The fully-coupled model output indicates that the embankment is not in thermal equilibrium with the underlying soils. Instead, groundwater flowing through the porous gravel embankment in the summer causes thaw into underlying, ice-rich foundation soils. This results in thermal degradation, which is manifested as longitudinal and transverse cracks and an irregular driving surface. Given the advective nature of groundwater flow, the thermal degradation will be ongoing, resulting in continual repairs to the embankment surface.

Based on these research results, we recommend the following:

1) Employ terrain analysis as an early step in the route selection of infrastructure. This will allow the identification of thaw-sensitive permafrost as areas to avoid. For areas where re-routing proposed or existing infrastructure is not possible, then eco-geomorphologic terrain unit maps are tools that can aid in the identification of areas where near-surface groundwater flow will require additional mitigation techniques (such as intercepting ditches, culverts, drainage ditches, retention basins, impervious membranes, and porous embankments).

2) Incorporate groundwater flow in thermal modeling for areas where it is recognized as an issue. Caution must be used in selecting governing equations and model input parameters.

3) In order to catch and direct groundwater flow through an embankment, conduct modeling of proposed mitigation techniques with a fully-coupled model. Test the selected techniques as experimental features at a heavily instrumented test site underlain by thaw-sensitive permafrost and demonstrating near-surface groundwater flow.

TABLE OF CONTENTS

LIST OF FIGURES

iv

LIST OF TABLES

LIST OF APPENDICES

ACKNOWLEDGMENTS

CHAPTER 1

BACKGROUND

A warming climate has been identified as unequivocal by the Intergovernmental Panel on Climate Change (IPCC, 2007) with greater and faster temperature increase demonstrated at northern latitudes, and with an overall increase in precipitation. Analysis of field data collected throughout the arctic and subarctic corroborates with IPCC's findings, demonstrating an overall warming of permafrost temperatures (Christiansen et al., 2010; Romanovsky et al., 2010; Smith et al., 2010; Zhao et al., 2010). The IPCC also identified infrastructure as a key vulnerability to long-term climate change. Thermal modeling using conductive heat transfer has indicated that permafrost stability below roadway embankments is greatly affected by the surface temperatures (Darrow, 2011); thus as climate warms, permafrost degradation represents a major issue for the design and maintenance of embankments. This problem will be further exacerbated by thermal effects of increased snow accumulation along embankment side slopes (Stieglitz et al., 2003; Zhang, 2005).

While the thermal stability of embankments in a warming climate has been investigated, the impact of groundwater and advective heat transfer on permafrost degradation below embankments largely has been overlooked. Some studies have shown that permafrost degradation from groundwater flow along the permafrost table, within the permafrost, or through taliks will occur one to several orders of magnitude faster than by atmospheric warming alone (de Grandpre et al., 2010, 2012; Fortier et al., 2007). Despite its tremendous effects, groundwater flow is not typically taken into account in permafrost models, nor in the design of embankments built over ice-rich, thaw-sensitive permafrost.

Adequate drainage along transportation infrastructure is a major element of design, especially for embankments built on permafrost. It is recognized that inadequate drainage may result in surface water ponding and various forms of thermal erosion (Brown et al., 1984), which affects travel safety and the environment, and results in ongoing maintenance costs (see Figure 1 for examples). While surface drainage is accommodated by bridges and culverts, there are no commonly applied designs for accommodating groundwater flow. Groundwater flow-induced permafrost degradation has a tremendous effect on the stability of an overlying roadway embankment (de Grandpre et al., 2010), yet this process has received little attention from the scientific and engineering communities.

Many researchers in Alaska, as well as Canada, Russia, China, and other countries at high latitudes, have investigated the thermal interaction between embankments and the underlying permafrost, and much work has been done to develop innovative designs to stabilize embankments over degrading permafrost, such as using thermosiphons, insulation, and air ducts. A search of the Alaska Department of Transportation and Public Facilities (ADOT&PF) research records yields a wealth of studies aimed at the prevention of thaw settlement of ice-rich foundation soils due to an embankment's thermal effects; a summary of many of these studies was provided by Beaulac and Doré (2006). These studies, however, did not focus on the often compounding thermal impact of groundwater flow on frozen soils. One reconnaissance-level project (Brown et al., 1984) investigated the interaction between embankments and culverts, indicating that insufficient drainage design led to ponded water, the degradation of ice wedges,

Figure 1. Water ponding on the uphill side of the Alaska Highway embankment, near Beaver Creek, Yukon, Canada. (Photography courtesy of D. Fortier)

Figure 2. Transverse depressions in the surface of the Alaska Highway due to permafrost degradation. (Photograph courtesy of D. Fortier)

and the subsequent formation of drainage paths beneath the embankment; however, field measurements were limited to temperature readings and visual observations.

A search of the TRB *Research In Progress* database yields similar results, with essentially no research on permafrost degradation due to groundwater flow and its effect on embankment stability. Some research conducted in the 1990's by researchers at Université de Montréal yielded excellent general design guides and innovative stabilization measures for embankments over permafrost (Goodrich, 1996; Ladanyi, 1994). The most relevant research listed in the TRB database is the Kangirusk Landing Runway project in northern Canada (Tremblay and Doré, 1988). This airport embankment has demonstrated severe thaw settlement due to permafrost degradation. A few previous studies have examined the relationships among frozen ground, hydraulic conductivity, and unfrozen water content (Egginton and Dyke, 1990; Kane et al., 2001; Mackay, 1983; Quinton et al., 2005).

While a few commercially available finite element models allow for the coupled analysis of groundwater and heat flow, the models use the assumption that a thermo-dynamic equilibrium exists between the groundwater and the surrounding soil. Recent research indicates that this is not the case; rather groundwater transfers heat to the surrounding soil (de Grandpre et al., 2010). Few models address the hydraulic conductivity of partially frozen soils (Daanen et al., 2008), although previous research indicates that hydraulic conductivity, unfrozen water content, and related thermal shrinkage cracks have a significant contribution to groundwater movement in organic, ice-rich soils (Quinton et al., 2005).

RESEARCH OBJECTIVES

The overall goal of this research was to develop a relationship among groundwater flow, permafrost degradation, and embankment stability. In particular we proposed to answer: how does groundwater flow contribute to permafrost degradation? The individual tasks developed to obtain the research goal were as follows:

- To measure groundwater flow and heat loss for a highway embankment;

- To develop laboratory procedures for the measurement of hydraulic conductivity and heat loss in frozen soil samples;

- To measure the unfrozen water content of undisturbed permafrost soils for the research area;

- To produce a numerical model that includes both conductive heat transfer and heat advection by groundwater flow; and

- To compare the model results against measured heat and water flow for the research area.

CHAPTER 2

RESEARCH APPROACH

This research focused on the Alaska Highway test section (AHTS), located near Beaver Creek, Yukon, Canada (see Figure 3 for the project location). This test site was the location of the Shakwak Highway Project, which involved designing and constructing eleven different mitigation strategies in order to study permafrost rehabilitation (Coulombe et al., 2012; M-Lepage et al., 2012a and b; Remchein et al., 2009; Remchein et al., 2010). The previous research required the installation of many temperature sensors, water observation wells, and piezometers, thus making the AHTS an ideal location for this current research project. The site was selected in 2007 after a coring campaign that confirmed the very ice-rich nature of the permafrost and the occurrence of massive syngenetic ice wedges buried at depth but inactive today. This portion of the highway has long been observed to experience large amounts of settlement due to permafrost degradation under the embankment. The embankment surface is in poor condition, and characterized by longitudinal and transverse depressions, longitudinal cracks, and numerous bumps, dips, and potholes, all of which require ongoing maintenance.

During the construction period in 2008, removal of berms paralleling the embankment revealed the presence of both isolated and interconnected saturated taliks under the embankment. Results from additional drilling indicated that the embankment material "sunk" into the natural ground as a result of permafrost degradation. Continuous groundwater flow was observed, and two French drains were installed to direct groundwater beneath and away from the embankment. Groundwater observation wells were installed in an area demonstrating standing surface water. Monitoring groundwater flow in 2009 and 2010 indicated that water was circulating and standing within portions of the embankment (i.e., within gravel having high hydraulic conductivity) that was below the original ground level and possibly within underlying thawed silt. Despite the installation of mitigation techniques, permafrost degradation was still ongoing in 2010, two years after construction. de Grandpré et al. (2012) showed that heat advection from groundwater flow contributed to this degradation. Because of the ongoing degradation, the Yukon government decided to excavate an intercepting parallel ditch on the uphill (east) side of the embankment to collect surface and groundwater flow. This ditch was excavated on October 8, 2010, and was originally 1.5- to 2.5-ft deep and about 2.5-ft wide (see Figure 4). Snowmelt, surface runoff, slumping, and retrogressive erosion of the ditch walls contributed to enlarge the ditch significantly. In 2012, the ditch was between 10- and 16-ft wide and between 2.5- and 5-ft deep (see Figure 5). In spite of the ditch's presence, monitoring of groundwater flow indicated that water was still flowing under the embankment. This suggests that lateral or deep groundwater flow is still active at the test site.

Researchers from the University of Alaska Fairbanks (UAF) and the Université de Montréal (UdeM) collaborated on this project. We formulated five main tasks to achieve our research objective of developing a relationship among groundwater flow, permafrost degradation, and embankment stability. These tasks were divided between the two collaborating institutions. In this chapter, we present each task in detail.
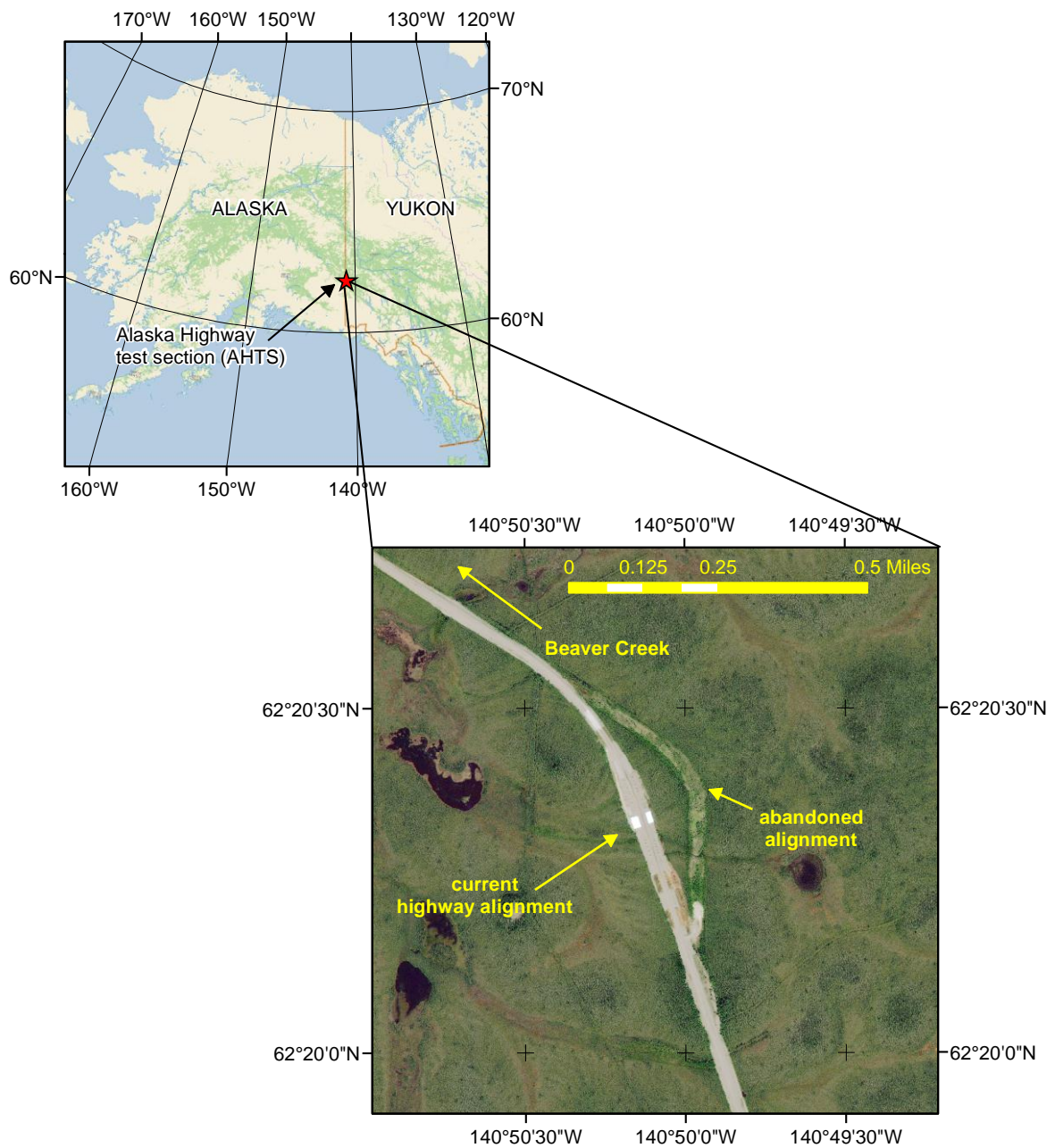
Figure 3. Research location. Inset is a false-color satellite image of the project area showing the location of the current and abandoned highway alignments. Base map courtesy of DeLorme and ESRI.
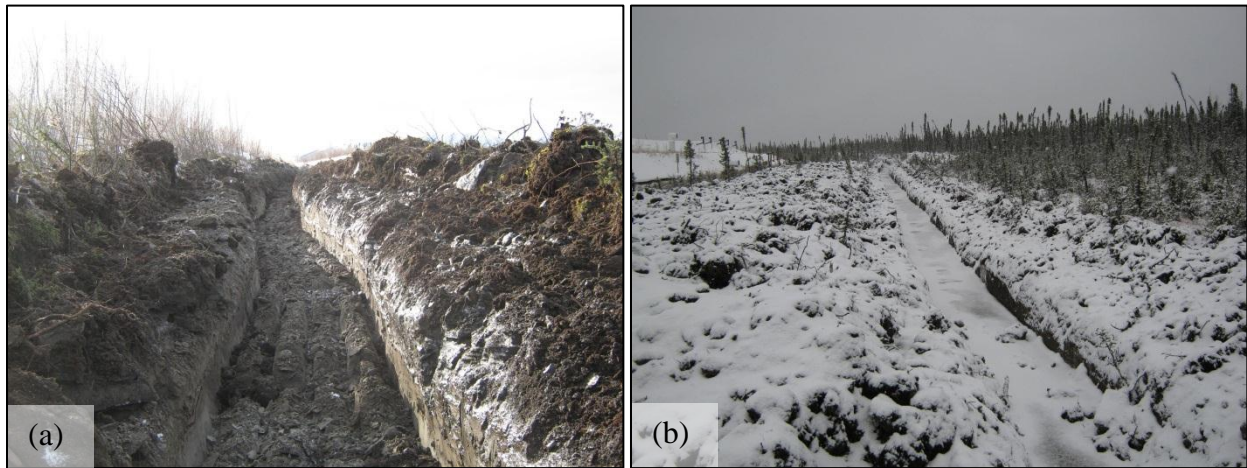
Figure 4. Photographs of the ditch excavated on October 8, 2010 at the AHTS. (a) View to the south, and (b) to the north. The ditch is to the east of the Alaska Highway, which is visible at the extreme left of (b). (Photography courtesy of D. Fortier)

Figure 5. The ditch as of July 2011. (Photograph by M. Darrow)

TASK 1: TO MEASURE GROUNDWATER FLOW AND HEAT LOSS AT THE AHTS

Field work summary

Researchers from each of the collaborating institutions made both joint and individual trips to the AHTS to conduct fieldwork throughout the length of this project. Table 1 is a summary of all the fieldwork conducted for this project. We concentrated our efforts on cross section A-A' (CS A-A') (see Figure 6), which was chosen because of the concentration of previous data in this area and because visual observations indicated significant groundwater flow in this area. Overall, we installed 38 water observation wells and 2 piezometers (see Figure 4 for a visual summary of the installation locations and Appendix A for installation details). In addition to the piezometer installations, in 2011 we installed four temperature sensors (CS107), four water content reflectometers (CS616), and two experimental vibrating wire (VW) piezometers uphill of the embankment to measure typical temperatures, soil moisture, and water pressure in an "undisturbed" location (see Figure 7). We installed an automated data acquisition system (ADAS) for data collection. The VW piezometers were "experimental" as the manufacturer had equipped each sensor with a disc of closed-cell foam to protect the diaphragm against the pressure exerted by volume expansion of water changing phase into ice. Data obtained from the VW piezometers in 2011 was erroneous; we suspected errors in the laboratory calibration conducted in 2011 before the piezometers were installed. In early May 2012 when the surface began to thaw, we extracted the VW piezometers and returned them to the laboratory for additional calibration. In late May 2012, we moved the ADAS to a new location at the west toe of the Alaska Highway embankment, and reinstalled the VW piezometers. The resulting experimental VW piezometer data continued to be suspect, and thus will not be included here. More information on all of the installations is provided in Appendix A.

In May 2012, both UAF and UdeM personnel mobilized to the AHTS to conduct a drilling campaign. We experienced difficulties drilling through the embankment. First, a drilling company that was hired to drill through the embankment near the roadway centerline arrived on site with equipment unsuitable to drill holes of the diameter required to install monitoring equipment. Thus, the centerline embankment boreholes were not drilled as scheduled. UdeM procured a Winkie drill, which blew two motors in two days. Despite our efforts in rebuilding motors and trouble-shooting equipment, we were unable to drill through the thicker portion of the embankment. Nevertheless, we worked with two hand-held drills and were able to install additional piezometers through the granular soils along both the west and east sides of the highway embankment. As we were unable to penetrate through the embankment with the available drilling equipment, we did not install additional temperature, heat flux, or water pressure measurement devices within the embankment. Instead, we used data from existing thermistor strings in the west side slope near CS A-A' for model validation.

We performed a suite of laboratory tests on soil samples collected in 2011. Results from the geotechnical laboratory tests are summarized in Appendix B, and Appendix C is a summary of the thermal conductivity procedure and results. Finally, Appendix D is a summary of thaw depth measurements made during 2011 and 2012. All of these data were used to fine-tune the model input parameters in Task 4. Additionally, we made multiple sets of measurements of water levels and water temperature in water wells throughout the AHTS. From all of the field work, we produced an eco-geomorphological terrain unit map. The water level data and a preliminary version of the map are included in Appendix E.

Table 1. Summary of field work at the AHTS.

Dates	Affiliation of Personnel	Tasks completed
June 2011	UAF, UdeM	Installation of water observation wells; soil sample collection; water level and thaw depth measurements. Water pressure logger installation in some water wells.
July 2011	UAF, UdeM	Installation of piezometers, VW piezometers, soil moisture probes, ADAS; soil sample collection; water level and thaw depth measurements. Water pressure logger installation in some piezometers.
August / September 2011	UAF	Download data from ADAS, thaw depth measurements, manual water level measurements
September 2011	UdeM	Water level and thaw depth measurements; download data from water pressure loggers; measurement of depressions in road surface.
March 2012	UdeM	Snow depth measurement survey parallel and normal to the embankment; described snow stratigraphy and measured snow density in eight snow pits.
May 2012	UAF	Retrieve VW piezometers for recalibration
May 2012	UAF, UdeM	Major drilling program; installation of piezometers; soil sample collection; relocated ADAS; reinstalled temperature sensors, soil moisture reflectometers, VW piezometers; water level and thaw depth measurements.
June 2012	UdeM	Installation of surface temperature loggers, temperature probes, and water pressure loggers in some piezometers; water level and thaw depth measurements.
July 2012	UdeM	Water level and thaw depth measurements.
August 2012	UdeM	Water level and thaw depth measurements.
September 2012	UAF	Download data from ADAS, thaw depth measurements.
September 2012	UdeM	Water level and thaw depth measurements; download data from water pressure loggers.
October 2012	UdeM	Water level and thaw depth measurements.
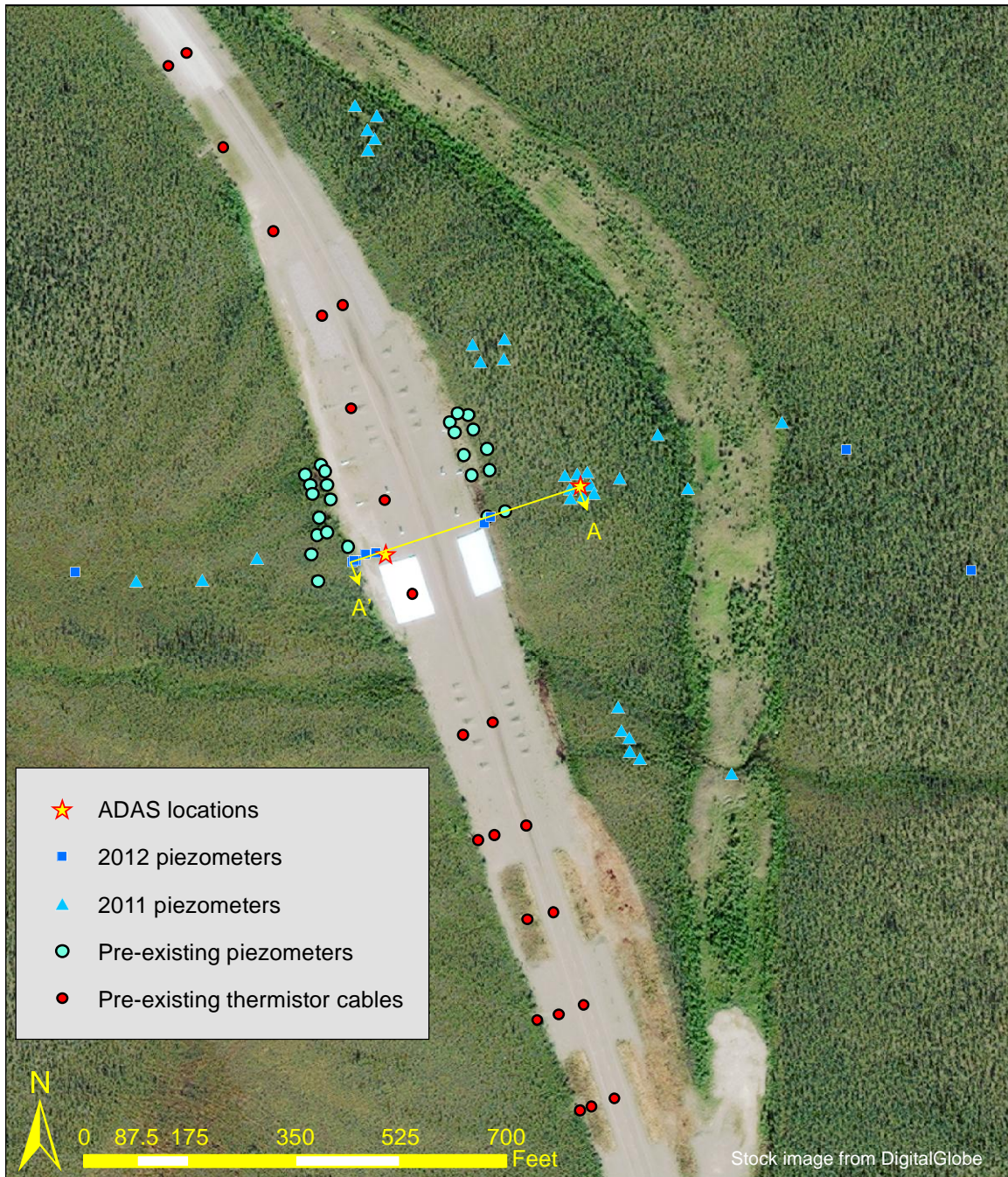
Figure 6. Instrument locations. All of the 2011 and 2012 installations are presented, as well as the locations of previously installed piezometers and thermistor cables, the data from which we were able to use for this analysis. Cross section A-A' is indicated by the yellow line and arrows. Image acquired by satellite WorldView2 on August 4, 2010, 50 cm resolution.
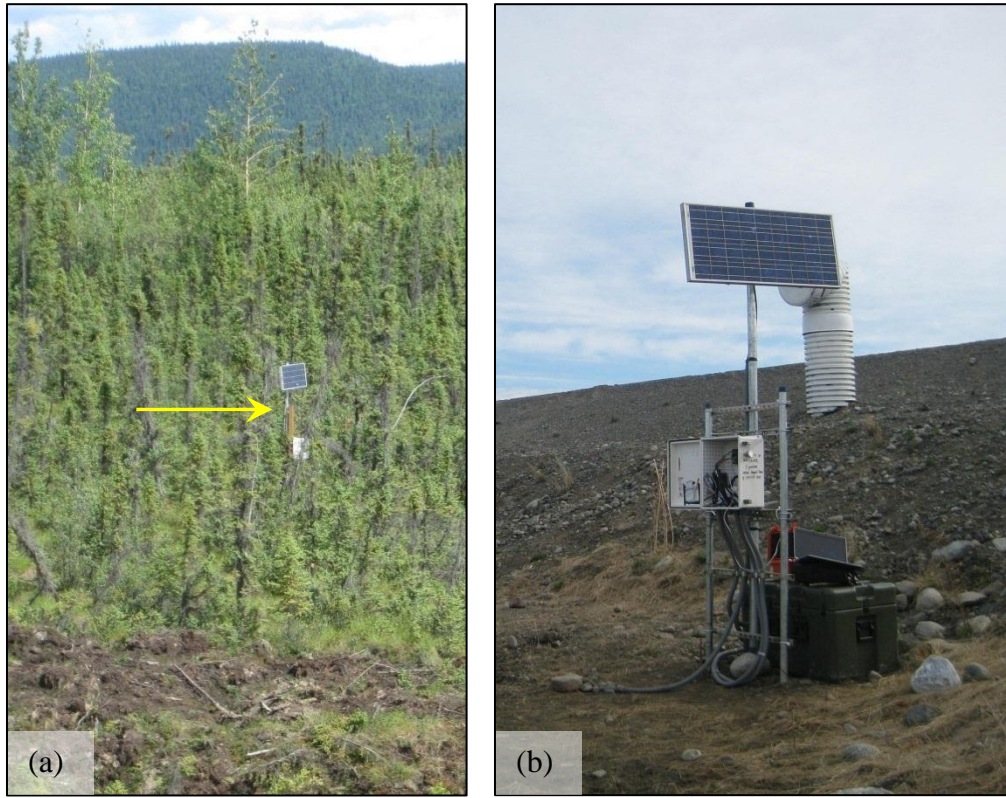
Figure 7. Two locations of the ADAS during this research project. (a) 2011 ADAS location (indicated by the yellow arrow) uphill of the current Alaska Highway alignment (photograph taken from the highway embankment). The excavated soils from the ditch are visible in the foreground, and the taller poplar trees growing on the abandoned highway embankment make it visible behind the ADAS location. (b) 2012 ADAS location at the west toe of the Alaska Highway embankment. One of the experimental mitigation treatments, an air convection duct, is visible on the embankment side slope behind the ADAS. (Photographs by M. Darrow)

Road surface settlement survey

As part of Task 1, we proposed to obtain independent measurements of the roadway surface, which would be used in conjunction with data in the pre-existing digital elevation model for the research site. These measurements could be used to estimate volume change due to thaw settlement.

During summer 2008 as part of previous work at AHTS, depressions were observed along the centerline of the road at the test section. To quantify this settlement, hand-measurements were done during every field visit to the test site between June 2009 and October 2012 (usually two times per year, at the beginning and at the end of the summer). Figure 8 is an overview of the test section designators used for the description of the depressions.

Figure 9 illustrates the development of the depressions in the embankment surface observed during each trip to the field. Depressions were patched and filled with asphalt by the Beaver Creek maintenance crew several times per summer. Nevertheless, measurements of depressions on the road surface indicated that road subsidence was on the order of 2 to 4 in. per month between June and October, or between 8 to 16 in. over each summer. When we began measurements in 2009, the depression at the embankment centerline was restricted to sections YG6 and YG7. This depression increased in length and now affects now YG2 through YG9. In October 2011, we dug a hole at the centerline in section YG7 and intercepted 20 in. of patching material over the original pavement. Other local depressions appeared during the observation period in YG1 and YG12. In October 2012, only YG10 and YG11 remained unaffected.

In order to develop a more systematic and rigorous approach to quantify the volume and the development of these depressions, new tests were performed in September 2012 using a Trimble VX spatial station on a localized depression in section YG12. A laser scan of the depression (which was 138-in. long, 40-in. wide, and 1.4 to 2.5-in. deep) was performed using the terrestrial laser scanner with a resolution of 0.4 in. Figure 10 contains both a photograph of the depression and the results of the laser scan.

The Trimble Realwork Advanced software was used to calculate the surface and volume of the depression from the scan, which consisted of 5,424 points. Results were compared to those obtained from the manual method using a measuring tape, and to an electronic topographical survey method using a VX total station. With results from the latter two methods, we used the Trimble Business Center software and 50 points to evaluate the surface and volume of the depression.

For an area of 40.58 ft^2, the resulting depression volume from the laser scanner, manual measurements, and total station survey were 1.42 ft^3, 1.22 ft^3, and 1.38 ft^3, respectively. The differences in these values may be attributed to the greater number of points collected by the laser scan, leading to a better representation of the depression irregularities. Thus, these differences suggest that using a terrestrial laser scanner increases the precision of the volume estimation of road depressions. This work demonstrated the high potential to measure road depressions and corresponding volumes accurately and rapidly. This will allow for a mechanical monitoring of road damage due to permafrost degradation, and the method will be used to calibrate a future fully-coupled model that will incorporate the mechanical response of the embankment to permafrost degradation, thaw settlement, and subsidence.
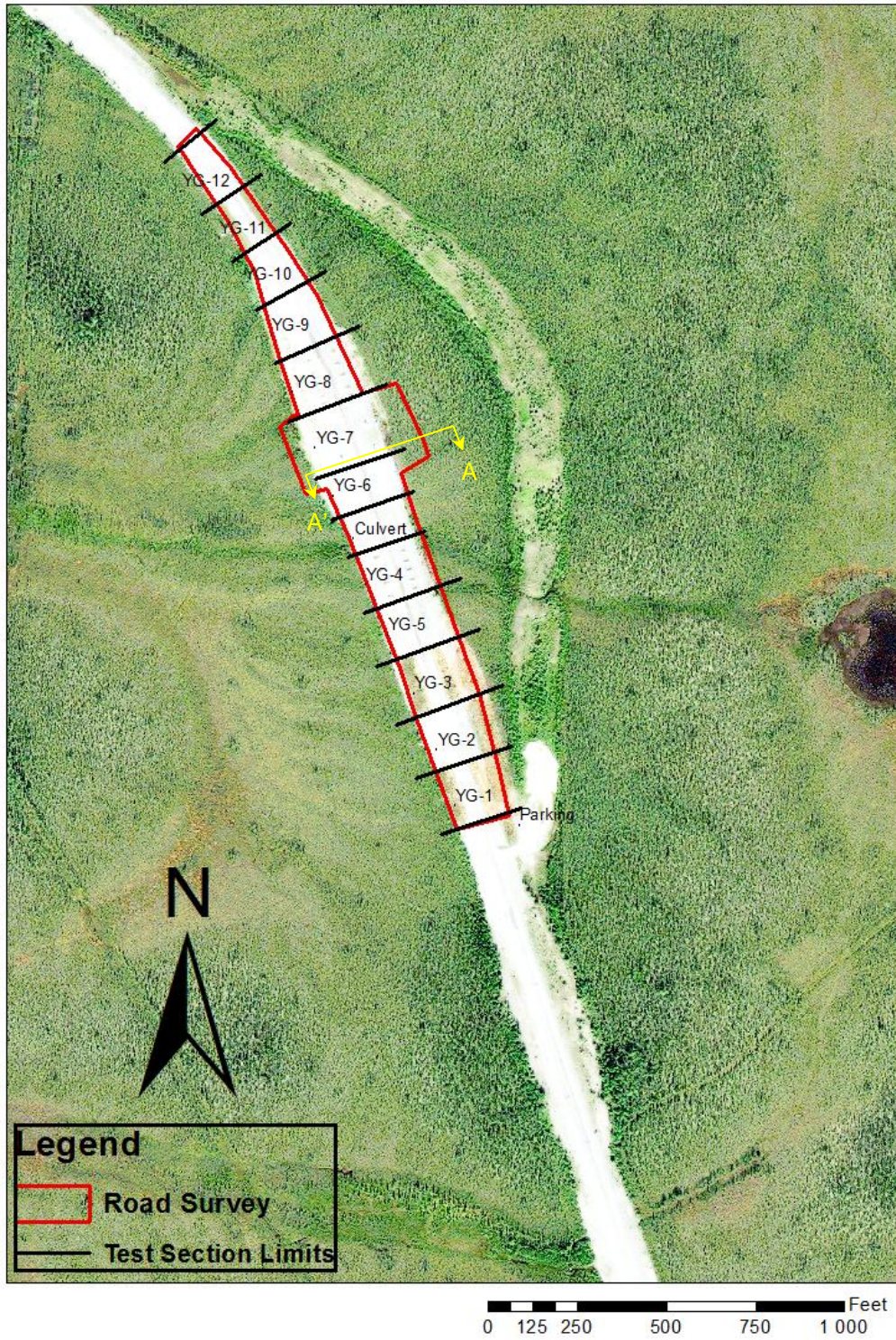
Figure 8. Test section designators used to describe embankment settlement. The location of cross section A-A' is shown with a yellow line and arrows.

Section	2009	2010	
	June	*May*	*September*
YG1			
YG2			Shallow depression at the centerline, 2" wide, 1"deep
YG3			Longitudinal depression from YG3 to YG8 recently filled with new material (thickness: 5"). New depressions/potholes and settlement beside the patches
YG5			
YG4		Depression at the centerline from YG3 to YG9, 47" wide, 5" deep	
YG6	Depression at the centerline from YG6 to YG9, 98" wide, 5"deep		
YG7			
YG8			
YG9			
YG10			
YG11			
YG12			

Figure 9. Development of depressions at the AHTS from June 2009 to September 2010. Shading indicates that no depression, pothole, crack, or thaw settlement was observed. (CONTINUED ON NEXT PAGE).

13

Section	2011	
	May	*October*
YG1		Longitudinal depression, 59" wide, 2" deep
YG2		
YG3		
YG5		Repaving done in August (1½ month earlier). Depression at the centerline from YG5 to YG6, 55" wide, 2" deep
YG4		
YG6	Longitudinal depression, 40" wide, 6" deep	
YG7		
YG8		
YG9		
YG10		
YG11		
YG12		Longitudinal depression at the centerline, 35" wide, 2" deep

Figure 9 (CONTINUED). Development of depressions at the AHTS from May to October 2011. Shading indicates that no depression, pothole, crack, or thaw settlement was observed. (CONTINUED ON NEXT PAGE).

Section	2012	
	June	*October*
YG1	Longitudinal crack in the middle of the section 	Longitudinal crack in the middle of the section
YG2	Well-defined depression at the centerline of the road, 40" wide, 3" deep 	Road pavement maintenance at the end of the August, with 4"-thick fill. The longitudinal fill extends between YG2 and YG9. A new depression 47" wide and between 1 and 2" deep is now forming in the previously filled depression
YG3	Longitudinal depression from YG3 to YG8 at the centerline of the road formed in recently filled depressions, 75" wide, 3" deep 	
YG5		
YG4		
YG6		
YG7		
YG8		
YG9		
YG10		
YG11		
YG12	Depression at the centerline of the road, at the end of the section, 35" wide, 2" deep 	Longitudinal depression at the centerline, 40" wide, 3" deep

Figure 9 (CONTINUED). Development of depressions at the AHTS from June to October 2012. Shading indicates that no depression, pothole, crack, or thaw settlement was observed.
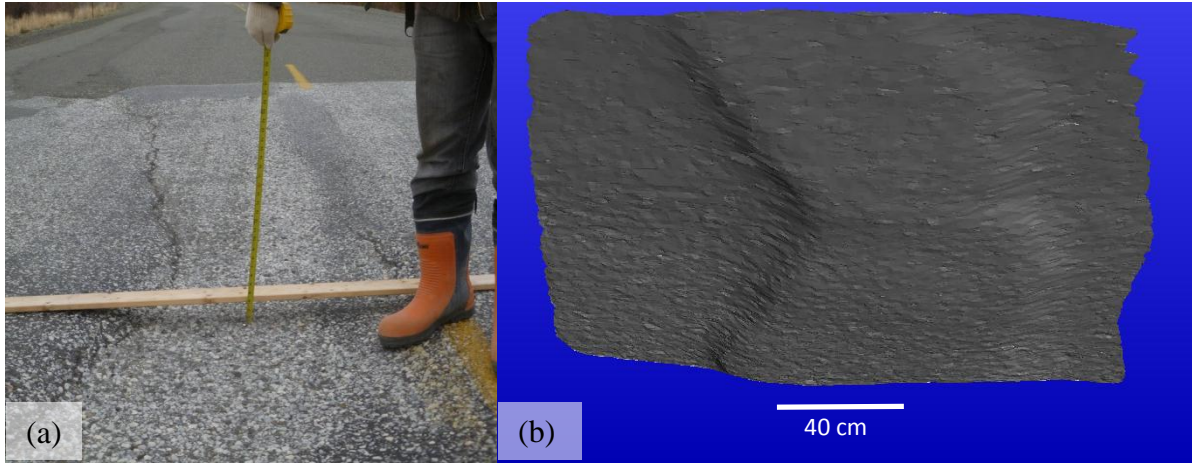
Figure 10. Road depression at Section YG12. (a) Photograph and (b) scan result for the same depression

40 cm

TASK 2: TO DEVELOP LABORATORY PROCEDURES FOR THE MEASUREMENT OF HYDRAULIC CONDUCTIVITY AND HEAT LOSS IN FROZEN SOIL SAMPLES

One of the goals of this research project was to develop the laboratory apparatus and procedures for measuring hydraulic conductivity and heat loss in frozen soil samples. This laboratory was to be located at UdeM, with UAF personnel assisting in the development. Unforeseen environmental issues with UdeM laboratory spaces prohibited the development of the laboratory for this testing during the project duration. Instead, UdeM personnel developed a temporary laboratory where preliminary hydraulic conductivity tests were conducted. We were unable to determine the hydrologic properties of frozen soils at temperatures just below phase-change due to these laboratory constraints; however, we were able to determine these properties in undisturbed soils that had just thawed (similar to field conditions). The following is a summary of preliminary laboratory testing, and *in situ* field testing of hydraulic conductivity.

Laboratory permeameter tests on unfrozen soil samples

We conducted unfrozen hydraulic conductivity tests on soil samples from AHTS using a standard permeameter (i.e., 2.5-in. diameter, 2-in. length). Based on Darcy's law, the hydraulic conductivity of a soil can be determined by measuring the amount of time it takes for a given volume of water to flow through a soil sample within the permeameter. Due to the relatively low permeability of the tested soils, the falling head method was used.

"Dry" (i.e., sample with degree of saturation (S) = 0), "humid" (i.e., sample with S = 0.5), or "saturated" (i.e., sample with S = 1) samples were placed into the permeameter in 0.2 to 0.8-in. thick lifts. Each lift was compacted by applying 15 blows with one of two devices. The first device consisted of a spoon folded in 90º to reach the bottom of the cylinder; compaction was obtained by pushing with a force of about 10 lb. The second device was a steel bar 1 ½ in. in diameter and 8-in. long; each blow consisted of a drop of the bar on the soil sample from a relative elevation of 8 in. As the hydraulic conductivity for a given soil type varied by as much as one order of magnitude depending on the compaction device used, the adjectives "lightly packed" and "compacted" were used to indicate compaction with the folded spoon and the steel bar, respectively. For the "liquefied" silt samples, the soil was stirred and shaken, then allowed to settle due to gravity. A summary of the tests conducted and the results is provided in Appendix F.

In situ tests at the AHTS

The tension infiltrometer is a field device used to validate hydraulic conductivity values derived from laboratory permeameter tests. We conducted field measurements of hydraulic conductivity using a mini-disk infiltrometer (see Figure 11a). Measurements were made from the surface to a depth of 13.8 in. near cross section A-A'. We placed the tension infiltrometer over an even soil surface, and allowed water to flow out of the device through a porous stone into the underlying material. Infiltration rates were measured until a steady state was reached. We retrieved a soil sample from this location for water content analysis and laboratory hydraulic conductivity testing. Results are summarized in Table B-2.

Figure 11. Tension infiltrometer tests (a) in the field and (b) in the laboratory.

Laboratory infiltrometer tests on unfrozen soil samples

We conducted laboratory measurements of hydraulic conductivity using the mini-disk infiltrometer on the soil samples that were collected during the *in situ* testing. Each sample was mixed, leveled, and packed into a plastic container about 12 in. in diameter and 6 in. high with a spoon and a spatula (see Figure 11). Results are summarized in Table B-3.

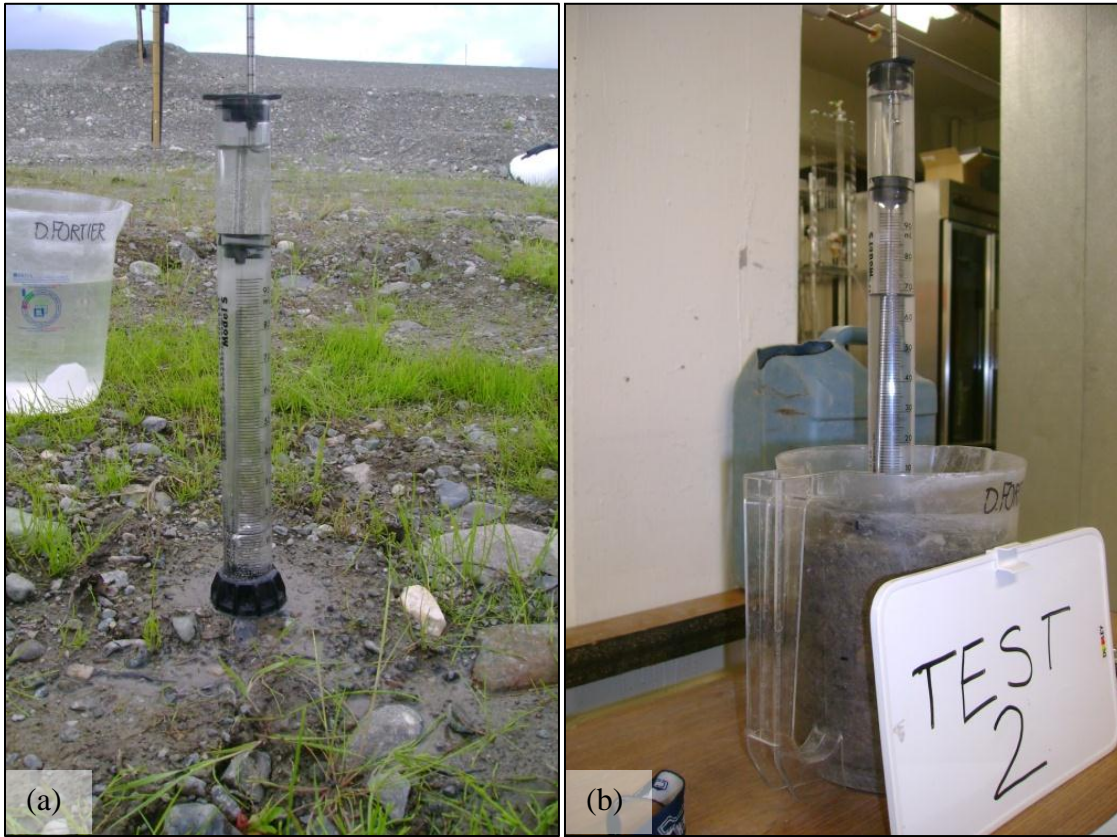## TASK 3: TO MEASURE UNFROZEN WATER CONTENT OF UNDISTURBED PERMAFROST SOILS FROM THE AHTS

We originally proposed to measure the unfrozen water content of soil samples obtained from the AHTS. The proposed measurement device was a MARAN Ultra 23 MHz Nuclear Magnetic Resonance (NMR) apparatus, complete with a variable temperature probe, located in the UAF Geological Materials Engineering laboratory. In the process of testing the device for temperature stability, the silicon oil fluid that we used for cooling leaked into the device, contaminating the NMR probe. The probe then had to be shipped to the manufacturer for cleaning. These delays prevented us from measuring the unfrozen water content of the samples in the laboratory.

To rectify this issue so as to continue with the modeling in a timely fashion, we developed an unfrozen water content curve based on field measurements. Unfrozen water can be measured *in situ* using Time Domain or Frequency Domain Reflectometry (TDR, FDR), which is also called Time Domain Transmissometry (TDT) (Yoshikawa and Overduin, 2005). During the first year of our study, we installed four FDR instruments (i.e., the CS616 water content reflectometers) to measure volumetric soil moisture during the summer months and the unfrozen water content during the winter months. For two locations (referred to as "upslope" and "downslope") that were immediately adjacent to ADAS-1, we installed both an FDR instrument and a temperature sensor (CS107) at depths of 4 in. (in the surficial organic soil) and 8 in. (in silty mineral soil). The soil moisture data and temperature data are summarized in Figure 12 and Figure 13 respectively. In general, the surficial organic soil has a lower moisture content during both the summer and winter months than does the silty mineral soil. The exception to this trend occurs in early summer, when the organic soil contains the moisture from snowmelt but the silty soil has not yet thawed. There is a higher variation in temperatures at the 4 in. depth during the summer months and colder temperatures in the winter months due to its closer proximity to the surface.

Using FDR instruments to measure unfrozen water content in soils is possible because the device uses the dielectric constant as a proxy for liquid water. In a heterogeneous soil, the reading depends on the dielectric constant of all of the soil components. The dielectric constants of mineral soil, water, and air are 4, 80, and 1, respectively (note that the dielectric constant is unitless as it is a ratio between the permittivity of a substance to the permittivity of a vacuum). Since water has the highest dielectric constant, this method is sensitive to soil moisture. When freezing occurs, the liquid water changes to ice, which has a dielectric constant of 3. Because the dielectric constant of ice is a little higher than that of air, the factory calibration may result in reduced accuracy; however, previous research indicates that this error is small (Boike et al., 2008; Spaans and Baker, 1996). Veldkamp and O'Brien (2000) presented a correction, which includes the substitution of the dielectric constant of air with that of ice. These devices are factory-calibrated for mineral soil; to measure volumetric soil moisture accurately for a site, the FDR instruments should be calibrated for the *in situ* soil type, which holds especially true for organic soils. Without calibration, the soil moisture measurement accuracy is ±2.5%.
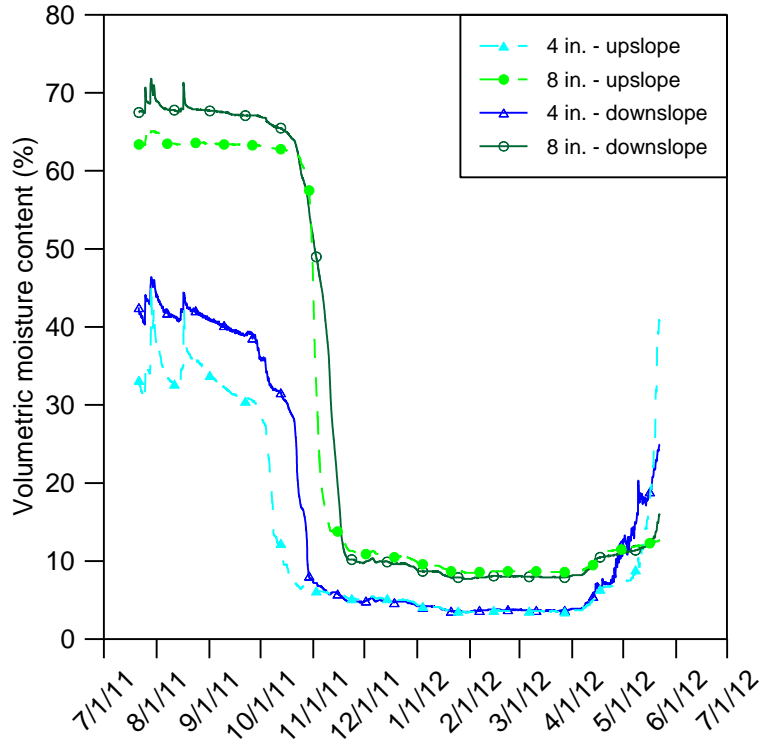
Figure 12. *In situ* soil moisture measurements versus time for all of the FDR (CS616) sensors.
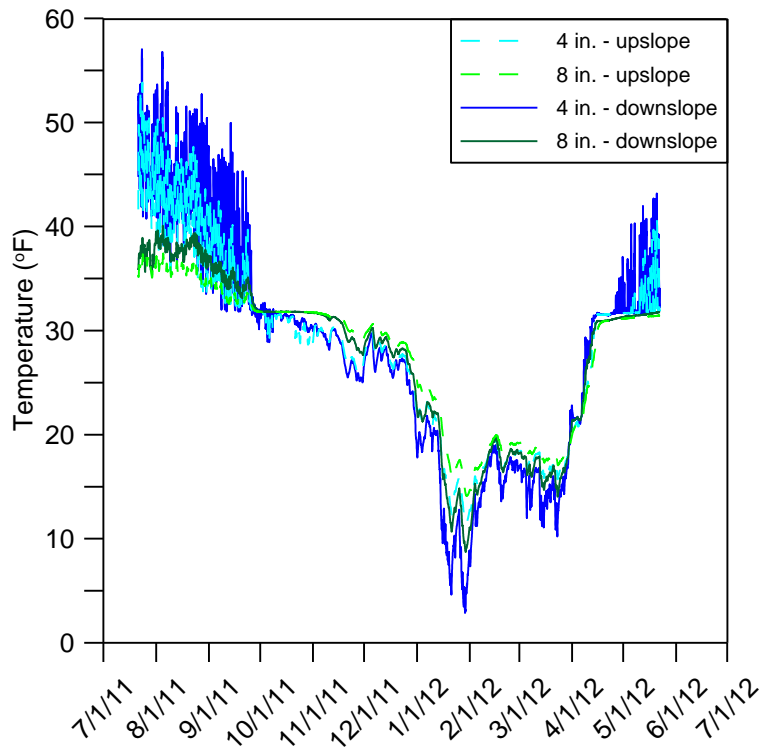

Figure 13. *In situ* soil temperature measurements versus time for all of the CS107 sensors.

20

We used two equations to relate the soil moisture content measured with the FDR instrument to soil temperature measured at the same location. First, the general Clapeyron equation relates the freezing temperature to a liquid water pressure head:

$$h = \left(\frac{L_f}{273.15*g}\right)T + h_i \tag{1}$$

where h is the liquid water pressure head, L_f is the latent heat of fusion, g is the acceleration of gravity, T is the temperature of the freezing mixture, and h_i is the ice pressure. In the case where ice pressure is zero (non-heaving soils), the liquid water pressure becomes a linear function of the freezing temperature, $h = 122T$ (with T in °C and h in m). Spaans and Baker (1996) suggest that the liquid water pressure head can be related to the suction pressure head in drying soils, incorporating the similarity between the freezing characteristic and the soil moisture characteristic curves. For our modeling purpose, we used the Van Genuchten (1980) curve for the soil moisture characteristic:

$$S_l = \left(\frac{1}{(\alpha h)^n + 1}\right)^m \tag{2}$$

where S_l is the liquid water saturation, and α, n, and m are fitting parameters (used to fit the curve to the measured data). The value for S_l is found using the following relationship:

$$\theta_l = \theta_r + (\theta_s - \theta_r)S_l \tag{3}$$

where θ_l, θ_s, and θ_r are the liquid water content, the saturated liquid water content (also termed porosity) and the residual liquid water content, respectively. Fitting parameters for the Van Genuchten curve, as well as values for porosity and residual water content, can be found in the literature. The advantage of using the Van Genuchten curve is that the fitting parameters also help fit the relative hydraulic conductivity for the soil:

$$K = K_s S_l \left(1 - \left(1 - \left(S_l^{(1/m)}\right)\right)^m\right)^2 \tag{4}$$

where K is the relative hydraulic conductivity, and K_s is the saturated hydraulic conductivity. Figure 14 and Figure 15 illustrate the comparison of the fitted curves to the measured data for the surficial organic soil and silty mineral soil, respectively. There is much greater variation in moisture content with temperature for the organic soil since it was unsaturated.

To check the suitability of the unfrozen water content functions prior to their use in the rest of the modeling, the fitted curves were first evaluated in the COMSOL Multiphysics numerical model. To simplify the solution, the model was designated as non-heaving, and used the Richard's equation for liquid water movement in saturated and unsaturated porous media and Fourier's law for heat flow in porous media as the governing equations. A more in-depth discussion on these governing equations and the numerical model is provided under TASK 4.

Comparisons of the modeled to measured temperatures are provided in Figure 16 for the 4 in. depth, and in Figure 17 for the 8 in. depth. Likewise, Figure 18 and Figure 19 provide similar comparisons of the modeled soil moisture values to the measured values at depths of 4 in. and 8 in., respectively. Despite some variation, the modeled fit produced is reasonable considering the limited length of data and variation among the readings from each depth.
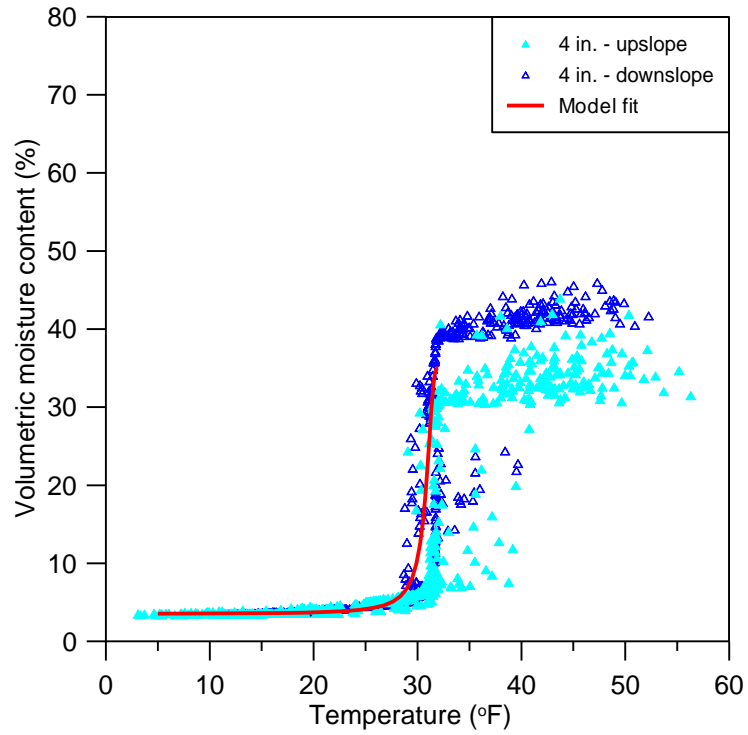
Figure 14. Comparison of fitted curve to the measured soil moisture data for the surficial organic soil (4 in. depth).
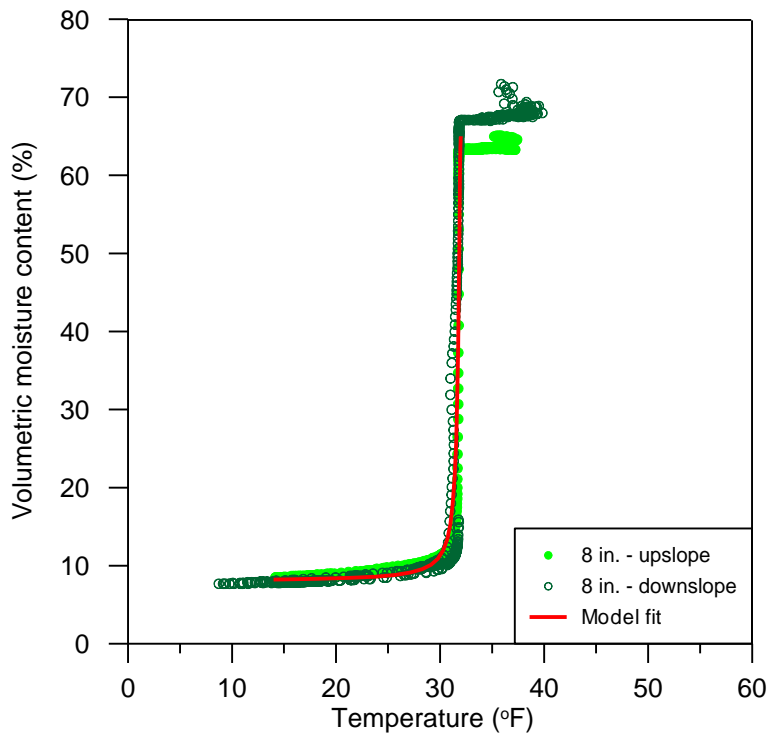
Figure 15. Comparison of fitted curve to the measured soil moisture data for the silty mineral soil (8 in. depth).

Figure 16. Comparison of modeled to measured soil temperatures from the 4 in. depth (i.e., the surficial organic soil).

Figure 17. Comparison of modeled to measured soil temperatures from the 8 in. depth (i.e., the silty mineral soil).

23
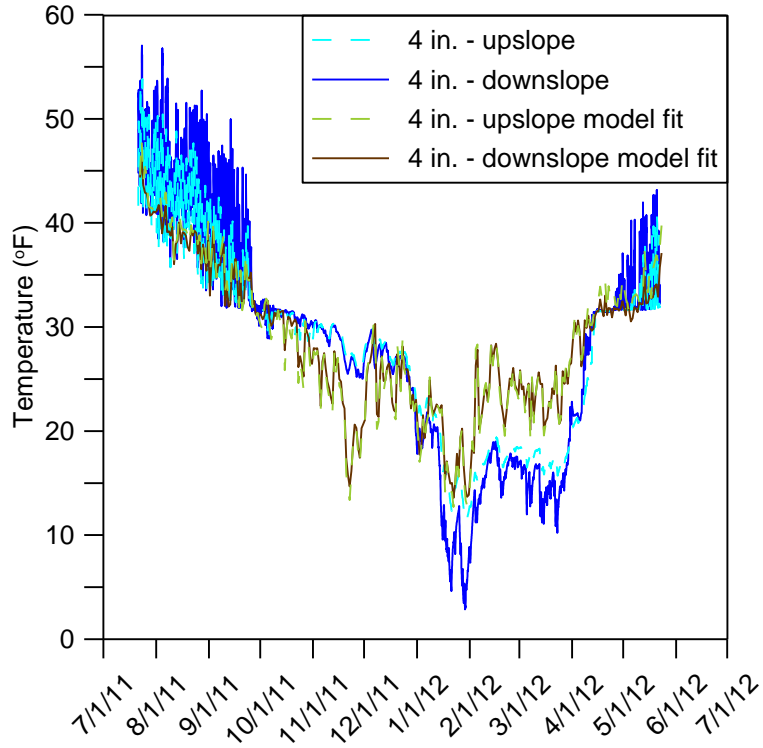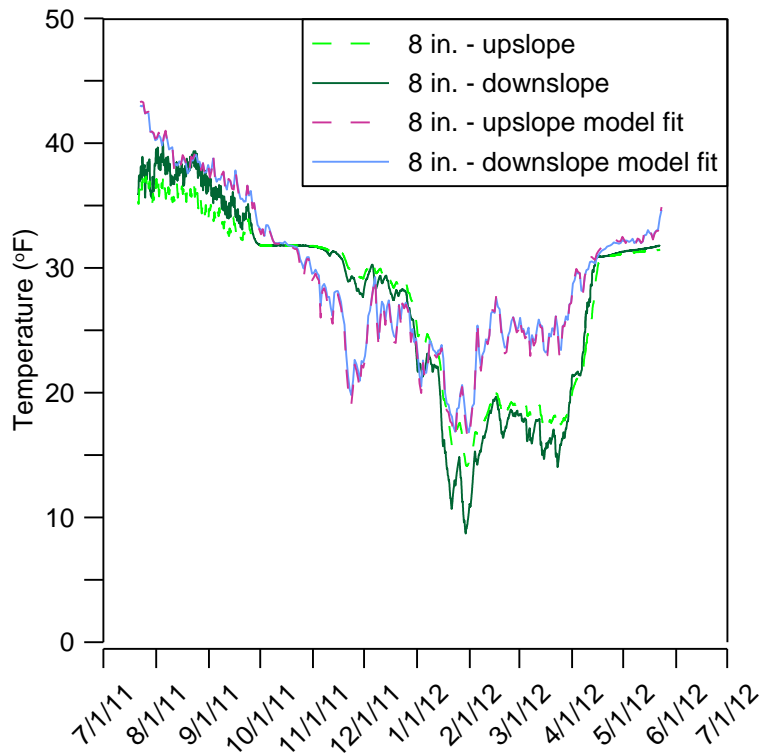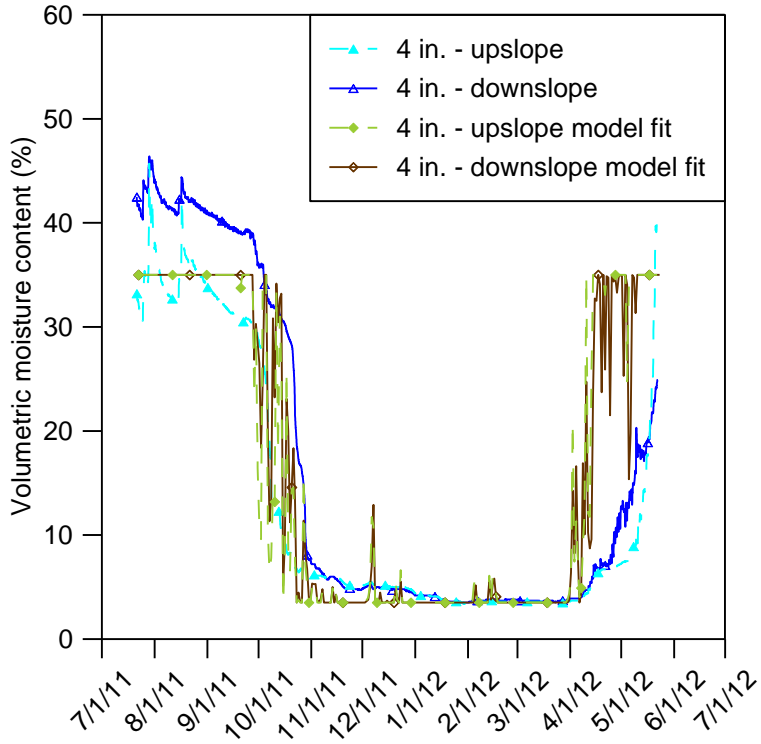
Figure 18. Comparison of modeled to measured soil moisture content from the 4 in. depth (i.e., the surficial organic soil).
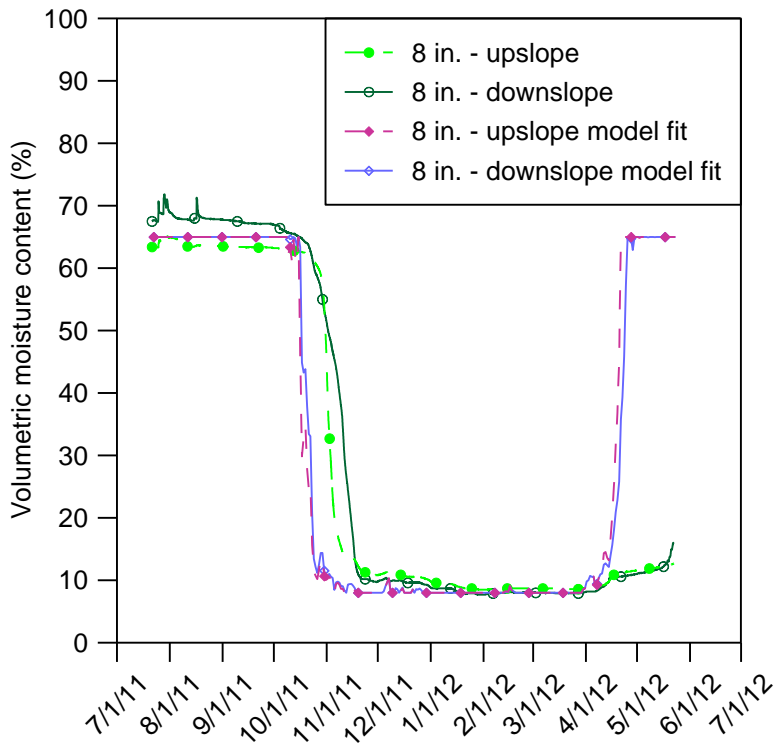

Figure 19. Comparison of modeled to measured soil moisture content from the 8 in. depth (i.e., the silty mineral soil).

TASK 4: TO PRODUCE A NUMERICAL MODEL THAT INCLUDES BOTH CONDUCTIVE AND ADVECTIVE HEAT TRANSFER

For this task, we proposed to develop a numerical model that includes both conductive and advective heat transfer, using COMSOL Multiphysics, a commercially available software package. In order to produce this final model, it was necessary to develop a series of simulations to test the model stability and to validate against measured parameters. Figure 20 is a graphical summary of the steps in the modeling process. First, a one-dimensional (1D) steady state model was produced to determine the overall temperature distribution of the foundation soils and the lower extent of the permafrost. Next a 1D transient model was produced to determine the appropriate upper boundary conditions for an active layer depth that is reasonable for the area. The results of both models were compared to measured data available from the AHTS area.

The input parameters and results from the 1D models were used as input parameters for the suite of two-dimensional (2D) models. First, a model was produced that only incorporated heat conduction. Next, a fully coupled model where the groundwater flow "was turned on" was produced. Results from each of these models were compared against the measured data, and adjustments to the input parameters were made as needed. As a final step, we developed a fully coupled model using the GEO-STUDIO software package, using a combination of the TEMP/W and SEEP/W modules (referred to hereafter as TSW). We also produced a COMSOL model using the same set of input parameters to compare the results from the two different software packages. The governing equations and input parameters for each model will be discussed separately, and the results of the TSW – COMSOL model comparison are included in Appendix G.

1D MODELS

Governing equation

We developed the 1D models to verify the thermal regime within the foundation soils before introducing the highway embankment into the modeling domain. These models only included conductive heat transfer, as we assumed that the natural ground is in thermal equilibrium with the near-surface groundwater flow. The equation for heat transfer in fluids used in the program is the following form of Fourier's Law:

$$\left(\rho C_p\right)_{eq} \frac{\partial T}{\partial t} + \rho C_p u \cdot \nabla T = \nabla \cdot (k \nabla T) + Q \tag{5}$$

where ρ is fluid density, C_p is the fluid heat capacity at constant pressure, T is temperature, t is time, u is Darcy's fluid velocity field, k is fluid thermal conductivity, and Q is a source term.

Input parameters

The subsurface in this 1D model consisted of a 1.15-ft thick peat layer placed above silt. The silt extended to the bottom of the model (i.e., 2,625 ft bgs), as the depth to the bedrock surface in this area is unknown. The thickness of the peat layer was based on field measurements at the AHTS. The mesh applied to the 1D model had a greater density of nodes near the top with distance between nodes increasing with depth. At the surface, nodes were spaced every 0.8 in. and increased to 0.6 ft apart at the model bottom.

The three materials used in the 1D models were peat, silt, and water. The input parameters for the peat and silt included functions for thermal conductivity and heat capacity (see Figure 21
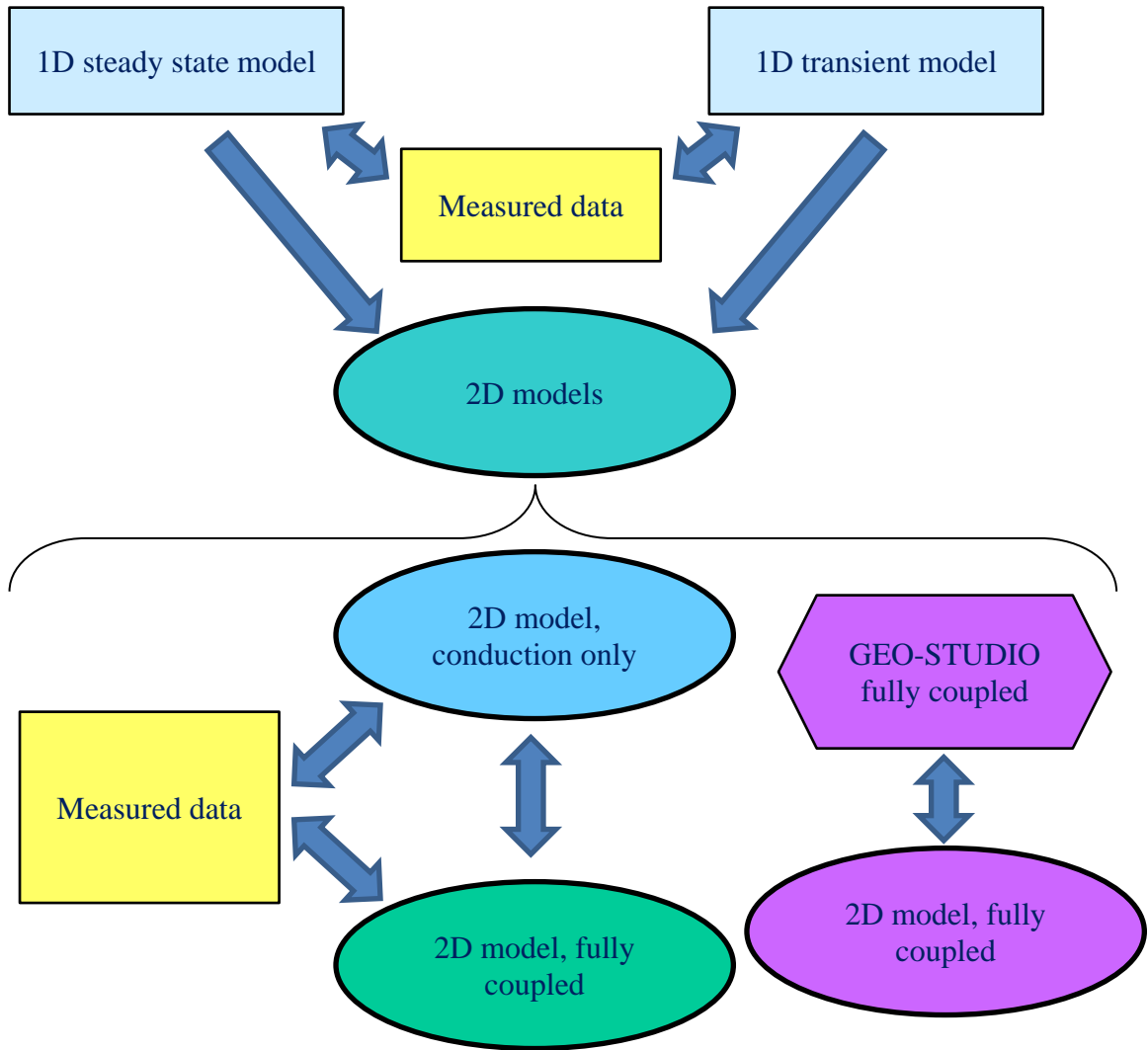
25

Figure 20. Flow chart detailing steps in the modeling process. All of the models were produced using the COMSOL Multiphysics software, unless otherwise noted.
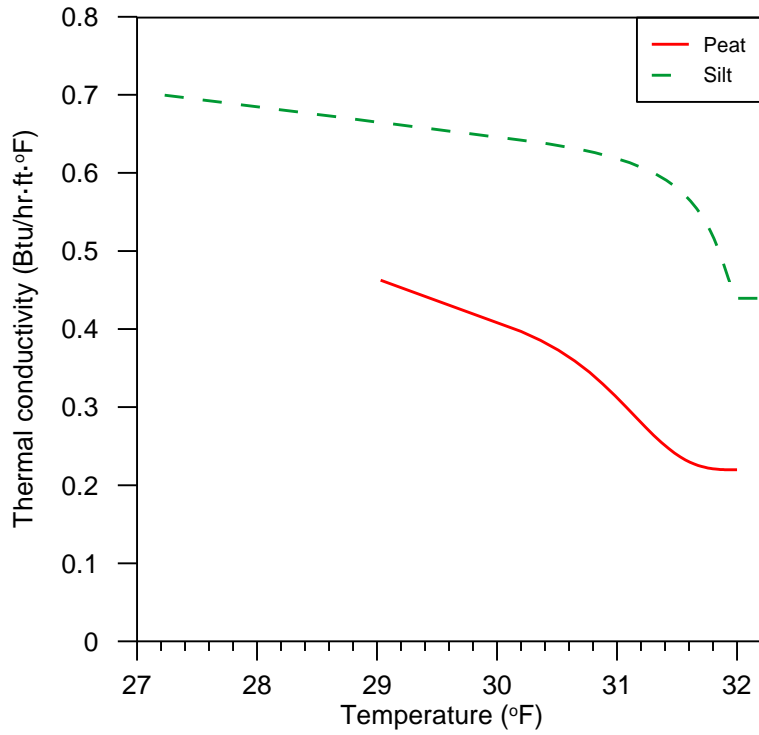
Figure 21. Thermal conductivity functions for the peat and silt layers in the 1D models.
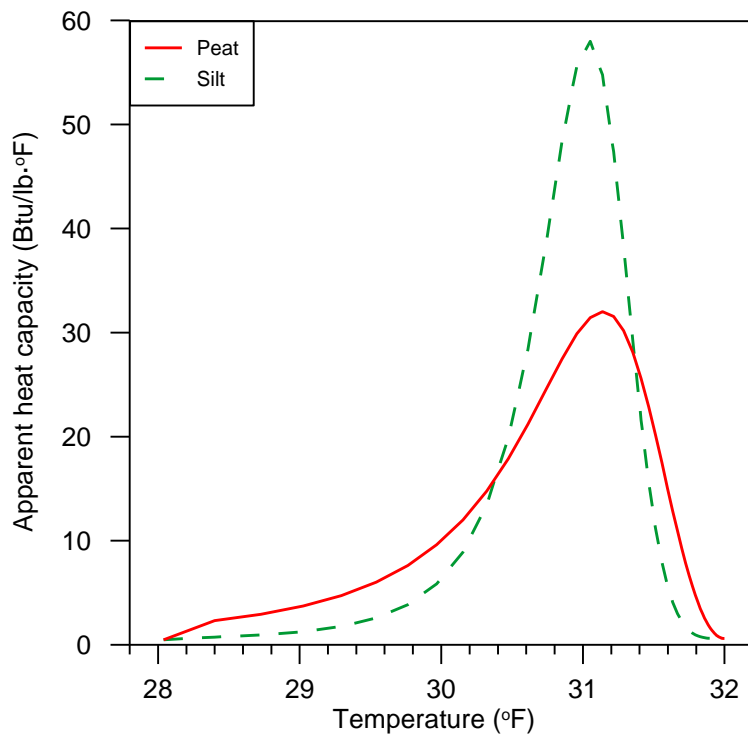

Figure 22. Apparent heat capacity functions for the peat and silt layers in the 1D models.

and Figure 22). The step-functions developed from average thermal conductivity values obtained from laboratory measurements (see Appendix C) were scaled and smoothed using the unfrozen water content curves from Task 3. The saturated liquid volume fraction for the silt was set at 0.65, based on measured values at the AHTS. For peat, the saturated liquid volume fraction was estimated to be 0.90. This value was based on literature and prior experience in the field, as our measured values indicated the peat was unsaturated during the measurement period. The apparent heat capacity in Figure 22 incorporates latent heat effects, thus resulting in the high values around phase change. Properties for water in the model were defined by the software and included specific heat, heat capacity at constant pressure, density, thermal conductivity, and dynamic viscosity.

Boundary conditions

For both 1D models, we applied a geothermal heat flux of 0.008 Btu/hr·ft^2 as the lower boundary condition, which is an average value used for heat flux in modeling in Alaska (Marchenko et al., 2008). As part of the upper boundary condition for these models, we used a 30-year average daily temperature data set measured in Chicken, Alaska. We used this data set because the climatic conditions for Chicken are similar to Beaver Creek, Yukon, and because consistent, long-term data were not available for Beaver Creek. For the 1D steady state model, we applied a mean annual surface temperature of 26.2ºF as the upper boundary condition. This value was obtained by applying an *n*-factor of 0.45 to the mean annual air temperature of 20.0ºF calculated from the 30 year data set. For the 1D transient model, we applied a surface temperature function as the upper boundary condition. We developed a sinusoidal function from the 30 year data set using a mean annual temperature of 20.0ºF and an amplitude of 70.9º (see Figure 23). Table 2 contains a comparison of the freezing and thawing indices calculated from both the measured data and fitted curve. Because of the good agreement, we employed the sinusoidal function in the model to save computational time. The air temperature function was modified using an *n*-factor of 0.45 to represent the effects of the mossy vegetation at the surface.

2D MODELS

Governing equations

The 2D model that only incorporated heat conduction also used Eqn. 5. For the 2D model that incorporated groundwater flow, in addition to Eqn. 5, we used the Richard's equation for flow in variably saturated porous media:

$$\rho \left(\frac{C_m}{\rho g} + S_e S \right) \frac{\partial p}{\partial t} + \nabla \cdot \left(\frac{-\rho \kappa_s k_r(\epsilon_p)}{\mu} (\nabla p + \rho g \nabla D) \right) = Q_m \tag{6}$$

where ρ is fluid density, C_m is the specific moisture capacity, g is gravitational acceleration, S_e is the effective saturation, S is the storage coefficient, p is pressure, t is time, κ_s is hydraulic permeability, k_r is relative permeability, ϵ_p is a volumetric weighting factor, μ is the fluid dynamic viscosity, D is elevation, and Q_m is the fluid source (or sink). This equation is used to solve both the saturated and unsaturated domains. In the unsaturated domain, the soil water retention characteristic in the Richard's equation was approximated with the van Genuchten equation (van Genuchten, 1980):

$$\theta = \left(\frac{1}{1+(\alpha \psi)^n} \right)^m \tag{7}$$
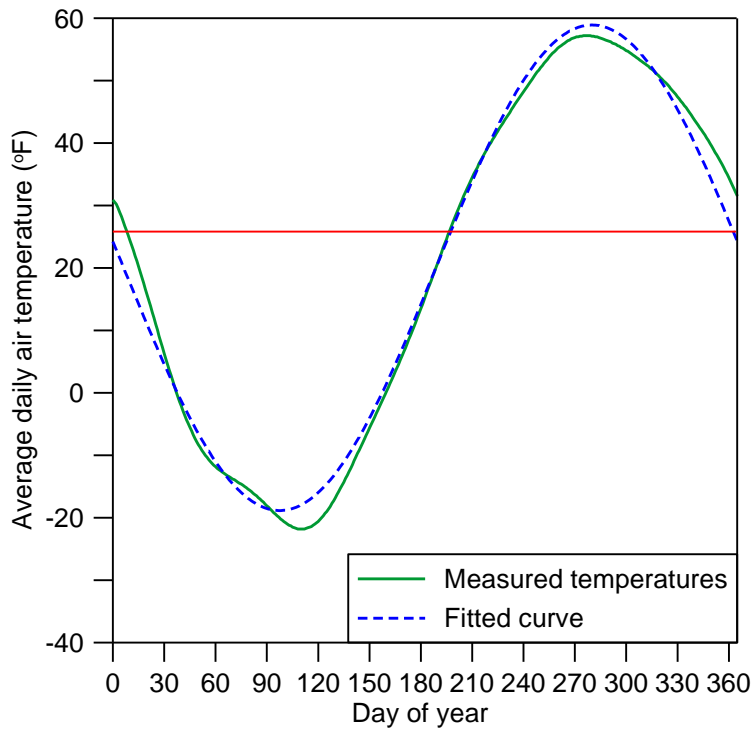
28

Figure 23. 30-year daily temperature average temperature function used for 1D model.

Table 2. Freezing and thawing indices for measured data and fitted curve.

	Freezing index (ºF-days)	Thawing index (ºF-days)
Measured data	6912	2549
Sinusoidal	6917	2548

where θ is volumetric water content, ψ is capillary pressure head, $\alpha, m,$ and n are equation parameters, and m is a function of n:

$$m = 1 - \left(\frac{1}{n}\right) \tag{8}$$

Thus, the liquid saturation depends on the liquid water pressure head and the three equation parameters, $\alpha, m,$ and n. These parameters are specific for a particular soil, and can be found in the literature or fitted to laboratory data. For our model, we selected parameters both from the literature and based on previous experience. To account for storage, a linearized storage model was used with the Richard's equation:

$$S = \epsilon_p \chi_f + (1 - \epsilon_p)\chi_p \tag{9}$$

where S is storage, χ_f is the compressibility of the fluid, and χ_p is the effective compressibility of the matrix (Gerke and van Genuchten, 1993).

Input parameters

For the 2D models, we chose cross section A-A' (CS A-A'), as indicated in Figure 6. We measured the ground surface of the cross section using a hand level and tape. At this location, the embankment is approximately 213-ft wide from toe to toe, and approximately 26-ft high from the driving surface to the surface of the surrounding natural ground. The subsurface of the model consisted of a 1.15-ft thick peat layer (based on field measurements), underlain by silt to the bottom of the model (see Figure 24).

Table 3 is a summary of the material input parameters for the 2D models. The unfrozen water content function was calculated using the van Genuchten curve (see Task 3 and Figure 14 and Figure 15). Using the van Genuchten parameters listed in Table 3, it was necessary to reduce the freezing pressure (FP) parameter to 20 for peat and silt, and to 1 for the gravel embankment to make the solution numerically stable. The FP parameter is found from:

$$h = FP \cdot T \tag{10}$$

where h is liquid water pressure (m) and T is temperature (°C). Theoretically, FP can be as high as 122 (see the discussion in Task 3), but this requires a moving boundary solution scheme or an extremely fine grid of 0.1 in, neither of which are practical solutions for this modeling. Changing the FP parameter distributes the amount of latent heat released over a wider range of temperatures just below freezing, while maintaining the total amount of energy released during freezing.

The energy of freezing (i.e., latent heat) was added to the heat capacity in Fourier's Law (Eqn. 5). The heat capacity was multiplied by the temperature gradient, which required that the latent heat be converted to the same units. This was calculated using the differential or liquid water content curve for each soil type, which is termed the soil freezing characteristic (SFC) curve. Figure 25 contains SFCs for four different FPs and the associated liquid water saturation curves. The FP controls the amount of liquid water that freezes at a given temperature, and the shape of the curve is determined by the parameters in the van Genuchten equation (note: for the 1D models, we used an FP of 122 because it is easy to simulate a fine grid spacing in one dimension).

In addition to its dependence on temperature, the amount of latent heat released also depends on the saturation of the soil before it freezes. An unsaturated soil will not release latent heat before
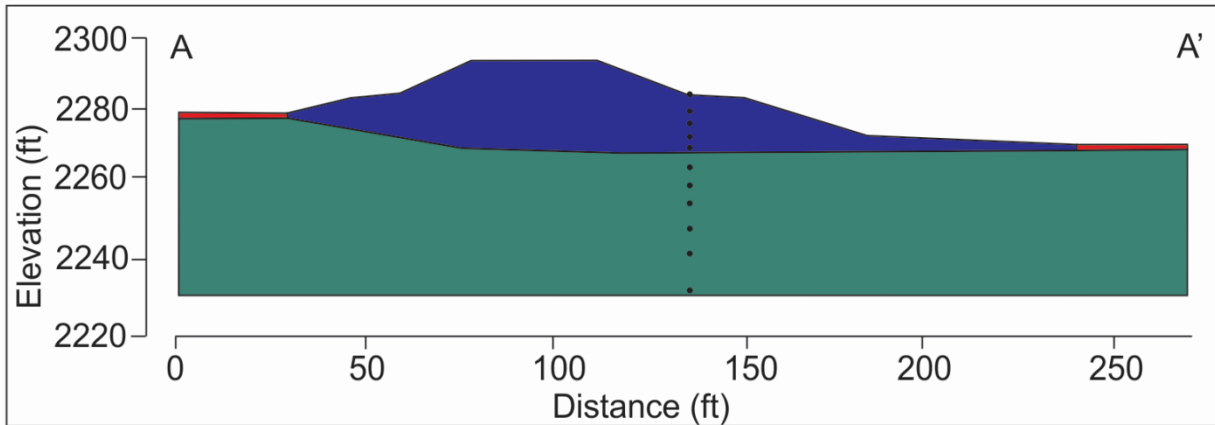
Figure 24. Modeled cross section CS A-A' facing south along the roadway embankment. The silt, peat, and embankment layers are shown in green, red, and blue, respectively. Thermistor beads from a string located near CS A-A' are indicated by the line of vertical black dots.

Table 3: Soil input parameters for the 2D models. [a] denotes measured laboratory values, [b] denotes measured field values, and [c] denotes estimated values derived from the literature.

| Variable	Embankment	Peat	Silt
Dry Thermal Conductivity (Btu/hr·ft·°F)[b]	0.62	0.02	1.22
Dry Heat Capacity (Btu/ft^3·F)[b]	20.87	29.61	22.63
Frozen Saturated Hydraulic Conductivity (ft/s)[c]	3.3e-07	2.9e-06	9.8e-08
Unfrozen Saturated Hydraulic Conductivity (ft/s)[b]	3.3e-04	2.9e-04	9.8e-06
Dry unit weight (lb/ft^3)[c]	124.9	59.3	103.0
Residual Water Content (ft^3/ft^3)[c]	0.01	0.01	0.06
van Genuchten[c]			
α	2	0.1	0.1
n	2	2.5	1.6
m (1-1/n)	0.5	0.6	0.375
Porosity (%)	5	95	55

31
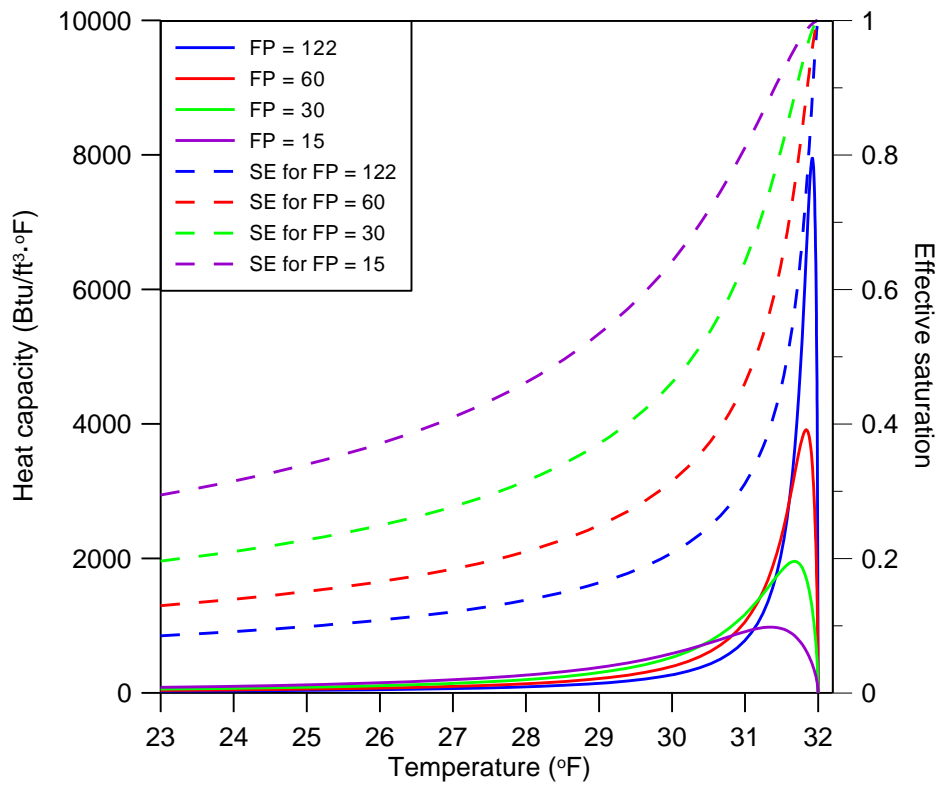
Figure 25. Variation in heat capacity with temperature, freezing pressure (FP) and effective saturation (SE) during a COMSOL simulation. This example was calculated for silt with a dry unit weight of 103 lb/ft^3.

its freezing temperature drops below the liquid saturation level for that soil compared with the saturation level in the Richard's equation. In the model, this was dynamically accounted for by using the liquid saturation in the Richard's equation to determine if there is latent heat release for a given temperature.

Similarly, the hydraulic conductivity was scaled using a temperature-dependent liquid saturation curve. The frozen and unfrozen parameters listed in Table 3 were scaled over a specified temperature interval where phase change occurred according to the liquid saturation. The hydraulic conductivity was also dependent on the saturation level in the Richard's equation, and was scaled using the following form of the van Genuchten equation:

$$K(Se) = \sqrt{Se} * \left[1 - \left(Se^{1/m}\right)^m\right]^2 \tag{11}$$

where K is hydraulic conductivity, and Se is the effective saturation of the soil.

The thermal conductivity was scaled directly using the saturation level from the Richard's equation. The COMSOL software uses a volumetric average based on the contents of the domain, which vary with temperature and saturation. Thus, the thermal properties (i.e., heat capacity and thermal conductivity) are calculated based on the amount of solid porous material, liquid water, and ice in the domain. The solid porous material in our model was gravel, peat, and silt, the liquid water fraction was based on the Richard's equation, and the ice volume fraction was calculated based on the difference between the water content in the Richard's equation and the liquid water content calculated from the freezing temperature. The dry heat capacities for the solid porous materials are listed in Table 3. The value for heat capacity of water is given in COMSOL as a function of temperature. At freezing, the heat capacity of water and pure ice are 62.38 Btu/ft^3·°F and 28.8 Btu/ft^3·°F, respectively. The thermal conductivity of water and ice were set at 0.35 Btu/hr·ft·°F and 1.27 Btu/hr·ft·°F, respectively.

Due to the dependence of thermal conductivity and heat capacity on temperature, effective saturation, and ice content, they cannot be plotted as traditional functions. Rather, Figure 26 through Figure 30 illustrate each parameter's distribution through the model space for November 30. As the COMSOL Multiphysics software is setup for calculations in SI units, it does not provide the Imperial unit equivalent of many of the input parameters and thus most of these screen shots from the model are in SI units; however, the range of the variable plotted is provided in Imperial units in the figure caption where necessary.

Boundary conditions

The sides of the model are zero flow boundaries. We tested the model using two lower boundary conditions: a fixed temperature of 31.3°F (measured in a deep borehole below the depth of zero annual amplitude at the AHTS) and a heat flux of 0.008 Btu/hr·ft^2 (Marchenko et al., 2008).

For all models, the upper boundary condition was air temperature scaled using n-factors to obtain surface temperatures. Table 4 is a summary of the n-factor used in the 2D models. The n-factors for the embankment surface are based on a dark driving surface in the summer and a plowed surface in the winter. For the side slopes, we used the thermistor string data from 0.3 ft bgs to determine n-factors of 1.0 for summer and 0.5 for winter. These values represent a lighter surface in the summer, and additional snow cover accumulated from plowing of the driving surface. We used slightly higher n-factors for natural ground for the winter as compared to the
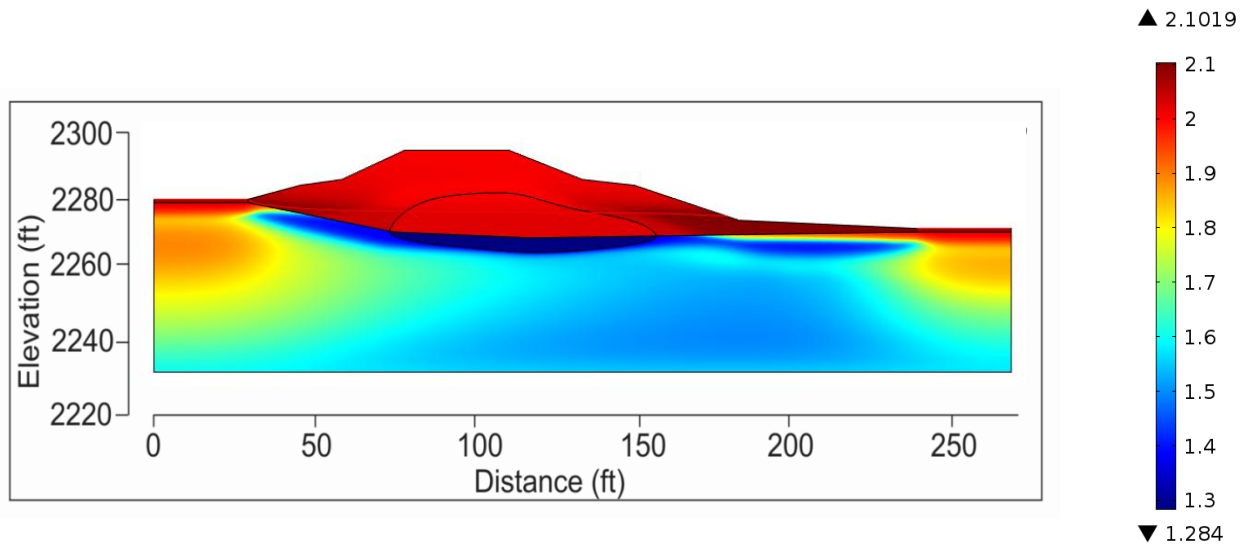
Figure 26. Thermal conductivity distribution for the 2D model domain. This value depends on temperature and degree of saturation (plot from November 30). The thermal conductivity values from COMSOL can only be output in SI units (i.e., W/m·K). The range of thermal conductivity shown is 0.742-1.214 Btu/hr·ft·^{o}F.
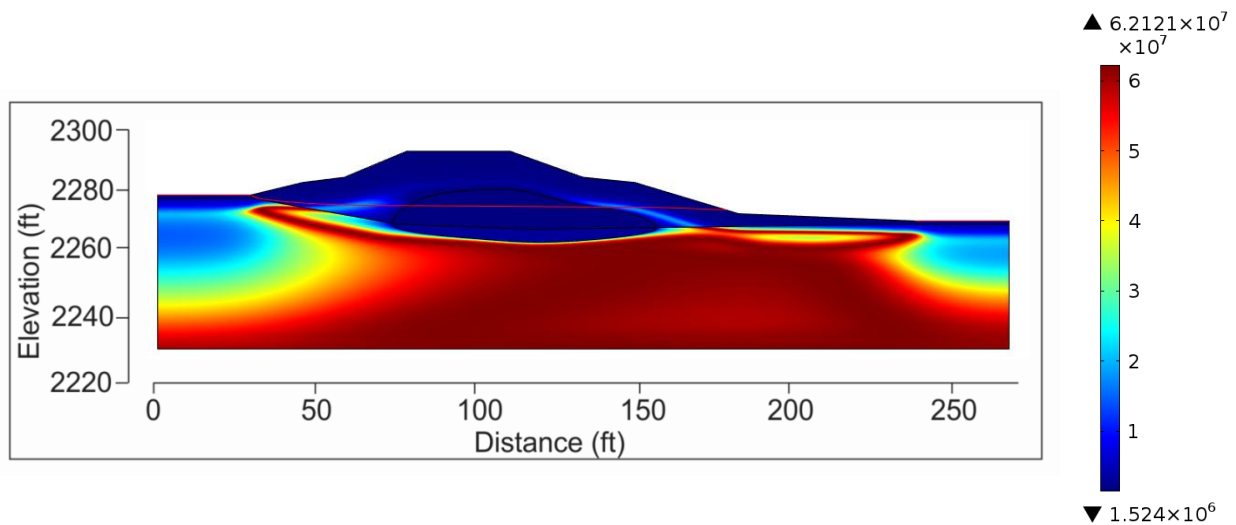

Figure 27. Equivalent volumetric heat capacity distribution for the 2D model domain. This value depends on temperature and degree of saturation (plot from November 30). High values represent phase change, the biggest source of heat consumption or release. The heat capacity values from COMSOL can only be output in SI units (i.e., J/m^3 K). The range of equivalent volumetric heat capacity shown is 22.7-926.2 Btu/ft^3·F.
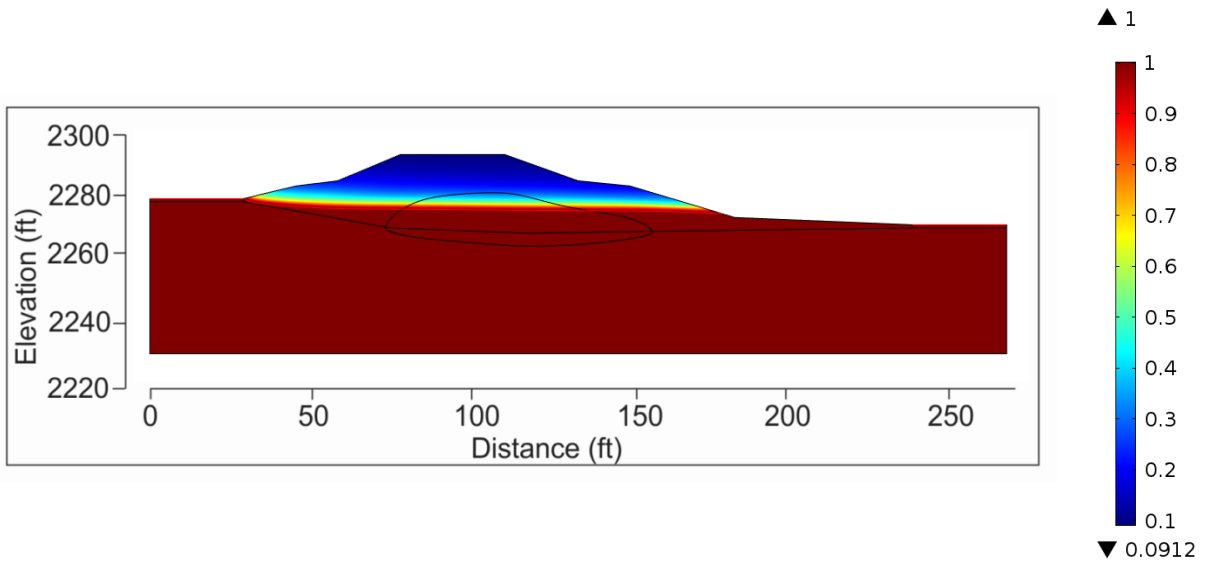
Figure 28. Effective saturation for the 2D model domain. The water content of the embankment is low above the water table (indicated by the red line). Effective saturation does not depend on temperature, and ranges from 0 to 1 (plot from November 30).
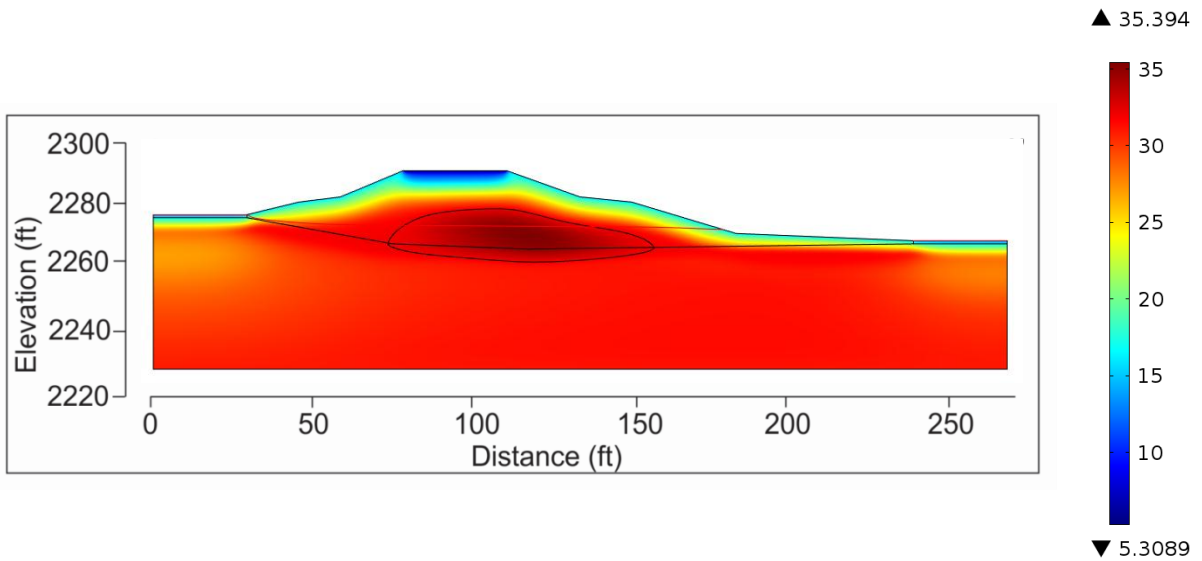

Figure 29. Temperature distribution in the 2D model domain. Temperatures are provided in ºF (plot from November 30).
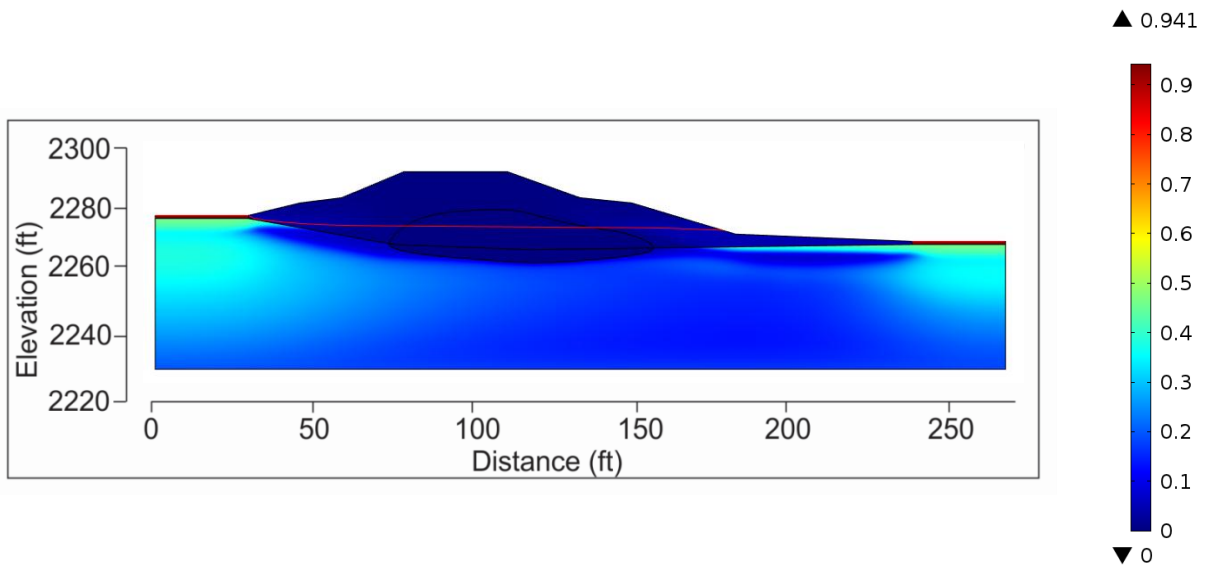
Figure 30. Volumetric ice content distribution in the 2D model domain. Volumetric ice content was determined using a combination of the Richard's equation and the soil freezing characteristic curve, and ranges from 0 to 1 (plot from November 30).

Table 4. *n*-factors used in the 2D models.

Surface type	Summer	Winter
Embankment surface	1.6	0.8
Side slopes	1.0	0.5
Natural ground	0.45	0.6

1D models, because we assumed that snow cover was more continuous near the embankment side slopes, allowing less heat to escape from below the snow.

We conducted three different simulations, each using different air temperature data sets for the upper boundary condition. For Part I, we used the daily air temperatures measured at AHTS from October 2008 to October 2009 (see Figure 31). We compared the results of the fully-coupled and conduction-only models to each other and to measured temperatures for six times during this year. For Part II, we used hourly air temperature data measured at AHTS from April 2009 through the fall of 2012. We compared the results of the fully-coupled model only to measured temperatures for three different depths. The same model mesh was used for Parts I and II, consisting of 11, 654 elements. Finally, Part III was a long-term simulation that was driven by the sinusoidal fitted curve from 30 years of air temperature data also used in the 1D transient model (see Figure 23). Two versions of the model were investigated, one using a fixed temperature and one using a geothermal heat flux for the lower boundary condition We ran these simulations for 50 years to compare the long-term results. Because of the longer run time, we made the model mesh coarser, reducing the number of elements to 4,232. For all models, the maximum time step was the same as the input data, and the minimum time step was determined based on the model solutions.

Initial conditions

The initial conditions in the 2D model domain were estimated using a steady-state solution with a mean surface temperature of 27.5°F for the natural ground surface, and a lower boundary temperature of 31.3°F (see Figure 32). This model was run for one year, and the resulting temperature distribution was used for the initial conditions in the remaining models (see Figure 33).
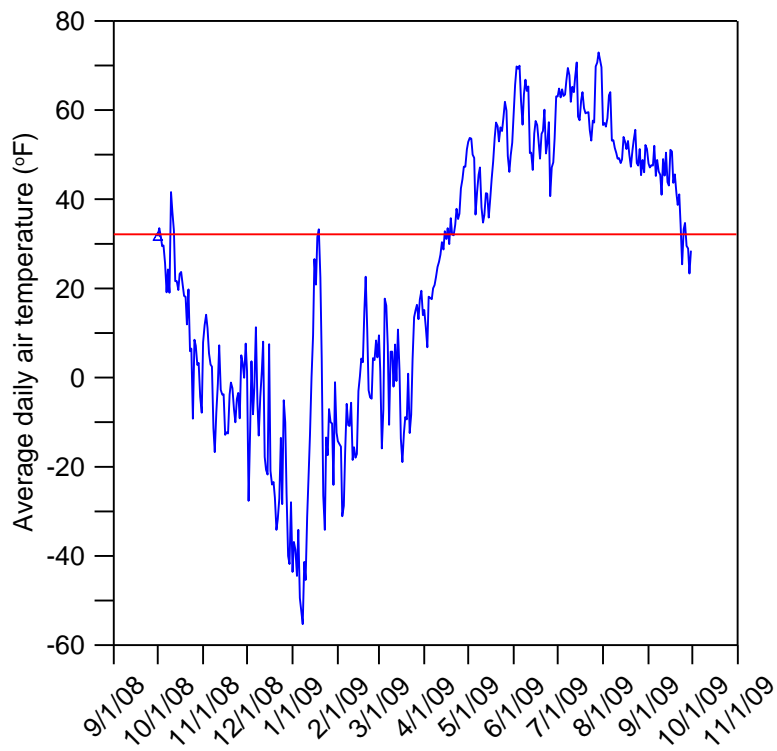
Figure 31. Average daily air temperature measured at the AHTS, Beaver Creek, Yukon, Canada. The phase-change isotherm is indicated by the horizontal red line.
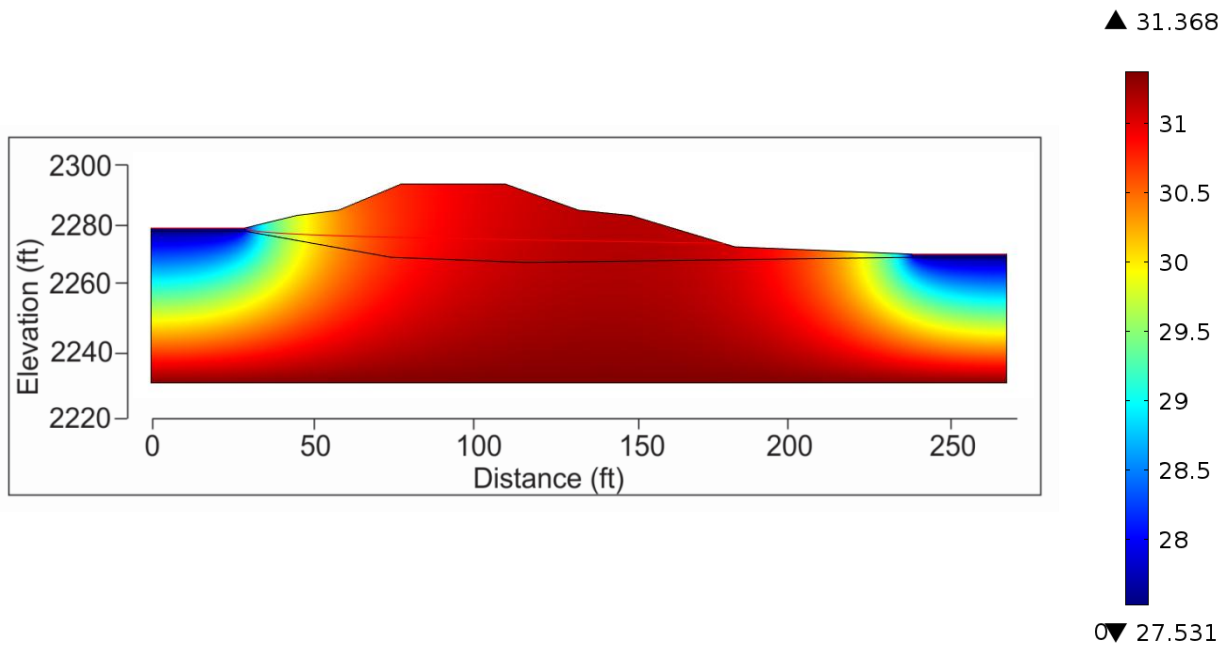
Figure 32. Initial conditions for the 2D model domain. Temperatures are provided in °F.
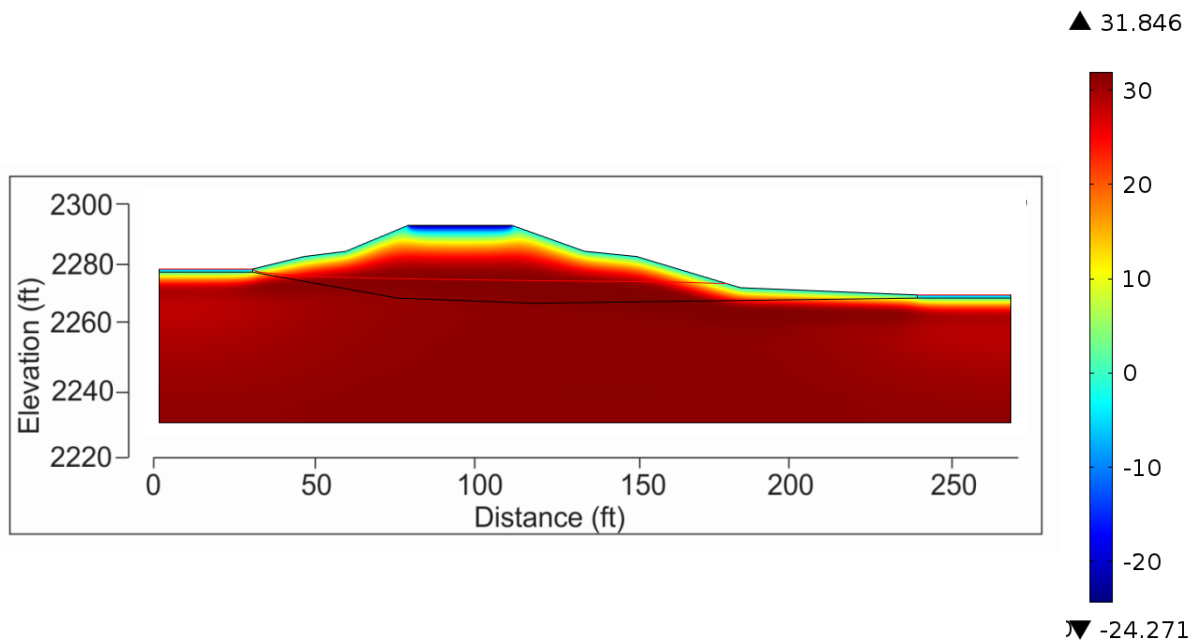

Figure 33. Results after a single year of simulation. This temperature distribution was used as the initial condition for the remaining simulations, starting on January 1. Temperatures are provided in °F.

TASK 5: TO COMPARE THE MODEL RESULTS AGAINST MEASURED HEAT AND WATER FLOW AT THE AHTS

We proposed to "ground-truth" the model against heat and water flow measurements within the embankment at the AHTS. Unfortunately due to the scheduling and equipment difficulties detailed under Task 1, we were unable to install additional sensor within and beneath the embankment. Despite the lack of measurements made at CS A-A' specifically for this project, we were able to utilize the wealth of data already acquired from the AHTS as additional input data and for comparison to the model results. For example, we used water level data from our measurements in 2011 and 2012 (see Appendix E).

To "ground-truth" the model, we compared modeled temperatures to those acquired from the two nearest thermistor strings to CS A-A'. These strings are YG7, which was installed in the embankment side slope near one of the longitudinal culverts (i.e., the red dot to the north of CS A-A' in Figure 6), and YG6, which was installed in the side slope and then covered with the snow shed treatment (i.e., the red dot to the south of CS A-A' in Figure 6; the white rectangles in the image are the snow sheds). Both strings consisted of 16 thermistors; however, we only used data from selected depths. For the Part I simulations, we compared the modeled temperatures to the YG7 thermistors located at 0.33, 4.9, 8.2, 11.5, 14.8, 19.7, 24.6, 29.5, 42.7, and 52.5 ft bgs. For the Part II simulations, we compared modeled temperatures to thermistor data from both YG6 and YG7 from common depths of 0.33, 5.9, and 8.2 ft bgs. The data from each of these strings is included in Chapter 3 within the comparison to the modeled results.

CHAPTER 3

FINDINGS

1D MODEL RESULTS

Figure 34 contains the temperature distribution for the 1D steady state model. This model indicates that the bottom of the permafrost is approximately 315 ft bgs, which is dependent on the geothermal heat flux. The geothermal gradient warms the soils from the bottom up. Based on published data from adjacent areas in Alaska (Jorgenson et al., 2008) and conversations with people who have experience drilling in this and similar areas, the expected lower boundary of permafrost is between 150 to 250 ft. Since we could not find any data from deep boreholes in this area, however, we consider the modeled result as a maximum depth of permafrost for the AHTS.

Figure 35 is a temperature profile from the 1D transient model. This figure contains model results between Day 110 and Day 290, showing results from every 20 days (with the exception of the warmest day; this was 30 days from the previous result so that the warmest temperature distribution for this year could be shown). These results indicate that the depth of zero annual amplitude is approximately 40 ft bgs. While there was some change in the lower temperatures as the model adjusted to the upper boundary condition, this change was less than one-hundredth of a degree and therefore minor. The model results indicate an active layer of approximately 2.4 ft. Since this 1D model was driven by the sinusoidal curve fit to 30 yrs of data, the model result reflects the long-term average active layer depth. It is in good agreement with measured thaw depths at the end of the summer in 2011, and difference can be attributed to the nature of the long-term data set used as the upper boundary condition and changes in the thermal properties of the active layer material. Additionally, there is good agreement in the modeled temperatures at depths of 4 and 8 in. to the measured temperatures (see Figures 16 and 17 in Task 3). This indicates good overall performance in the modeled active layer dynamics.

2D MODEL RESULTS

Part I

Results from this simulation are shown in Figure 36 through Figure 41. Each figure contains screen shots from the fully-coupled model (a) and the conduction-only model (b) for the selected date, and the temperature difference between the two model results (c). For each pair of model results, the range of temperatures from the fully-coupled model is larger than that from the conduction-only model, containing both colder and warmer temperatures within the domain for the given date. For the fully-coupled model, the warmer temperatures result in a thaw bulb within the embankment that persists longer into January (see Figure 38). The shape of the thaw bulb under the uphill shoulder for October 30 (see Figure 36a) suggests that super-cooled water is entering under the embankment and causing the early freezing of these soils. As this is unrealistic, this thaw bulb shape (which should parallel the embankment surface) indicates that the hydraulic conductivity of the frozen soil is too high, a parameter that could be fine-tuned for future models. Water redistribution continues within the thawed zone until January, as indicated by the tiny flux arrows. The water table is roughly horizontal during the winter models, with no
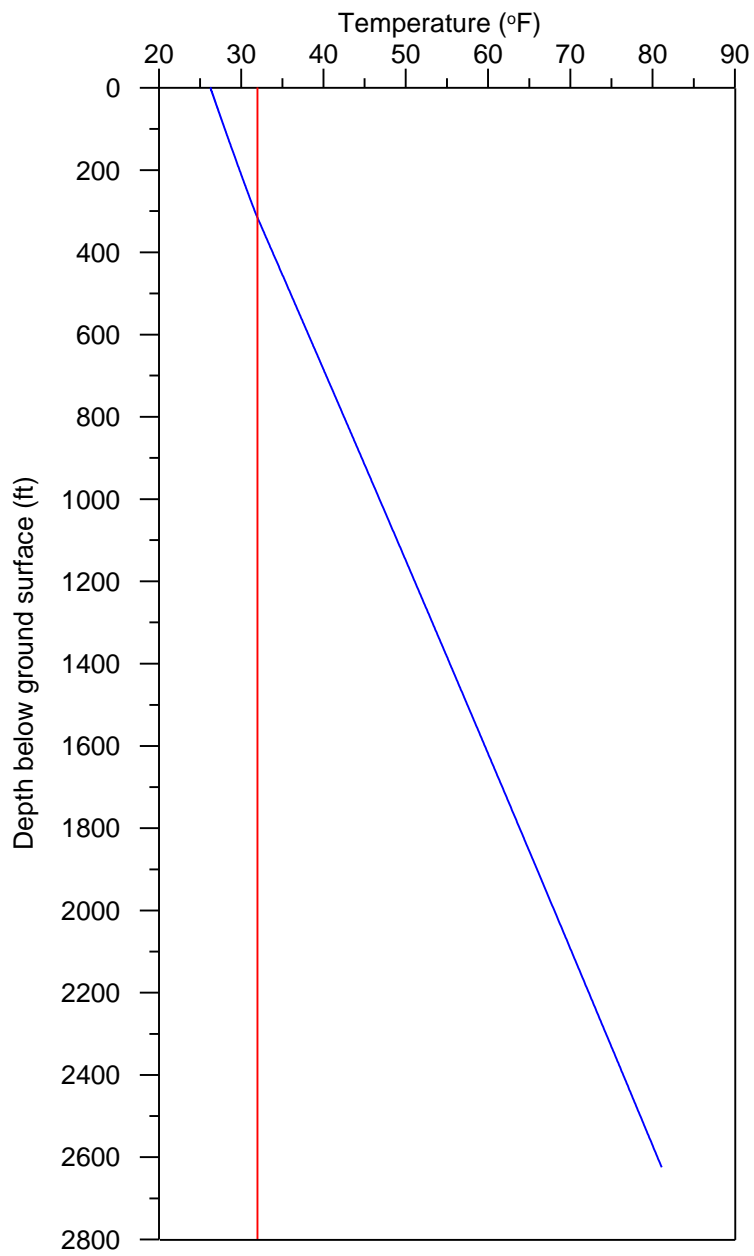
Figure 34. Modeled temperatures from the 1D steady state COMSOL model. The vertical red line represents the phase change isotherm.
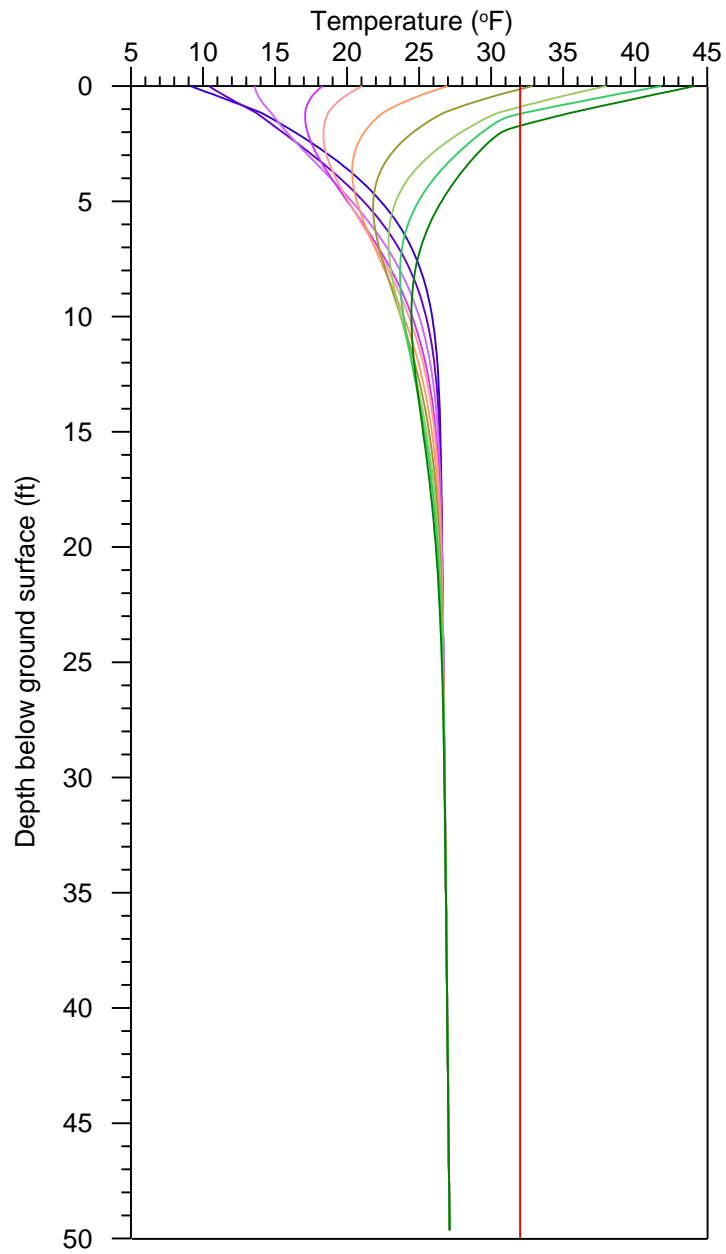
Figure 35. Modeled temperatures from the 1D transient COMSOL model. Beginning with the left most plot, temperatures are plotted from Day 110 through Day 290 of the model, every 20 to 30 days apart. The vertical red line represents the phase change isotherm.
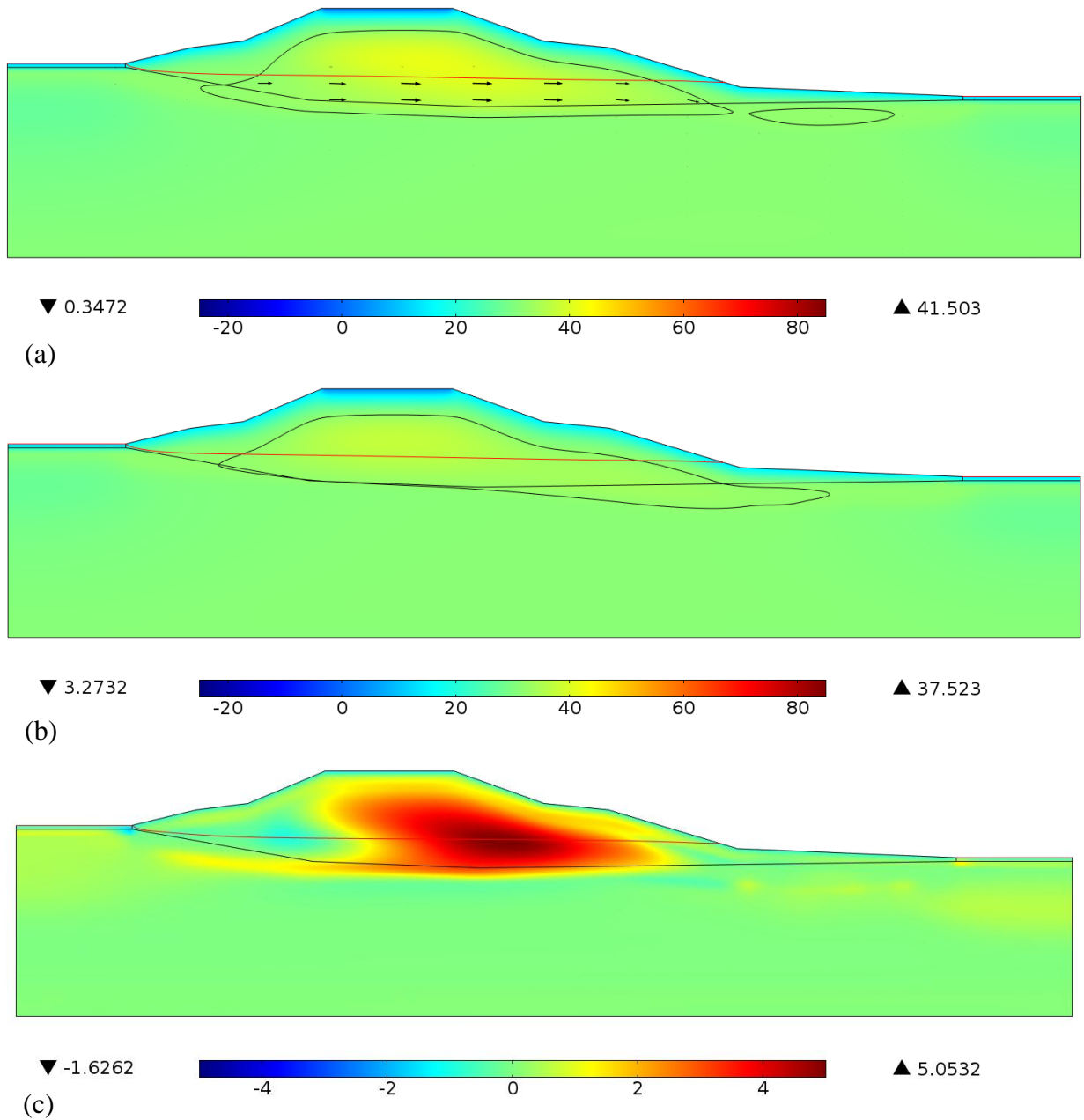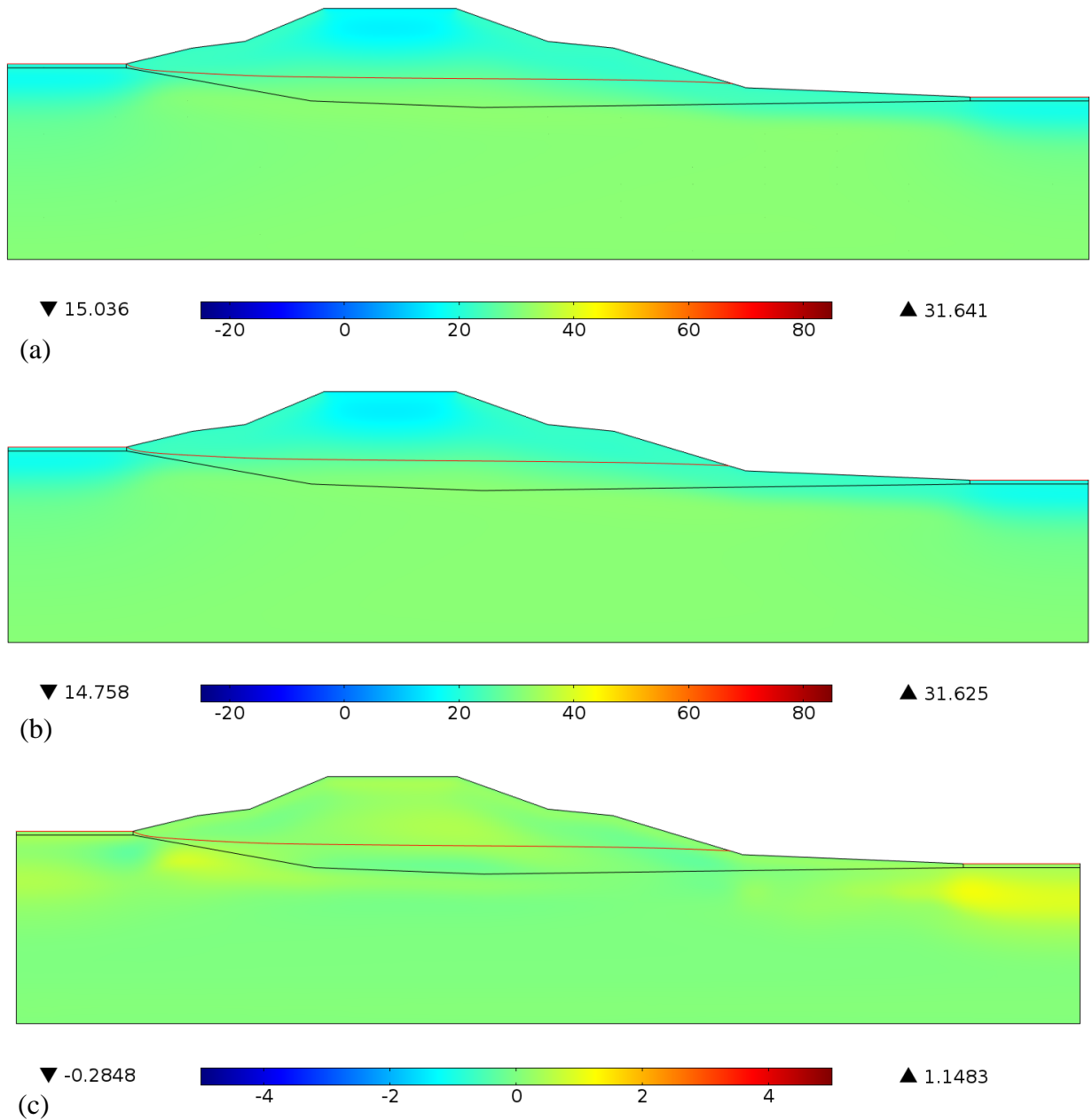
Figure 36. Comparison of temperature distribution for October 30, 2008. The images shown are of (a) the fully-coupled COMSOL model results, (b) the conduction-only model results, and (c) the difference in temperature between (a) and (b). For (c), positive temperatures indicate that the fully-coupled model is warmer. Temperatures are provided in ºF, and the vertical and horizontal scales are the same as in Figure 24. The red line indicates the water table in the embankment, the black line indicates the phase change isotherm, and the arrows in (a) indicate the liquid water flux.
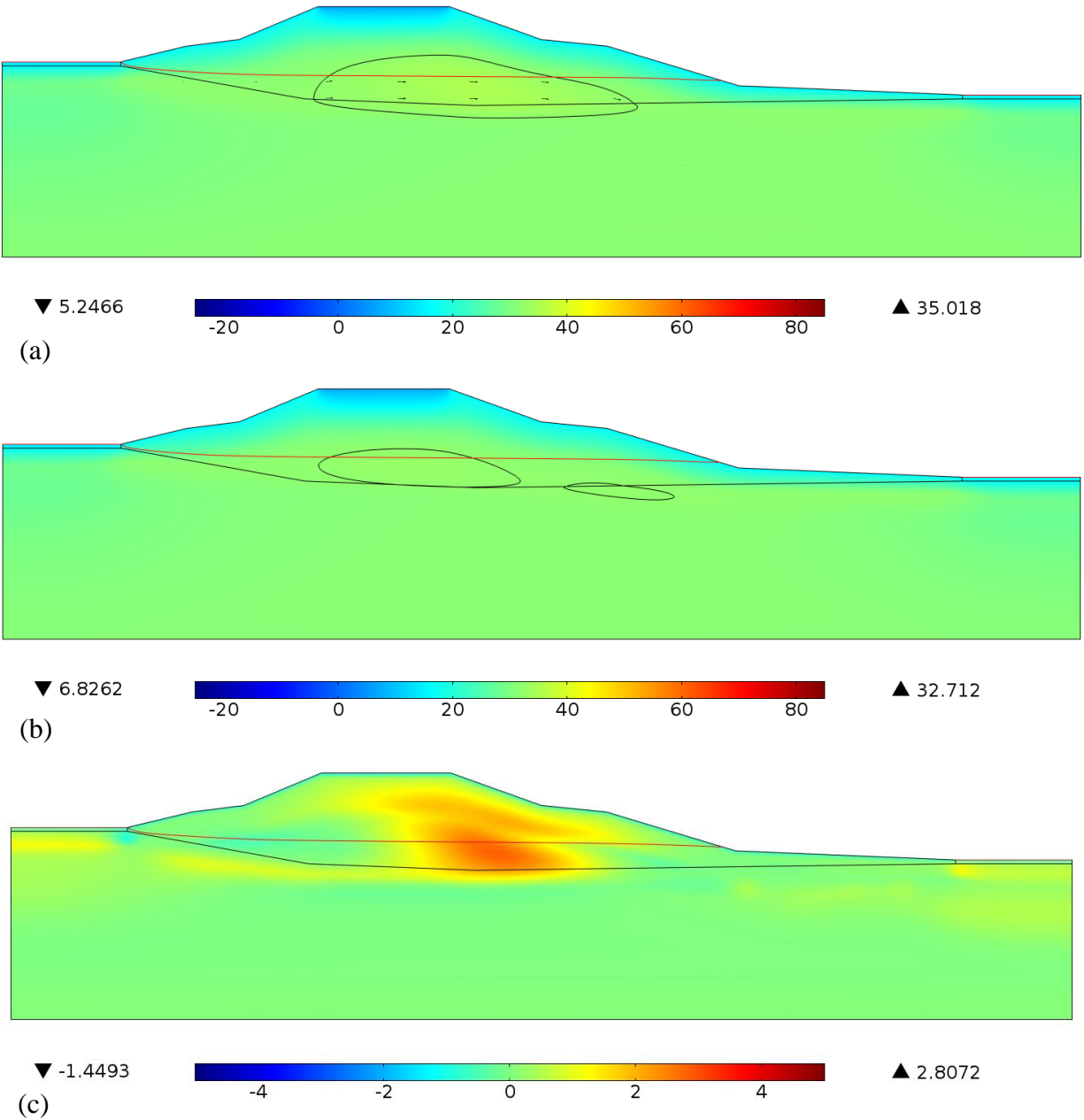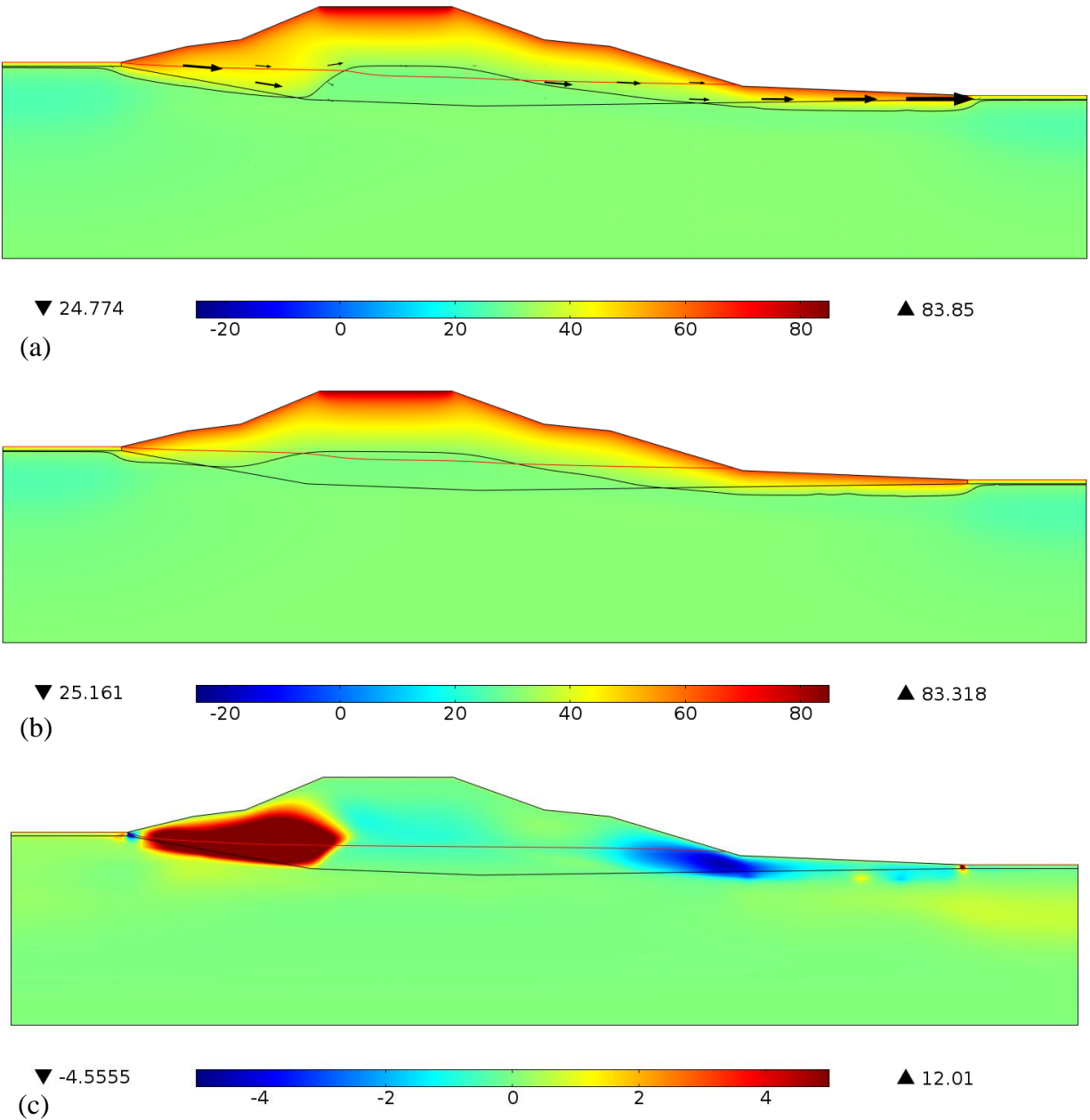
Figure 37. Comparison of temperature distribution for November 30, 2008. The images shown are of (a) the fully-coupled COMSOL model results, (b) the conduction-only model results, and (c) the difference in temperature between (a) and (b). For (c), positive temperatures indicate that the fully-coupled model is warmer. Temperatures are provided in ºF, and the vertical and horizontal scales are the same as in Figure 24. The red line indicates the water table in the embankment, the black line indicates the phase change isotherm, and the arrows in (a) indicate the liquid water flux.
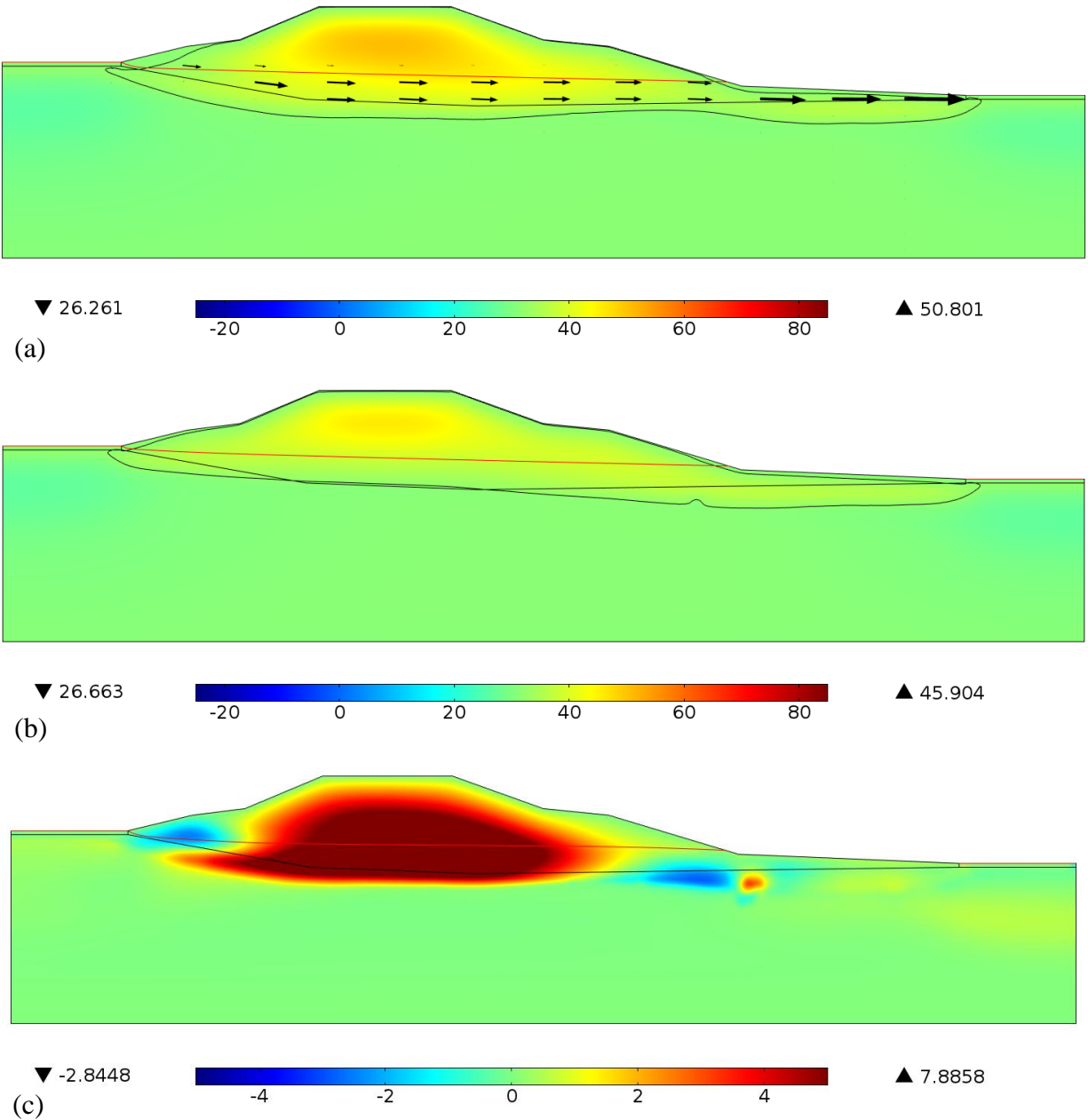
45

(a)

▼ -23.517   ▲ 32.248

(b)

▼ -24.217   ▲ 31.9

(c)

▼ -0.7918   ▲ 1.8889
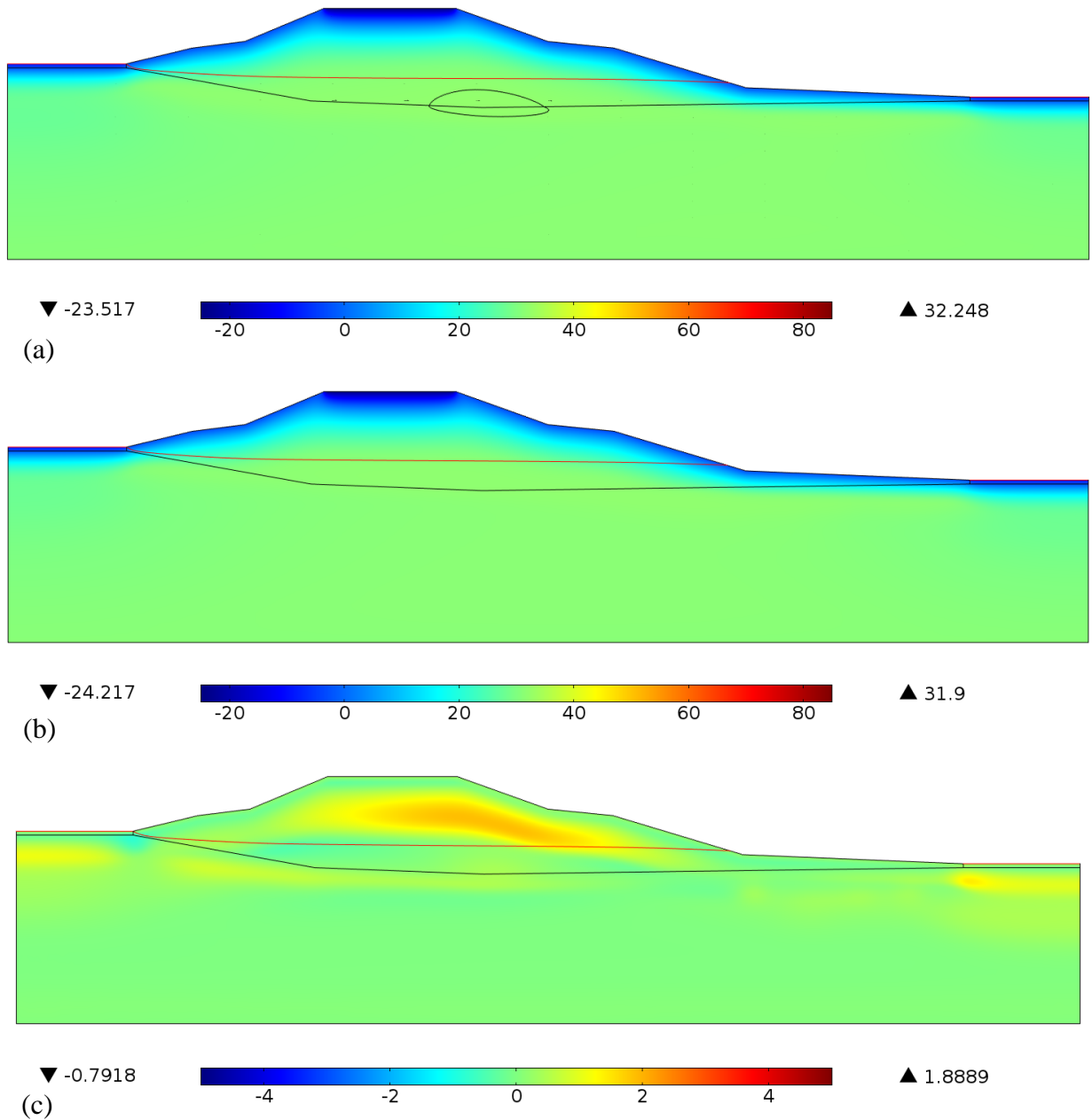
Figure 38. Comparison of temperature distribution for January 1, 2009. The images shown are of (a) the fully-coupled COMSOL model results, (b) the conduction-only model results, and (c) the difference in temperature between (a) and (b). For (c), positive temperatures indicate that the fully-coupled model is warmer. Temperatures are provided in ºF, and the vertical and horizontal scales are the same as in Figure 24. The red line indicates the water table in the embankment, the black line indicates the phase change isotherm, and the arrows in (a) indicate the liquid water flux.

46

(a)

▼ 15.036   ▲ 31.641

(b)

▼ 14.758   ▲ 31.625

(c)

▼ -0.2848   ▲ 1.1483

Figure 39. Comparison of temperature distribution for April 1, 2009. The images shown are of (a) the fully-coupled COMSOL model results, (b) the conduction-only model results, and (c) the difference in temperature between (a) and (b). For (c), positive temperatures indicate that the fully-coupled model is warmer. Temperatures are provided in ºF, and the vertical and horizontal scales are the same as in Figure 24. The red line indicates the water table in the embankment, the black line indicates the phase change isotherm, and the arrows in (a) indicate the liquid water flux.

Figure 40. Comparison of temperature distribution for July 1, 2009. The images shown are of (a) the fully-coupled COMSOL model results, (b) the conduction-only model results, and (c) the difference in temperature between (a) and (b). For (c), positive temperatures indicate that the fully-coupled model is warmer. Temperatures are provided in °F, and the vertical and horizontal scales are the same as in Figure 24. The red line indicates the water table in the embankment, the black line indicates the phase change isotherm, and the arrows in (a) indicate the liquid water flux.

Figure 41. Comparison of temperature distribution for September 30, 2009. The images shown are of (a) the fully-coupled COMSOL model results, (b) the conduction-only model results, and (c) the difference in temperature between (a) and (b). For (c), positive temperatures indicate that the fully-coupled model is warmer. Temperatures are provided in ºF, and the vertical and horizontal scales are the same as in Figure 24. The red line indicates the water table in the embankment, the black line indicates the phase change isotherm, and the arrows in (a) indicate the liquid water flux.

49

flow out of the embankment. During the summer, the groundwater flow under the uphill portion of the embankment contributes to the thawing of the frozen zone in the center of the embankment, as shown in Figure 40. The hydraulic gradient is steeper, with water entering at the uphill toe and exiting at the downhill edge of the embankment. A small amount of cooling is present in the lower portion of the embankment in July, which may be caused by relatively cool water flowing out of the embankment. Flux is greater at the downhill edge of the embankment, indicating the contribution of melted ice stored within the embankment. The effects of the groundwater flow persist into September and October (see Figure 41 and Figure 36, respectively), with a deeper depth of thaw under the structural core of the embankment. It must be stressed that these models do not account for any kind of strain, or thaw settlement, within the model mesh. As the foundation soils in the AHTS area are ice-rich, the depth of deeper thaw in the fully-coupled model will result in ongoing degradation of the foundation soils and damage to the driving surface, as was observed in the field (see Task 1).

Differences between the fully-coupled and conduction-only models are presented two ways. For Figure 36 through Figure 41, image (c) displays the temperature difference throughout the domain between the two models for that specific date. The largest difference in the results presented occurs in July (see Figure 40), when groundwater flow into the uphill side of the embankment results in temperatures 12ºF warmer than the conduction-only model. Overall, a quick visual inspection of these temperature difference images illustrates the overall warmer embankment produced by the fully-coupled model through the summer and fall months. There is little difference between the model results from December through April.

The differences between the two different models also are presented in graphs of temperature for selected depths (see Figure 42 and Figure 43). Spikes in the thermistor data represent periods when no data was obtained, and are plotted as 32ºF. As these spikes are present for most of the measured depths, this may be due to moisture in the wiring connections, or intermittent power failures at the ADAS for this thermistor string. Figure 42 illustrates the comparison between modeled and measured temperatures for a depth of 0.33 ft, which is presented in a larger image as this data set was used to calibrate the side slope n-factors for the upper boundary condition. For all of the selected depths, the fully-coupled and conduction-only modeled temperatures are compared to temperatures from string YG7, which is located to the north of CS A-A'. Generally, the modeled temperatures match each other, and are cooler than measured temperatures in the winter and warmer in the summer. The modeled temperatures differ from each other significantly only for the depth of 11.5 ft (see Figure 43d), which may correspond to the thawed part of the saturated portion of the embankment. Otherwise, there is relatively close agreement between the two different models. The 2D temperature differences presented in Figure 36c through Figure 41c, however, illustrate major differences between the two models, with the largest differences occurring in the uphill portion of the embankment. This indicates that the thermistor string should be installed in the uphill side of the road to capture the temperature dynamics better.

Part II

For Part II, we used measured air temperatures from 2008 to 2012 as the upper boundary condition and compared the model results to thermistor data from the same period of time. We conducted this set of simulations because it compares a longer data set with greater resolution, as the measured air temperatures were hourly measurements. Comparisons of the modeled to

Figure 42. Modeled versus measured temperature data from a depth of 0.33 ft for the Part I 2D models. This data set was used to calibrate the side slope *n*-factors.
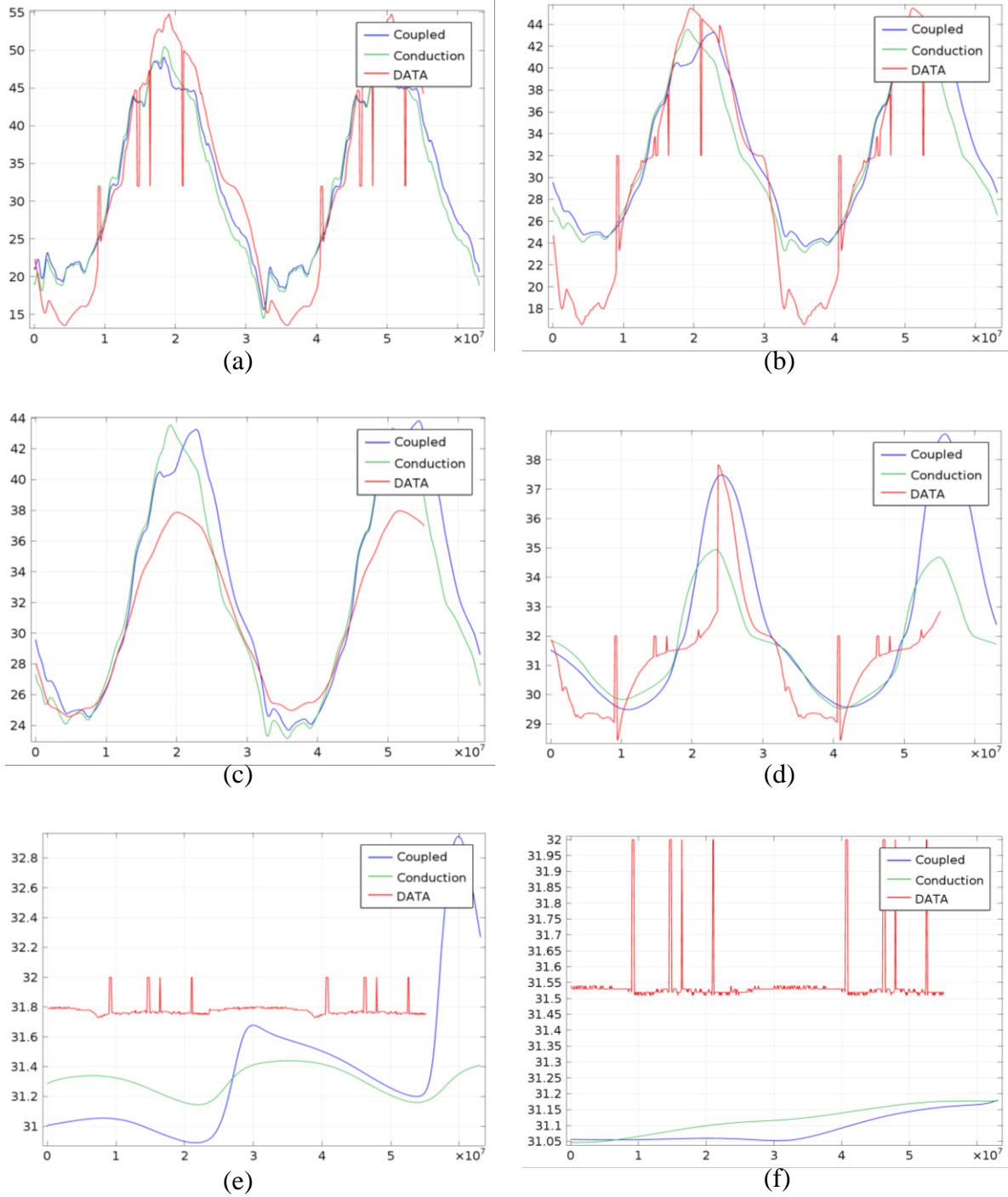
Figure 43. Measured versus modeled temperatures for the Part I 2D models. Temperatures (in °F) are plotted for the period January 1, 2008 to December 31, 2009. Measured data from the thermistor at each depth are shown in green, and COMSOL model results are shown in blue. Comparisons made for depths of (a) 0.33 ft, (b) 4.9 ft, (c) 8.2 ft, (d) 11.5 ft, (e) 14.8 ft, (f) 19.7 ft. (CONTINUED ON NEXT PAGE).
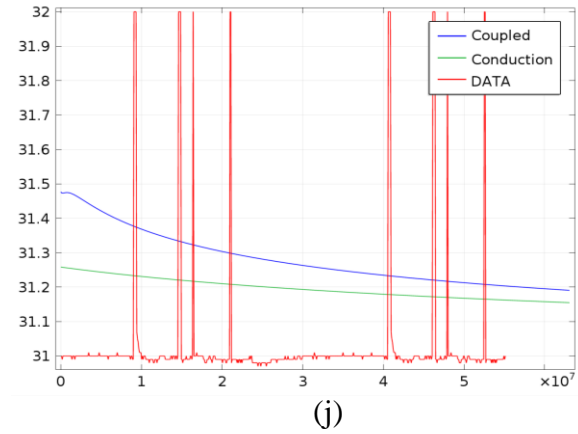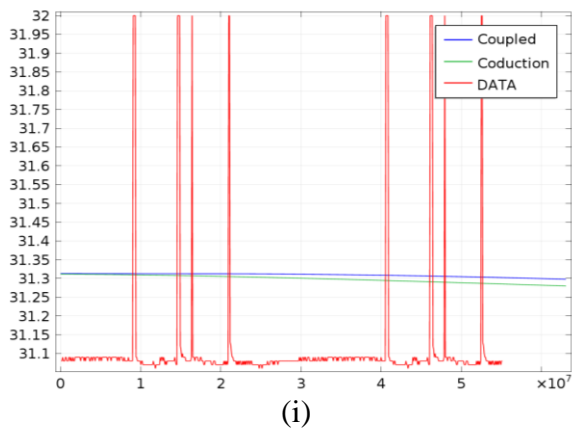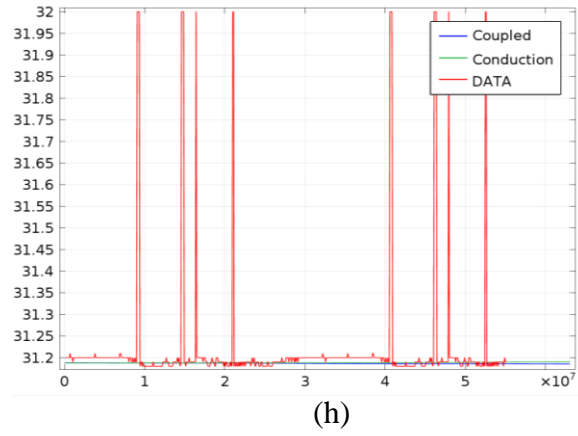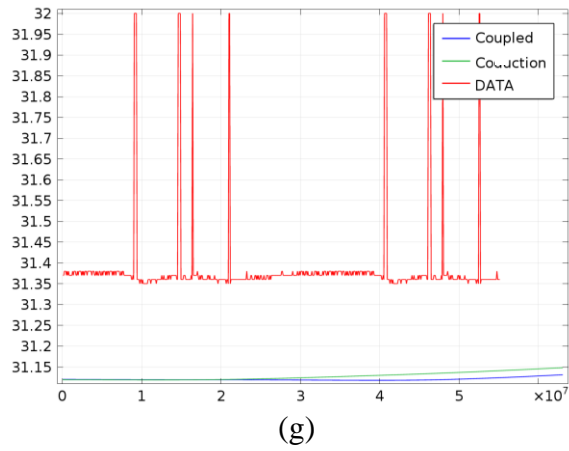
Figure 43 (CONTINUED). Comparisons made for depths of (g) 24.6 ft, (h) 29.5 ft, (i) 42.7 ft, (j) 52.5 ft.

53
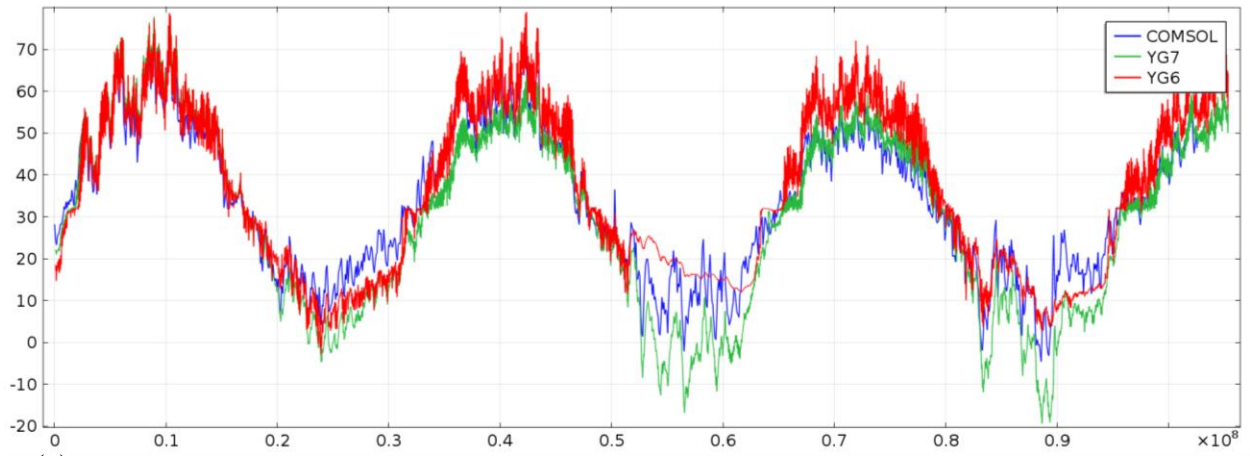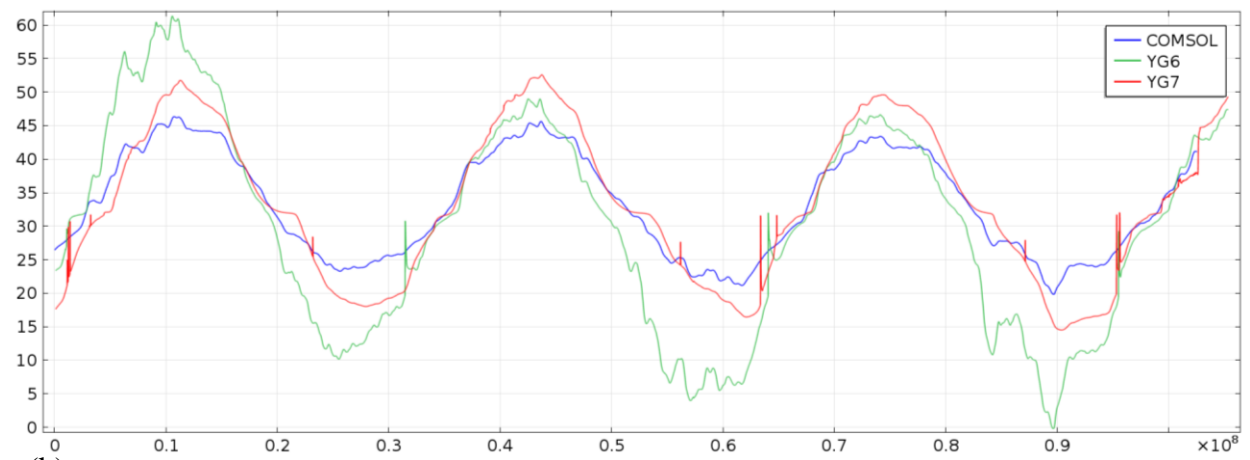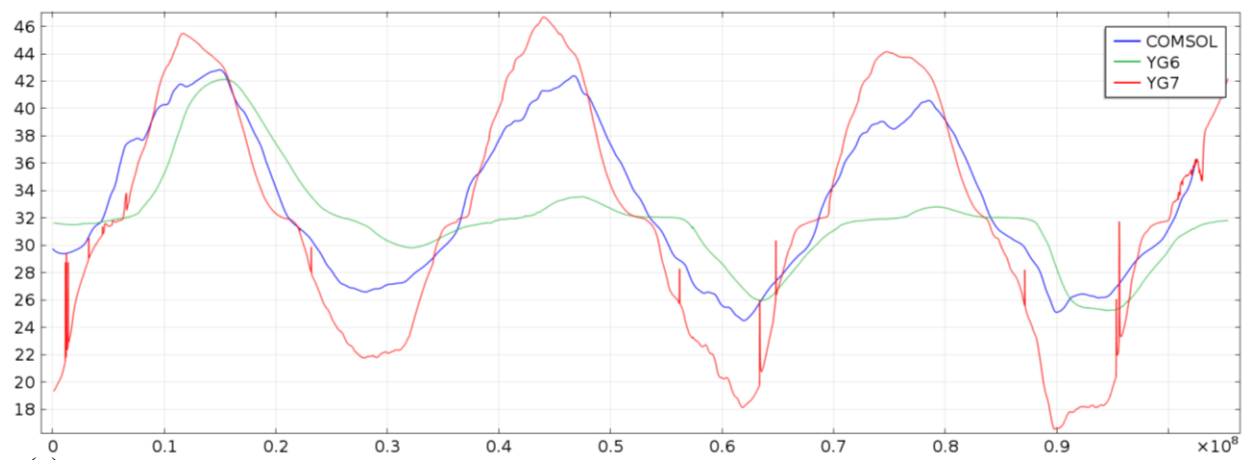
Figure 44. Comparison of modeled temperatures to measured ground temperatures for the Part II 2D models. Results from the fully-coupled COMSOL model are compared to measured thermistor temperatures for depths of (a) 0.33 ft, (b) 5.9 ft, and (c) 8.2 ft bgs from strings YG6 and YG7.

measured temperatures for three different depths are shown in Figure 44. The measured data are from two thermistor strings, YG6 and YG7, which are south and north of the modeled cross section, respectively. Generally, the modeled temperatures are cooler in the summer and warmer in the winter for a given depth. Differences may be attributed to model input parameters that do not match exactly those of the cross section soils and require fine-tuning. Additionally, thermistor string YG7 was installed adjacent to a longitudinal culvert, and YG6 is located under a snow shed. Both of these mitigation techniques may influence the adjacent temperatures within the embankment, which our model did not address.

Part III

Figure 45 and Figure 46 contain the results from the 50 yr simulations. We conducted these simulations to visualize long-term degradation, to compare the long-term results of the fully-coupled and conduction-only models, and to compare the effects on the different lower boundary conditions. Overall, using the geothermal heat flux causes minor long-term cooling at depth in the natural ground and very minor warming at depth under the embankment as compared to the fixed temperature model; otherwise, there is no appreciable difference between these two lower boundary conditions.

The screen shots shown in Figure 45 and Figure 46 are from slightly different days because of the nature of the model output; however, we selected results from mid-August to early September from every 10 yrs for a wide range in temperatures with deeper thaw depths. A comparison of the decadal results indicates that there is little change in any of these models over 50 yrs, suggesting that each model reaches equilibrium within the first 10 yrs. Additionally, there is no long-term thaw bulb formation, as the embankment freezes back completely every winter.

Both the fully-coupled and conduction-only models demonstrate thaw that exceeds the depth of the existing embankment below the embankment toes and portions of the side slopes. For the conduction-only model, there is less thaw under the structural core of the embankment at the end of the summer. As the phase change isotherm does not reach the lower boundary of the embankment materials, this result suggests that the center portion of the embankment is in thermal equilibrium with the natural ground and will not experience thaw degradation. The fully-coupled model yields different results. The thaw depth passes below the embankment materials, penetrating into the underlying ice-rich foundation soils under the uphill portion of the embankment. As previously mentioned for Part I, these models do not account for thaw settlement. Thus, the deeper thawing indicated by the fully-coupled model will result in thermal degradation of the foundation soils. Given the advective nature of groundwater flow, the thermal degradation will likely be ongoing, regardless of how thick the embankment becomes with continual maintenance.

[A]   [B]

(a)

(b)

(c)

(d)

(e)
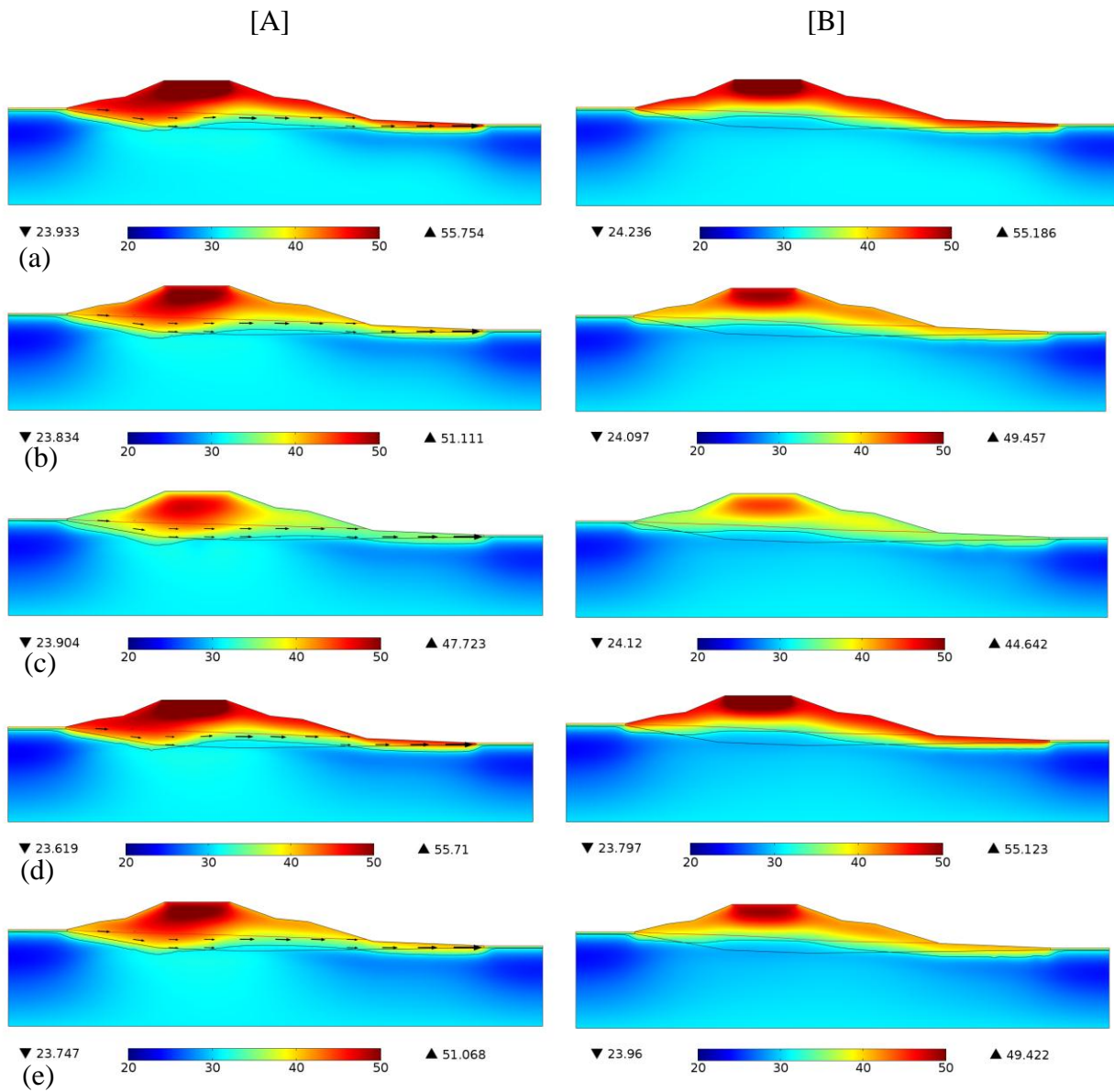
Figure 45. Model results from the 50-yr simulations using a fixed temperature of 31.3ºF for the lower boundary condition. Screen shots in column A are from the fully-coupled model, and screen shots in column B are from the conduction-only model. Results in the rows are for (a) August 14 (10 years), (b) August 22 (20 years), (c) September 2 (30 years), (d) August 14 (40 years), and (e) August 24 (50 years); the exact date varies due to the model output time step parameter. Temperatures are provided in ºF, and the vertical and horizontal extents are the same as in Figure 24. The red line indicates the water table in the embankment, the black line indicates the phase change isotherm, and the arrows in column A indicate the liquid water flux.

Figure 46. Model results from the 50-yr simulations using a geothermal heat flux of 0.008 Btu/hr·ft^2 for the lower boundary condition. Screen shots in column A are from the fully-coupled model, and screen shots in column B are from the conduction-only model. Results in the rows are for (a) August 14 (10 years), (b) August 22 (20 years), (c) September 2 (30 years), (d) August 14 (40 years), and (e) August 24 (50 years); the exact date varies due to the model output time step parameter. Temperatures are provided in ºF, and the vertical and horizontal extents are the same as in Figure 24. The red line indicates the water table in the embankment, the black line indicates the phase change isotherm, and the arrows in column A indicate the liquid water flux.

57

CHAPTER 4

CONCLUSIONS, RECOMMENDATIONS, AND SUGGESTED RESEARCH

The overall goal of this research was to develop a relationship among groundwater flow, permafrost degradation, and embankment stability. To achieve this goal, we investigated the Alaska Highway test section (AHTS) near Beaver Creek, Yukon, Canada, as this site is well-known for the ongoing thermal degradation of the permafrost below the embankment, demonstrates significant groundwater flow, and is heavily instrumented from previous work. As part of this research project, we:

- Conducted field work over two summers: installing 40 additional water wells and piezometers, and other temperature and soil moisture measurement devices; measuring water level, thaw depth, and snow cover as applicable; conducting innovative laser scanning the embankment surface to measure settlement and surface depressions volume;
- Produced a preliminary eco-geomorphologic terrain unit map, based on field mapping, water level measurements, and laboratory testing;
- Conducted a suite of geotechnical laboratory tests on soil samples collected in the field, including thermal conductivity and hydraulic conductivity;
- Measured unfrozen water content from *in situ* field instrumentation;
- Produced a numerical model that includes both conductive and advective heat transfer, and compared the model result to measured temperatures in the field.

Results from the fully-coupled conductive and advective heat transfer model indicate that the thermal effects from groundwater flow are significant, producing warmer temperatures than those from the conduction-only model. The fully-coupled model output indicates that the embankment is not in thermal equilibrium with the underlying foundation soils; instead, groundwater flowing through the porous gravel embankment in the summer causes the foundation soils below the embankment materials to thaw. As the foundation soils in the AHTS area are ice-rich, this will result in thermal degradation, which is manifested at the surface in the form of longitudinal and transverse cracks and an irregular driving surface. Given the advective nature of groundwater flow, the thermal degradation will likely be ongoing, without reaching a thermal balance, regardless of how thick the embankment becomes with continual maintenance.

Based on the results from this research, we recommend the following:

- The first step in solving the problems associated with groundwater flow is recognizing where these problems are likely to exist. Terrain analysis, including identification of vegetation patterns that suggest near-surface groundwater flow, is invaluable to identifying problem areas. Thaw-sensitive permafrost can be identified using quickly available resources, such as Google Earth, as well as higher resolution aerial photographs or satellite imagery. For areas where re-routing proposed or existing infrastructure is not possible, then eco-geomorphologic terrain unit maps are tools that can aid in the identification of areas where near-surface groundwater flow will require additional mitigation.
- Thermal modeling of embankments over permafrost is good, but including groundwater flow in the thermal model is better. These research results indicate that the effects of groundwater flow cannot be ignored, as the flowing groundwater causes continual

58

thermal degradation. This research also indicates that the model results depend not only on the input parameters, but also on the way the commercially-available model couples the physics within the calculations. Given the same input parameters, two different modeling programs may produce two different results.

- The next step for this form of research is to develop mitigation techniques to catch and direct groundwater flow through an embankment. The ditch excavated in 2008 at the AHTS is successful in diverting some of the groundwater flow away from problem areas in the embankment; however, since its excavation, it has increased in size from significant erosion, and does not intercept all of the groundwater flow at the test section. As an alternative, proposed mitigation techniques could be simulated using a fully-coupled model. Then, we suggest incorporating the most successful techniques as experimental features at a new, heavily instrumented test site underlain by thaw-sensitive permafrost and demonstrating near-surface groundwater flow.

  o As part of instrumentation at a new test section, thermistor strings should be distributed uniformly across the embankment to obtain a full cross section of temperatures. When this cannot be accomplished, thermistor strings should be placed on the side of the embankment with the greater hydraulic gradient, in order to capture the temperature dynamics as groundwater flows into the embankment.

  o Because of the previous work done in the area and the nature of the groundwater flow and underlying permafrost, the AHTS had many advantages for this research; however, there were a few drawbacks as well. The site remote, requiring a day's drive from any major population. Additionally, researchers in Alaska had to cross an international border to perform field work, which added a level of complexity to the work. Should a site in Alaska be selected for a new test section, the site should be accessible for large drill rigs in order to penetrate the embankment. A site with pre-existing borehole data and as-builts is preferable.

CHAPTER 5

REFERENCES

Beaulac, I., and G. Doré, "Permafrost degradation and adaptations of airfields and access roads, Nunavik, Quebec, Canada." *in* Davies, M., and Zufelt, J., eds., *Cold Regions Engineering 2006*, Vol. 13: ASCE, Orono, ME (2006) 11 pp.

Boike, J., Ippisch, O., Overduin, P. P., Hagedome, B., Roth, K. "Water, heat, and solute dynamics of a mud boil, Spitsbergen." *Geomorphology*: Vol. 95, No. 1-2 (July 9, 2008) pp. 61-73, doi:10.1016/j.geomorph.2006.07.033

Brown, J., Brockett, B. E., Howe, K. E., *Interaction of Gravel Fills, Surface Drainage, and Culverts with Permafrost Terrain*, State of Alaska Department of Transportation and Public Facilities, Fairbanks, Alaska (1984) 41 pp.

Christiansen, H. H., Etzelmüller, B., Isaksen, K., Juliussen, H., Farbrot, H., Humlum, O., Johansson, M., Ingeman-Nielsen, T., Kristensen, L., Hjort, J., Holmlund, P., Sannel, A.B.K., Sigsgaard, C., Åkerman, H. J., Foged, N., Blikra, L. H., Pernosky, M. A., Ødegård, R. S. "The thermal state of permafrost in the nordic area during the international polar year 2007–2009." *Permafrost and Periglacial Processes*: Vol. 21, No. 2 (April/June 2010) pp. 156-181, doi: 10.1002/ppp.687

Coulombe, S., Fortier, D., Stephani, E. "Using air convection ducts to control permafrost degradation under road infrastructures: Beaver Creek experimental site, Yukon, Canada." 15th International Conference on Cold Regions Engineering, Proceedings, Québec City, Québec, Canada (August 2012) pp. 21-31.

Daanen, R. P., Misra, D., Epstein, H., Walker, D., Romanovsky, V. "Simulating nonsorted circle development in arctic tundra ecosystems." *Journal of Geophysical Research*: Vol. 113, G03S06 (July 2008) 10 pp., doi:10.1029/2008JG000682

Darrow, M. M. "Thermal modeling of roadway embankments over permafrost." *Cold Regions Science and Technology*: Vol. 65, No. 3 (March 2011) pp. 474-487, doi:10.1016/j.coldregions.2010.11.001

de Grandpré, I., Fortier, D., Stephani, E. "Impact of groundwater flow on permafrost degradation: implications for transportation infrastructures." GEO2010, Calgary, Alberta, Proceedings (2010) pp. 534-540.

de Grandpré, I., Fortier, D., Stephani, E. "Groundwater flow under transport infrastructure: potential heat flow impacting the thermal regime of permafrost and the degradation of ground ice." *Canadian Journal of Earth Sciences*: Vol. 49, No. 8 (2012) pp. 953-962, doi:10.1139/e2012-018

Egginton, P. A., and L. D. Dyke. "Apparent hydraulic conductivities associated with thawing, frost-susceptible soils." *Permafrost and Periglacial Processes*: Vol. 1, No. 1 (January/March 1990) pp. 69-77, doi: 10.1002/ppp.3430010109

Fortier, D., Allard, M., Shur, Y. "Observation of rapid drainage system development by thermal erosion of ice wedges on Bylot Island, Canadian Arctic Archipelago." *Permafrost and*

Periglacial Processes: Vol. 18, No. 3 (July/September 2007) pp. 229-243, doi: 10.1002/ppp.595

Gerke, H. H. and van Genuchten, M. T., 1993. "A Dual-Porosity Model for Simulating the Preferential Movement of Water and Solutes in Structured Porous Media." *Water Resources Research*, 29(2), 305-319.

Goodrich, L., *Evaluation of Passive and Active Methods for the Thermal Stabilization of Permafrost*: Université de Montréal (1996).

IPCC. *Climate Change 2007: Synthesis Report, Contributions of Working Groups I, II, and III to the Fourth Assessment Report of the Intergovernmental Panel on Climate Change*, in IPCC, ed., Geneva, Switzerland (2007) 103 pp.

Jorgenson, T., Yoshikawa, K., Kanevskiy, M., Shur, Y., Romanovsky, V., Marchenko, S., Grosse, G., Brown, J., Jones, B. "Permafrost characteristics of Alaska." Ninth International Conference on Permafrost, Fairbanks, Alaska (June/July 2008) extended abstracts, pp. 121-122.

Kane, D. L., Hinkel, K. M., Goering, D. J., Hinzman, L. D., Outcalt, S. I. "Non-conductive heat transfer associated with frozen soils." *Global and Planetary Change*: Vol. 29, No. 3-4 (June 2001), pp. 275-292, dx.doi.org/10.1016/S0921-8181(01)00095-9

Ladanyi, B., *Design and Rehabilitation Guide for Transportation Infrastructures in Northern Regions*: Université de Montréal (1994).

Mackay, J. R. "Downward water movement into frozen ground, western arctic coast, Canada." *Canadian Journal of Earth Sciences*: Vol. 20, No. 1 (January 1983) pp. 120-134, doi:10.1139/e83-012

Marchenko, S. S., Romanovsky, V. E., Tipenko, G. S. "Numerical modeling of spatial permafrost dynamics in Alaska." Ninth International Conference on Permafrost, Fairbanks, Alaska (June/July 2008) Vol. 2, pp. 1125-1130.

M-Lepage, J., Doré, G., Fortier, D. "Thermal effectiveness of the mitigation techniques tested at Beaver Creek experimental road site based on a heat balance analysis (Yukon, Canada)." 15th International Conference on Cold Regions Engineering, Proceedings, Québec City, Québec, Canada (August 2012) pp. 42-51.

M-Lepage, J., Doré, G., Fortier, D., Murchison, P. "Thermal performance of the permafrost protection techniques at Beaver Creek experimental road site, Yukon, Canada." 10th International Conference on Permafrost, Salekhard, Russia (June 2012) Vol. 1, pp. 261-266.

Quinton, W. L., Shirazi, T., Carey, S. K., Pomeroy, J. W. "Soil water storage and active-layer development in a sub-alpine tundra hillslope, southern Yukon Territory, Canada." *Permafrost and Periglacial Processes*: Vol. 16, No. 4 (October/December 2005) pp. 369-382, doi:10.1002/ppp.543

Remchein, D., Fortier, D., Doré, G., Stanley, B., Walsh, R. "Cost and Constructability of Permafrost Test Sections along the Alaska Highway, Yukon." Transport Association of Canada Annual Conference, Proceedings, Vancouver, British Columbia, Canada (2009) 20 pp.

Remchein, D., Stanley, B., Walsh, R., Doré, G., Fortier, D. "Reducing maintenance requirements on permafrost-affected highways: permafrost test sections along the Alaska Highway." Proceedings: 13th International Winter Road Congress, Québec City, Québec, Canada (February 2010).

Romanovsky, V. E., Drozdov, D. S., Oberman, N. G., Malkova, G. V., Kholodov, A. L., Marchenko, S. S., Moskalenko, N. G., Sergeev, D. O., Ukraintseva, N. G., Abramov, A. A., Gilichinsky, D. A., Vasiliev, A. A. "Thermal state of permafrost in Russia." *Permafrost and Periglacial Processes*: Vol. 21, No. 2 (April/June 2010) pp. 136-155, doi:10.1002/ppp.683

Smith, S. L., Romanovsky, V. E., Lewkowicz, A. G., Burn, C. R., Allard, M., Clow, G. D., Yoshikawa, K., Throop, J. "Thermal state of permafrost in North America: a contribution to the international polar year." *Permafrost and Periglacial Processes*: Vol. 21, No. 2 (April/June 2010) pp. 117-135, doi:10.1002/ppp.690

Soil Classification Working Group. *The Canadian System of Soil Classification*, 3rd ed: Agriculture and Agri-Food Canada Publication 1646 (1998) 187 p.

Spaans, E. J. A., and J. M. Baker. "The soil freezing characteristic: its measurement and similarity to the soil moisture characteristic." *Soil Science Society of America Journal*: Vol. 60, No. 1 (January 1996) pp. 13-19, doi:10.2136/sssaj1996.03615995006000010005x

Stieglitz, M., Déry, S. J., Romanovsky, V. E., Osterkamp, T. E. "The role of snow cover in the warming of arctic permafrost." *Geophysical Research Letters*: Vol. 30, No. 13 (July 2003) 1721, 4 p., doi:10.1029/2003GL017337

Tremblay, C., and G. Doré, "Airport network and housing construction programmes in northern Quebec, Canada," 5th International Conference on Permafrost, Trondheim, Norway, Proceedings (1988) pp. 1500-1506.

Yoshikawa, K., and P. P. Overduin. "Comparing unfrozen water content measurements of frozen soil using recently developed commercial sensors." *Cold Regions Science and Technology*: Vol. 42, No. 3 (March 2005) pp. 250-256, doi:10.1016/j.coldregions.2005.03.001

van Genuchten, M. Th. "A closed-form equation for predicting the hydraulic conductivity of unsaturated soils." *Soil Science Society of America Journal*: Vol. 44, No. 5 (September/October 1980) pp. 892-898, doi:10.2136/sssaj1980.03615995004400050002x

Veldkamp, E., and J. J. O'Brien. "Calibration of a frequency domain reflectometry sensor for humid tropical soils of volcanic origin." *Soil Science Society of America Journal*: Vol. 64, No. 5 (September, 2000) pp. 1549-1553, doi:10.2136/sssaj2000.6451549x

Zhang, T. "Influence of the seasonal snow cover on the ground thermal regime: An overview." *Reviews of Geophysics*: Vol. 43, RG4002 (December 2005) 23 pp., doi:10.1029/2004RG000157

Zhao, L., Wu, Q., Marchenko, S. S., Sharkhuu, N. "Thermal state of permafrost and active layer in Central Asia during the international polar year." *Permafrost and Periglacial Processes*: Vol. 21, No. 2 (April/June 2010) pp. 198-207, doi: 10.1002/ppp.688

APPENDIX A: SUMMARY OF FIELD INSTALLATIONS

Table A-1. Summary of automated data acquisition system (ADAS) installations. Coordinates were collected with a hand-held Garmin eTrex GPS (NAD83 datum), and are reported in UTM units (all in Zone 7). "CS616" is a water content reflectometer, "CS107" is a temperature sensor, and "bgs" is below ground surface.

Final ID	Coordinates	Date installed	Installation details (all measurements in inches)
ADAS-1	508587, 6911998	07/19/2011	Dismantled on 05/22/2012
"upslope"	508590, 6911998	07/19/2011	CS616, CS107 at 4.0 and 8.0 bgs
"downslope"	508585, 6911997	07/19/2011	CS616, CS107 at 4.0 and 8.0 bgs
ADAS-2	608489, 6911963	05/23/2012	---
"embankment"	508489, 6911966	05/24/2012	CS616, CS107 at 7.9, 15.7, 23.6, and 31.5 bgs

Table A-2. Summary of 2011 water well installations. Coordinates were collected with a hand-held Garmin eTrex GPS (NAD83 datum), and are reported in UTM units (all in Zone 7). "TD" is total depth of installation; "SU" is stick-up of casing above ground surface; "M" is manually-read piezometer; "VWP" is vibrating wire piezometer; "Hobo" is a Hobo U20 automated logger; and "bgs" is below ground surface. (CONTINUED ON NEXT PAGE)

Final ID	Field ID	Coordinates	Date Installed	Installation details (all measurements in inches)
P11_01	D7D	508473, 6912189	06/08/2011	SU 14.6, M
P11_02	G01G	508484, 6912186	06/08/2011	SU 28.0, M
P11_03	G01E	508482, 6912173	06/07/2011	SU 24.4, M
P11_04	G01F	508479, 6912178	06/08/2011	SU 9.1, Hobo
P11_05	G01C	508480, 6912167	06/07/2011	SU 11.4, Hobo
P11_06	DSD	508550, 6912073	07/20/2011	SU 29.1, M
P11_07	DSC	508533, 6912069	07/20/2011	SU 24.0, M
P11_08	DSB	508548, 6912061	07/20/2011	SU 24.4, M
P11_09	DSA	508537, 6912060	07/20/2011	SU 26.0, M
P11_10	G11N4	508689, 6912030	07/19/2011	SU1.6, Hobo
P11_11	G11N3W	508627, 6912023	07/19/2011	SU 2.8, Hobo
P11_12	G11N3E	508642, 6911996	07/19/2011	SU 2.0, Hobo
P11_13	G11N2	508608, 6912001	07/19/2011	SU 3.1, Hobo
P11_14	G11NW	508591, 6912005	07/20/2011	SU 15.0, M
P11_15	G11W	508586, 6912004	07/20/2011	SU 13.4, M
P11_16	G11SW	508579, 6912003	07/20/2011	SU 15.7, M
P11_17	G11SA	508583, 6911996	07/19/2011	SU 27.6; 170 kPa VWP installed 20 in. bgs; removed 05/22/2012
P11_18	G11SE	508582, 6911991	07/19/2011	SU 14.2, M
P11_19	G11E	508588, 6911992	07/19/2011	SU 18.5, M
P11_20	G11NE	508594, 6911994	07/19/2011	SU 17.7, M
P11_21	G11NA	508593, 6911998	07/19/2011	SU 3.1; 350 kPa VWP installed 20 in. bgs; removed 05/22/2012
P11_22	S3	508422, 6911960	07/21/2011	SU 16.9, M
P11_23	S2	508396, 6911950	07/21/2011	SU 16.1, M
P11_24	S1	508363, 6911949	07/21/2011	SU 15.0, M

Table A-2 (continued).

Final ID	Field ID	Coordinates	Date Installed	Installation details (all measurements in inches)
P11_25	D1D	508606, 6911887	06/09/2011	SU 14.6, M
P11_26	G17D+1	508608, 6911874	06/08/2011	SU 19.3, M
P11_27	G17E+2	508612, 6911870	06/09/2011	SU 16.9
P11_28	G18C	508612, 6911863	06/09/2011	SU 17.3, Hobo
P11_29	G17F	508617, 6911860	06/09/2011	SU 15.7, Hobo
P11_30	S	508664, 6911852		

Table A-3. Summary of 2012 water well and piezometer installations. Coordinates were collected with a hand-held Garmin eTrex GPS (NAD83 datum), and are reported in UTM units (all in Zone 7). "TD" is total depth of installation; "SU" is stick-up of casing above ground surface; "M" is manually-read piezometer; "VWP" is vibrating wire piezometer; "Hobo" is a Hobo U20 automated logger; "THM" is a string of manually read thermistors; and "bgs" is below ground surface.

Final ID	Field ID	Coordinates	Date installed	Installation details (all measurements in inches)
P12_01	S0	508332, 6911954	05/24/2012	TD 42.9, SU 14.6, Hobo, THM
P12_02	WEST 1	508484, 6911964	05/24/2012	170 kPa VWP installed 56 in. bgs
P12_03	WEST 2	508479, 6911963	05/24/2012	350 kPa VWP installed 86 in. bgs
P12_04	WEST 3	508474, 6911960	05/24/2012	TD 66.9, SU 34.6, Hobo, THM
P12_05	WEST 4	508472, 6911959	05/24/2012	TD 70.9, SU 34.6, Hobo
P12_06	WEST 5	508473, 6911960	05/24/2012	TD 70.9, SU 31.1, Hobo
P12_07	EAST 1	508539, 6911979	05/24/2012	TD 71.7, SU 17.3, Hobo
P12_08	EAST 2	508542, 6911982	05/24/2012	TD 59.1, SU 21.7, Hobo
P12_09	EAST 3	508722, 6912016	05/24/2012	TD 66.5, SU 29.9, Hobo, THM
P12_10	EAST 4	508785, 6911955	05/24/2012	TD 50.4, SU 15.0, Hobo, THM

APPENDIX B: SUMMARY OF GEOTECHNICAL LABORATORY TESTING

Table B-1. Moisture content results for 2011 and 2012 soil samples. (CONTINUED ON NEXT PAGE)

Sample No.	Final ID	Field ID	Depth bgs (in.)	Gravimetric water content (%)	Dry unit weight (lb/ft^3)	Volumetric water content (%)
1	P11_25	D1D	16.1-17.7	85.9	---	---
2	P11_25	D1D	22.1-23.6	63.5	---	---
4	P11_25	D1D	26.0-27.6	85.7	47.8	65.6
5	P11_25	D1D	24.0-26.0	50.2	---	---
10	P11_25	D1D	13.8-15.4	303.6	15.8	77.0
12	P11_05	G1C	22.8-24.4	114.2	37.5	68.7
16a	P11_05	G1C	3.2-4.7	46.2	69.8	51.7
20	P11_27	G17E+2	27.6-29.1	98.1	41.2	64.8
32	P11_27	G17E+2	12.6-14.2	110.9	35.8	63.6
37	P11_27	G17E+2	31.1-32.7	150.8	26.8	64.7
38	P11_02	G01E	17.7-19.3	98.4	42.4	66.8
41	P11_02	G01E	29.5-30.7	61.6	---	---
45	P11_02	G01E	11.4-12.6	114.3	38.6	70.6
46	P11_02	G01E	12.6-13.8	162.1	22.2	57.6
49	P11_29	G17F	5.5-7.1	71.8	46.1	53.1
53	P11_28	G18C	16.9-18.5	48.3	59.3	45.9
56	P11_28	G18C	24.0-25.2	59.4	56.3	53.6
59	P11_28	G18C	37.8-39.0	108.4	37.9	65.9
62	P11_04	G01F	3.2-4.7	43.6	69.2	48.4
65	P11_04	G01F	15.4-16.9	37.0	73.5	43.5
70	P11_01	G01H*	4.3-5.1	41.8	77.6	52.1
73	P11_01	D7D	4.3-5.5	31.2	79.2	39.6
75	P11_01	D7D	8.7-10.2	21.9	---	---
81	P11_01	D7D	35.0-36.6	74.8	51.3	61.5
85	P11_02	G01G	14.6-16.1	42.4	71.6	48.6
86	P11_02	G01G	16.1-17.7	101.6	42.2	68.7
87	P11_02	G01G	17.7-19.3	101.3	41.7	67.8

* This boring was abandoned due to water infiltration. P11_01 was immediately adjacent.

Table B-1 (CONTINUED).

Sample No.	Final ID	Field ID	Depth bgs (in.)	Gravimetric water content (%)	Dry unit weight (lb/ft^3)	Volumetric water content (%)
91	P11_12	G11N3E	24.4-26.0	36.7	70.6	41.5
94	P11_11	G11N3W	24.4-26.0	104.1	49.3	82.2
96	P11_15	G11W	15.8-17.3	28.0	89.0	39.9
108	ADAS-1	G11ADAS	31.1-32.7	131.9	32.4	68.5
111	ADAS-1	G11ADAS	48.4-50.0	103.9	39.3	65.5
119	P11_17	G11SA	33.1-34.3	147.6	31.7	75.1
124	P11_07	DSC	17.3-19.7	143.2	---	---
134	P11_13	G11N2	20.5-22.1	153.3	32.1	78.8
138	P11_18	G11SE	17.3-18.9	72.9	54.3	63.4
154	P11_20	G11NE	26.4-27.6	180.1	28.9	83.6
155	P11_20	G11NE	27.6-28.7	131.0	35.0	73.5

Table B-2. Summary of geotechnical soils data.

Sample No.	Final ID	Field ID	Depth bgs (in.)	Specific gravity	Liquid limit (%)	Plastic index
93	P11_11	G11N3W	21.7-24.4	2.51	28.8	6.2
103	P11_16	G11SW	17.7-21.7	2.62	29.4	---
113c	ADAS-1	G11ADAS	66.1-70.5	2.64	26.7	0.3
118/120	P11_17	G11SA	31.9-33.1, 34.3-37.0	2.47	41.8	---
128a	P11_14	G11NW	11.8-16.1	2.65	27.2	2.1
148	P11_22	S3	17.7-23.6	1.82	71.1	---
149	P11_22	S3	23.6-26.8	2.16	54.6	---
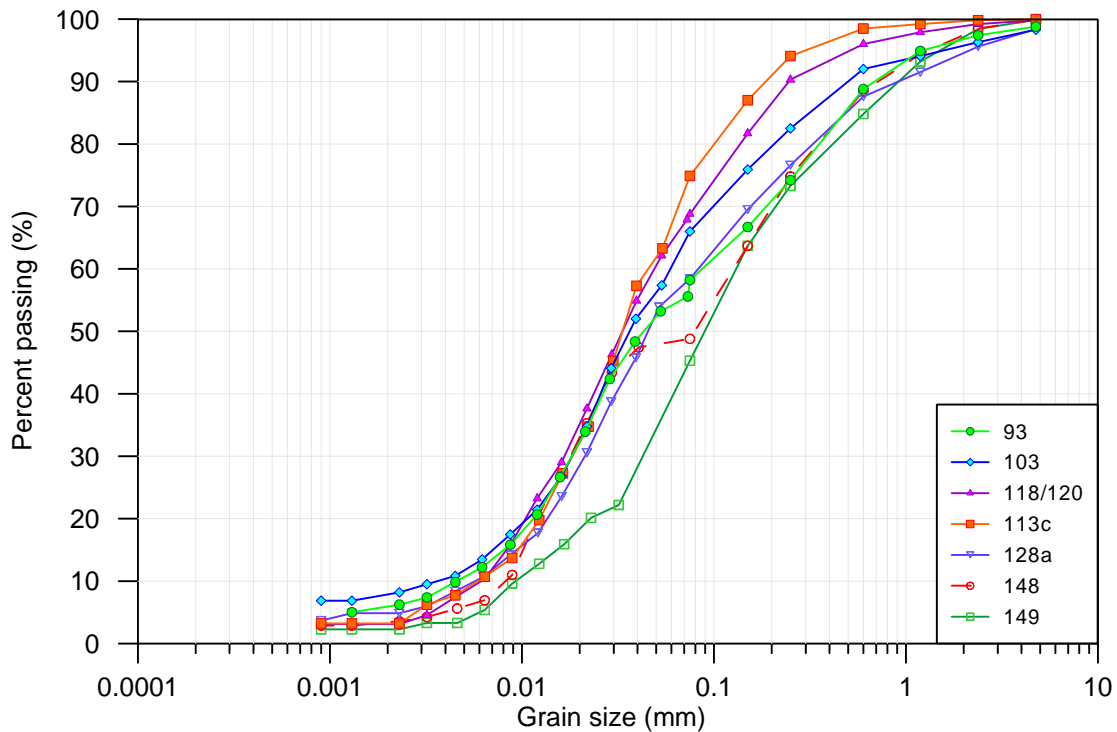
Figure B-1. Grain size distributions for tested samples.

APPENDIX C: THERMAL CONDUCTIVITY TEST RESULTS

THERMAL CONDUCTIVITY MEASUREMENT PROCEDURE

The following procedures were developed for the KD2 Pro thermal conductivity soil probe. Results are summarized in Tables C-1 through C-4.

Frozen Thermal Conductivity

1) Drill a hole in the center of the soil sample at one end. The hold should be deep enough for the probe to be fully inserted, and the sample should be twice the length of the probe. Place the sample back into the freezer overnight to equilibrate.

2) Insert thermal compound into the hole for good thermal connection between the probe and the soil. Place the sample back into the freezer overnight to equilibrate.

3) While keeping the sample in the freezer, fully insert the probe and closer freezer, being mindful not to damage the probe cable. Take readings at 15-minute intervals, for a total of three to five readings. Record the temperature as well as the thermal conductivity reading. Average the readings.

4) Alternatively, take one thermal conductivity reading, while also recording the temperature of the sample. Remove and reinsert the probe. Wait 15 minutes and take thermal conductivity and temperature readings. Repeat for a total of three to five readings. Average the readings.

Unfrozen Thermal Conductivity

1) Remove the soil sample from the freezer, remove any wrapping, record the mass, temperature, and start of thaw time.

2) Place the sample into a "thaw cell" (which can be constructed from ABS pipe and end caps), and cover the top of the cell to limit evaporation.

3) Let sample thaw overnight to reach room temperature.

4) Record the final temperature and the end of the thawing period. Insert the thermal conductivity probe and cover with plastic to limit evaporation. At 15-minute intervals, take thermal conductivity and temperature readings, for a total of three to five readings. Average the readings.

5) Alternatively, take one thermal conductivity reading, while also recording the temperature of the sample. Remove and reinsert the probe. Wait 15 minutes and take thermal conductivity and temperature readings. Repeat for a total of three to five readings. Average the readings.

6) Oven-dry the sample according to ASTM standards to obtain moisture content.

Table C-1. Summary of unfrozen thermal conductivity measurements made at 15-minute intervals without removing the probe.

Sample No.	Final ID	Field ID	Depth bgs (in).	Sample temperature (°F)	Thermal conductivity (Btu/hr·ft·°F)	Average Thermal conductivity (Btu/hr·ft·°F)
90	P11_12	G11N3E	19.7-24.4	72.5	0.567	0.566
				72.14	0.560	
				71.91	0.571	
99	P11_15	G11W	33.1-39.4	72.91	0.343	0.343
				72.59	0.344	
				72.30	0.344	
106	ADAS-1	G11ADAS	15.0-20.5	73.44	0.421	0.422
				72.97	0.421	
				72.59	0.422	
113a	ADAS-1	G11ADAS	55.5-61.0	72.78	0.551	0.552
				72.93	0.555	
				72.91	0.551	
137	P11_18	G11SE	11.0-17.3	71.96	0.451	0.449
				71.94	0.452	
				71.96	0.446	
140	P11_18	G11SE	24.8-29.5	72.97	0.461	0.462
				72.88	0.461	
				72.75	0.463	
158b	P11_24	S1	34.7-39.4	73.53	0.347	0.346
				73.51	0.346	
				73.49	0.318	
				73.47	0.347	

Table C-2. Summary of unfrozen thermal conductivity measurements made at 15-minute intervals after removing and replacing the probe.

Sample No.	Final ID	Field ID	Depth bgs (in).	Sample temperature (°F)	Thermal conductivity (Btu/hr·ft·°F)	Average Thermal conductivity (Btu/hr·ft·°F)
90	P11_12	G11N3E	19.7-24.4	71.94	0.591	0.455
				71.96	0.443	
				71.85	0.448	
				71.56	0.475	
99	P11_15	G11W	33.1-39.4	72.21	0.364	0.352
				72.34	0.347	
				72.32	0.345	
106	ADAS-1	G11ADAS	15.0-20.5	71.94	0.461	0.454
				70.86	0.375	
				70.84	0.508	
				72.64	0.474	
113a	ADAS-1	G11ADAS	55.5-61.0	72.82	0.449	0.605
				73.40	0.606	
				73.92	0.601	
				74.16	0.607	
137	P11_18	G11SE	11.0-17.3	72.30	0.431	0.434
				72.00	0.435	
				72.36	0.437	
140	P11_18	G11SE	24.8-29.5	72.66	0.437	0.414
				72.77	0.380	
				72.79	0.426	
158b	P11_24	S1	34.7-39.4	72.63	0.341	0.338
				72.48	0.342	
				72.32	0.331	

Table C-3. Summary of frozen thermal conductivity measurements made at 15-minute intervals without removing the probe.

Sample No.	Final ID	Field ID	Depth bgs (in).	Sample temperature (°F)	Thermal conductivity (Btu/hr·ft·°F)	Average Thermal conductivity (Btu/hr·ft·°F)
90	P11_12	G11N3E	19.7-24.4	1.08	0.852	0.861
				1.33	0.868	
				1.60	0.853	
				1.53	0.872	
99	P11_15	G11W	33.1-39.4	1.20	0.815	0.826
				1.13	0.814	
				1.42	0.852	
				1.56	0.821	
106	ADAS-1	G11ADAS	15.0-20.5	0.97	0.824	0.827
				0.86	0.835	
				1.06	0.822	
113a	ADAS-1	G11ADAS	55.5-61.0	0.84	0.893	0.898
				0.82	0.904	
				0.93	0.896	
137	P11_18	G11SE	11.0-17.3	0.64	0.752	0.757
				0.72	0.761	
				0.75	0.769	
140	P11_18	G11SE	24.8-29.5	0.55	0.888	0.866
				1.33	0.869	
				1.08	0.867	
				1.29	0.841	
158b	P11_24	S1	34.7-39.4	0.82	0.730	0.727
				0.99	0.739	
				1.26	0.717	
				1.04	0.724	

Table C-4. Summary of frozen thermal conductivity measurements made at 15-minute intervals after removing and replacing the probe.

Sample No.	Final ID	Field ID	Depth bgs (in).	Sample temperature (°F)	Thermal conductivity (Btu/hr·ft·°F)	Average Thermal conductivity (Btu/hr·ft·°F)
90	P11_12	G11N3E	19.7-24.4	0.37	0.839	0.829
				0.84	0.846	
				1.94	0.815	
				1.89	0.818	
99	P11_15	G11W	33.1-39.4	1.74	0.851	0.827
				1.78	0.822	
				2.30	0.808	
				2.53	0.827	
106	ADAS-1	G11ADAS	15.0-20.5	1.44	0.779	0.782
				2.28	0.775	
				2.35	0.757	
				2.64	0.819	
113a	ADAS-1	G11ADAS	55.5-61.0	0.59	0.916	0.858
				0.99	0.893	
				1.24	0.858	
				1.94	0.764	
137	P11_18	G11SE	11.0-17.3	-0.22	0.754	0.762
				0.37	0.765	
				0.41	0.761	
				0.77	0.766	
140	P11_18	G11SE	24.8-29.5	0.19	0.826	0.821
				0.10	0.841	
				0.59	0.787	
				0.82	0.829	
158b	P11_24	S1	34.7-39.4	0.99	0.683	0.692
				0.95	0.680	
				1.56	0.722	
				1.51	0.684	

APPENDIX D: THAW DEPTH MEASUREMENTS

Table D-1. Thaw depth measurements recorded by UAF personnel at AHTS.

Final ID	Field ID	Average thaw depth (in.), rounded to the nearest inch		
		08/28/11	05/14/12	09/01/12
South side of road close to embankment				
	18*	17	4	8
South side of road farther from embankment				
P11_22	S3	20	4	8
P11_23	S2	19	5	7
P11_24	S1	19	5	7
North side of road close to embankment				
	4*	20	8	8
ADAS transect north of ditch				
P11_10	G11N4	23	7	11
P11_12	G11N3E	27	5	11
P11_11	G11N3W	23	4	10
P11_13	G11N2	19	5	8
P11_17	G11SA	17	---	8
P11_21	G11NA	19	4	8
Parallel to ADAS transect north of ditch				
P11_16	G11SW	25	6	11
P11_15	G11W	20	6	8
P11_14	G11NW	22	5	9
P11_20	G11NE	21	8	8
P11_19	G11E	22	4	9
P11_18	G11SE	16	5	8

* These installations were installed prior to this project.

APPENDIX E: PRELIMINARY ECO-GEOMORPHOLOGICAL MAP AND WATER LEVEL MEASUREMENTS

Legend

Terrain Units
Class

- HighForest
- LowForest
- SpillArea
- WTrack
- Lake
- Gravel
- Pavement
- OldHwy
- Disturbed
- Streams

Feet
0   250 500   1 000   1 500   2 000
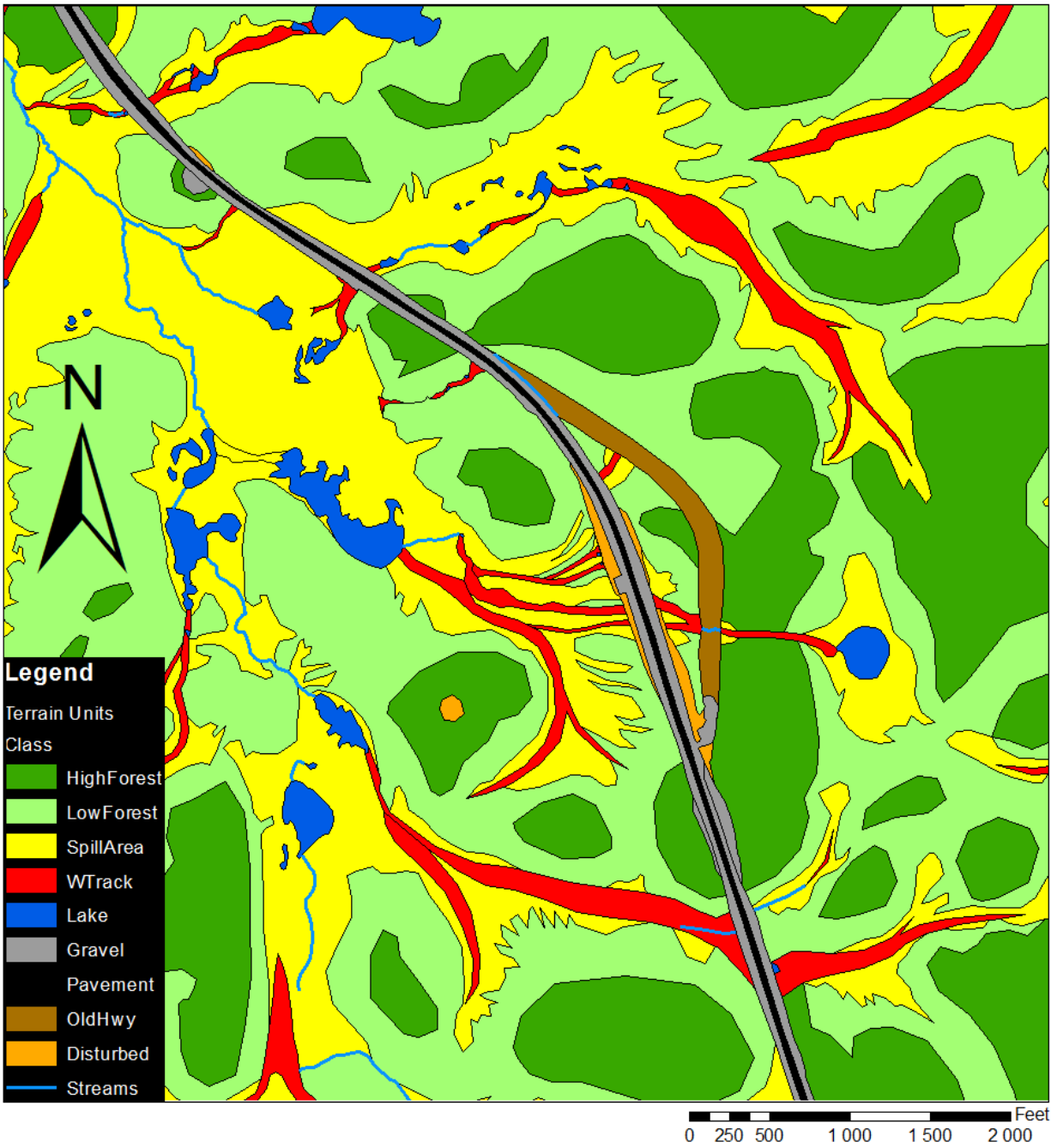
ROADSIDE

Ditch

Upstream, natural soil

PWPT5 - Water level
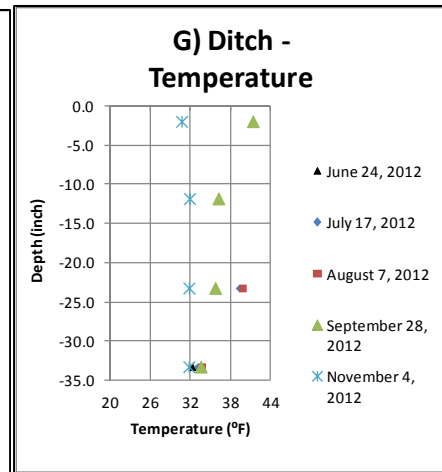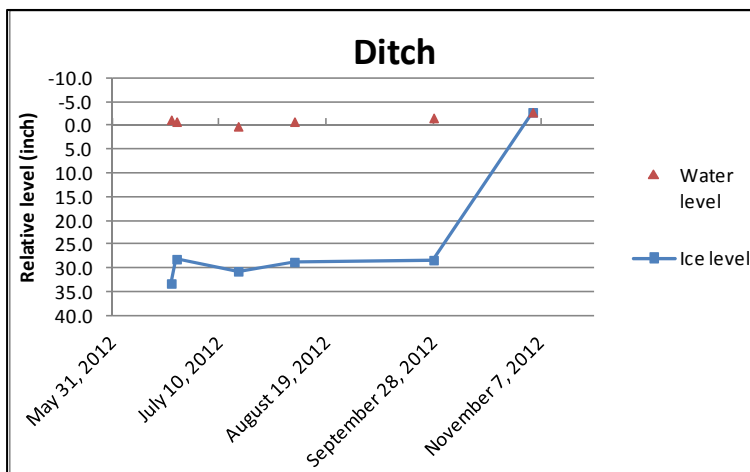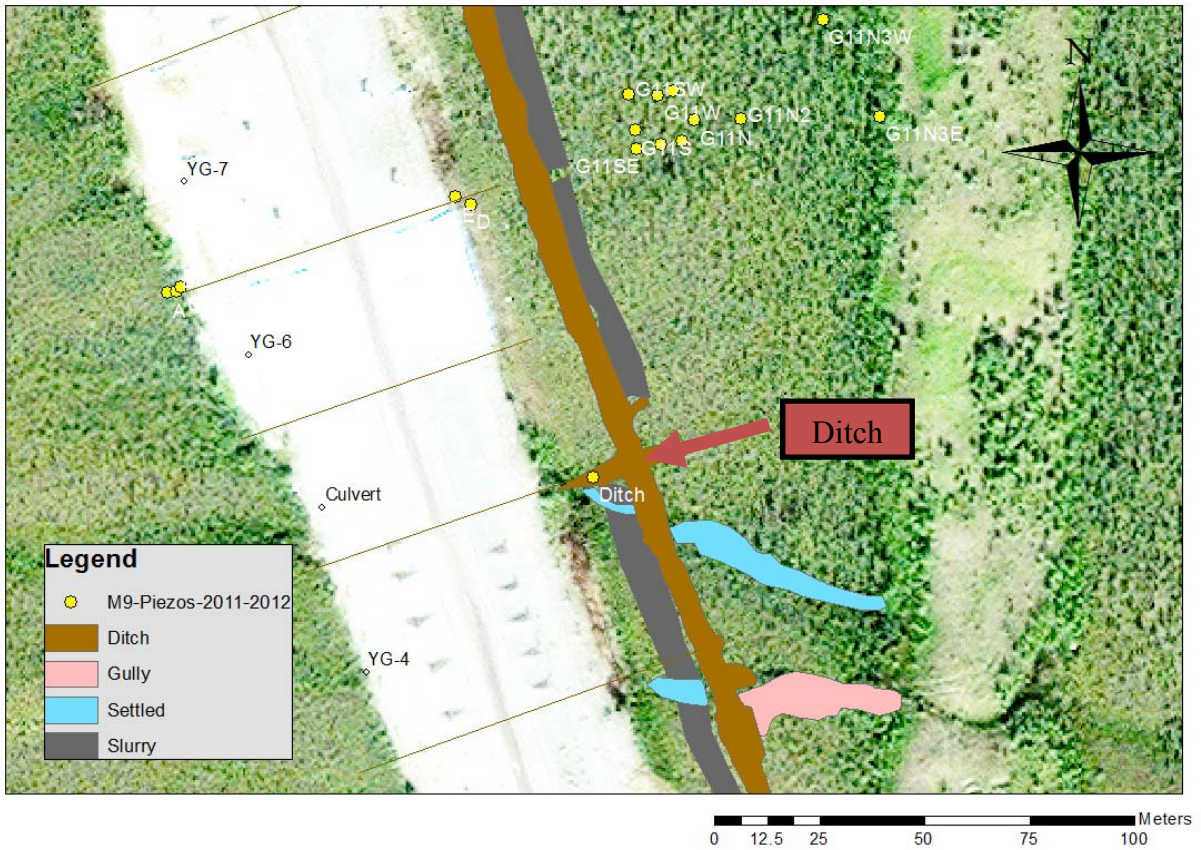
PWPT5 - Water level
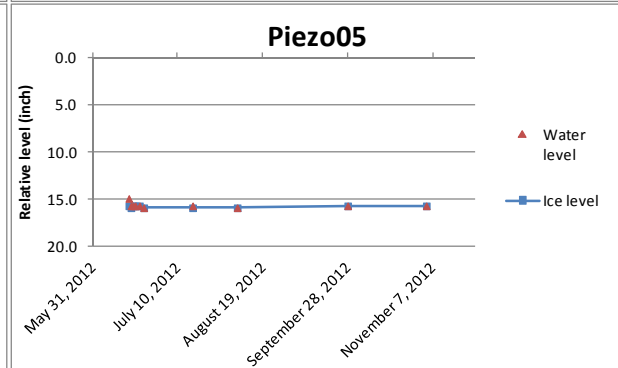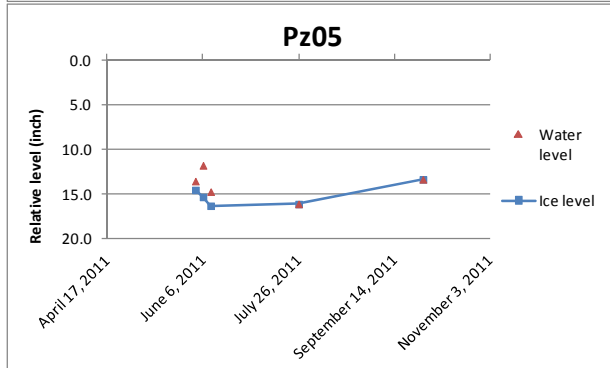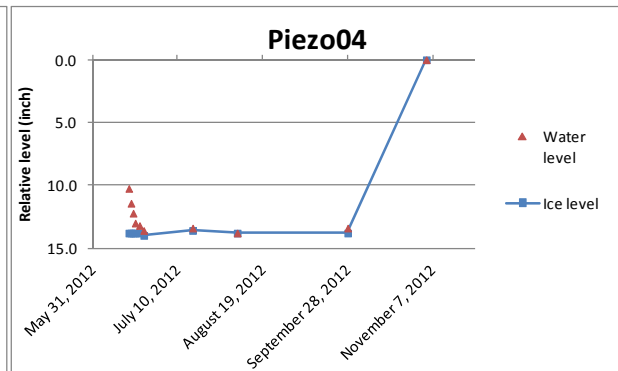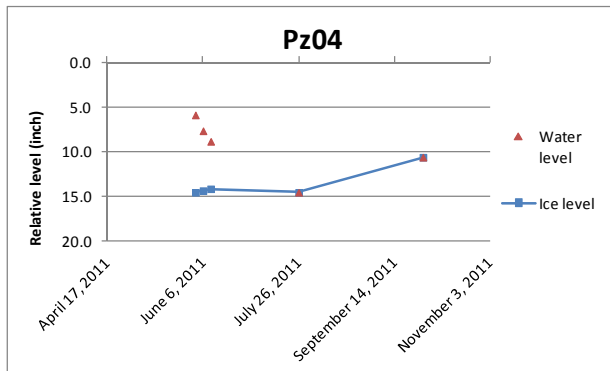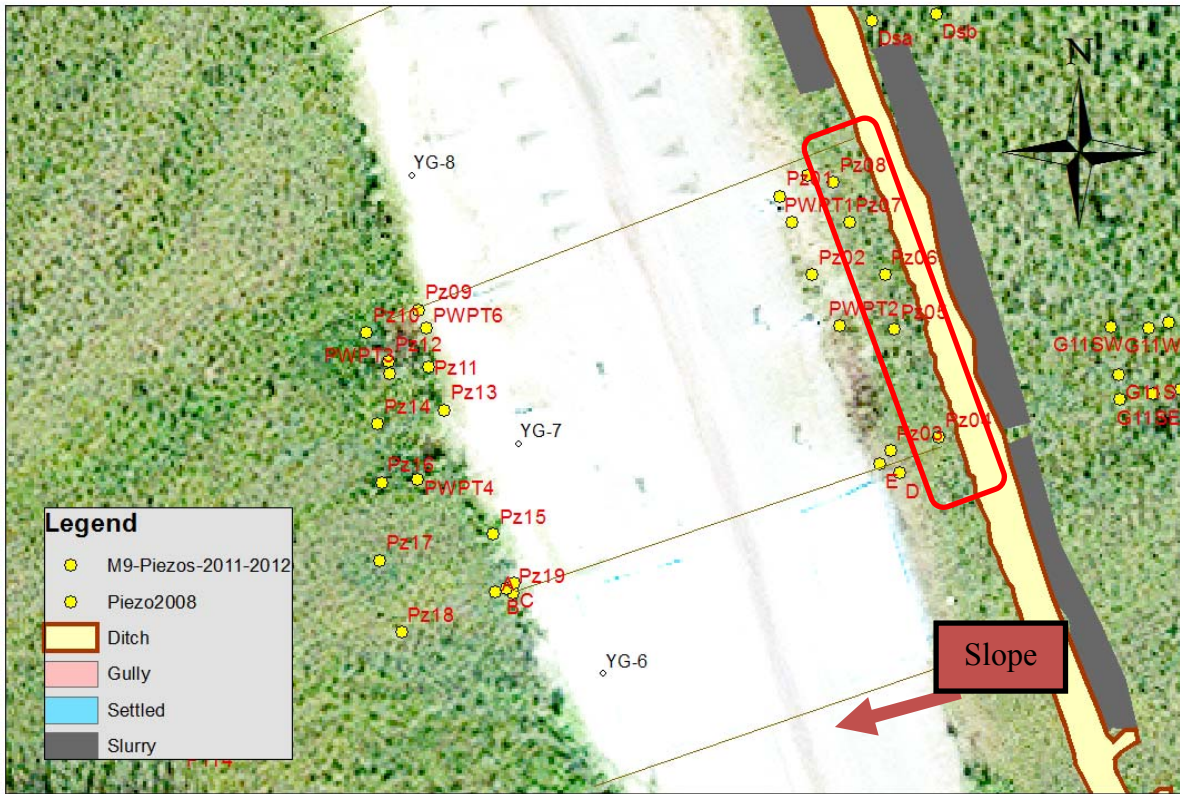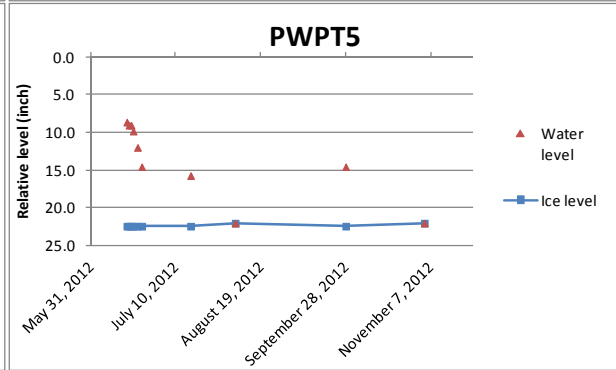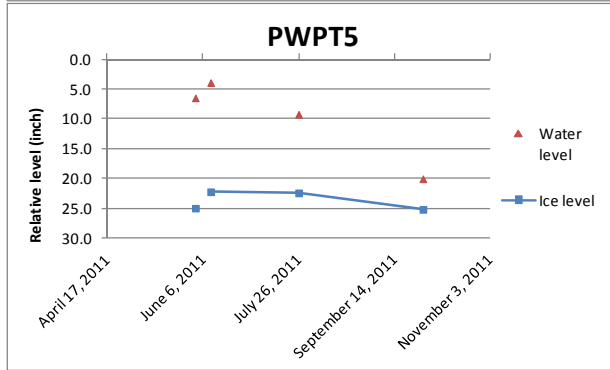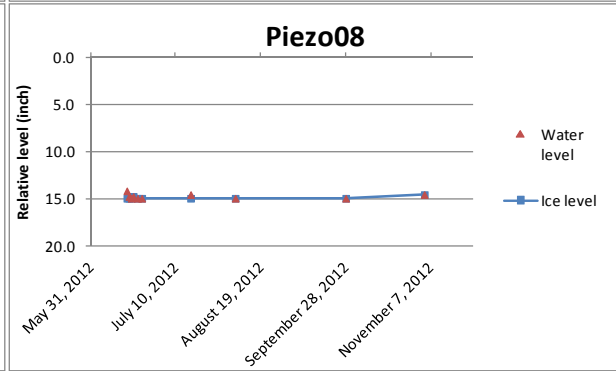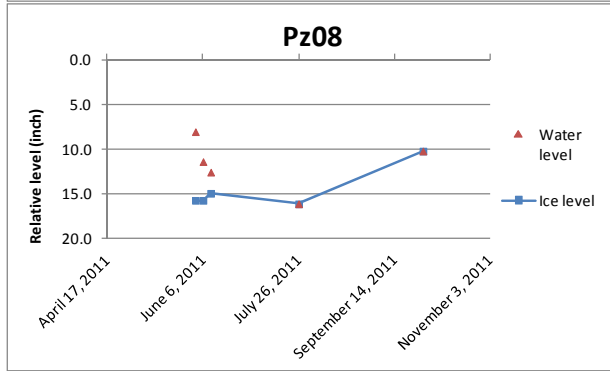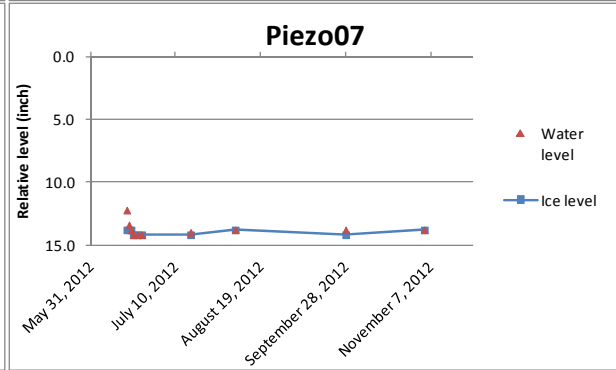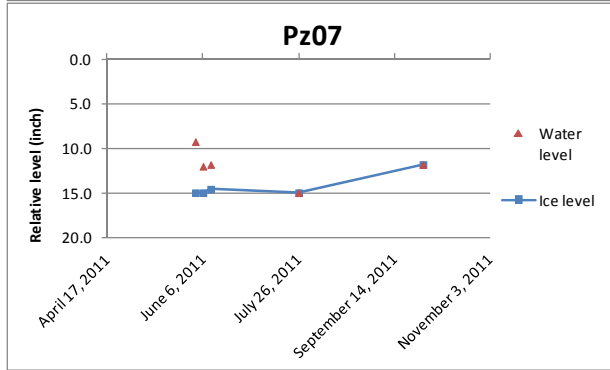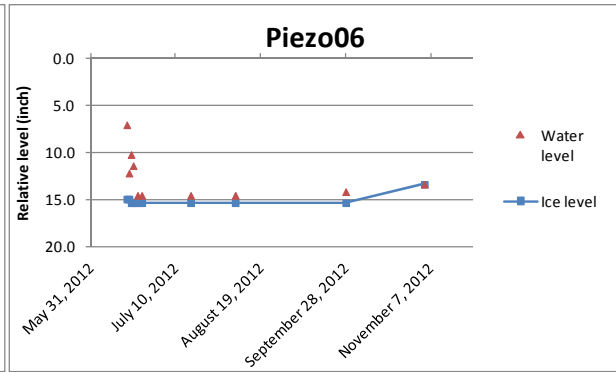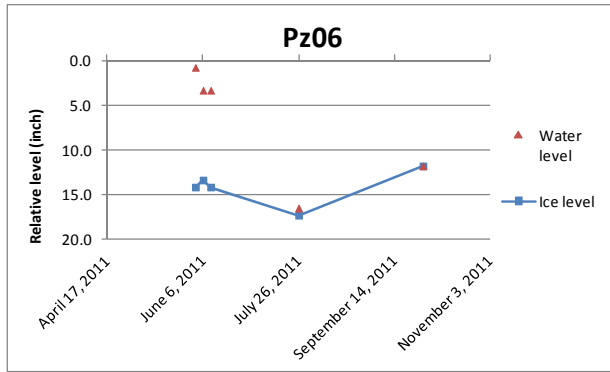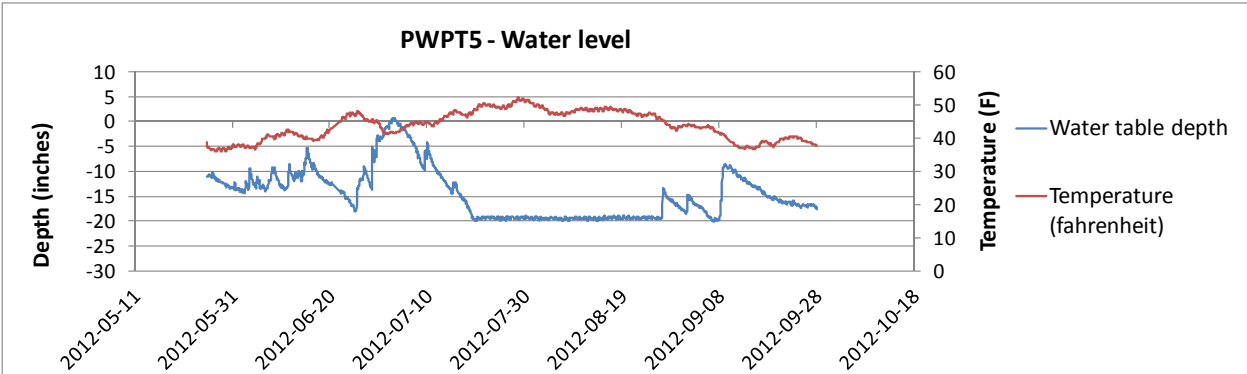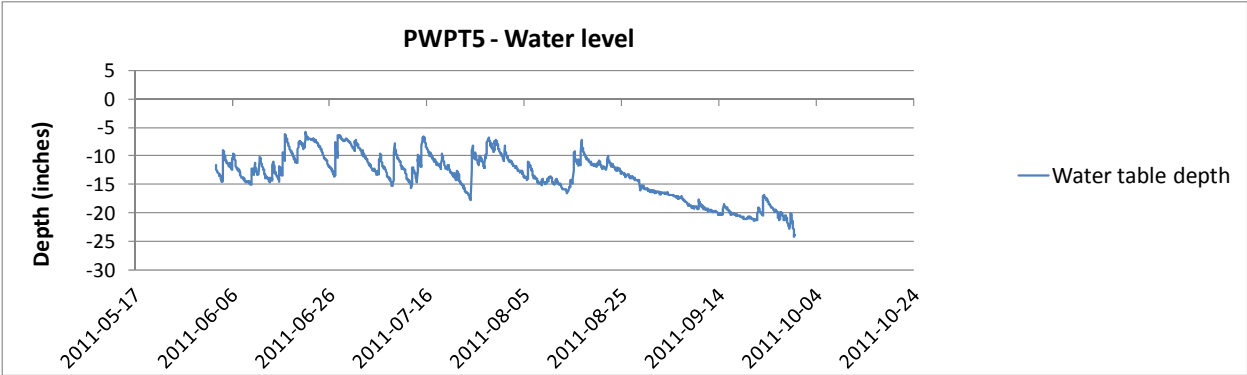
Upstream, disturbed soil

PWPT2 - Water level
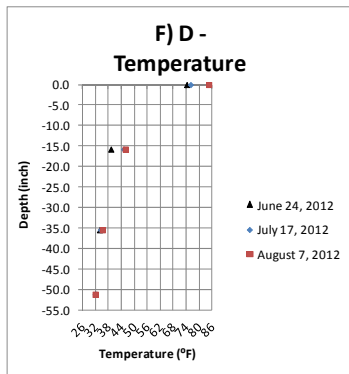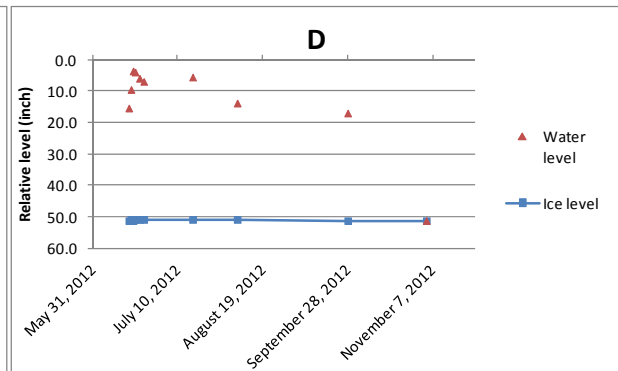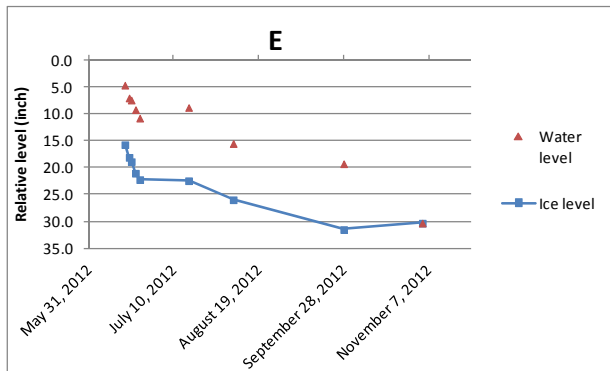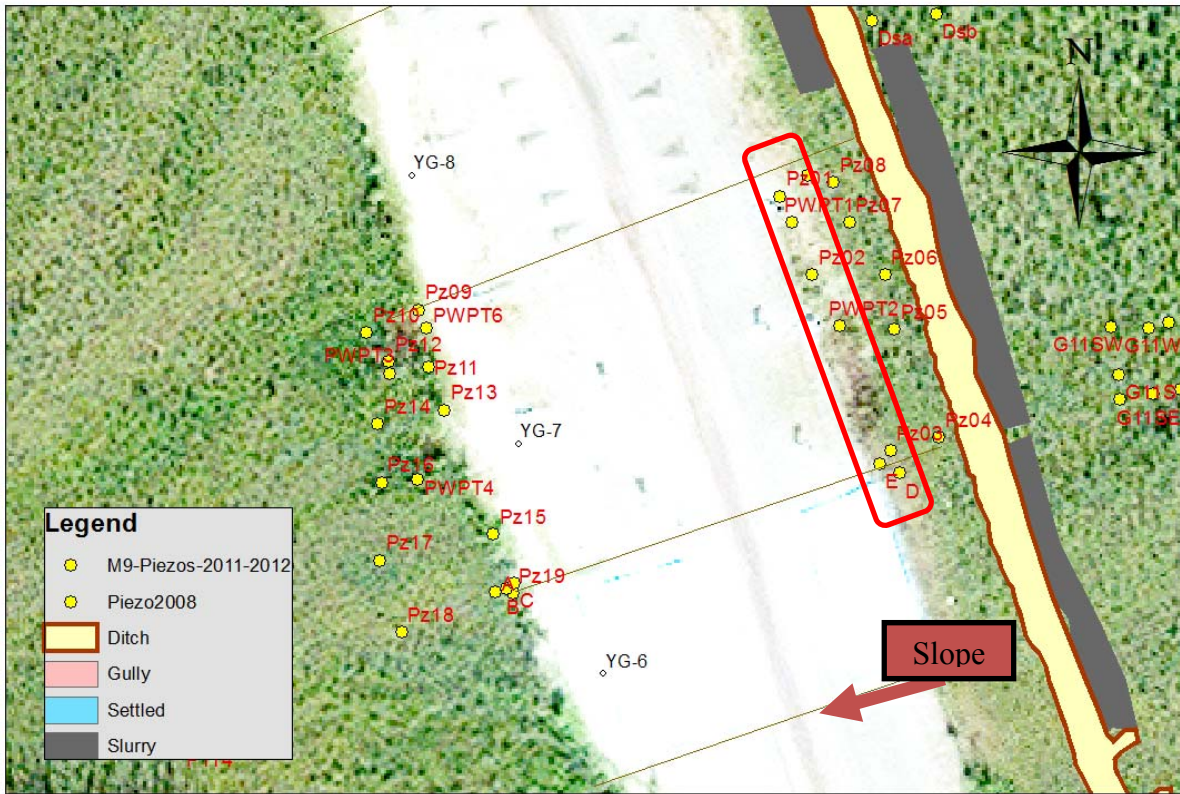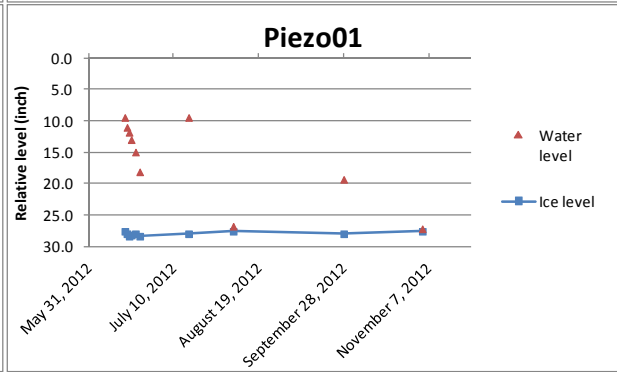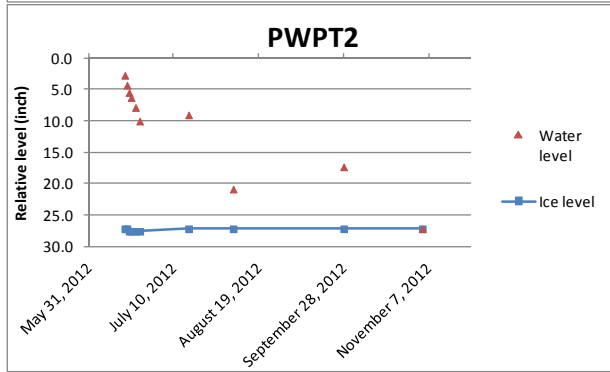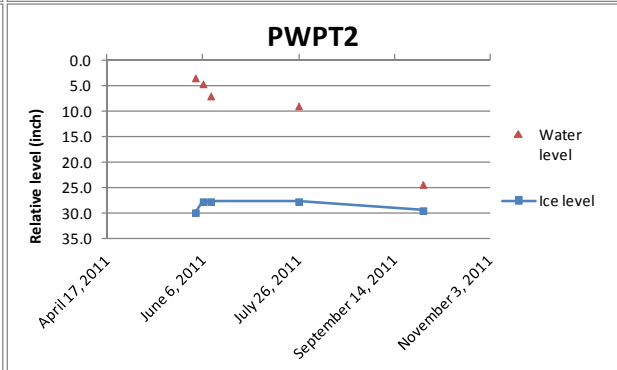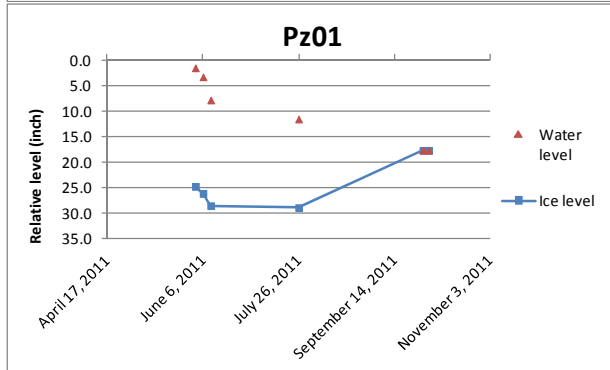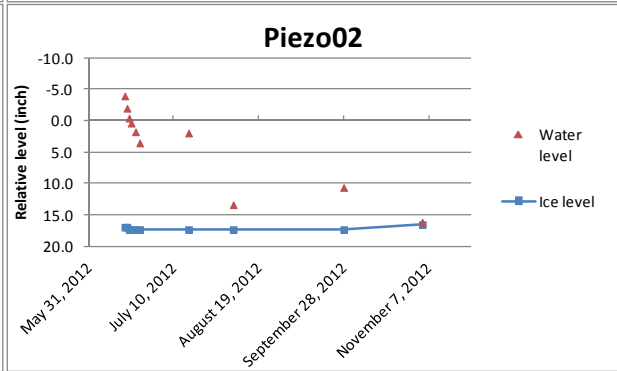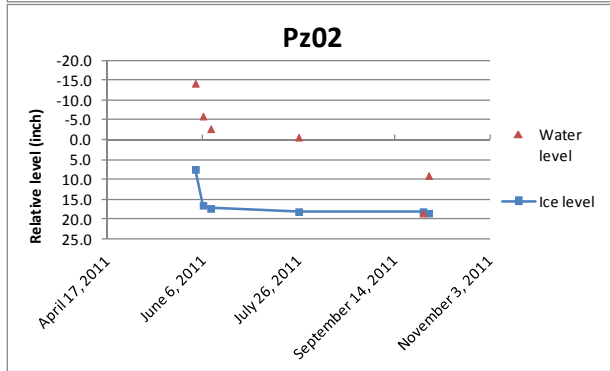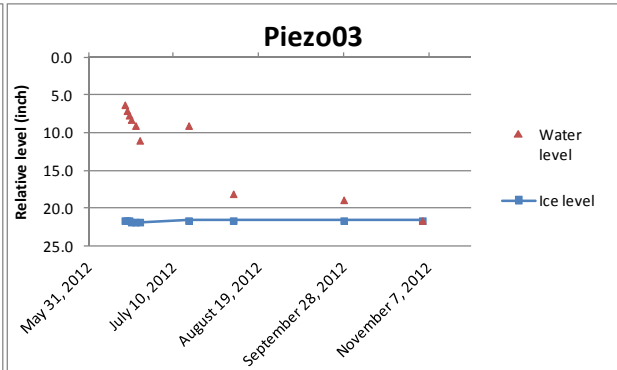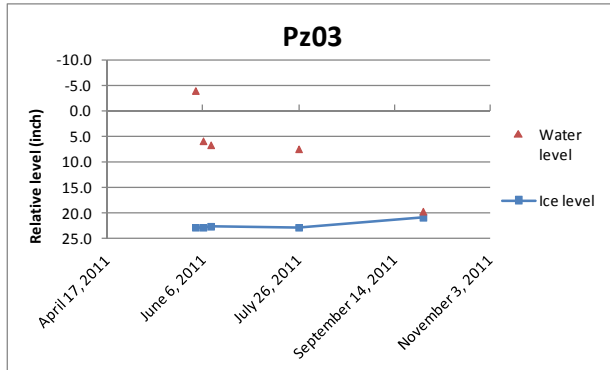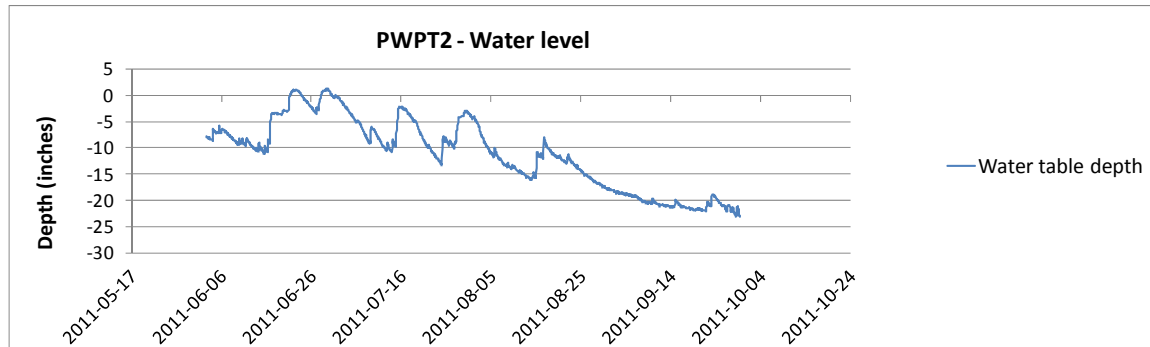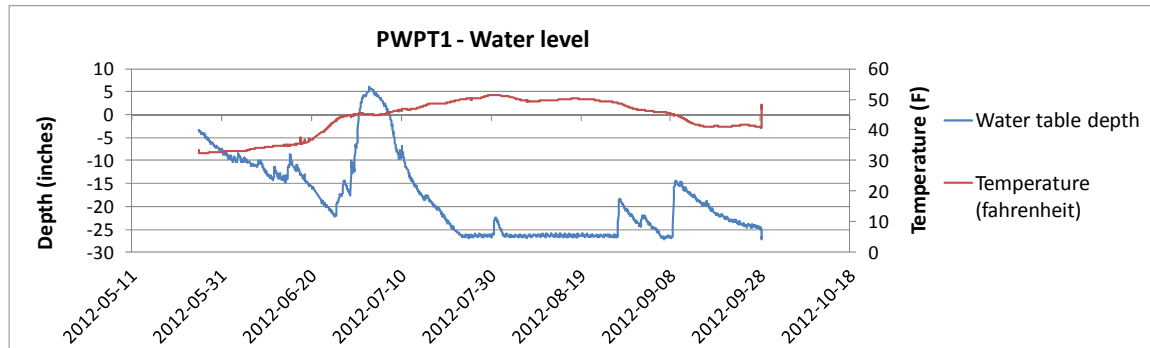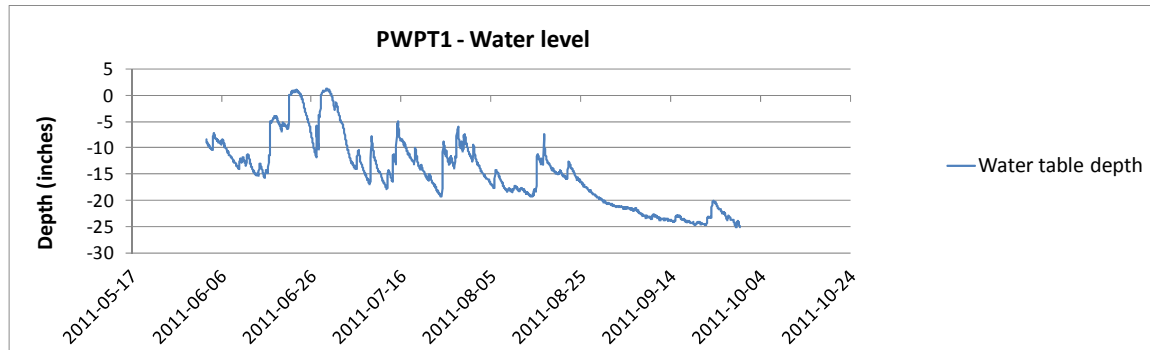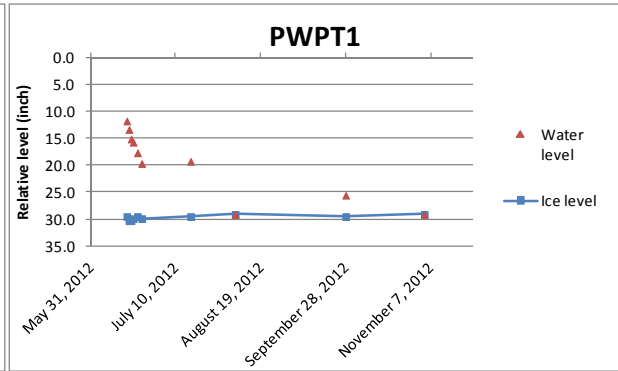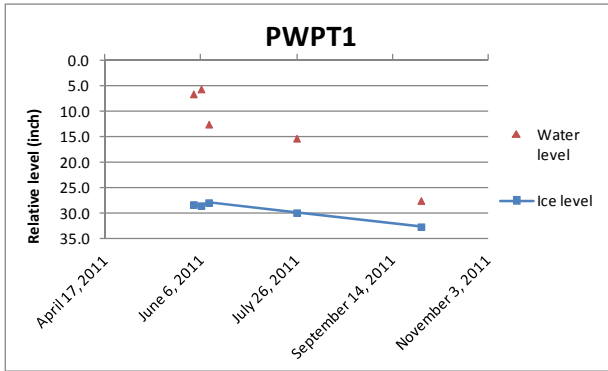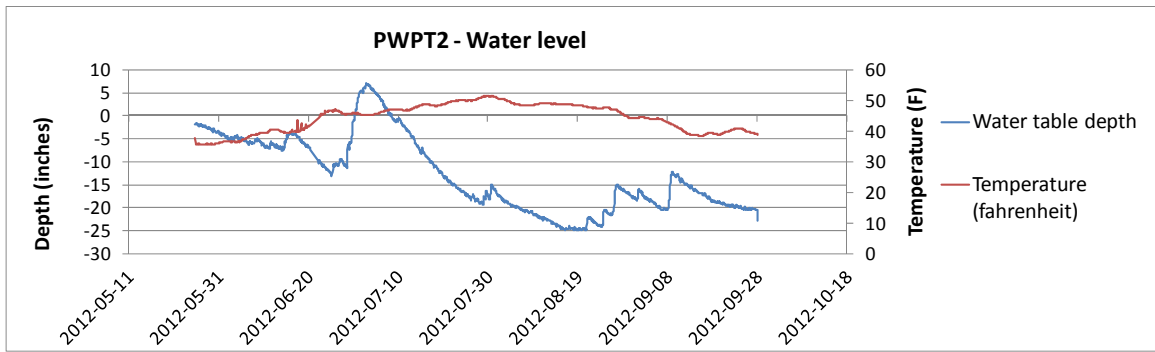
Downstream, disturbed soil

85
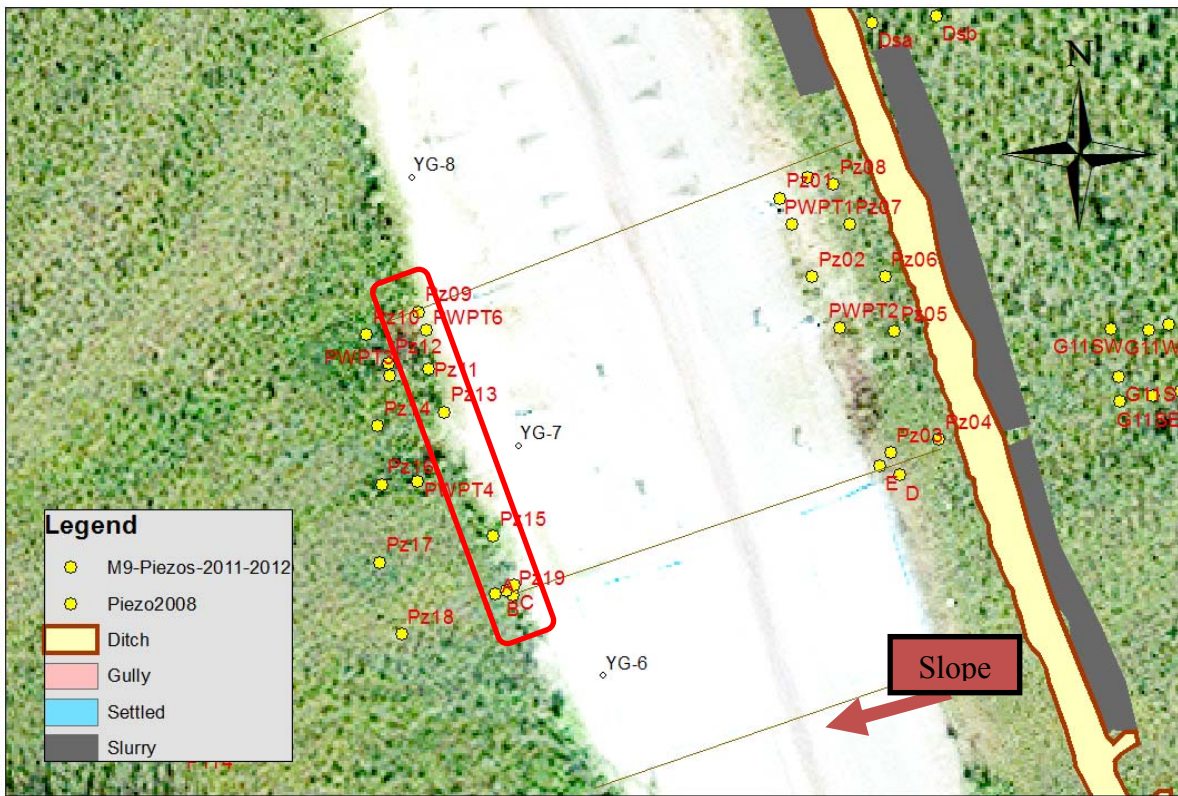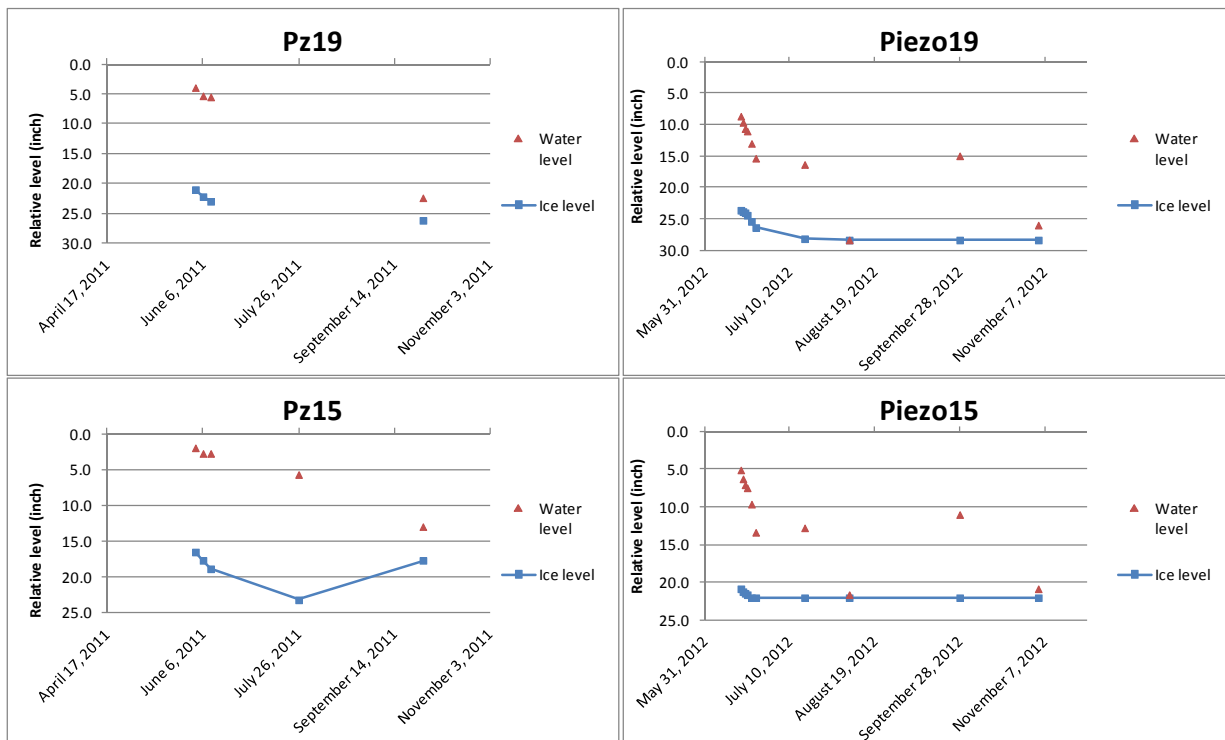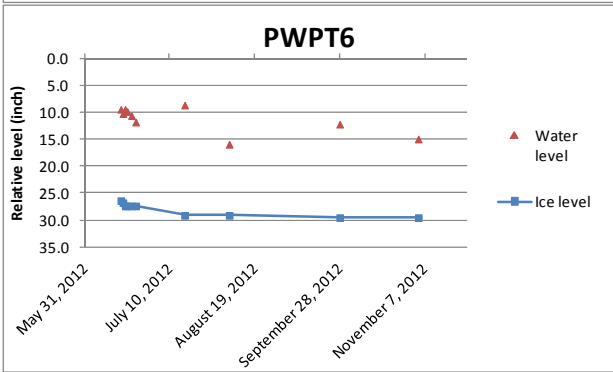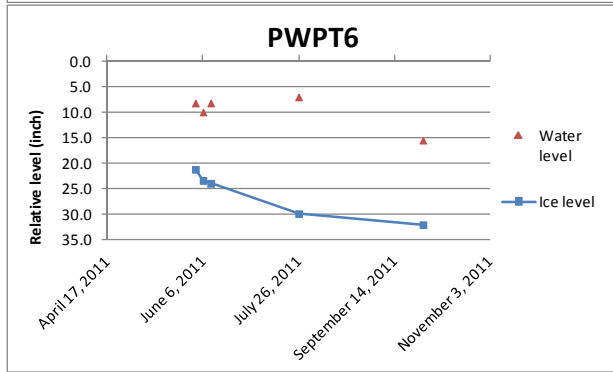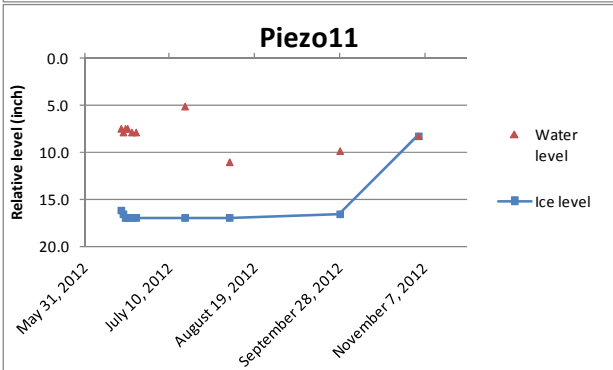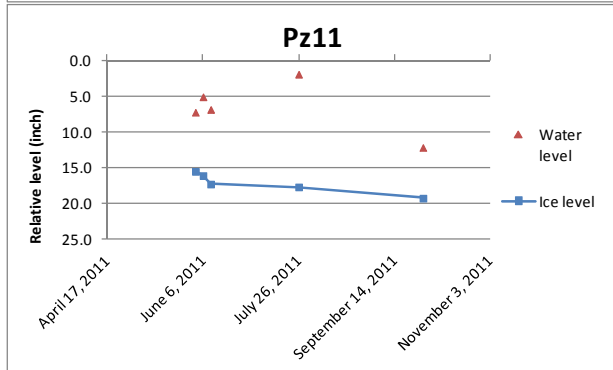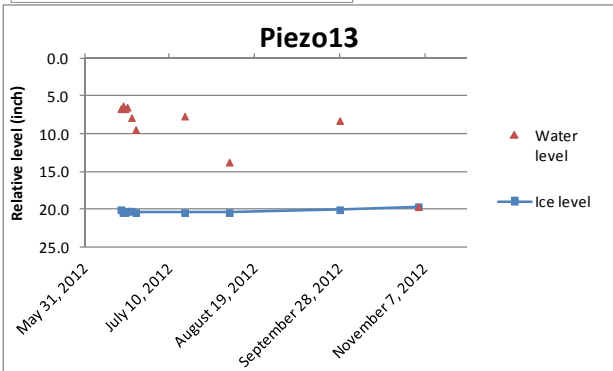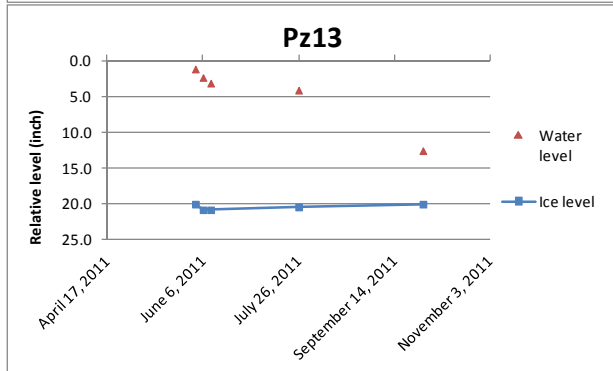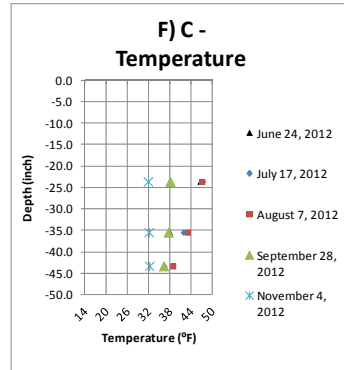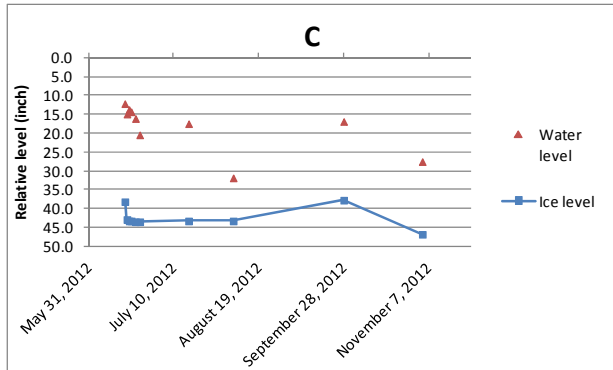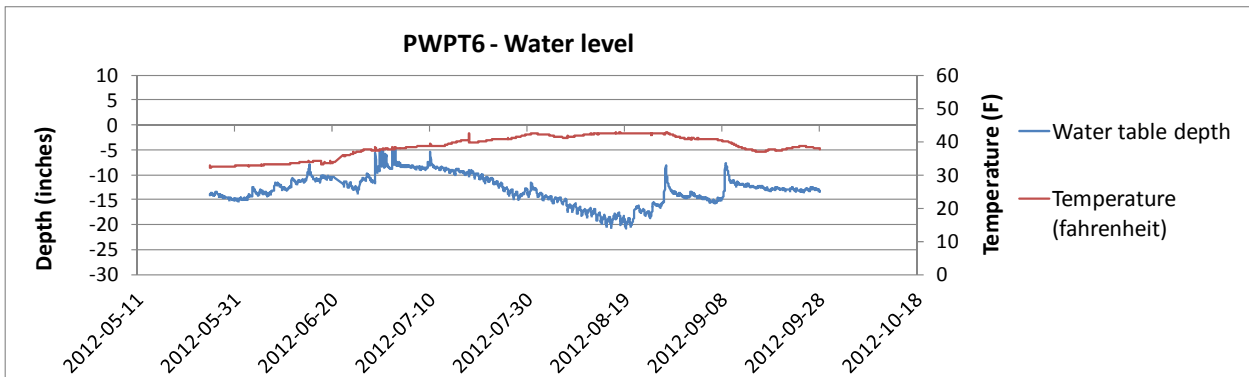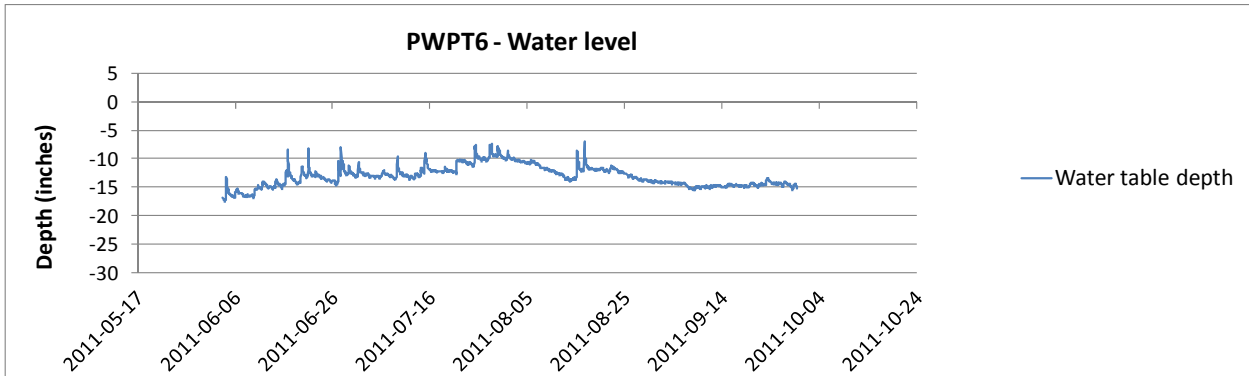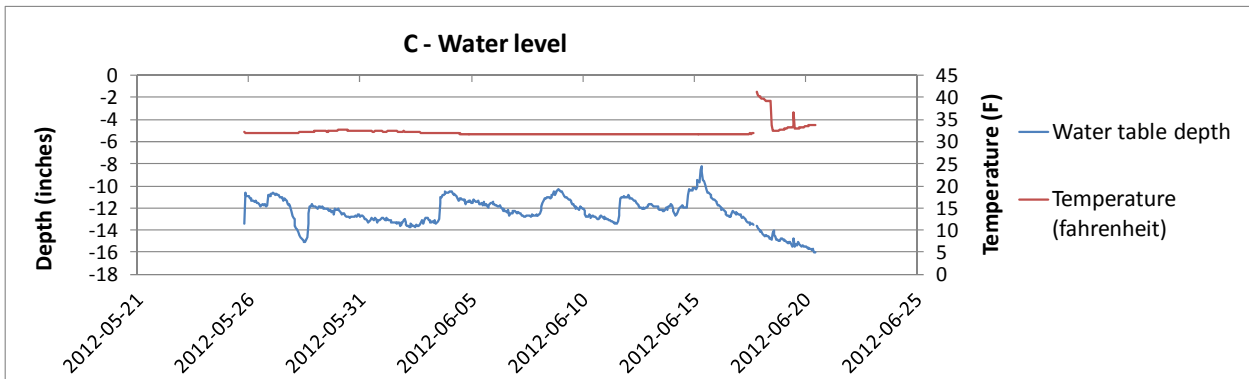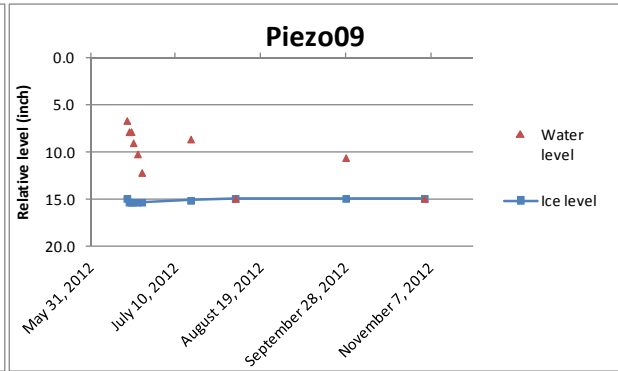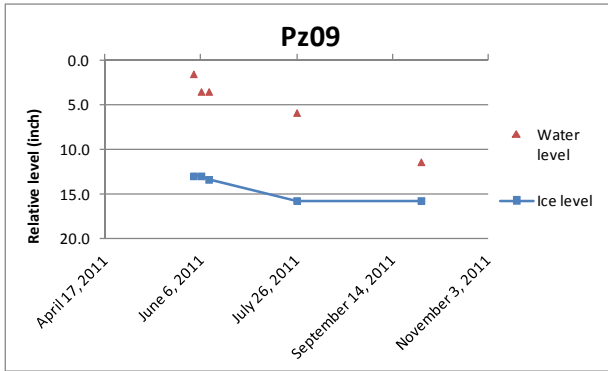
Downstream, natural soil
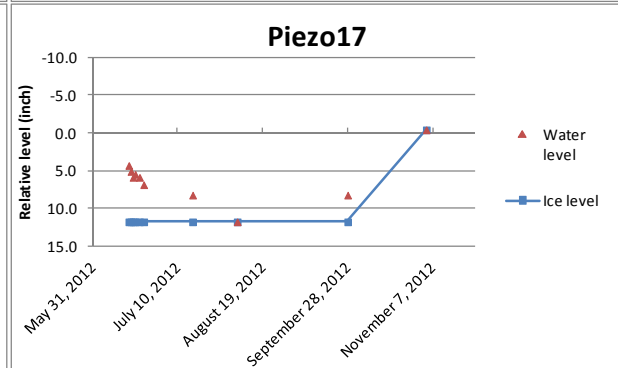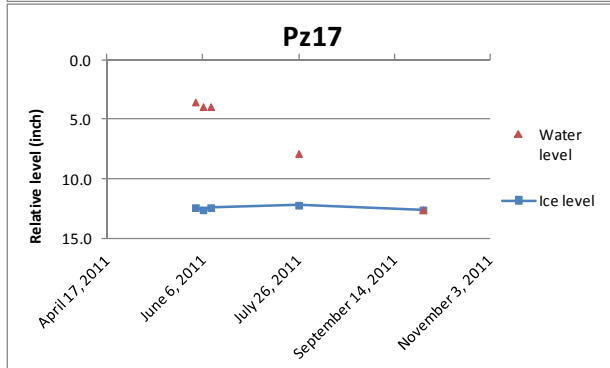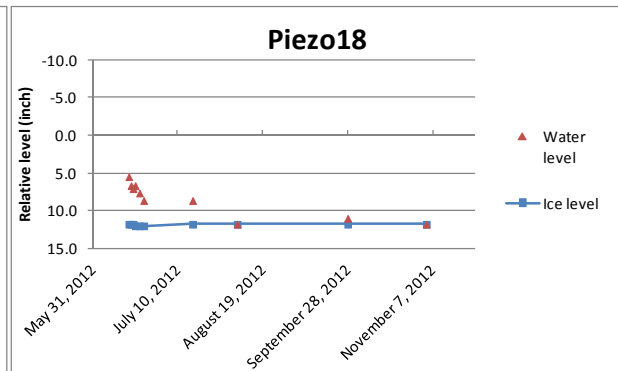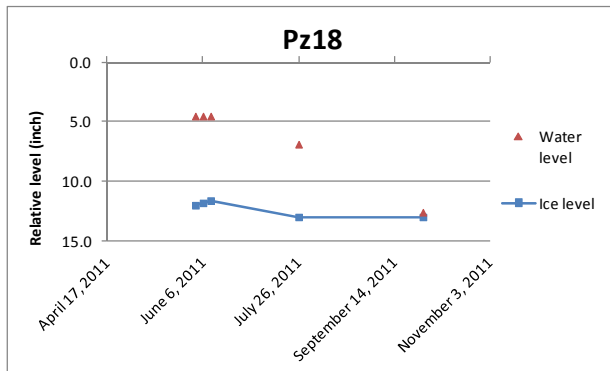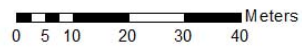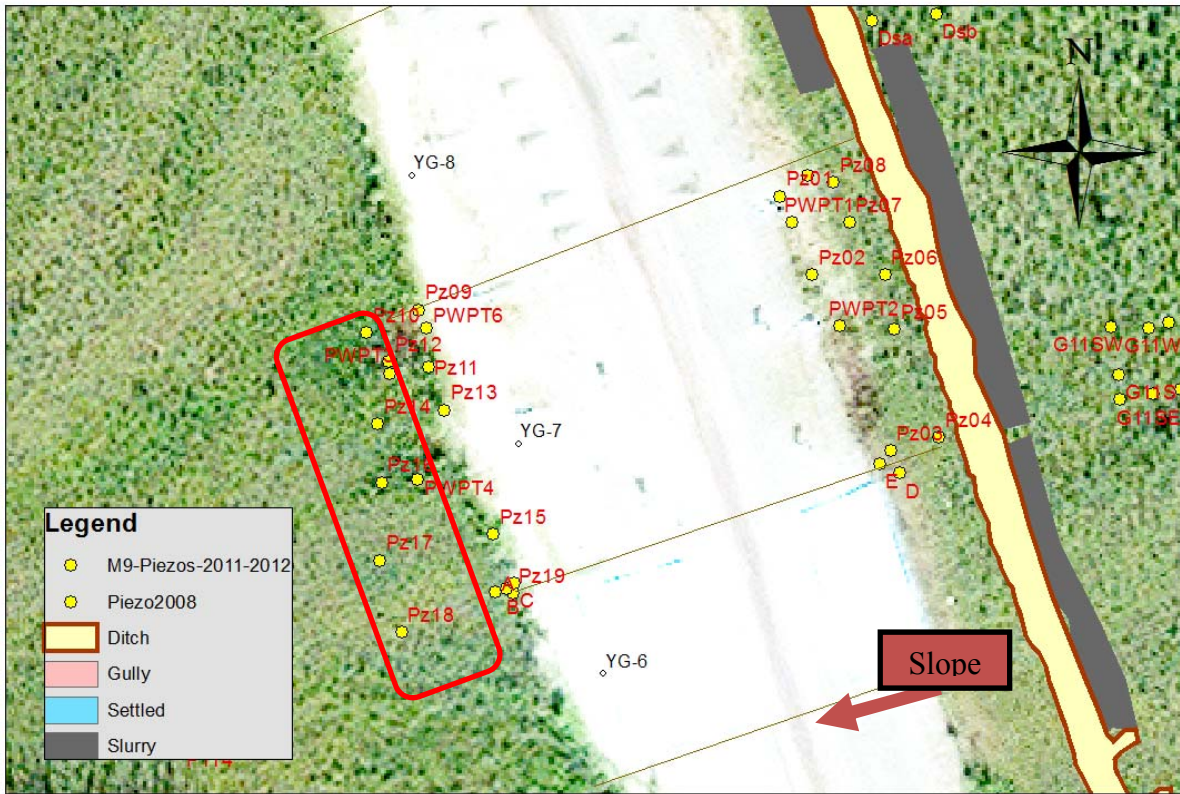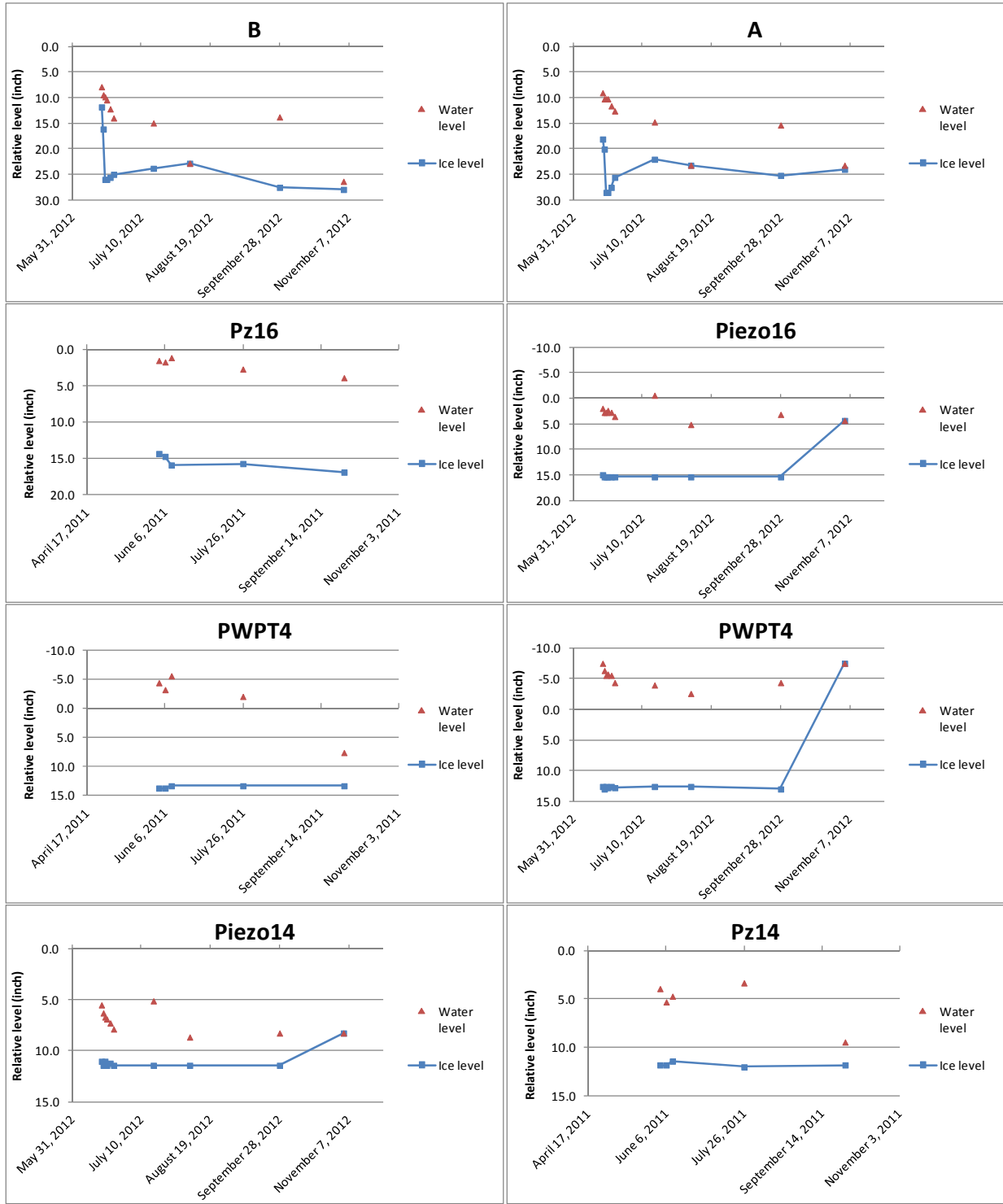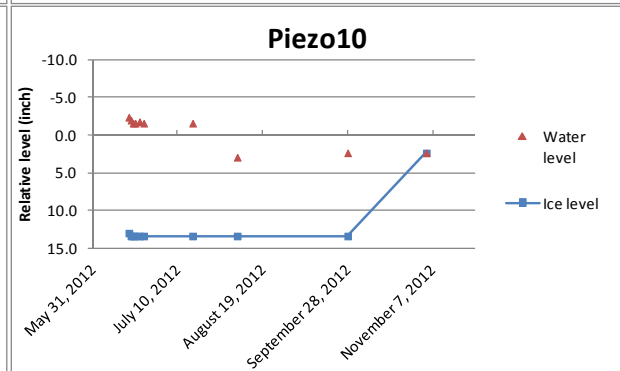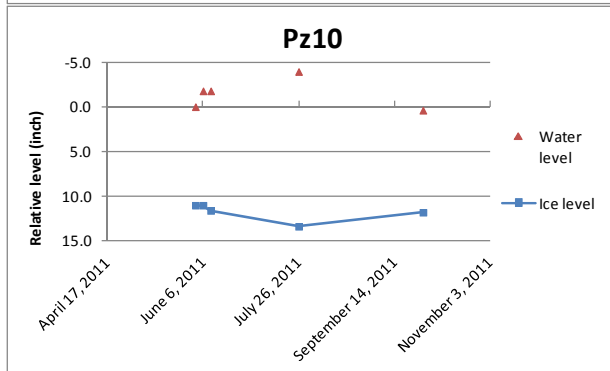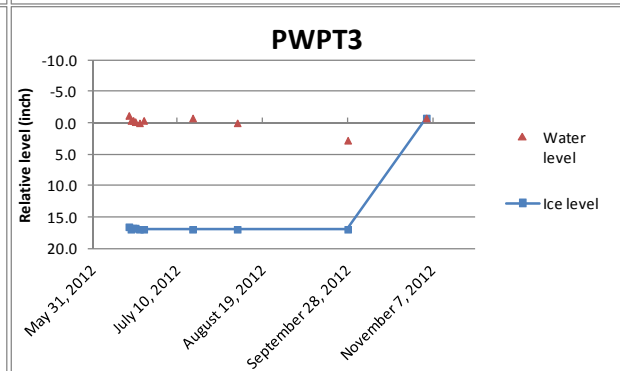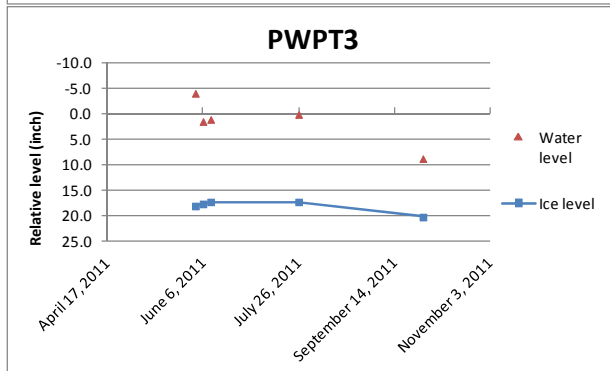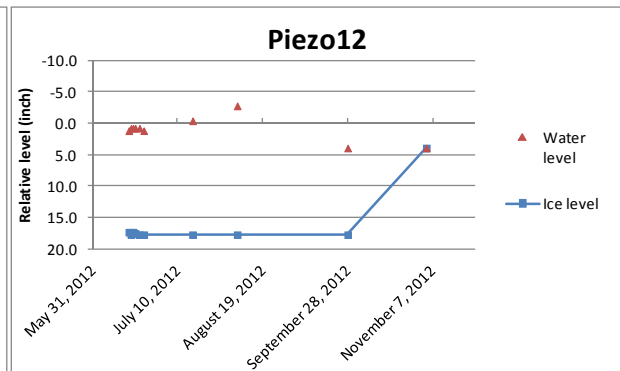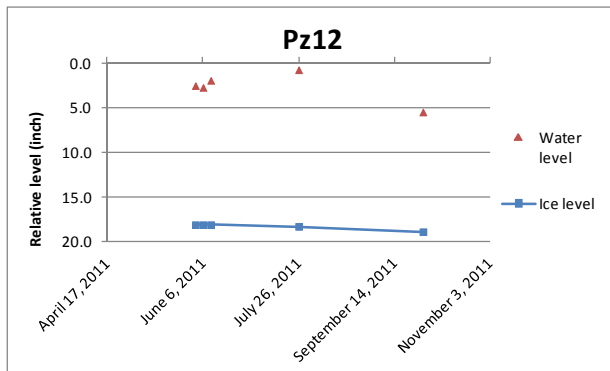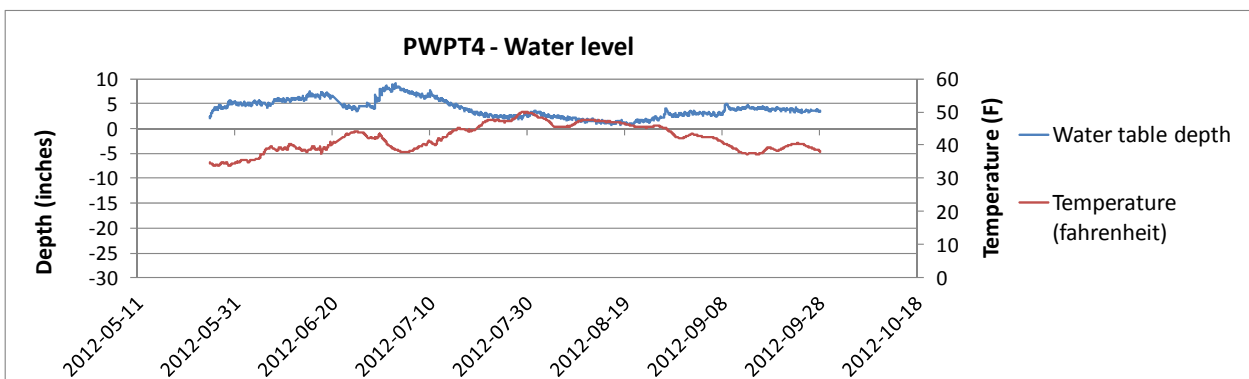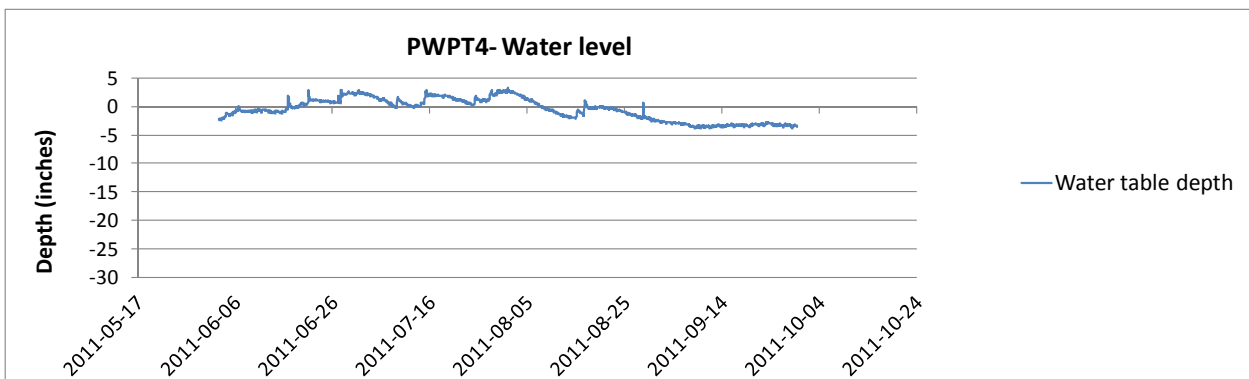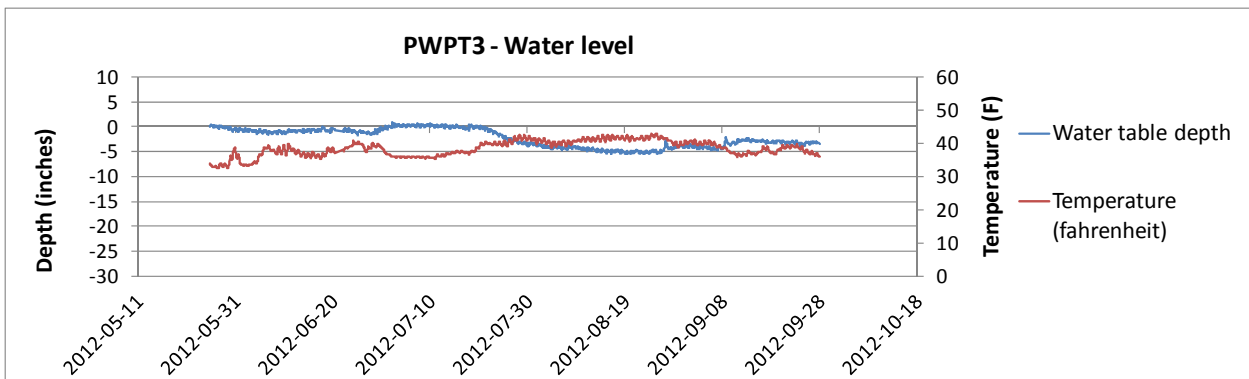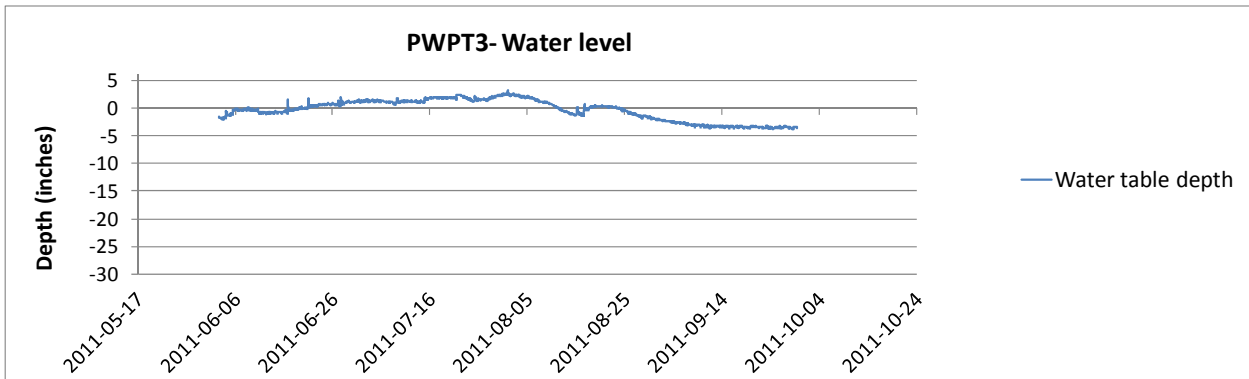
VARIOUS ECOGEOMORPHOLOGICAL TERRAIN UNITS
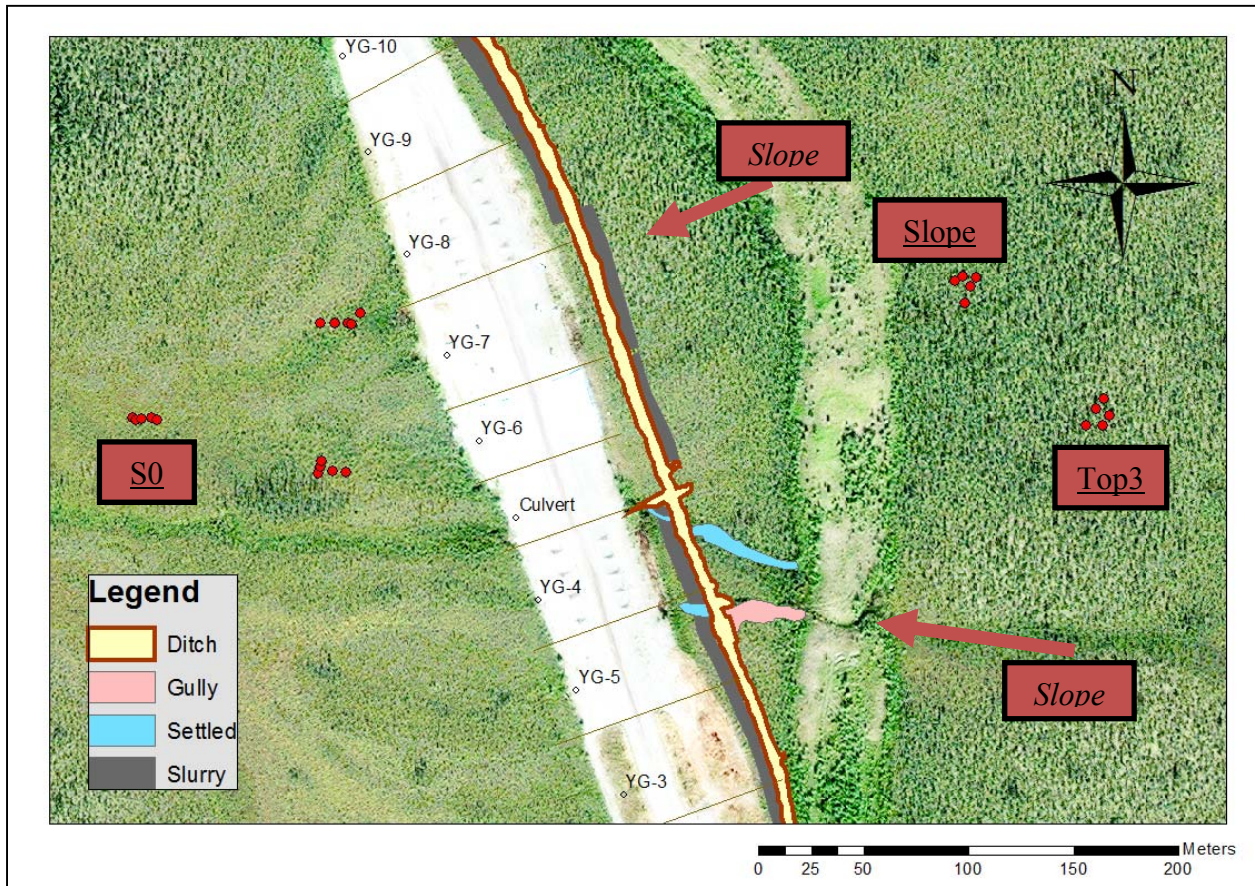
Lichen-floored boreal forest
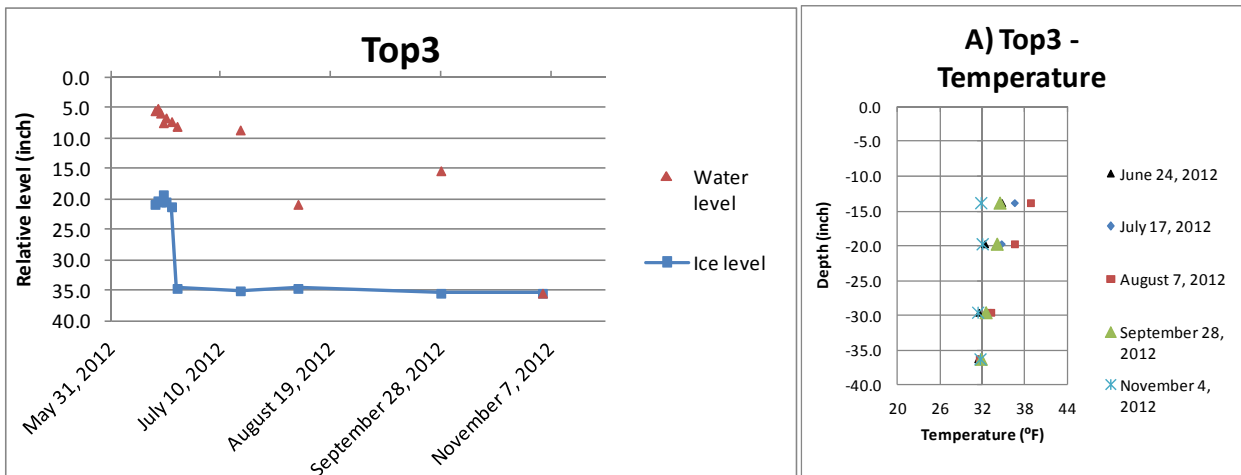
Moss-floored boreal forest
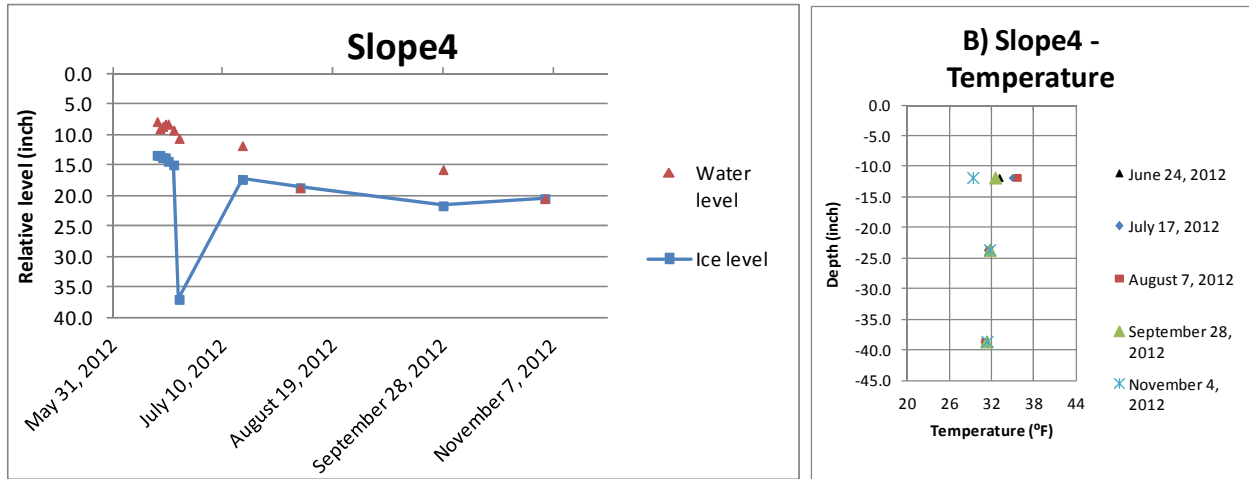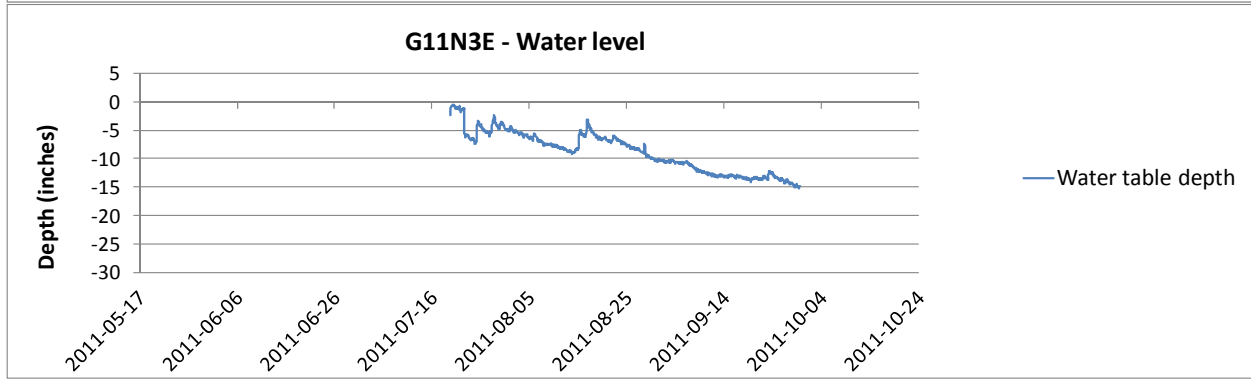

Water track
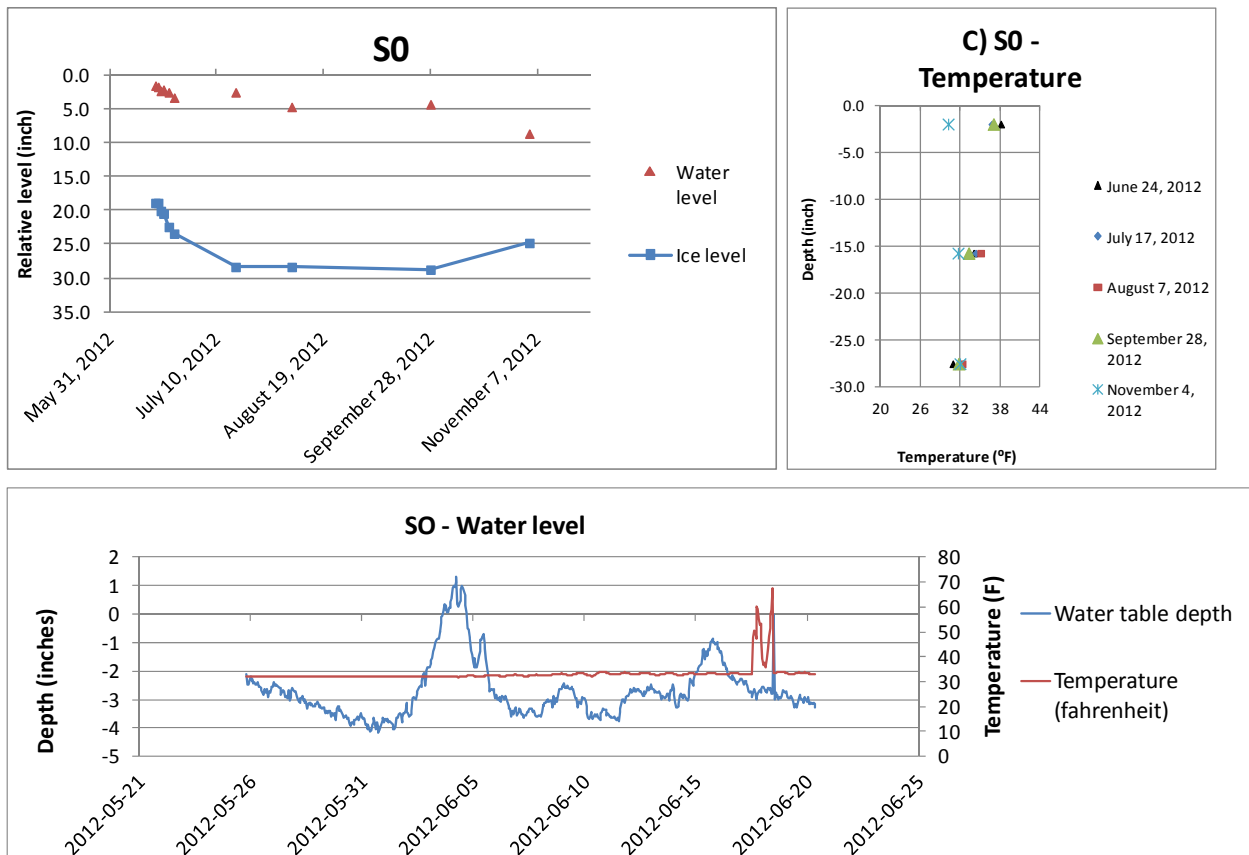
SPECIFIC ARRAYS

G01 water path
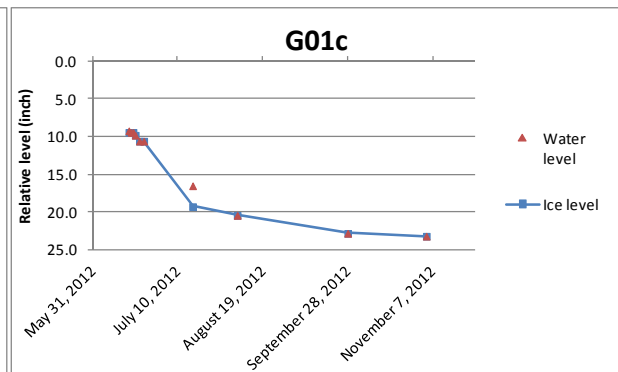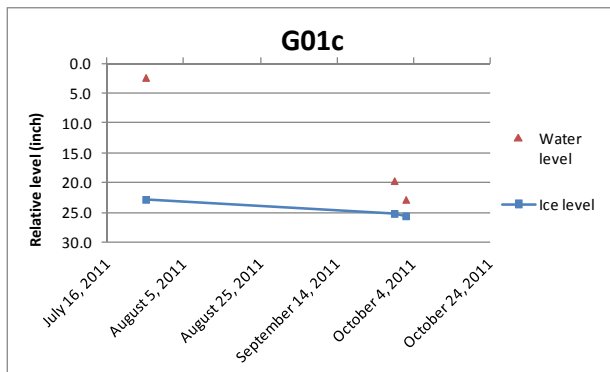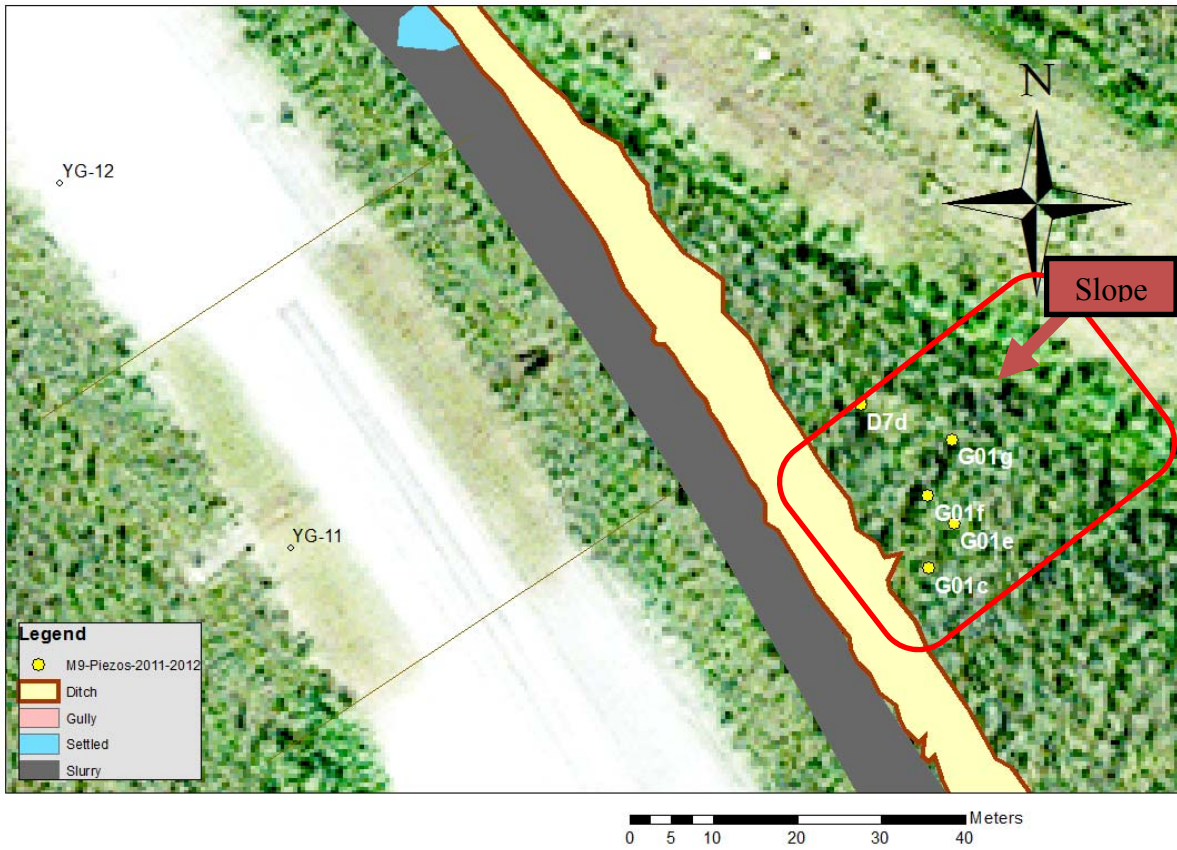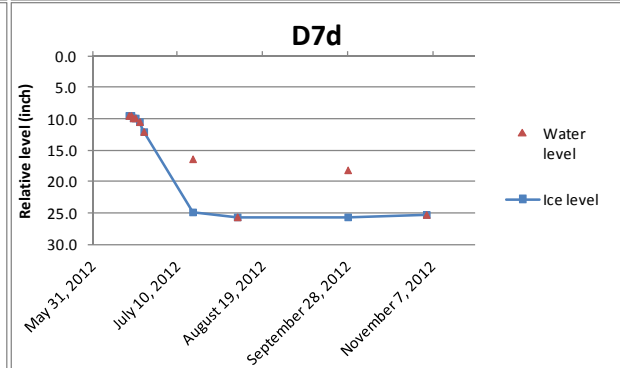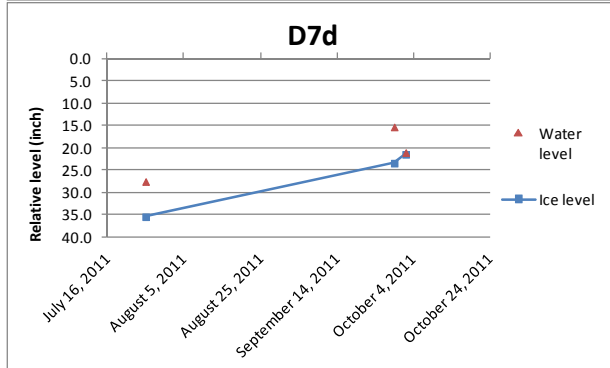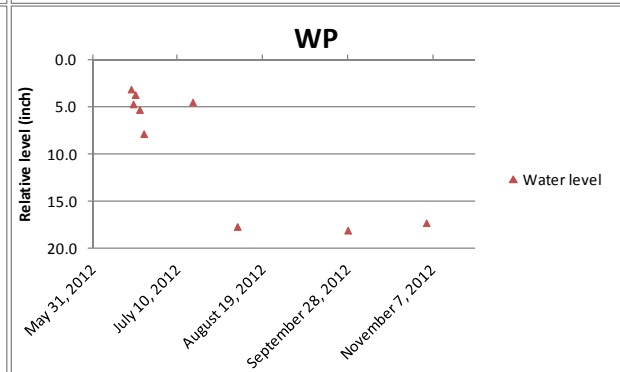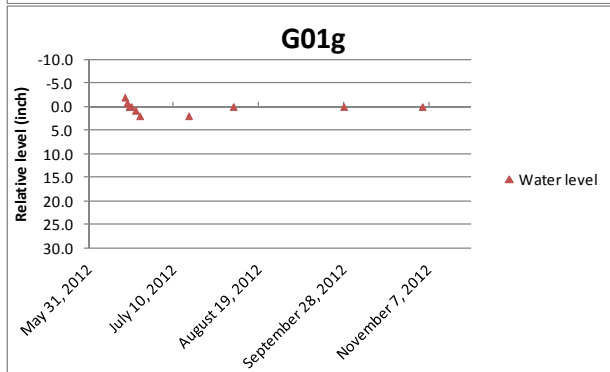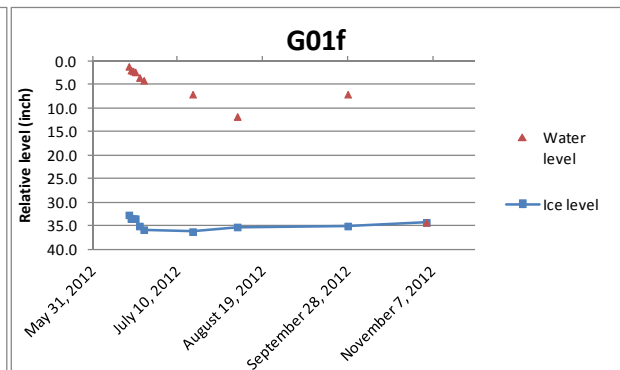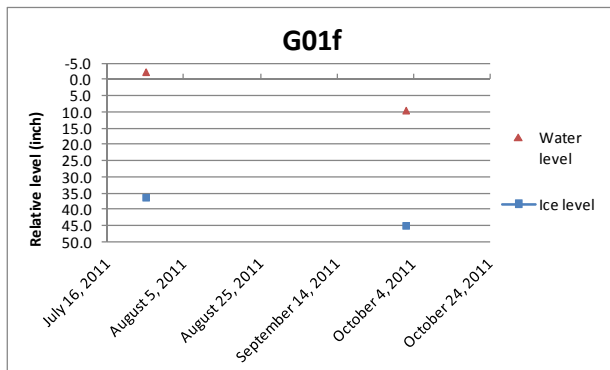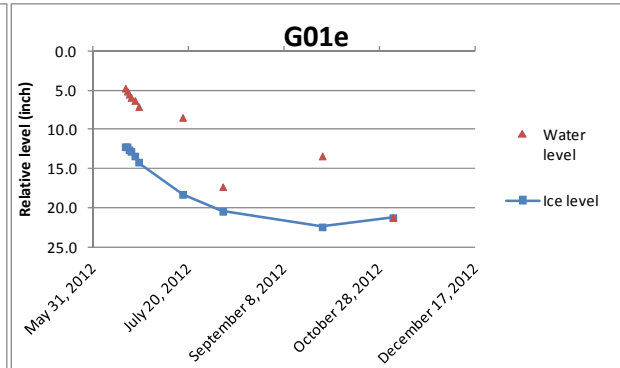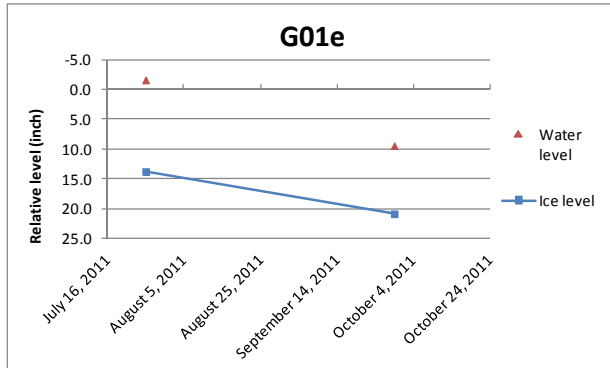
DS1 peat/silt contrast
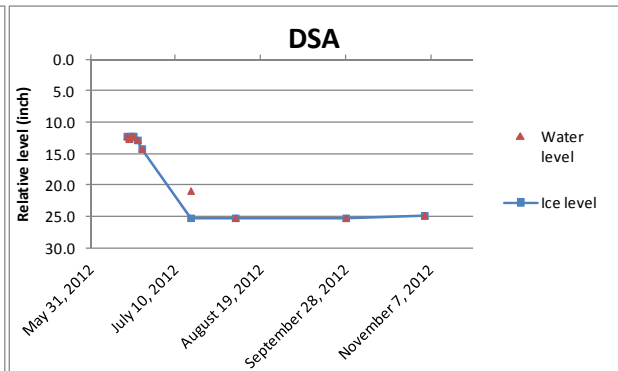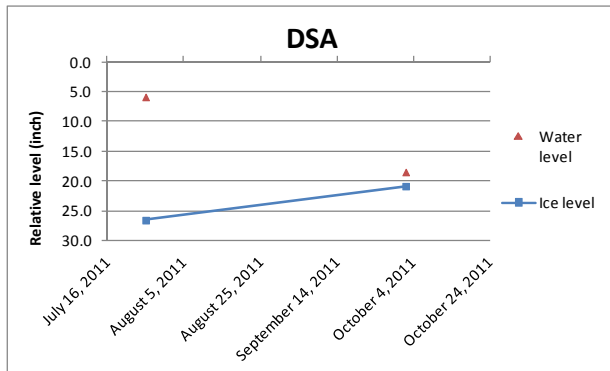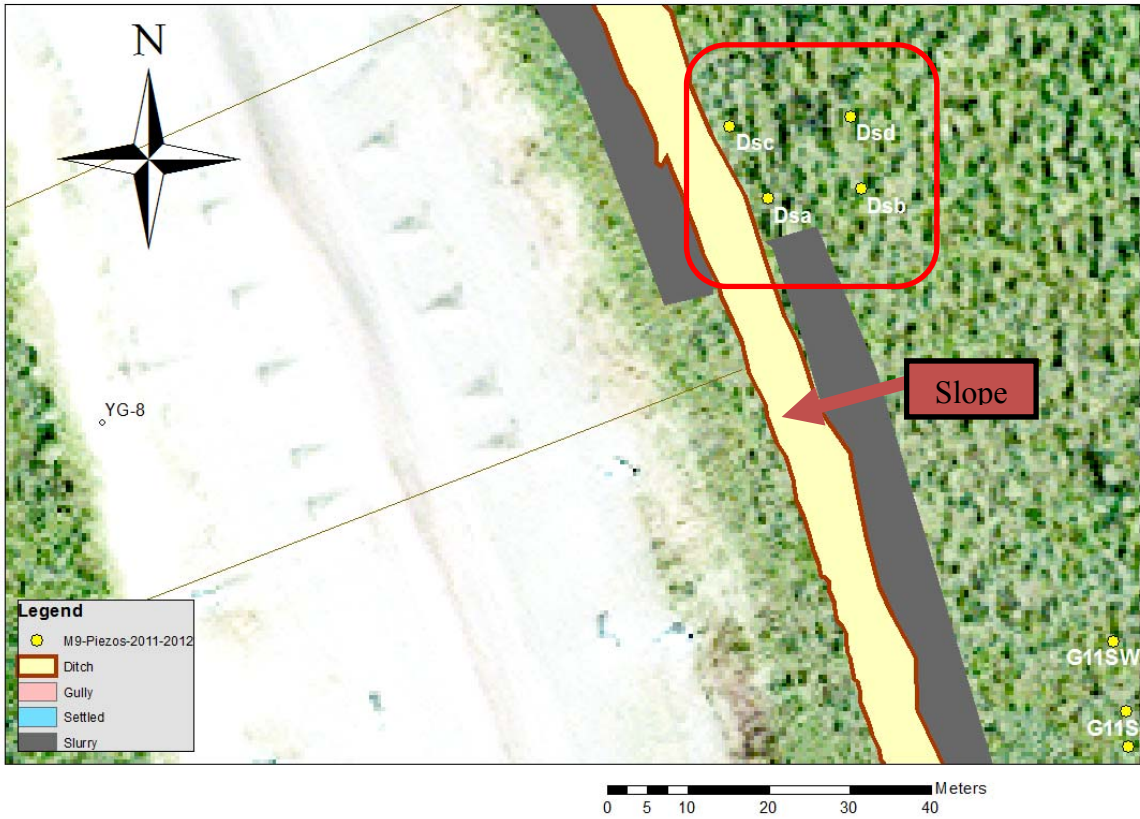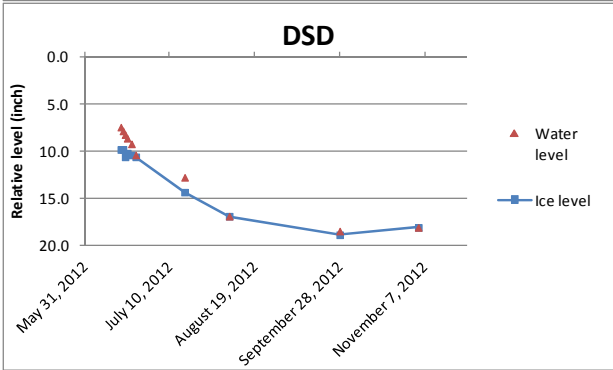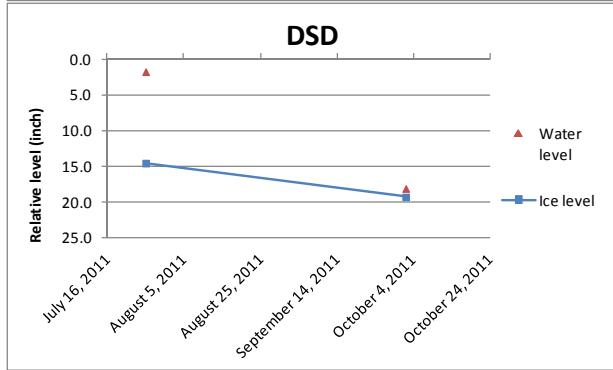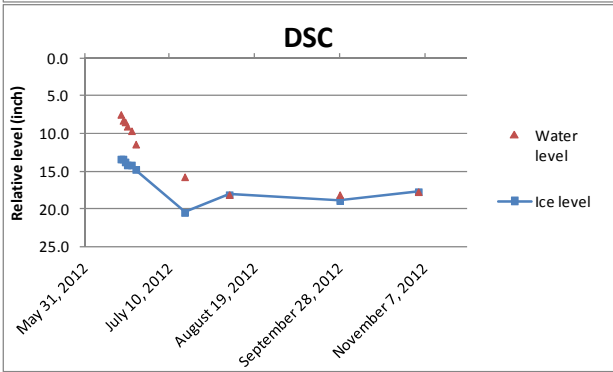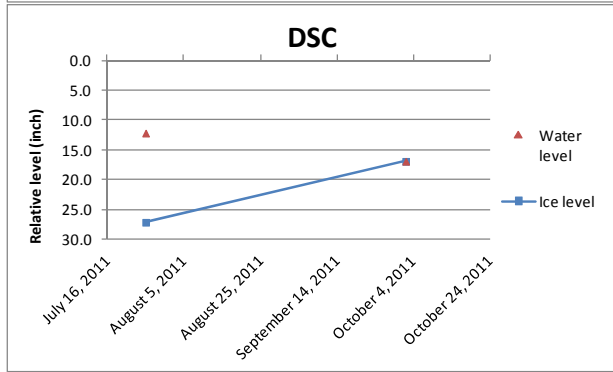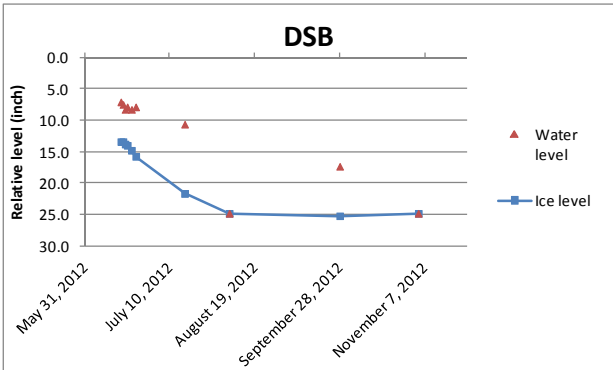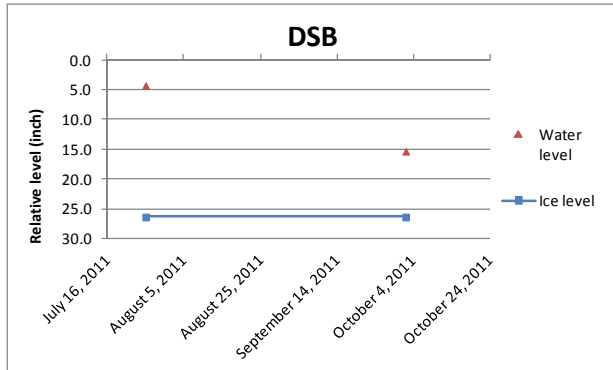
G11 downslope microtopography

99

G11N4 - Water level

G11N3W - Water level

G11N3E - Water level

G11N2 - Water level

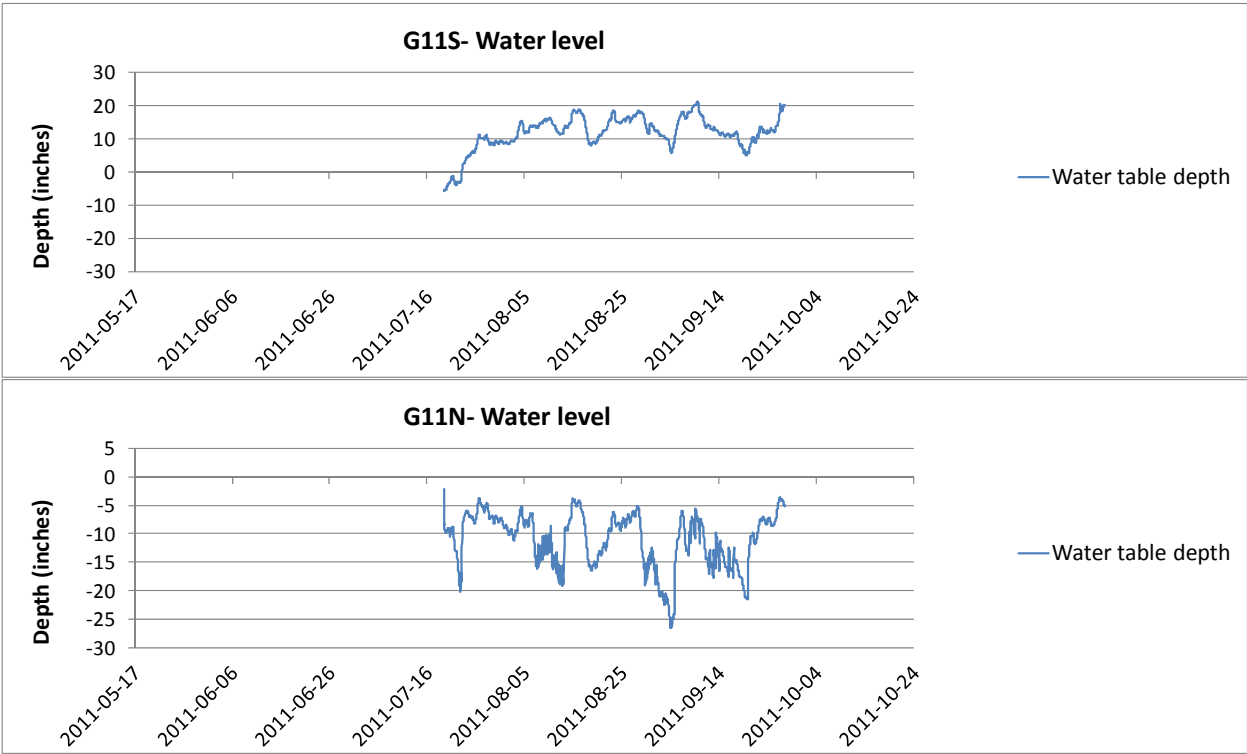100

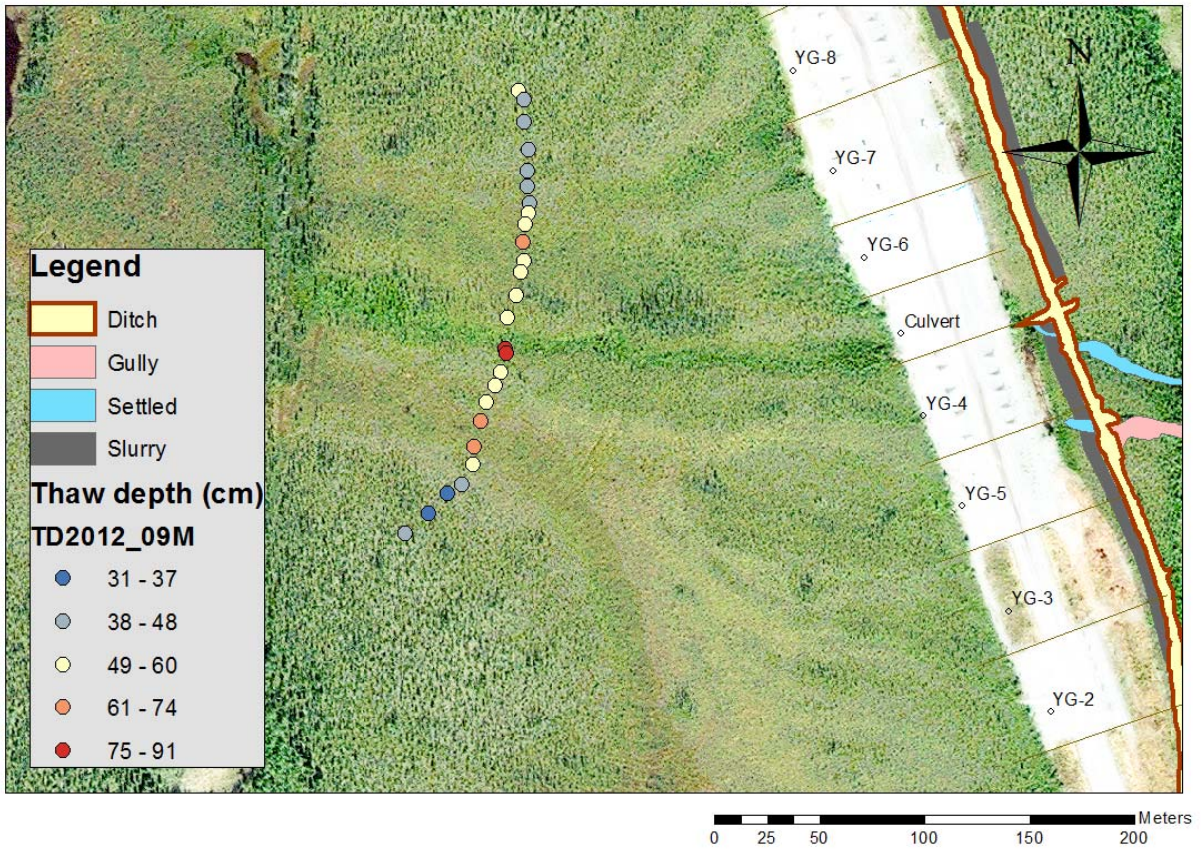## G11S- Water level

G11N- Water level

101
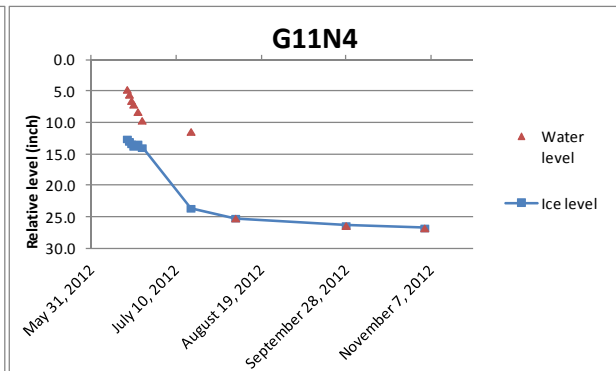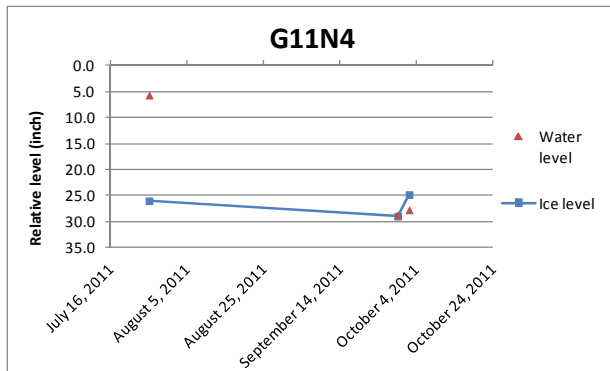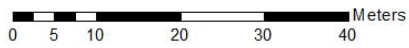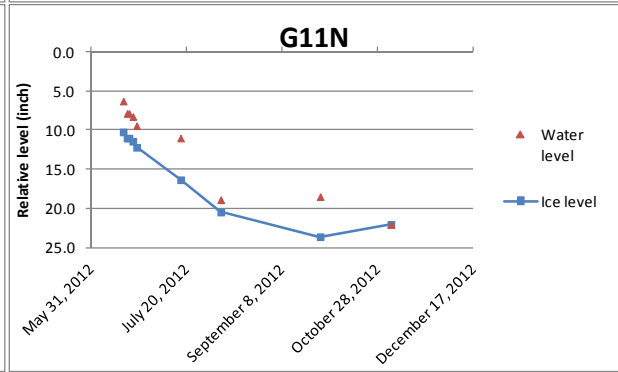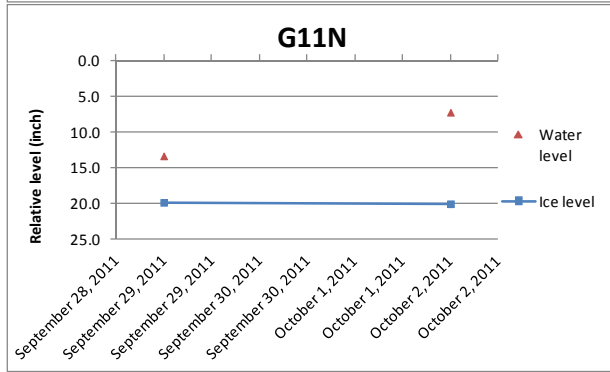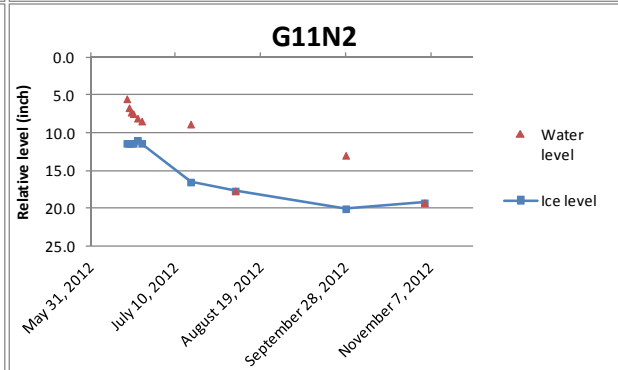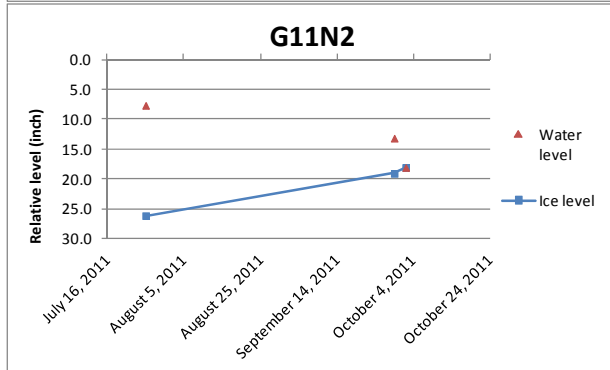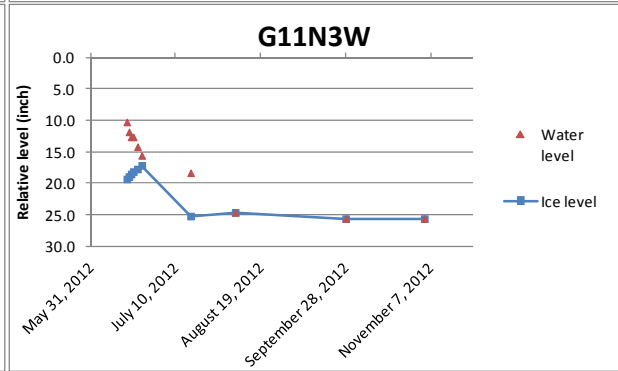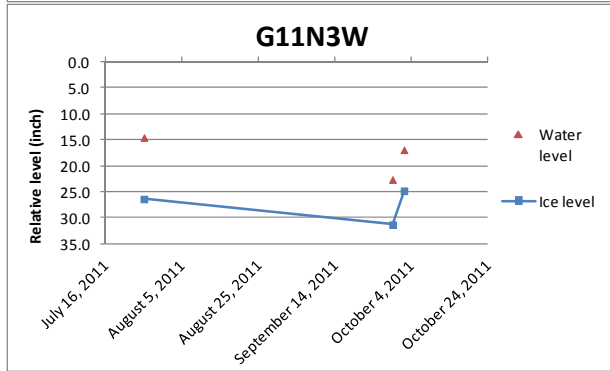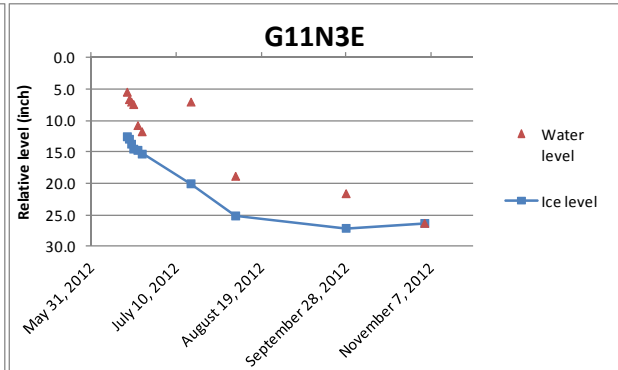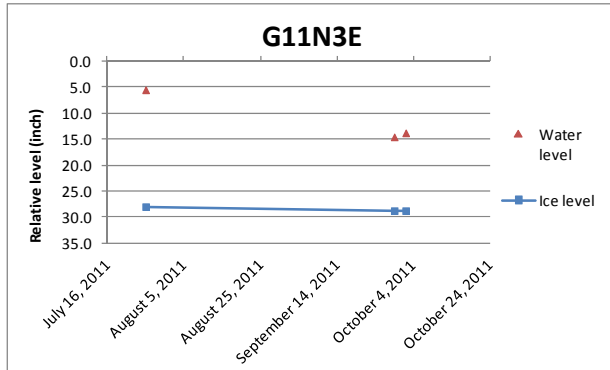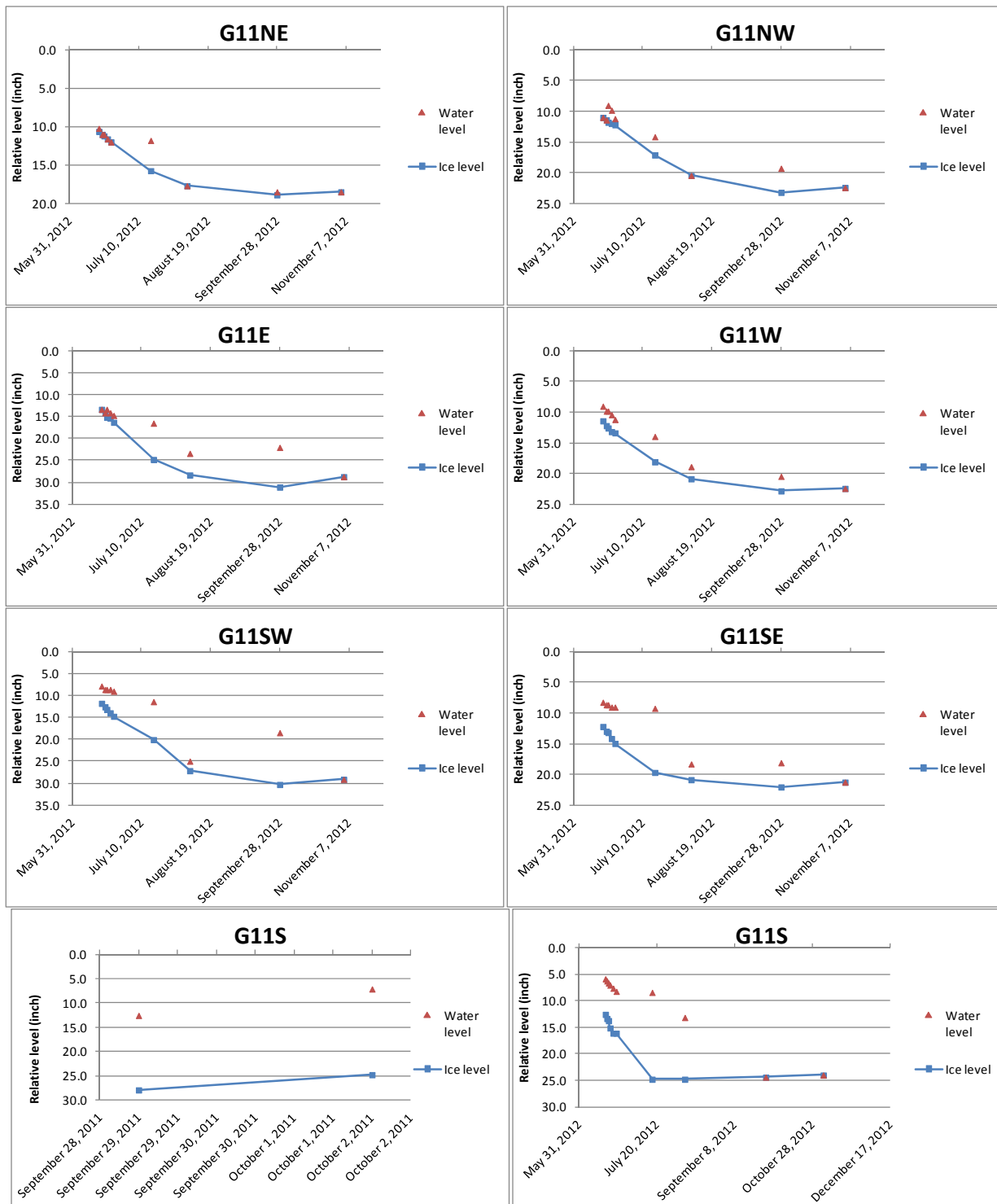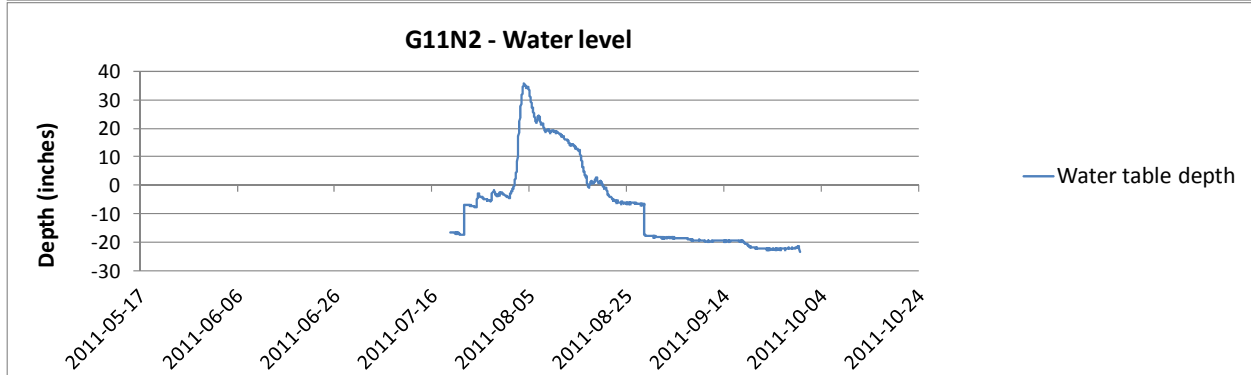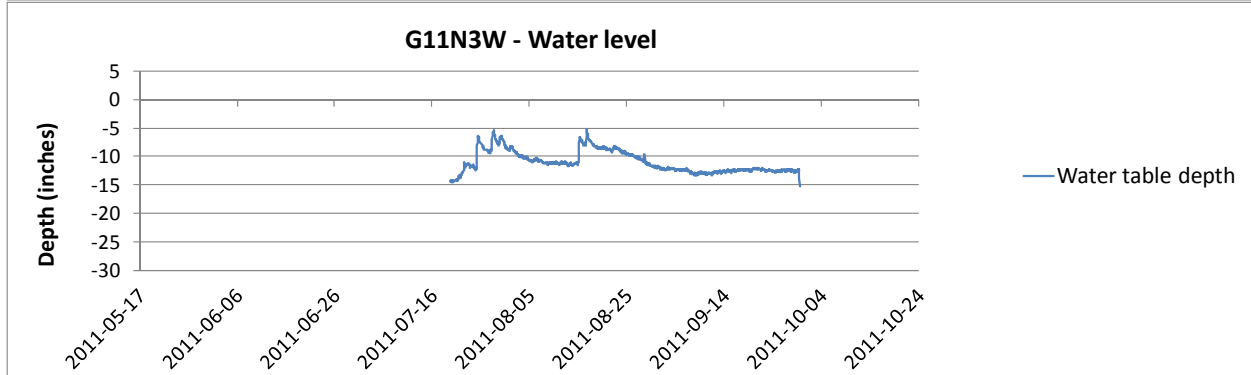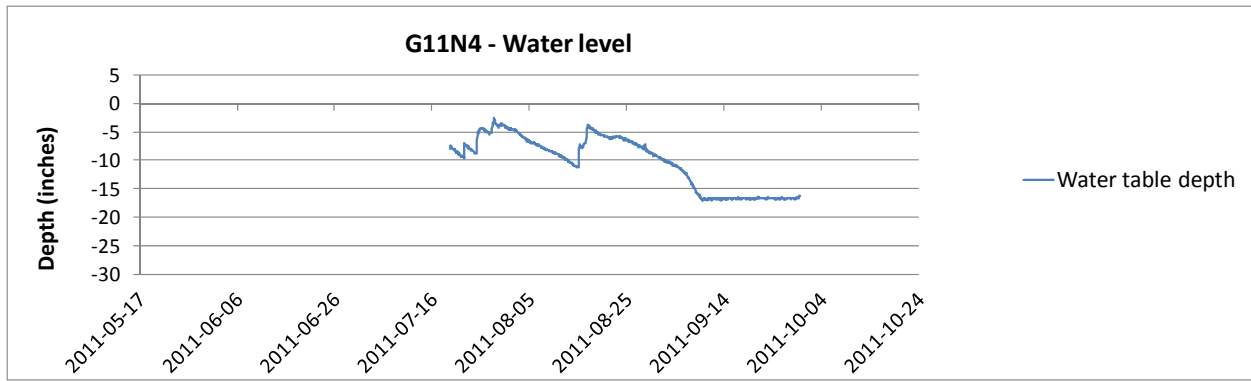
THAW DEPTH DEVELOPMENT FOR 2012

Across the slope and watertracks

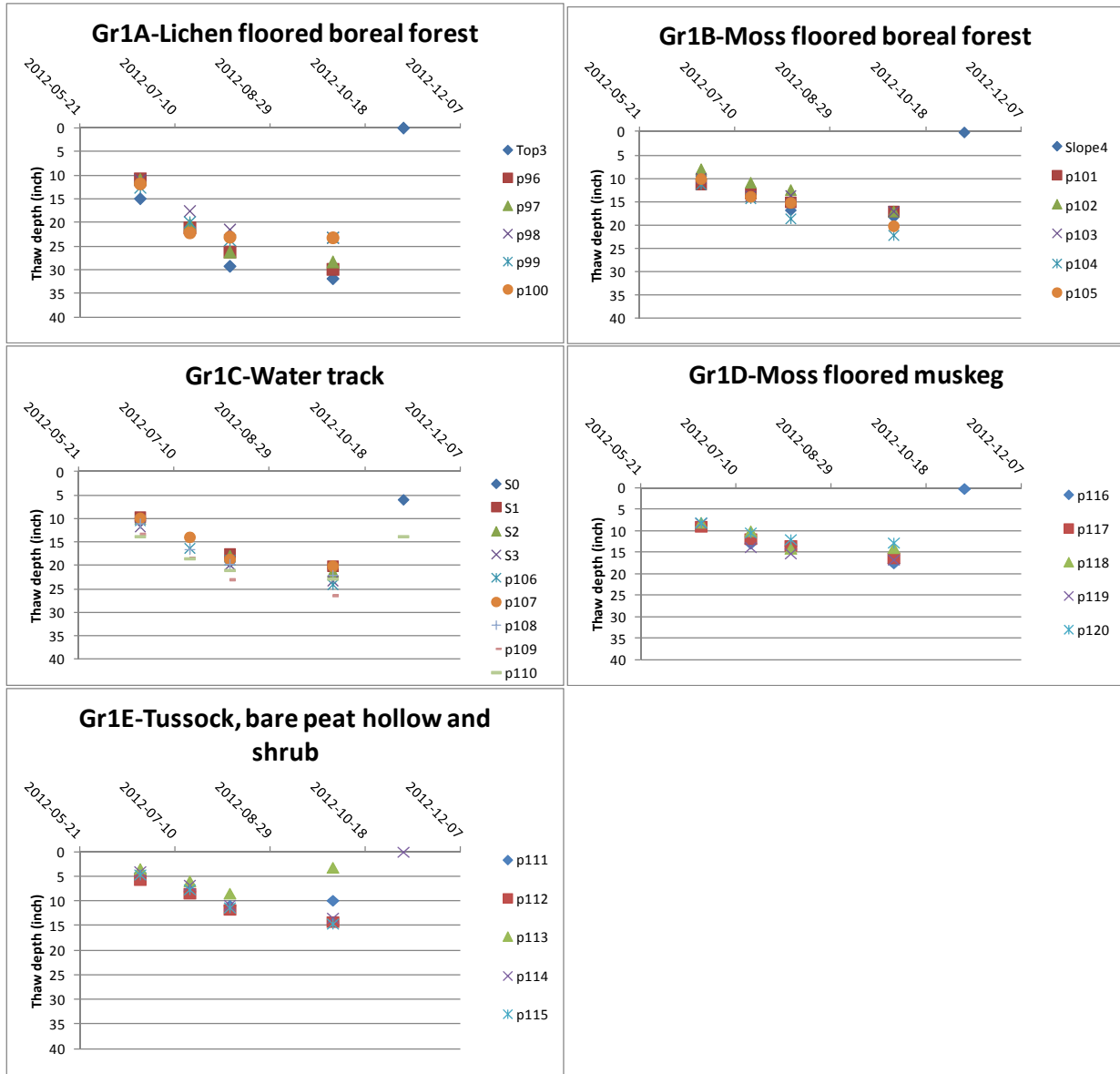# In various eco-geomorphological terrain units

Table F-1. Hydraulic conductivity of various soils from AHTS. Testing was conducted on thawed remolded samples. Hydraulic conductivity is presented in both cm/s and ft/s.

Soil type	Sample preparation	Hydraulic conductivity		Organic matter content (grav.) (%)	Thaw strain (%)	Dry unit weight (lb/ft^3)	Saturated water content (grav.) (%)
		cm/s	ft/s				
Sand silt Gravel 0% Sand 46.8% Silt 53.1%	Remolded; "humid"; packed in 0.4-in. thick layers; "lightly packed"	1.24×10^{-4}	4.07×10^{-6}	2.94	36	70.5	39
	Remolded; "dry"; 0.2-in. thick layers; "compacted"	3.47×10^{-5}	1.14×10^{-6}				
Gravelly silty sand Gravel 29.2% Sand 60.3% Silt 53.1%	"Saturated"; no compaction	1.78×10^{-5}	5.84×10^{-7}	8.66	29	64.3	49
	Remolded; "humid"; 0.2-in. thick layers; "compacted"	1.36×10^{-5}	4.46×10^{-7}				
Gravelly silty sand Gravel 29.2% Sand 60.3% Silt 53.1%	"Saturated"; settled by vibrations	5.06×10^{-5}	1.66×10^{-6}	8.66	29	64.3	49
Sand Gravel 0.9% Sand 99.1% Silt 0%	Remolded; "humid"; 0.6-in. thick layers; "lightly packed"	1.1×10^{-4}	3.61×10^{-6}	3.33	57	69.9	39
Silty sand Gravel 0% Sand 56.3% Silt 43.7%	Remolded; "humid"; 0.2-in. thick layers; "lightly packed"	5.28×10^{-6}	1.73×10^{-7}	2.83	12	74.9	37

Table F-2. Hydraulic conductivity measured *in situ* at the AHTS using an infiltrometer. For peaty soil, the range of decomposition is estimated using the Von Post scale (Soil Classification Working Group, 1998). "D_{50}" is provided as the representative grain size. Hydraulic conductivity is presented in both cm/s and ft/s. Multiple measurements were made for selected soils.

Soil type	Von Post scale	D_{50} (mm)	Hydraulic conductivity		Van Genuchten parameters		Water content (grav.) (%)
			(cm/s)	(ft/s)	α	n	
Gravel and silty sand (embankment material on natural ground surface)	---	1.69	1.07×10^{-5} 3.57×10^{-5}	3.51×10^{-7} 1.17×10^{-6}	0.124	2.28	7.02
Embankment material (i.e., gravel only)	---	7.6	1.52×10^{-3} 5.04×10^{-3}	4.99×10^{-5} 2.00×10^{-4}	0.145	2.68	---
Undecomposed peat	1	---	8.56×10^{-4} 2.89×10^{-4}	2.81×10^{-5} 9.48×10^{-6}	0.01	1.36	358.16
Slightly decomposed peat	3 to 4	---	4.54×10^{-4}	1.49×10^{-5}	0.01	1.36	---
Decomposed peat	5 to 6	---	7.22×10^{-4} 6.80×10^{-4} 2.37×10^{-4}	2.37×10^{-5} 2.23×10^{-5} 7.78×10^{-6}	0.01	1.36	---

Table F-3. Hydraulic conductivity of remolded AHTS samples measured in the laboratory using an infiltrometer. For peaty soil, the range of decomposition is estimated using the Von Post scale (Soil Classification Working Group, 1998). "D_{50}" is provided as the representative grain size. Hydraulic conductivity is presented in both cm/s and ft/s. Multiple measurements were made for selected soils.

Soil type	Von Post scale	D_{50} (mm)	Hydraulic conductivity		Van Genuchten parameters		Water content (grav.)
			(cm/s)	(ft/s)	α	n	(%)
Gravel and silty sand (embankment material on natural ground surface)	---	1.69	9.20×10^{-4} 8.00×10^{-5} 3.49×10^{-5}	3.02×10^{-5} 2.62×10^{-6} 1.15×10^{-6}	0.124	2.28	7.02
Embankment material (i.e., gravel only)	---	7.6	1.01×10^{-3} 1.96×10^{-3}	3.31×10^{-5} 1.00×10^{-4}	0.145	2.68	---
Sandy silt	---	0.05	3.33×10^{-4}	1.09×10^{-5}	0.059	1.48	49.82
Undecomposed peat	1	---	9.38×10^{-4} 8.00×10^{-4} 6.80×10^{-4} 2.37×10^{-4}	3.08×10^{-5} 2.62×10^{-5} 2.23×10^{-5} 7.78×10^{-6}	0.01	1.36	358.16

APPENDIX G: COMPARISON OF COMSOL-GEOSTUDIO MODEL RESULTS

Various commercially available modeling programs have different degrees of difficulty to learn to use, and also different degrees of freedom for the user. For this research, we modeled a simplified version of cross section A-A' (CS A-A') using both COMSOL Multiphysics and the GEO-STUDIO TEMP/W and SEEP/W modules (hereafter referred to as TSW). The purpose of this additional exercise was to see how the results from two models differed when using the same set of input parameters.

Figure G-1 is a screen shot from the TSW model, showing the simplified cross section developed for the modeling comparison; a similar model was used in COMSOL without any vertical exaggeration. The embankment was separated into unsaturated and saturated portions (yellow and blue in the figure, respectively), which helped the GEOSTUDIO software to converge at the limit of the water table. The surficial organic material (shown in green) was not included below the embankment, with the assumption that it was completely compressed and compacted. Beneath the embankment and surficial organic layer was silt extending to the bottom of the model. The embankment is 7-m high (9 m at its thickest where it subsided into natural ground), and 80 m in width. The thermistor cable in the embankment side slope was located 50.5 m from the left side of the model. Eleven of the sixteen thermistor beads were chosen to validate the model, at depths of 0.1, 1.5, 2.5, 3.5, 4.5, 6, 7.5, 9, 11, 13, and 16 m.

Table G-1 is a summary of the thermal and hydraulic input parameters used for each soil type. These values were used for both commercial models, with minor exceptions. For the COMSOL model, the dry densities listed in Table G-1 were used to convert the heat capacities to the necessary units. The various parameters were scaled between their frozen and unfrozen values using the van Genuchten relationship for each soil type. An example of this relationship for silt is shown in Figure G-2. In TSW, unfrozen water content is represented by an exponential decay function. Figure G-3 shows the unfrozen water content function for silty sand, which was chosen to represent the silty foundation soil.

Both models were started on a day representing January 1, 2008. The measured temperatures from the thermistor string were used to represent the initial conditions, as shown in Figure G-4 for the TSW model and in Figure G-5 for the COMSOL model. For both models, an air temperature function modified by *n*-factors was used as the upper boundary condition. No distinction was made between the embankment surface and side slopes as a simplification (see Table G-2). The final *n*-factors chosen were based on the best fit to measured temperatures from multiple numerical simulations. In both programs, the model was run using data from October 1, 2008 to September 20, 2009. A constant temperature of -0.41°C was applied as the lower boundary condition to the bottom nodes of the model.

For the fully-coupled models, differential pressure heads were applied to each of the models. As shown in Figure G-6, at the upstream (left) side of the embankment, the total head was 695 m. At the downstream (right) side of the embankment, the total head applied was 692.5 m. Although not shown, the same conditions were applied in the COMSOL simulation.

Figure G-7 and Figure G-8 are the TSW and COMSOL model results, respectively, showing the flow nets. These figures illustrate several differences between the models. Initial simulations
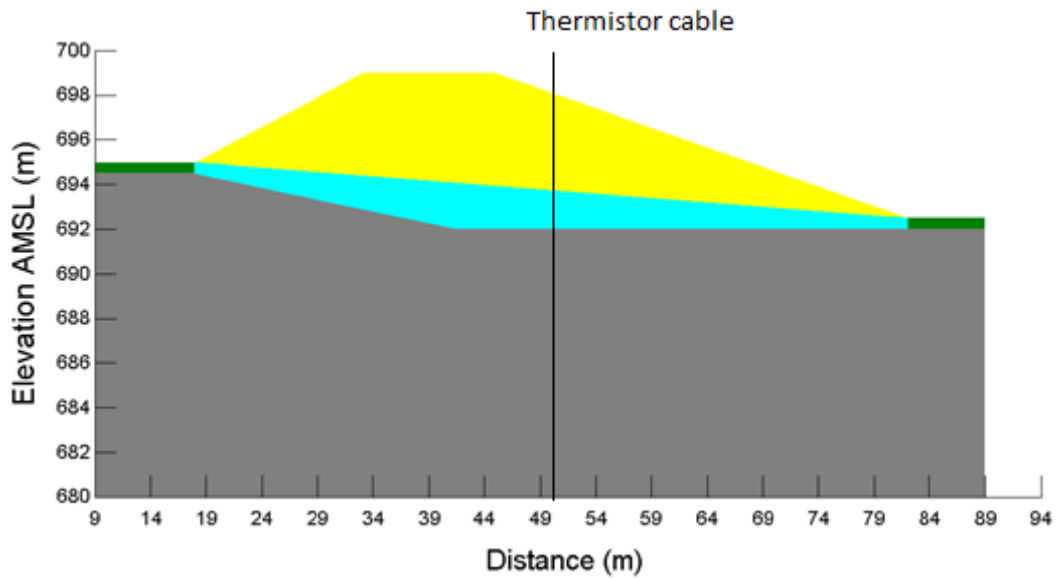
Figure G-1. Cross section used in the model comparison. The embankment is yellow where unsaturated and light blue where saturated. Surficial organic material is shown in green, and silty foundation soils are shown as gray. The location of a thermistor string installed within the embankment side slope is indicated by the vertical black line.

Table G-1. Soil input parameters. [a] denotes measured laboratory values, [b] denotes measured field values, and [c] denotes estimated values derived from the literature.

Variable	Embankment	Peat	Silt
Frozen Thermal Conductivity (W/m·K)[b]	1.45	1.20	2.00
Unfrozen Thermal Conductivity (W/m·K)[b]	0.83	0.38	0.76
Heat Capacity--Frozen (J/m^3·C)[b]	2.21e06	1.84e06	1.73e06
Heat Capacity--Unfrozen (J/m^3·C)[b]	3.13e06	3.50e06	2.51e06
Frozen Hydraulic Conductivity (m/s)[c]	1e-07	8.0e-07	3e-08
Unfrozen Hydraulic Conductivity (m/s)[b]	1e-04	8.7e-05	3e-06
Mass specific heat (J/g·C)[b]	800	2090	920
Dry density (kg/m^3)[c]	2000	950	1650
Volumetric Water Content (m^3/m^3)[b]	0.39	0.81	0.36
Unfrozen Water Content (m^3/m^3)[c]	0.01	0.01	0.06
van Genuchten[a]			
α	0.12	0.014	0.059
n	2.28	1.36	1.48
m (1-1/n)	0.56	0.26	0.32
Porosity (%)	40	85	55
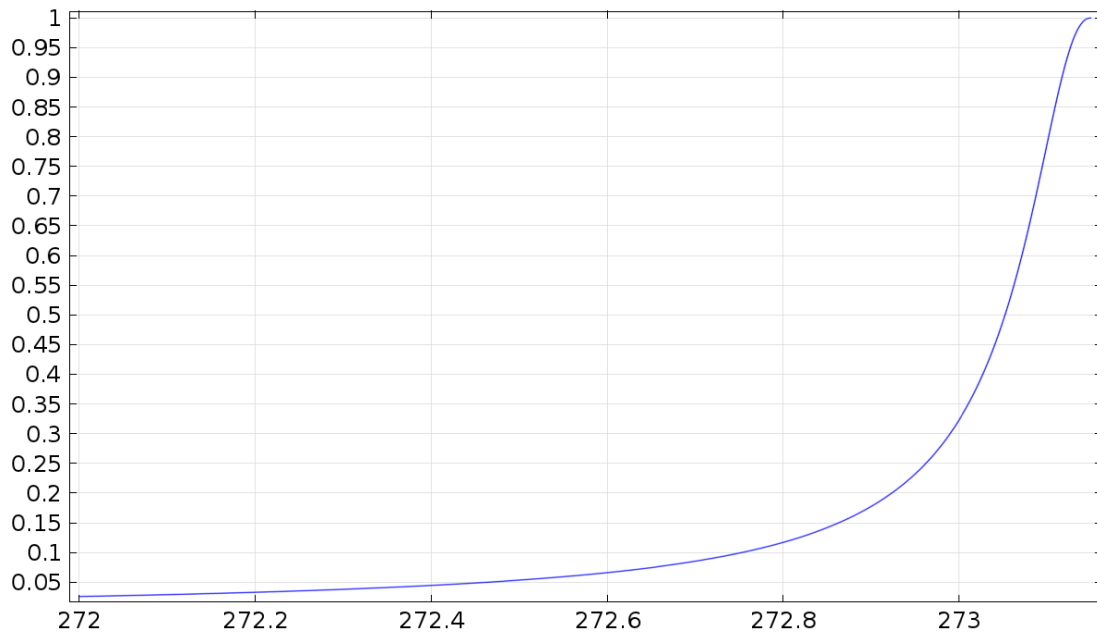
Figure G-2. Freezing curve for silt used in the COMSOL model, based on the van Genuchten equation. In this screen shot from the COMSOL model, the y-axis is degree of saturation and the x-axis is in Kelvin.
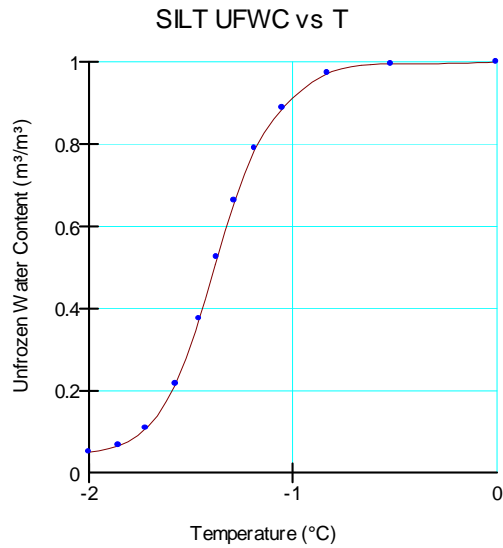
Figure G-3. Unfrozen water content function for silty sand. Screen shot from TSW.
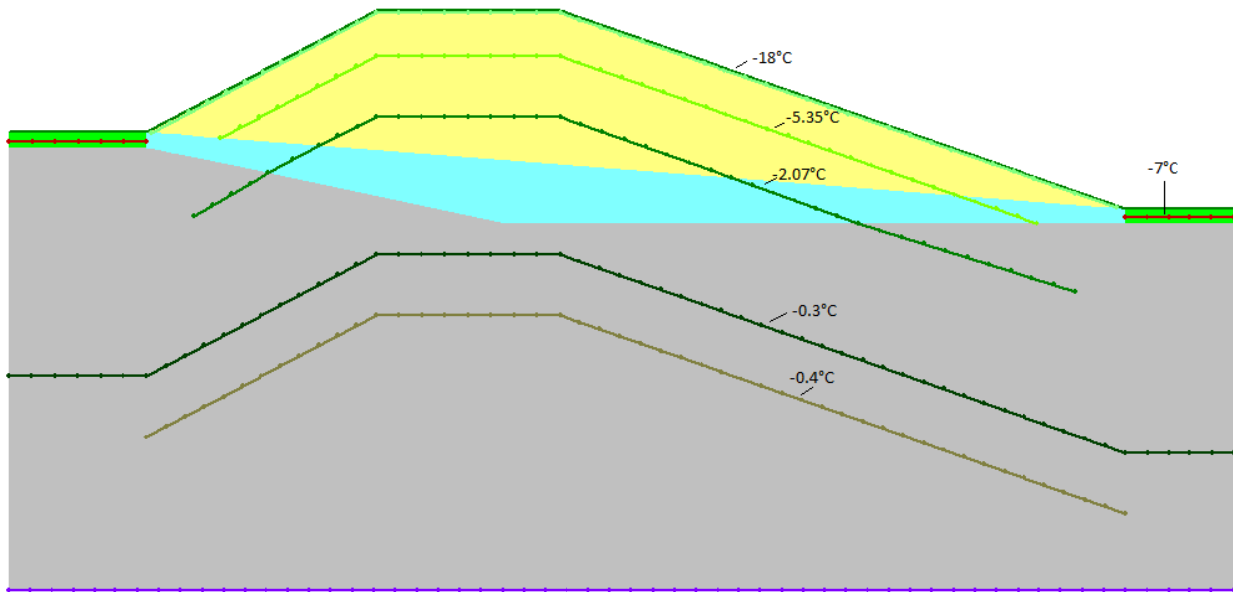
Figure G-4. Initial thermal conditions for the TSW model. Temperatures shown are in ºC, and the cross section has the same dimensions as Figure G-1. Screen shot from TSW.
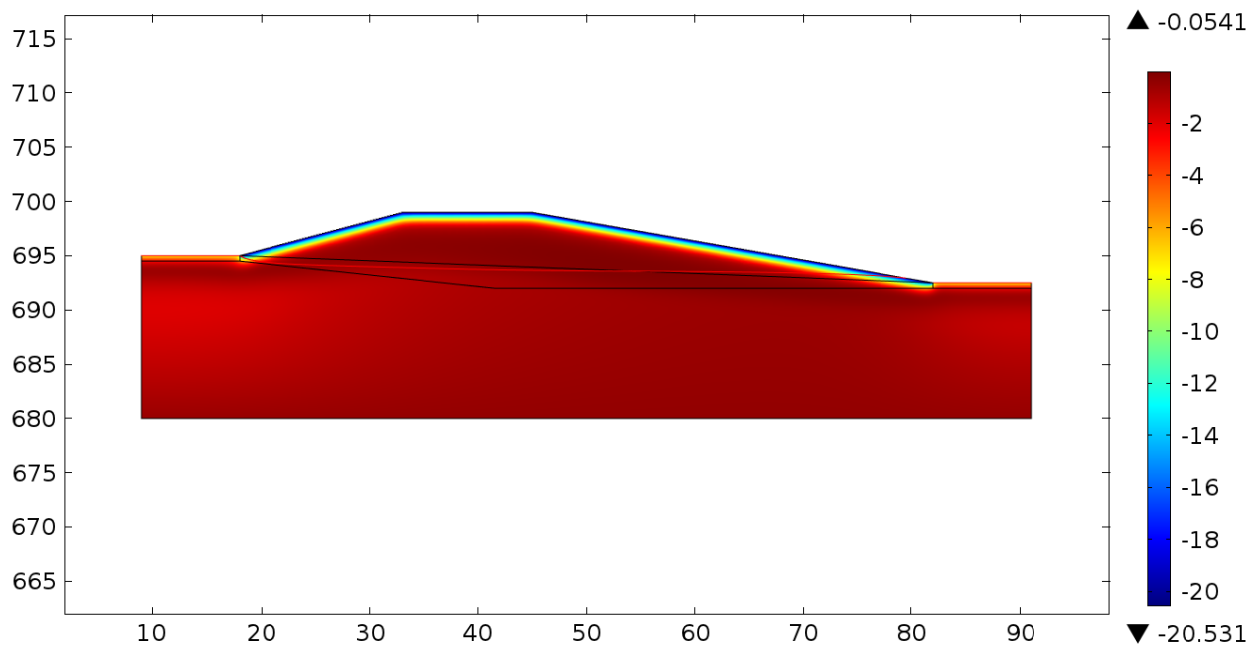
Figure G-5. Initial thermal conditions for the COMSOL model. Temperatures shown are in ºC, distances along the x-axis are in meters, and elevations along the y-axis are in meters above sea level. Screen shot from COMSOL.

111

Table G-2. Final *n*-factors used in both commercial models.

Material	n_t	n_f
Embankment	0.96	0.5
Peat	0.38	0.19
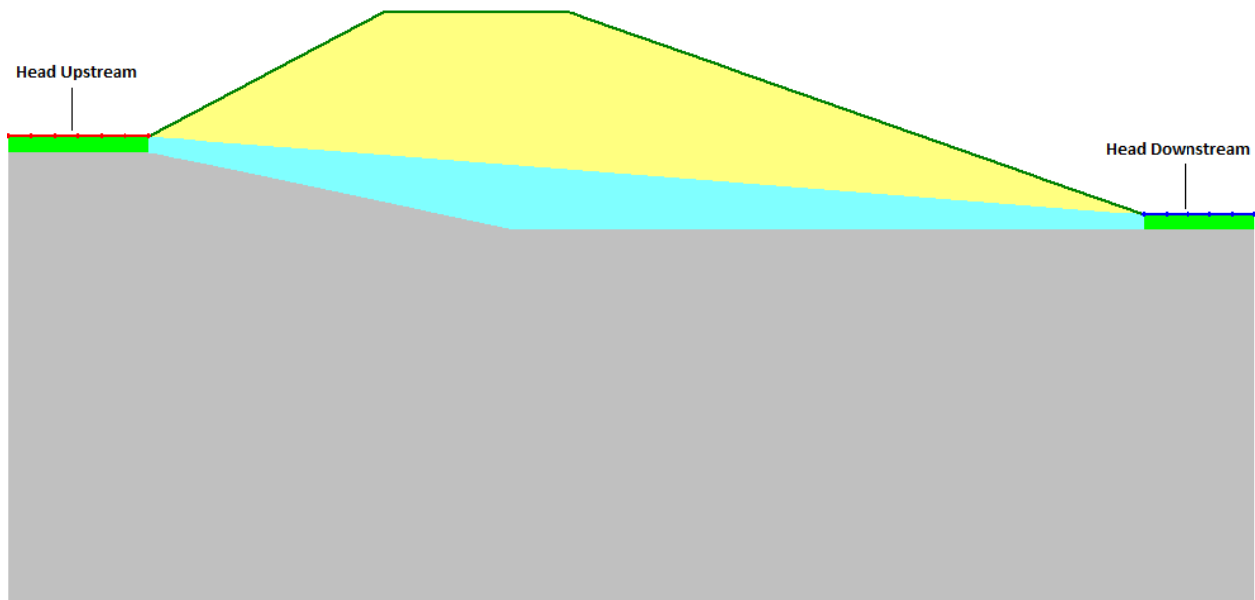
Figure G-6. Designation of initial seepage boundary conditions in the TSW model. The cross section has the same dimensions as Figure G-1. Screen shot from TSW.

with TSW indicated that that the model was not stable with the coupling of the Richard's equation and Darcy's law. This may have been due to the extreme non-linearity of the input parameters, or to a glitch in the software. To correct this problem with the TSW model, Darcy's law was applied to the saturated zone below the water table. As a result, in Figure G-7 no flow is present in the unsaturated portion of the embankment. Below the water table, the greatest flow occurs in the portion of the embankment that has settled below the original ground surface. In contrast, the COMSOL model, which uses the Richard's equation throughout, demonstrates the greatest flow in the unsaturated portion of the embankment (see Figure G-8). This is a result of the relatively high hydraulic conductivity value of the gravel coupled with a high unfrozen water content, which allows "wicking" to occur from left to right. Of course, this is unrealistic because such a combination in a soil does not exist. Another difference between the models is how the heat and water flux calculations are coupled.

These fundamental differences in the governing equation applications of each model resulted in different temperature distributions. Figure G-9 through Figure G-20 illustrate results from each of the fully-coupled models for various times during the year. The embankment in the COMSOL model is warmer than that in the TSW model, resulting in a thaw bulb within the embankment that remains until sometime in January in the COMSOL model. The shape of the temperature distribution is different for each model, which may be a result of how the initial conditions were applied, or the mesh configuration.

Figure G-21 contains plots of measured temperatures from thermistor string YG7 (to the north of CS A-A') to modeled temperatures from both of the models. Spikes in the thermistor data represent periods when no data was obtained, and are plotted as 32ºF. As these spikes are present for most of the measured depths, this may be due to moisture in the wiring connections, or intermittent power failures at the ADAS for this thermistor string. For the shallow thermistor depths, the TSW model provides a better fit to the measured data; however, with depth, both models deviate from the measured data. Below 6 m, the measured temperatures show little change for a given depth, whereas the modeled temperatures continue to demonstrate response to changes in air temperature.

Finally, Figure G-22 through Figure G-32 illustrate results from the conduction-only models. These model results also demonstrate differences in temperature distributions, with the COMSOL model generally results being slightly colder than the TSW model results. This is attributed to how the models scale the heat capacity with changing temperature. As with the fully-coupled models, the differences in the temperature distributions are attributed to how the initial conditions were applied and differences in the model meshes.
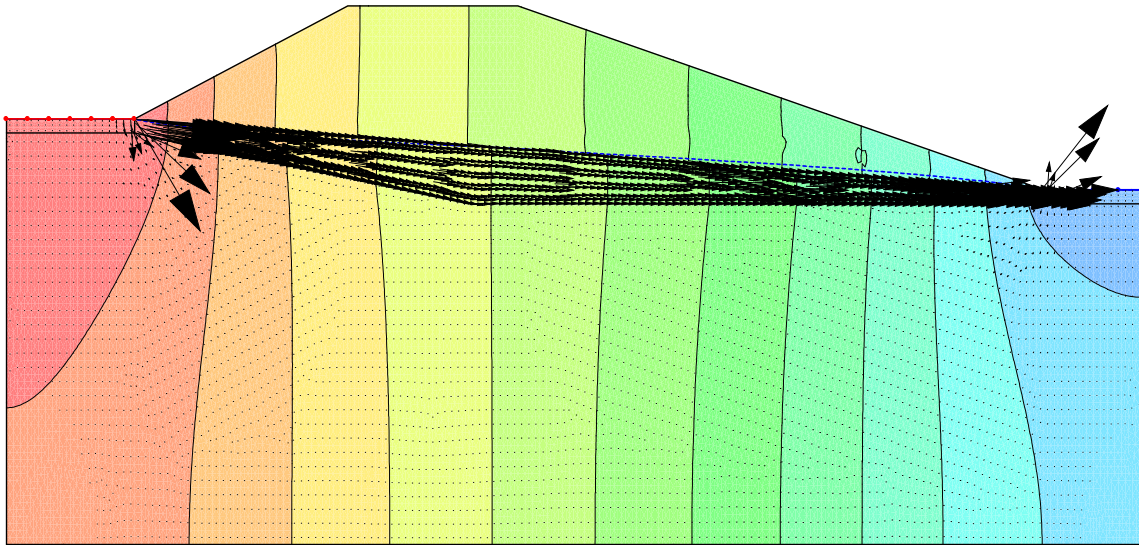
Figure G-7. Equipotential lines and hydraulic velocity vectors from the TSW model. The total head to the left of the embankment is 695 m, and 692.5 m to the right of the embankment, with a 0.2 m contour interval. The cross section has the same dimensions as Figure G-1. Screen shot from TSW.
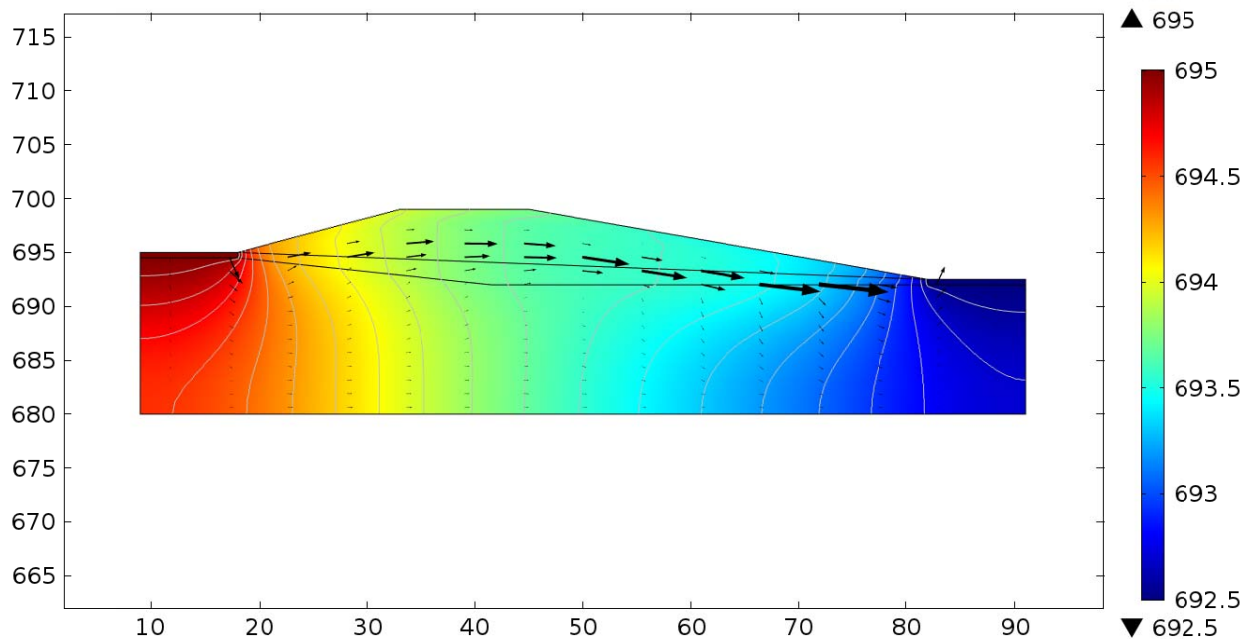

Figure G-8. Equipotential lines, flow lines, and hydraulic velocity vectors from the COMSOL model. Equipotential lines are shown in meters of water head as indicated by the scale to the right, distances along the x-axis are in meters, and elevations along the y-axis are in meters above sea level. Screen shot from COMSOL.
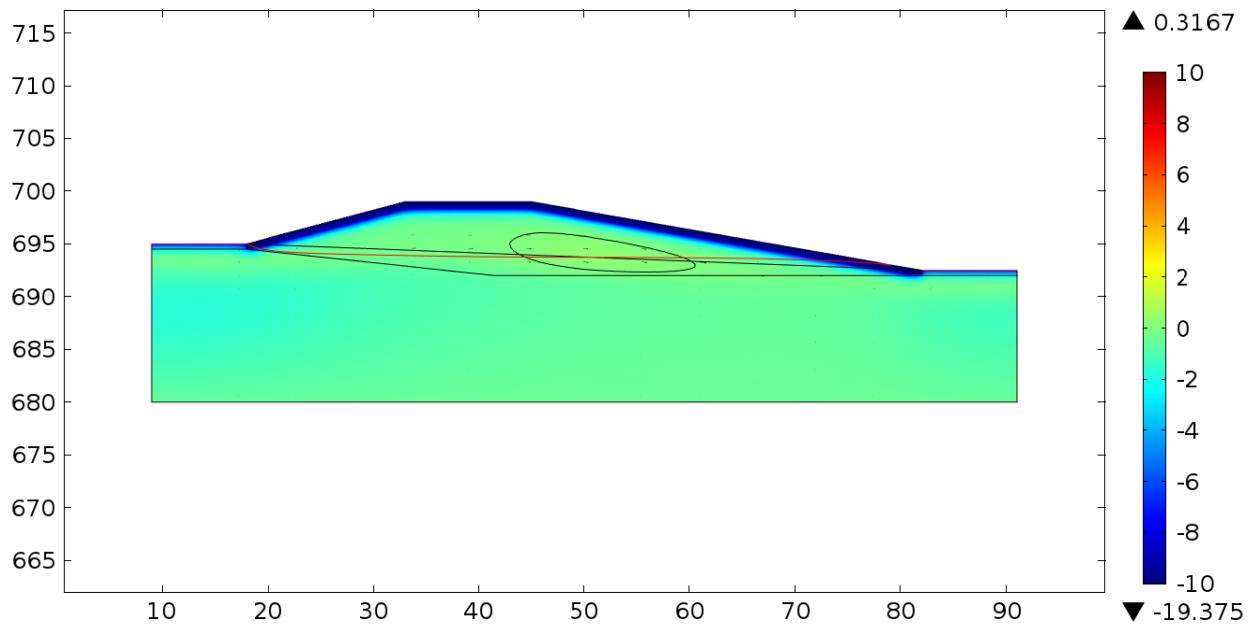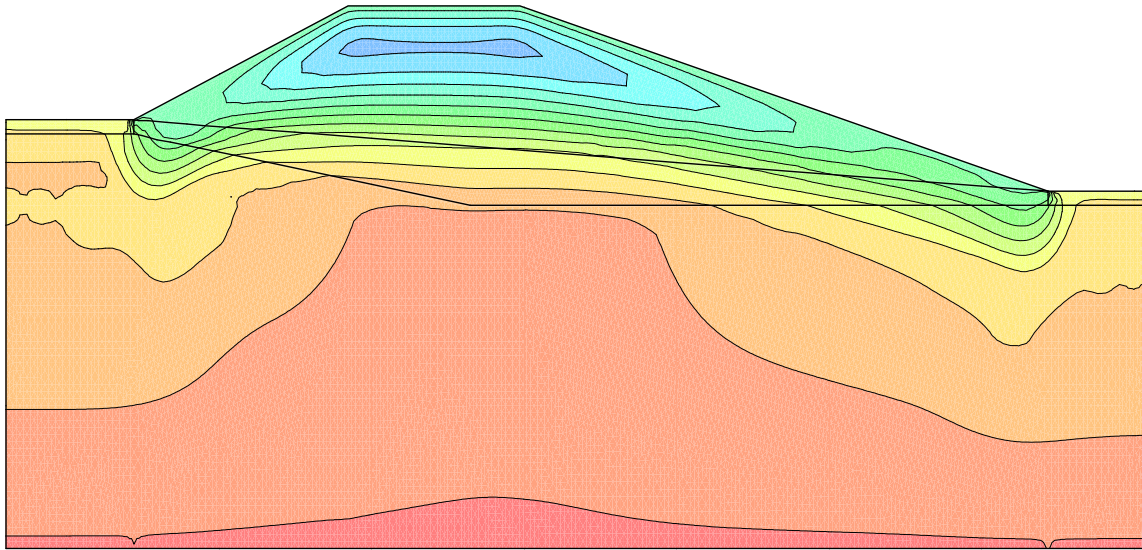
114
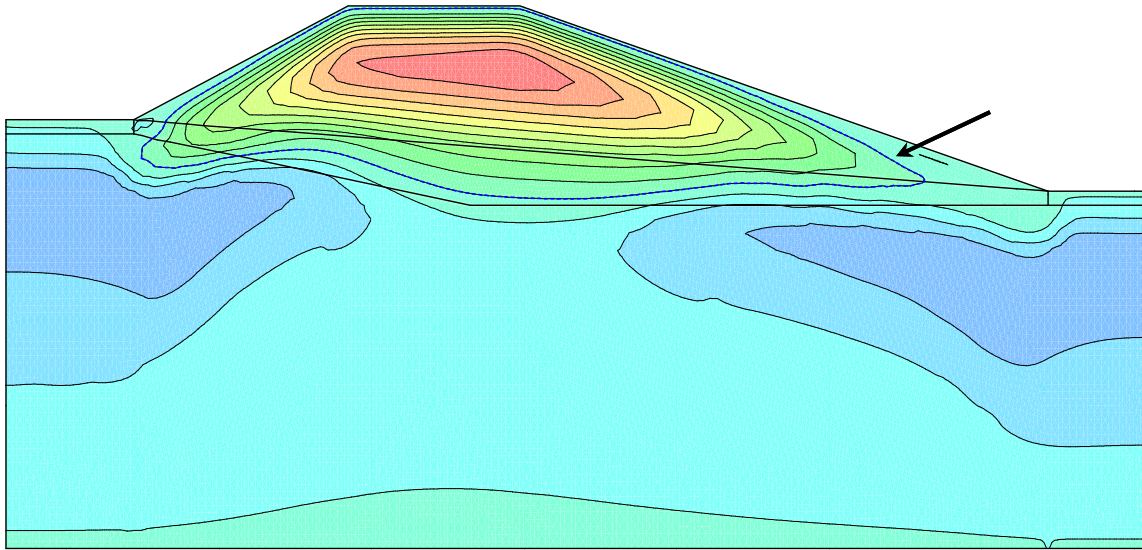
Figure G-9. Modeled temperatures for the fully-coupled TSW model for October 1. Cold temperatures are represented by shades of blue and warm temperature by shades of red, with T_{min}= -1.78°C and T_{max}= 4.93°C. The temperatures contours are incremented by 0.5°C, and the 0°C isotherm is indicated by the arrow. Screen shot from TSW.
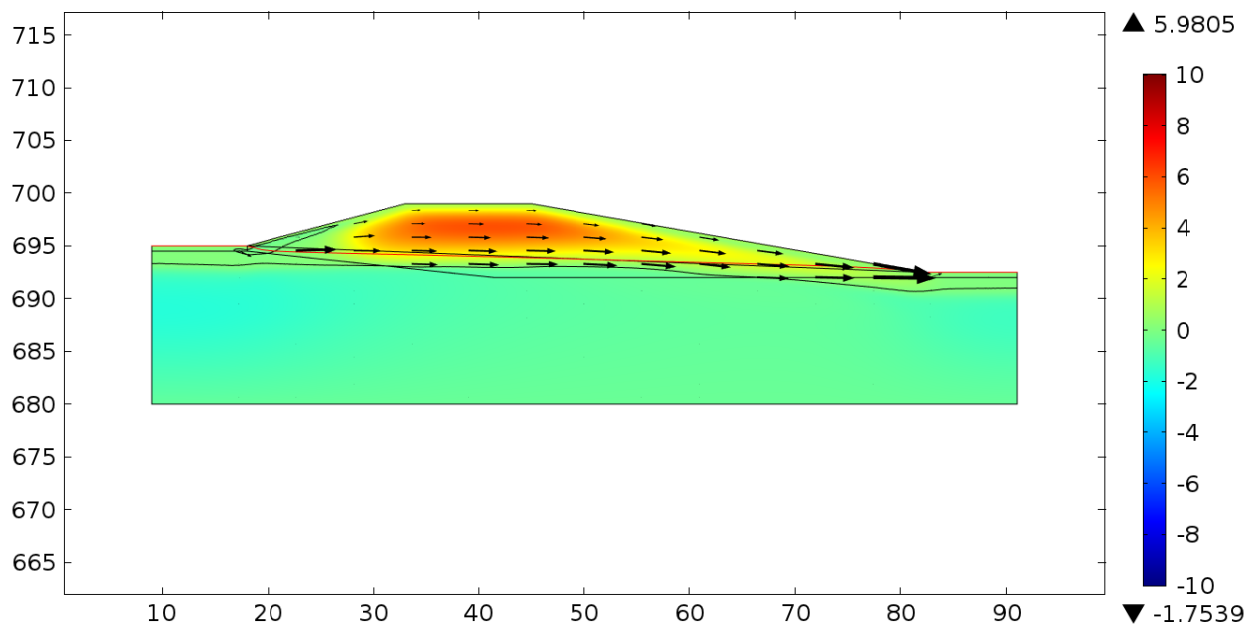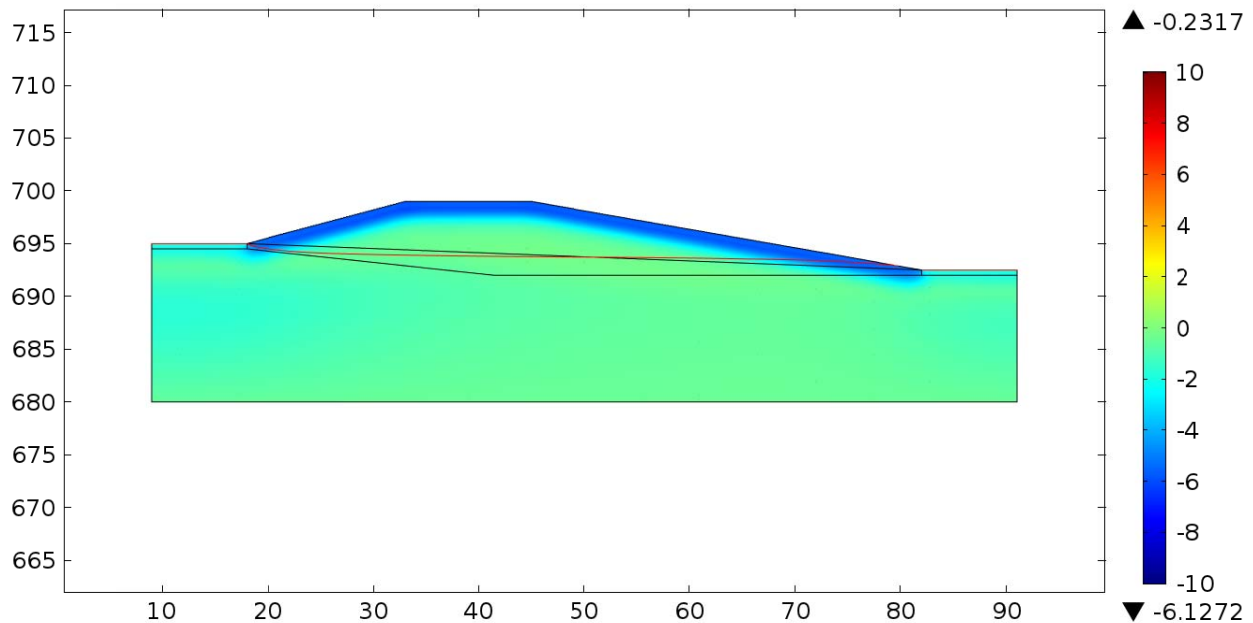

Figure G-10. Modeled temperatures for the fully-coupled COMSOL model for October 1. Cold temperatures are represented by shades of blue and warm temperature by shades of red, as indicated by the scale in °C to the right. The 0°C isotherm is indicated by the black line between the shades of yellow and light green. Distances along the x-axis are in meters, and elevations along the y-axis are in meters above sea level. Screen shot from COMSOL.
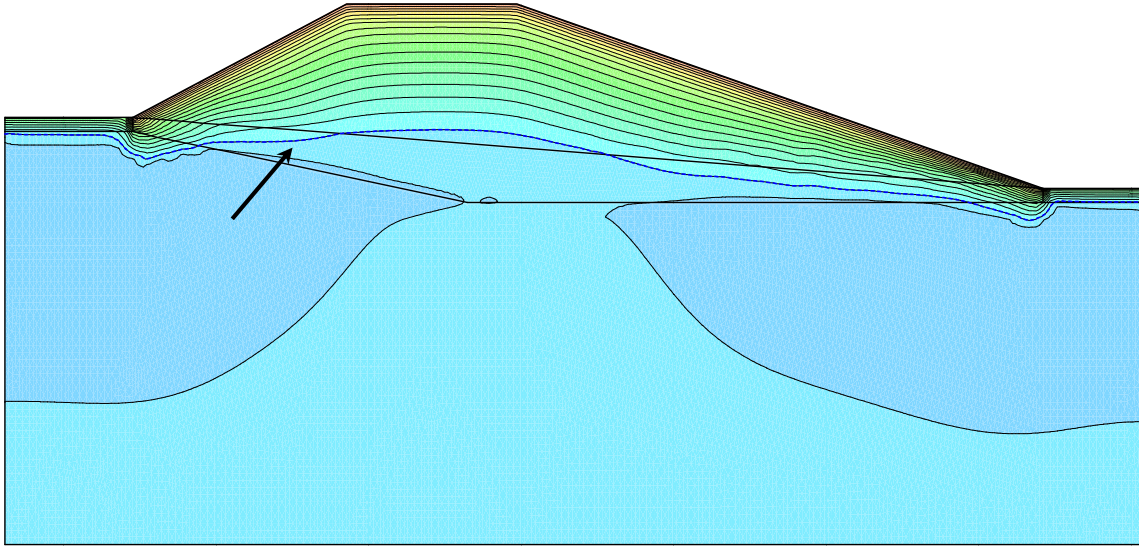
115
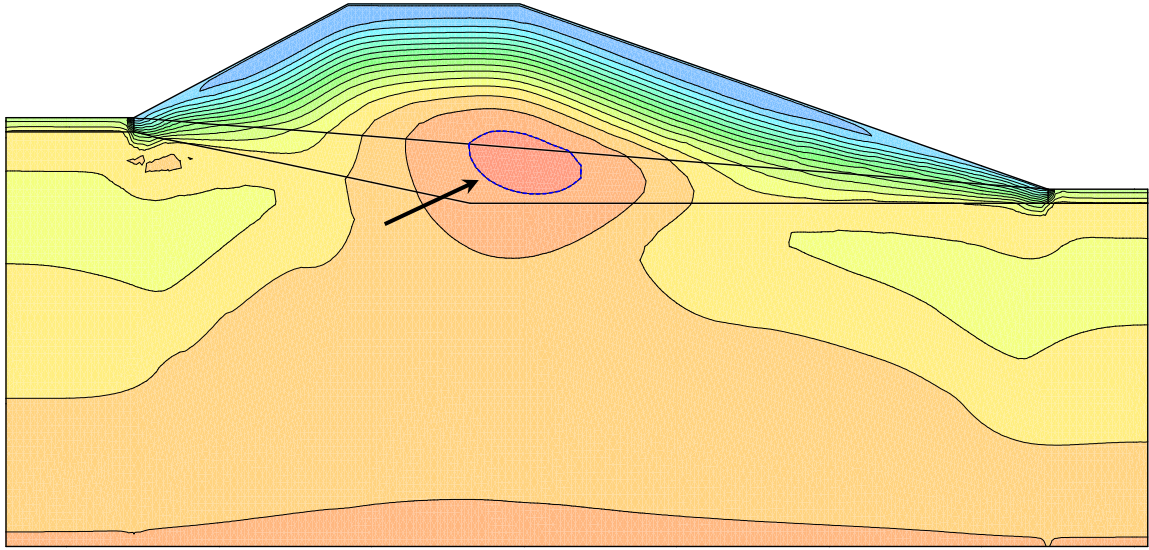
Figure G-11. Modeled temperatures for the fully-coupled TSW model for November 30. Cold temperatures are represented by shades of blue and warm temperature by shades of red, with T_{min}= -7.47°C and T_{max}= 0.16°C. The temperatures contours are incremented by 0.5°C, and the 0°C isotherm is indicated by the arrow. Screen shot from TSW.
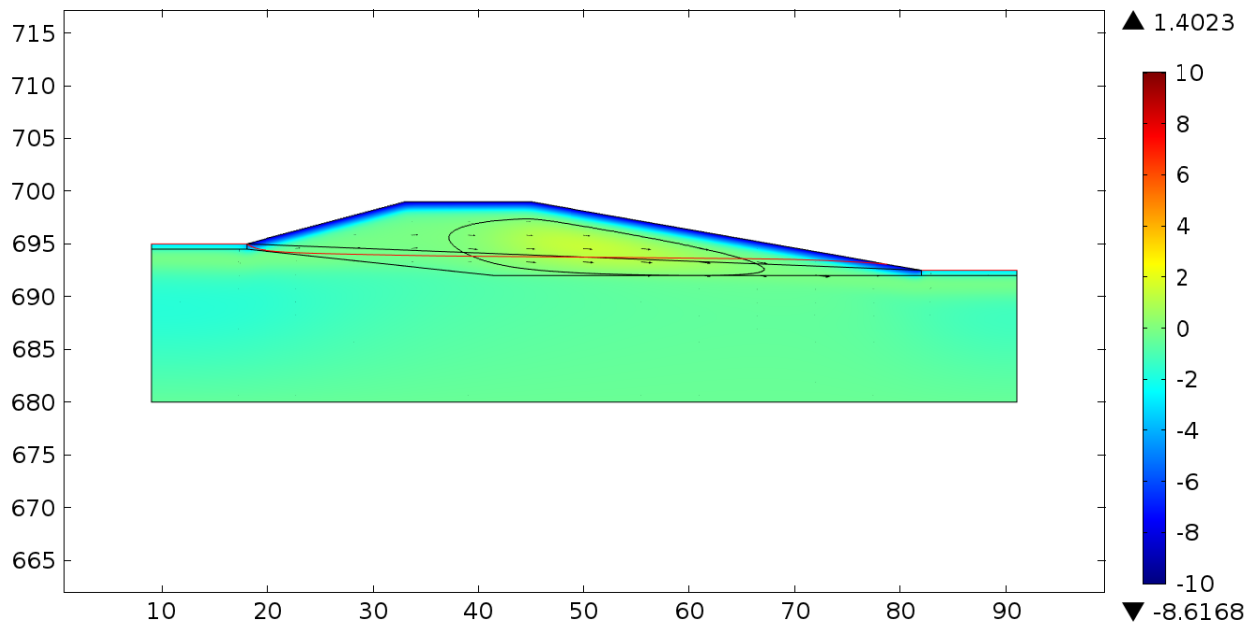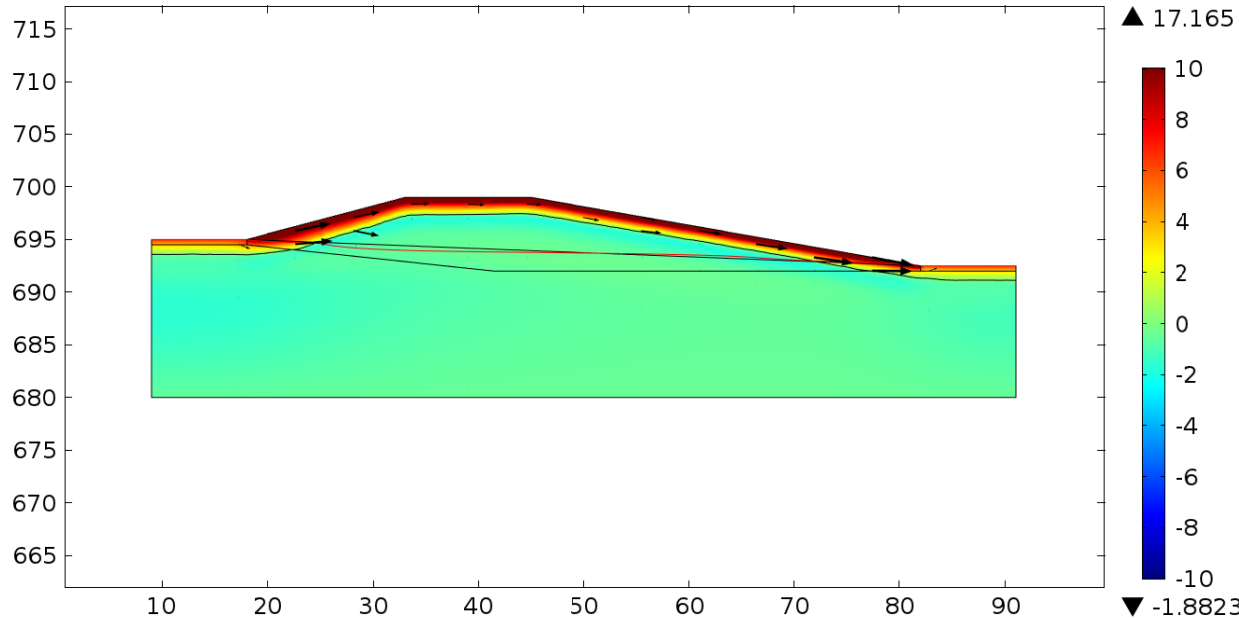

Figure G-12. Modeled temperatures for the fully-coupled COMSOL model for November 30. Cold temperatures are represented by shades of blue and warm temperature by shades of red, as indicated by the scale in °C to the right. The 0°C isotherm is indicated by the black line between the shades of yellow and light green. Distances along the x-axis are in meters, and elevations along the y-axis are in meters above sea level. Screen shot from COMSOL.
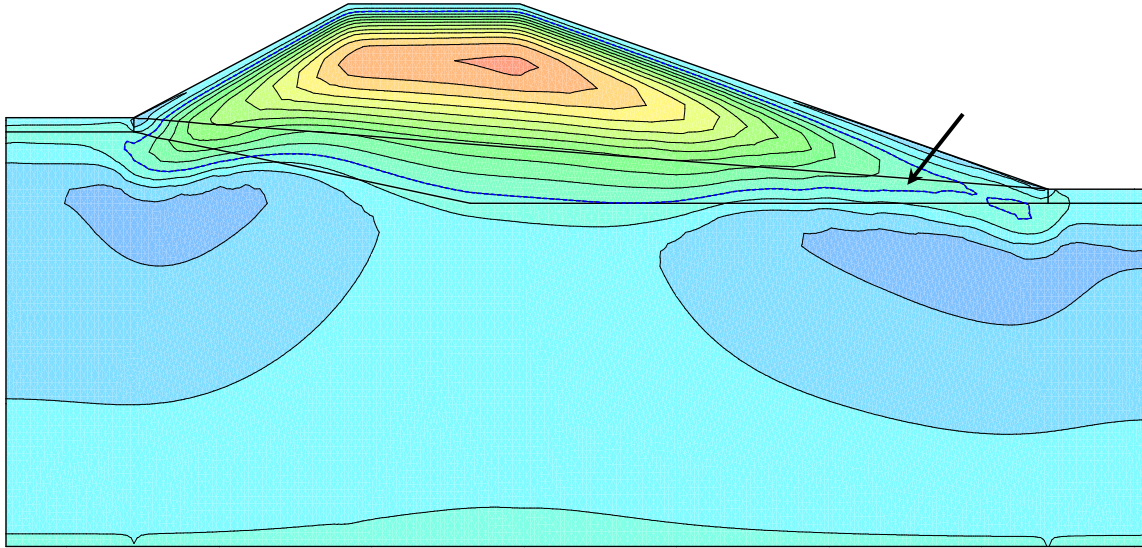
116
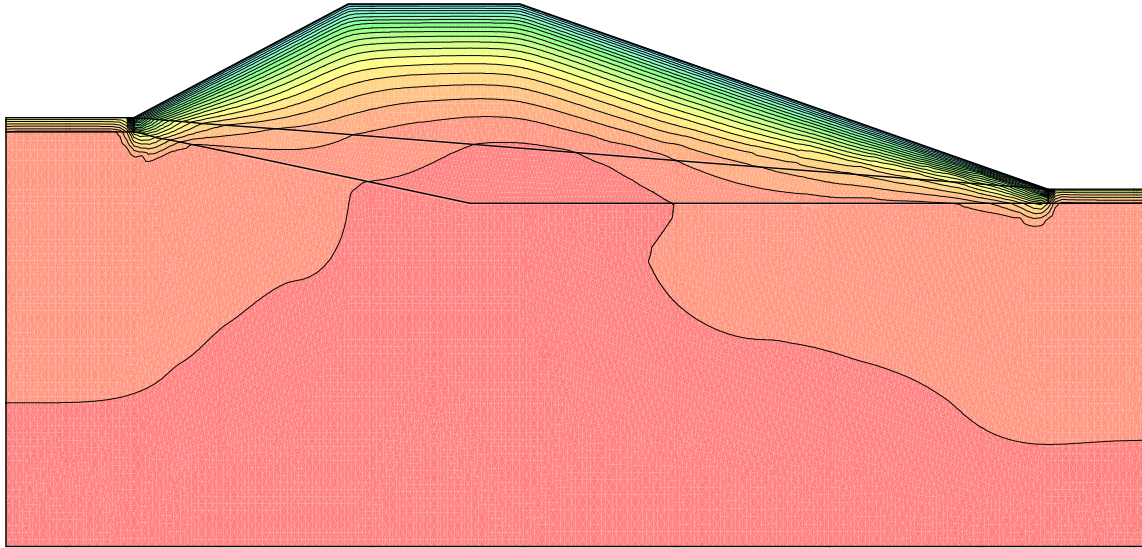
Figure G-13. Modeled temperatures for the fully-coupled TSW model for January 1. Cold temperatures are represented by shades of blue and warm temperature by shades of red, with T_{min}= -20.65°C and T_{max}= -0.39°C. The temperatures contours are incremented by 1°C. Screen shot from TSW.
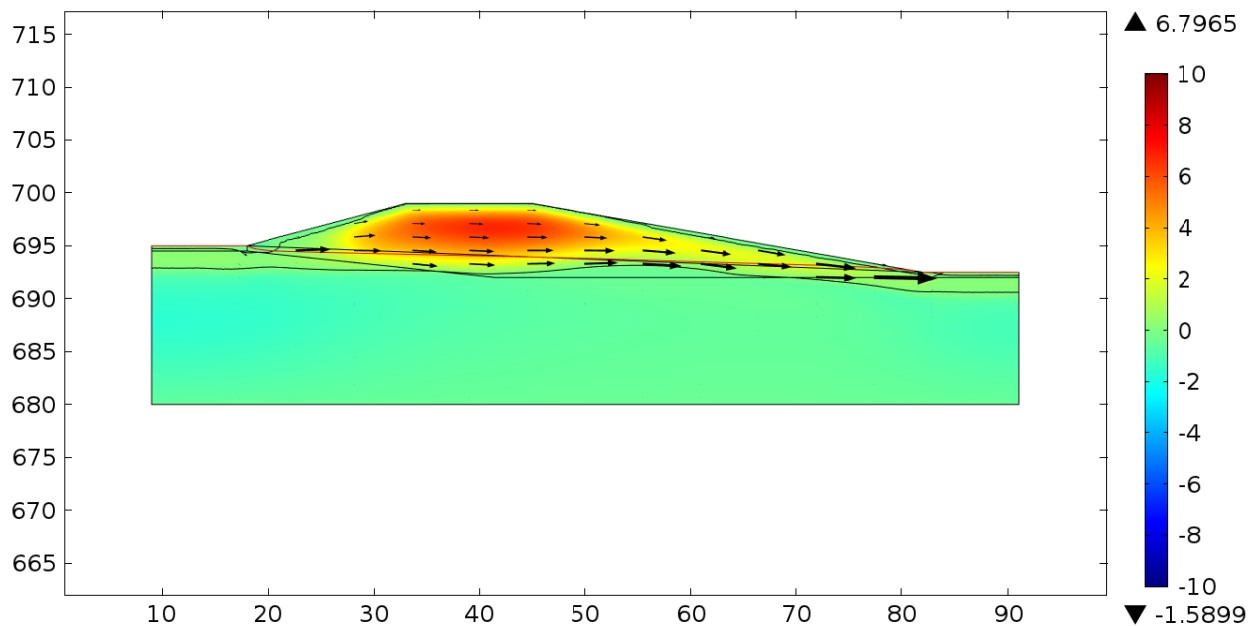

Figure G-14. Modeled temperatures for the fully-coupled COMSOL model for January 1. Cold temperatures are represented by shades of blue and warm temperature by shades of red, as indicated by the scale in °C to the right. The 0°C isotherm is indicated by the black line between the shades of yellow and light green. Distances along the x-axis are in meters, and elevations along the y-axis are in meters above sea level. Screen shot from COMSOL.

117

Figure G-15. Modeled temperatures for the fully-coupled TSW model for April 1. Cold temperatures are represented by shades of blue and warm temperature by shades of red, with T_{min}= -6.63°C and T_{max}= -0.45°C. The temperatures contours are incremented by 0.5°C. Screen shot from TSW.
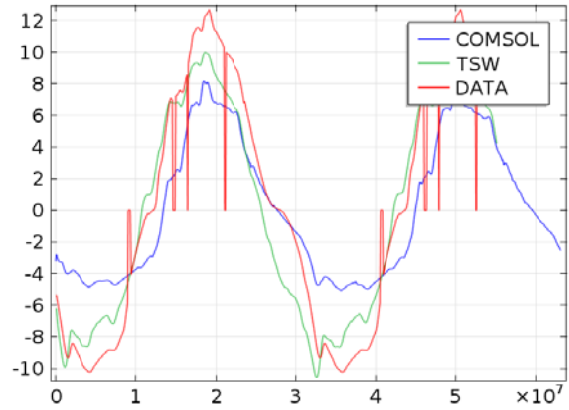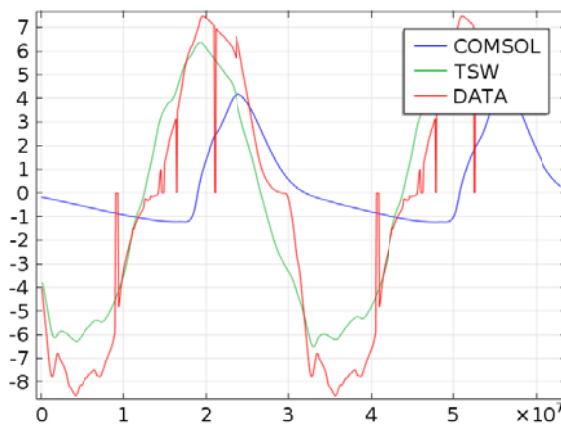

Figure G-16. Modeled temperatures for the fully-coupled COMSOL model for April 1. Cold temperatures are represented by shades of blue and warm temperature by shades of red, as indicated by the scale in °C to the right. The 0°C isotherm is indicated by the black line between the shades of yellow and light green. Distances along the x-axis are in meters, and elevations along the y-axis are in meters above sea level. Screen shot from COMSOL.
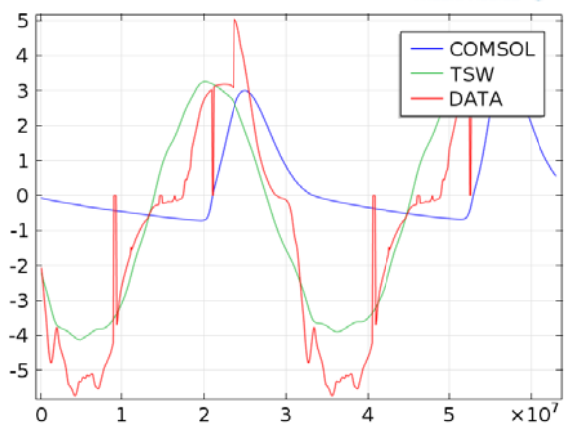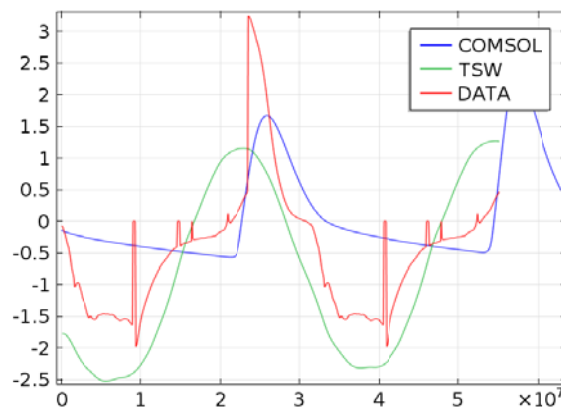
Figure G-17. Modeled temperatures for the fully-coupled TSW model for July 1. Cold temperatures are represented by shades of blue and warm temperature by shades of red, with T_{min}= -1.80°C and T_{max}= 16.48°C. The temperatures contours are incremented by 1°C, and the 0°C isotherm is indicated by the arrow. Screen shot from TSW.

Figure G-18. Modeled temperatures for the fully-coupled COMSOL model for July 1. Cold temperatures are represented by shades of blue and warm temperature by shades of red, as indicated by the scale in °C to the right. The 0°C isotherm is indicated by the black line between the shades of yellow and light green. Distances along the x-axis are in meters, and elevations along the y-axis are in meters above sea level. Screen shot from COMSOL.
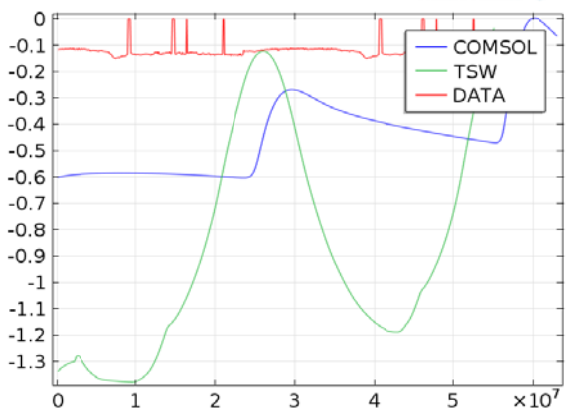
119

Figure G-19. Modeled temperatures for the fully-coupled TSW model for September 30. Cold temperatures are represented by shades of blue and warm temperature by shades of red, with T_{min}= -1.67°C and T_{max}= 5.12°C. The temperatures contours are incremented by 0.5°C, and the 0°C isotherm is indicated by the arrow. Screen shot from TSW.

Figure G-20. Modeled temperatures for the fully-coupled COMSOL model for September 30. Cold temperatures are represented by shades of blue and warm temperature by shades of red, as indicated by the scale in °C to the right. The 0°C isotherm is indicated by the black line between the shades of yellow and light green. Distances along the x-axis are in meters, and elevations along the y-axis are in meters above sea level. Screen shot from COMSOL.
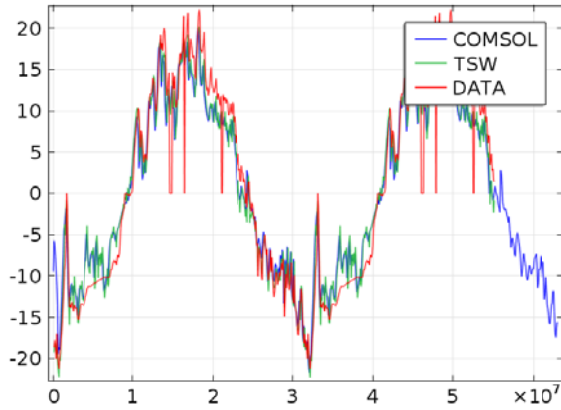
Figure G-21. Measured versus modeled temperatures. Temperatures in ºC are plotted for the period January 1, 2008 to December 31, 2009. Measured data from the thermistor at each depth are shown in red, COMSOL model results are shown in blue, and TSW model results are shown in green. Comparisons made for depths of (a) 0.1 m, (b) 1.5 m, (c) 2.5 m, (d) 3.5 m, (e) 4.5 m, (f) 6 m (CONTINUED ON NEXT PAGE).
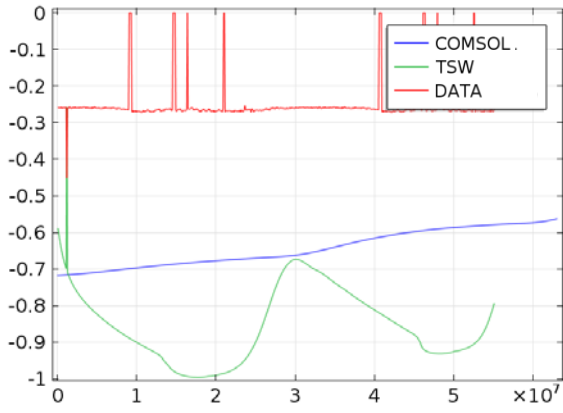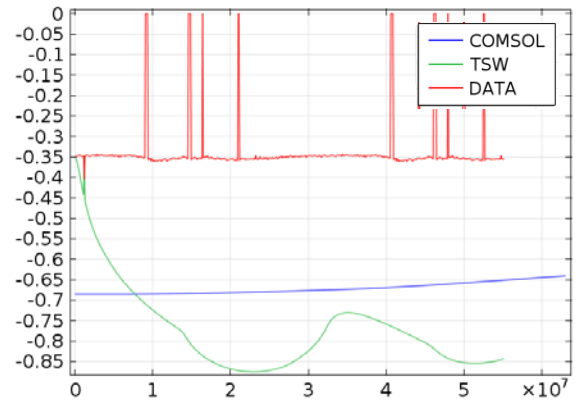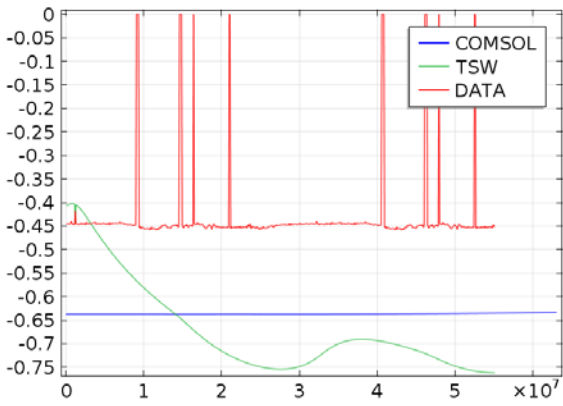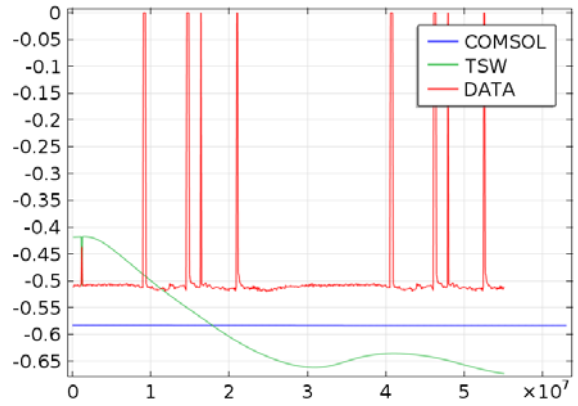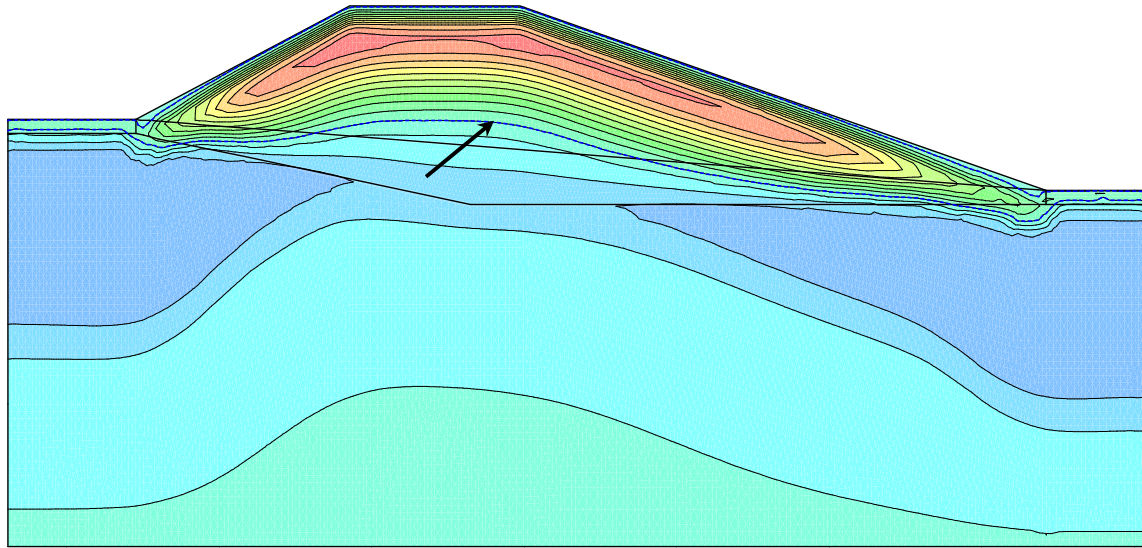
Figure G-21 (CONTINUED). Comparisons made for depths of (g) 7.5 m, (h) 9 m, (i) 11 m, (j) 13 m.
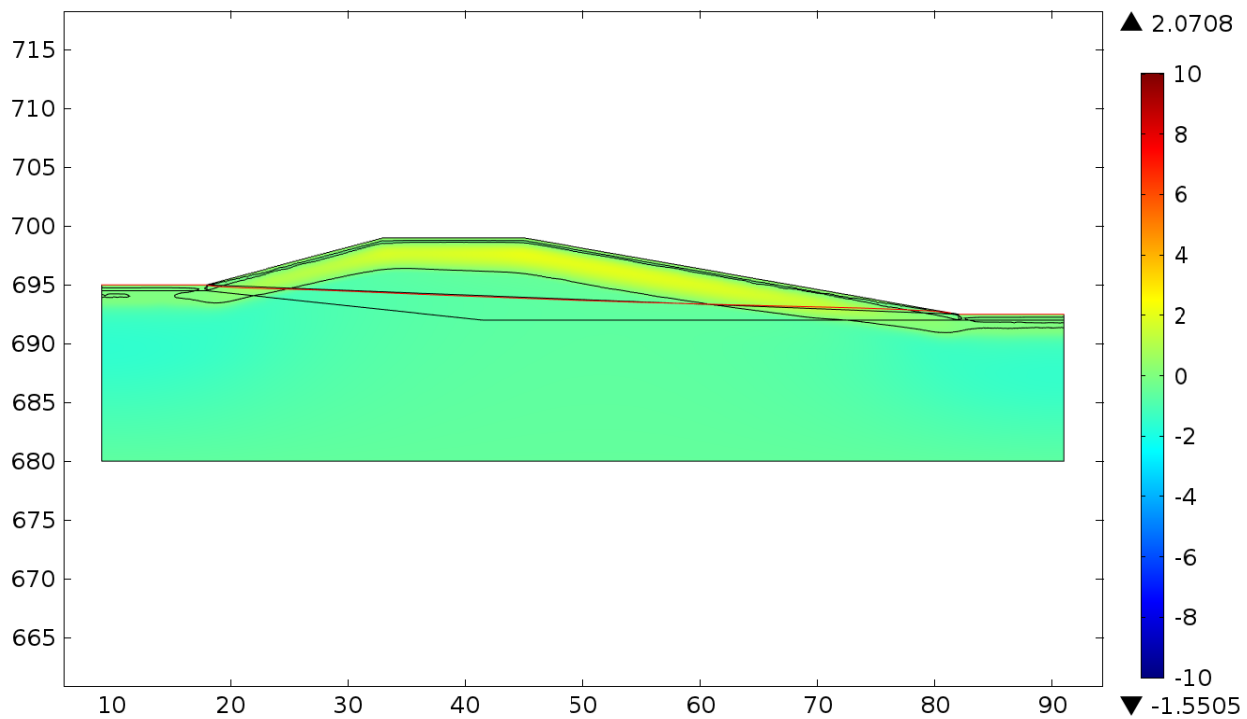
Figure G-22. Modeled temperatures for the conduction-only TSW model for October 1. Cold temperatures are represented by shades of blue and warm temperature by shades of red, with T_{min}= -1.95°C and T_{max}= 5.36°C. The temperatures contours are incremented by 0.5°C, and the 0°C isotherm is indicated by the arrow. Screen shot from GEOSTUDIO.

Figure G-23. Modeled temperatures for the conduction-only COMSOL model for October 1. Cold temperatures are represented by shades of blue and warm temperature by shades of red, as indicated by the scale in °C to the right. The 0°C isotherm is indicated by the black line between the shades of yellow and light green. Distances along the x-axis are in meters, and elevations along the y-axis are in meters above sea level. Screen shot from COMSOL.
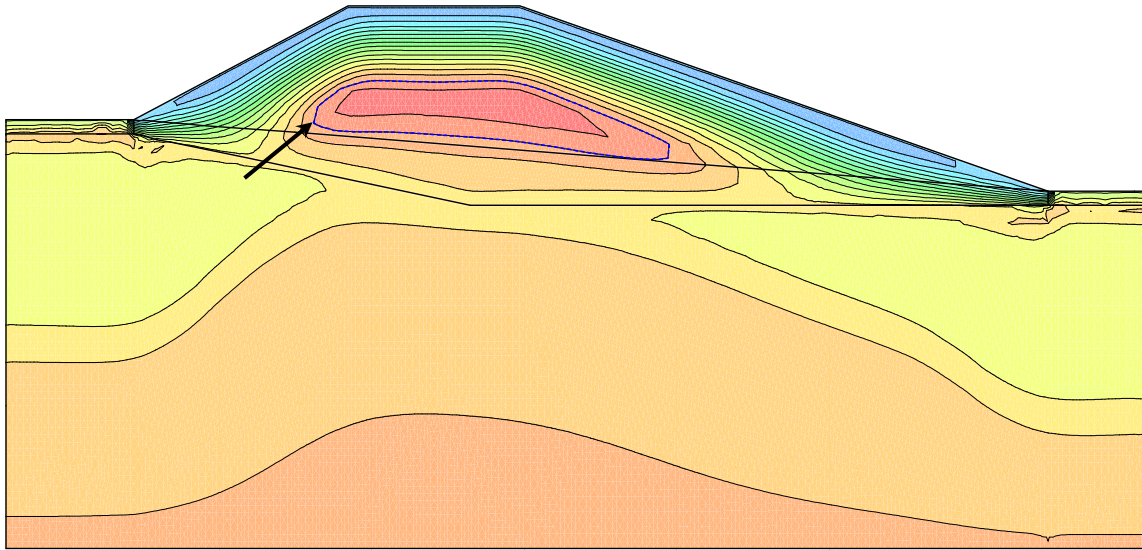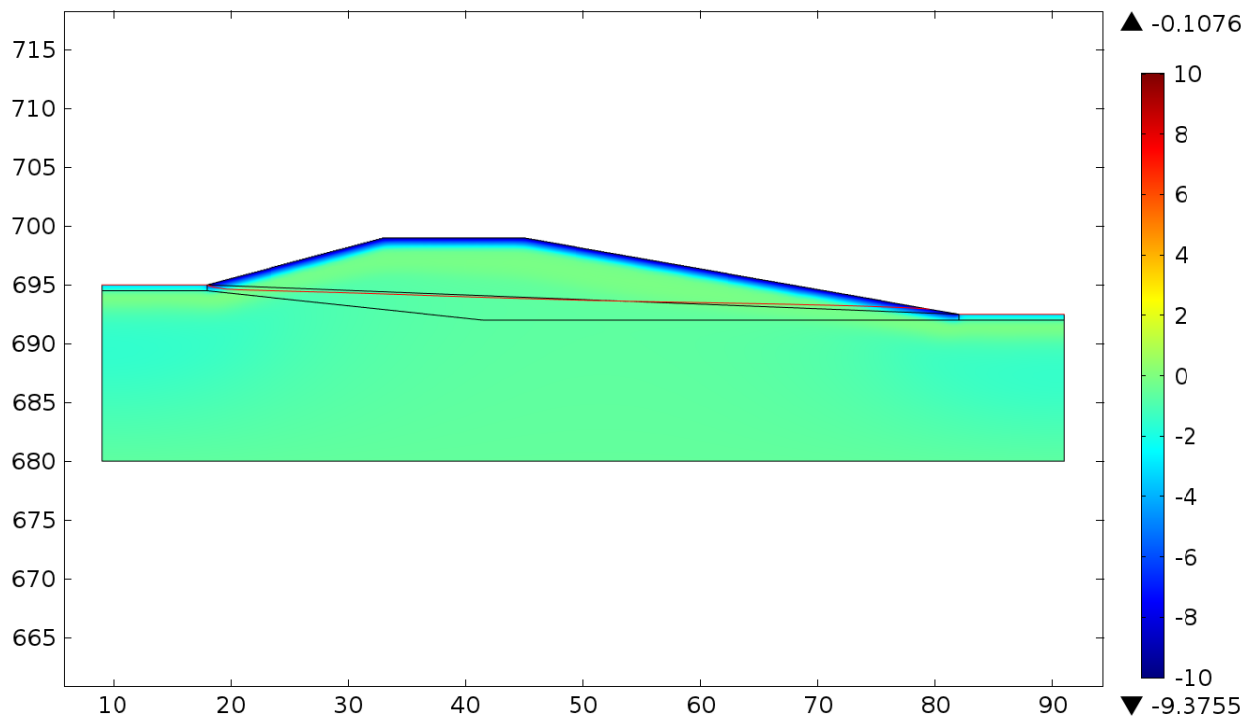
123

Figure G-24. Modeled temperatures for the conduction-only TSW model for November 30. Cold temperatures are represented by shades of blue and warm temperature by shades of red, with T_{min}= -7.40°C and T_{max}= 0.84°C. The temperatures contours are incremented by 0.5°C, and the 0°C isotherm is indicated by the arrow. Screen shot from GEOSTUDIO.

Figure G-25. Modeled temperatures for the conduction-only COMSOL model for November 30. Cold temperatures are represented by shades of blue and warm temperature by shades of red, as indicated by the scale in °C to the right. The 0°C isotherm is indicated by the black line between the shades of yellow and light green. Distances along the x-axis are in meters, and elevations along the y-axis are in meters above sea level. Screen shot from COMSOL.
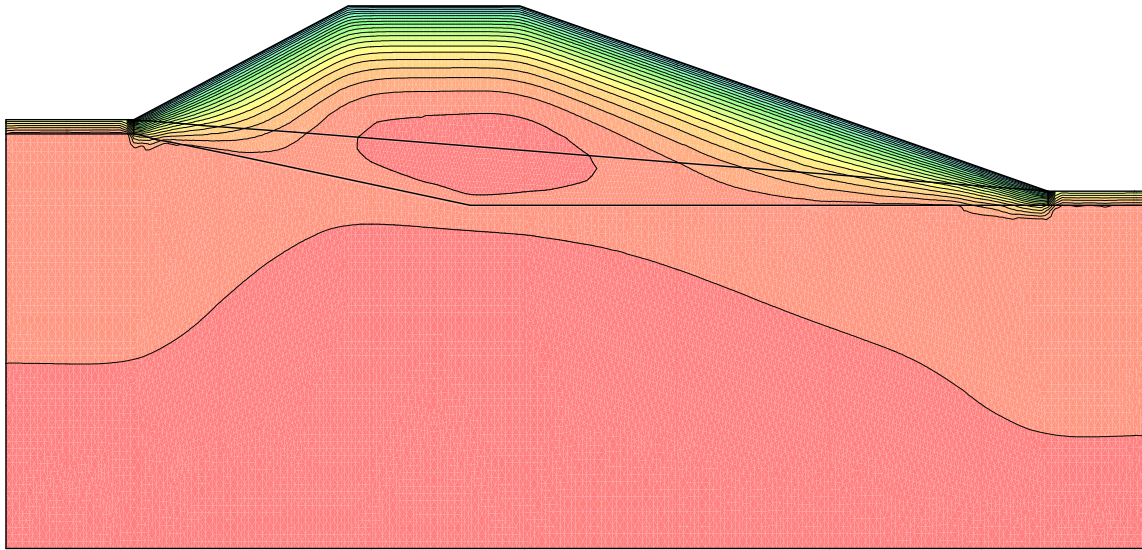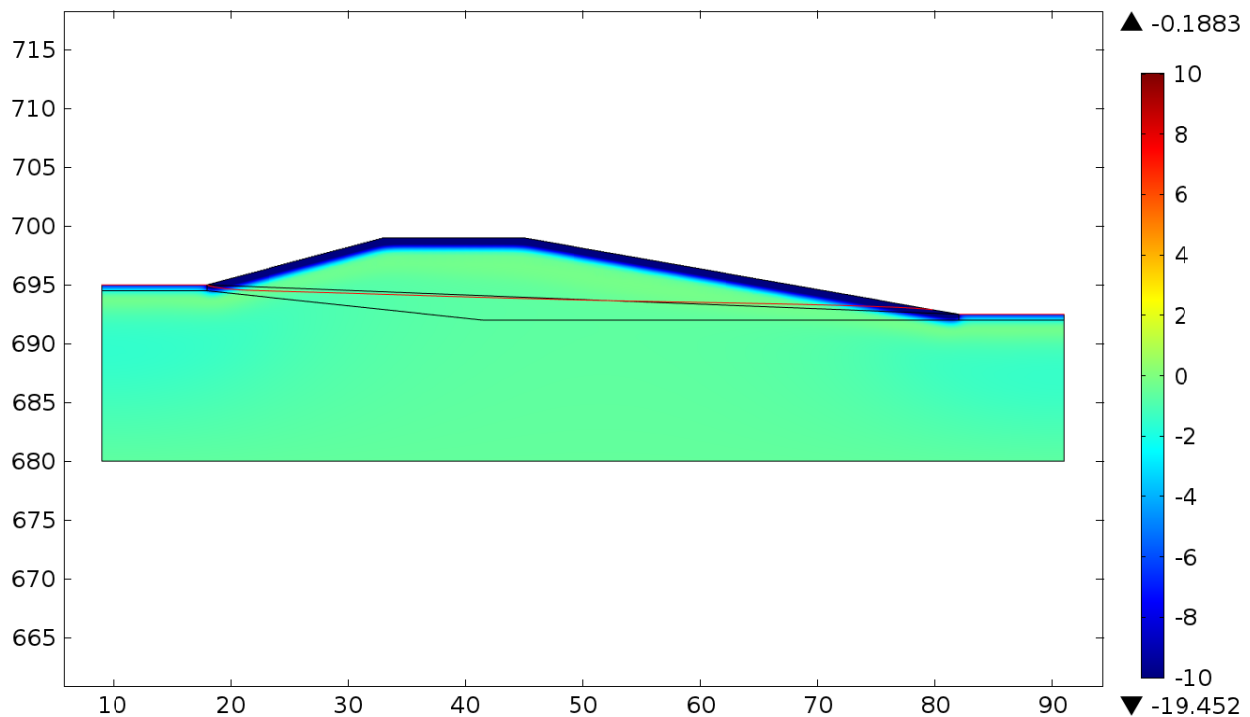
Figure G-26. Modeled temperatures for the conduction-only TSW model for January 1. Cold temperatures are represented by shades of blue and warm temperature by shades of red, with T_{min}= -20.65°C and T_{max}= -0.45°C. The temperatures contours are incremented by 1°C. Screen shot from GEOSTUDIO.

Figure G-27. Modeled temperatures for the conduction-only COMSOL model for January 1. Cold temperatures are represented by shades of blue and warm temperature by shades of red, as indicated by the scale in °C to the right. The 0°C isotherm is indicated by the black line between the shades of yellow and light green. Distances along the x-axis are in meters, and elevations along the y-axis are in meters above sea level. Screen shot from COMSOL.
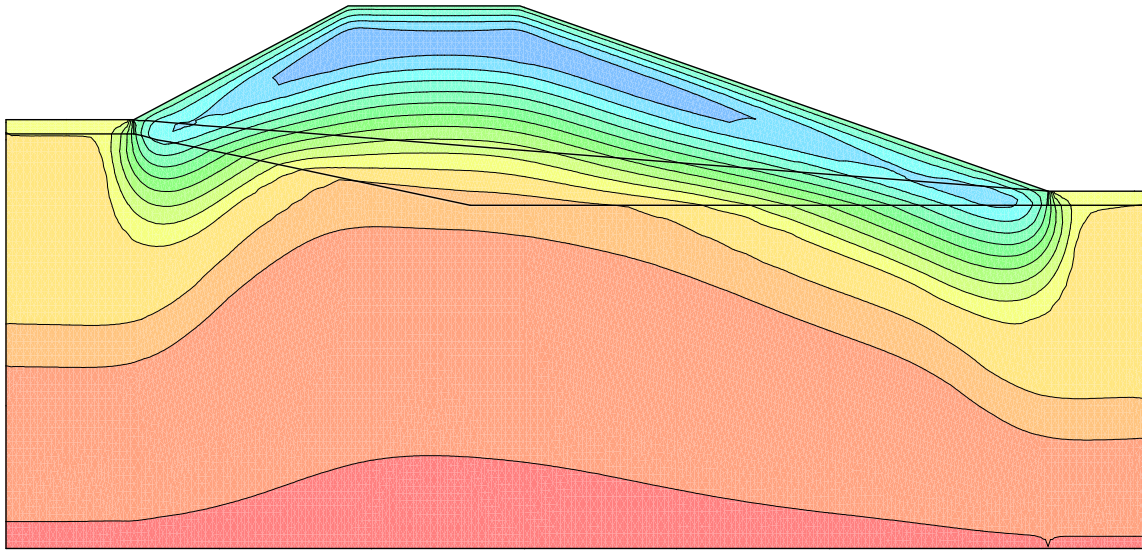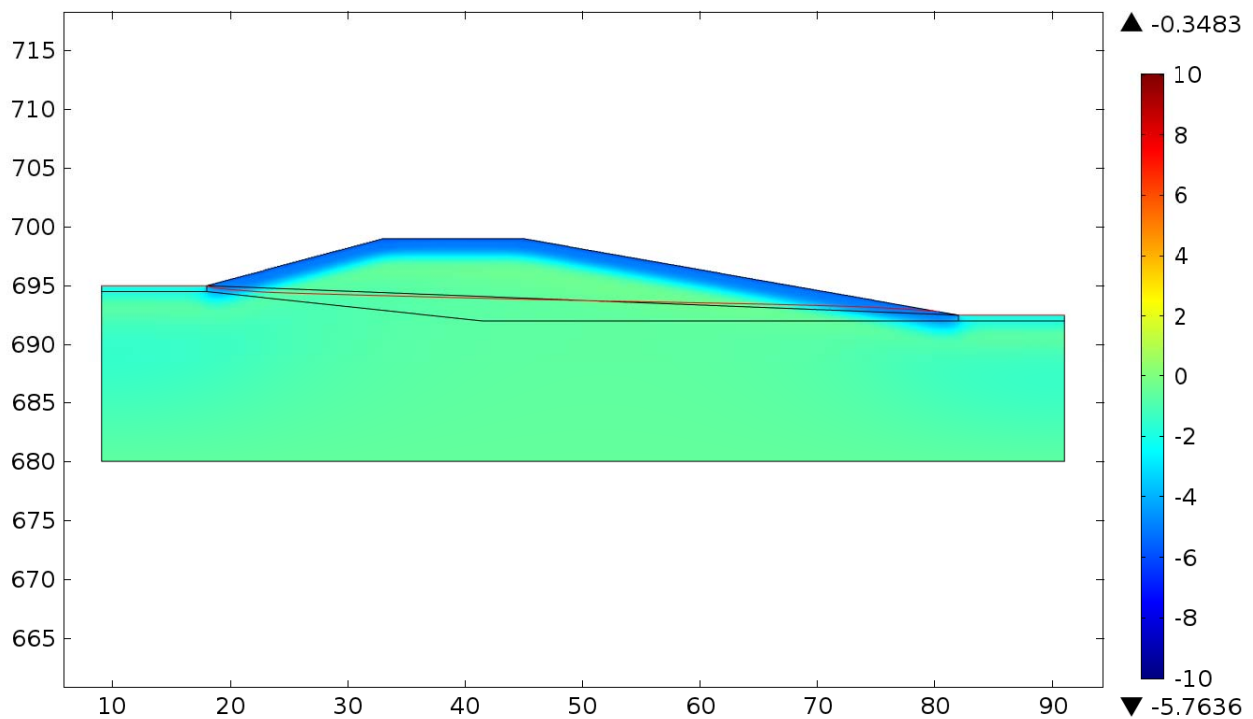
Figure G-28. Modeled temperatures for the conduction-only TSW model for April 1. Cold temperatures are represented by shades of blue and warm temperature by shades of red, with T_{min}= -6.98°C and T_{max}= -0.45°C. The temperatures contours are incremented by 0.5°C. Screen shot from GEOSTUDIO.

Figure G-29. Modeled temperatures for the conduction-only COMSOL model for April 1. Cold temperatures are represented by shades of blue and warm temperature by shades of red, as indicated by the scale in °C to the right. The 0°C isotherm is indicated by the black line between the shades of yellow and light green. Distances along the x-axis are in meters, and elevations along the y-axis are in meters above sea level. Screen shot from COMSOL.
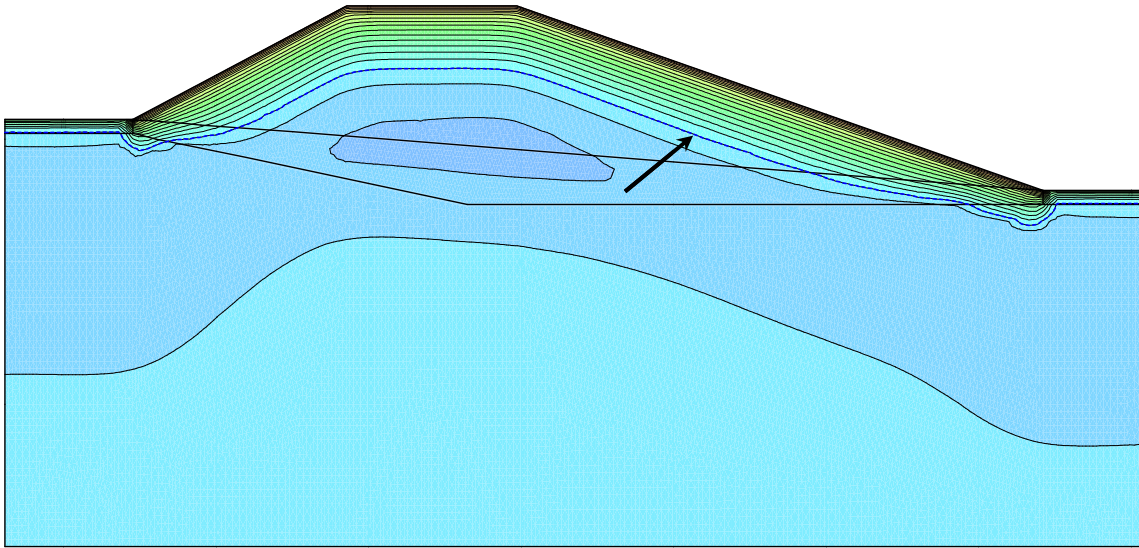
126

Figure G-30. Modeled temperatures for the conduction-only TSW model for July 1. Cold temperatures are represented by shades of blue and warm temperature by shades of red, with T_{min}= -2.26°C and T_{max}= 16.48°C. The temperatures contours are incremented by 1°C, and the 0°C isotherm is indicated by the arrow. Screen shot from GEOSTUDIO.
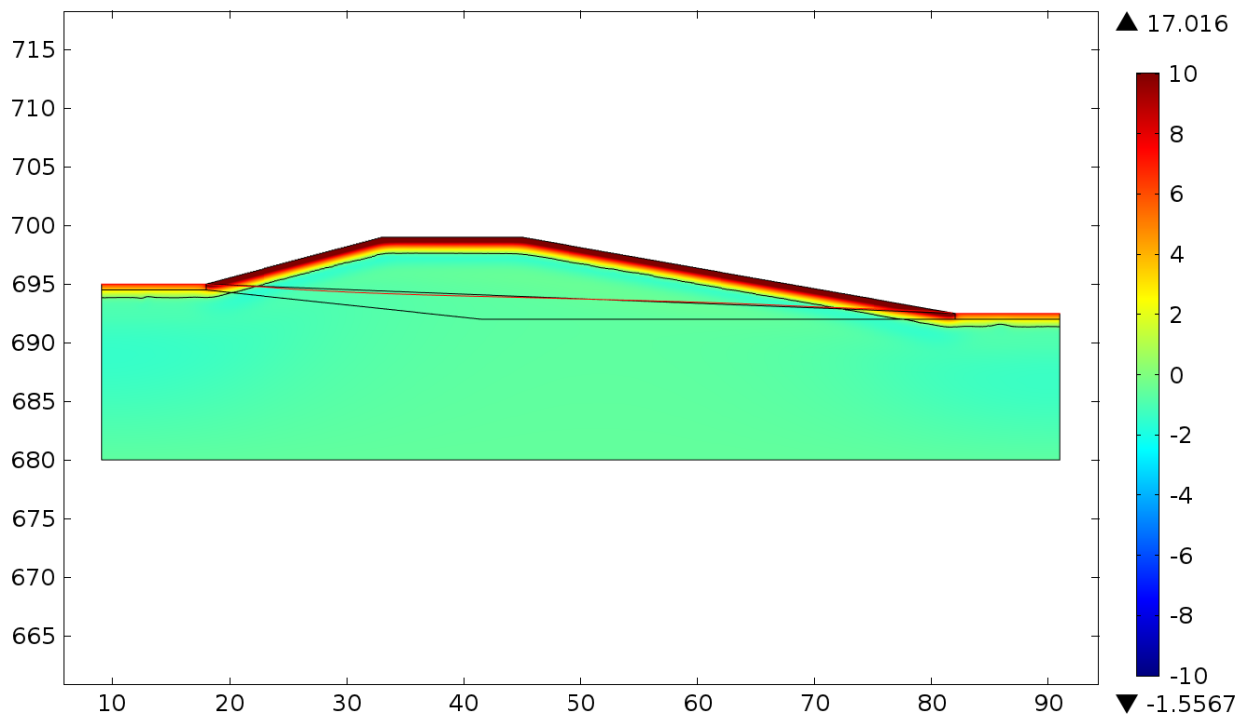

Figure G-31. Modeled temperatures for the conduction-only COMSOL model for July 1. Cold temperatures are represented by shades of blue and warm temperature by shades of red, as indicated by the scale in °C to the right. The 0°C isotherm is indicated by the black line between the shades of yellow and light green. Distances along the x-axis are in meters, and elevations along the y-axis are in meters above sea level. Screen shot from COMSOL.
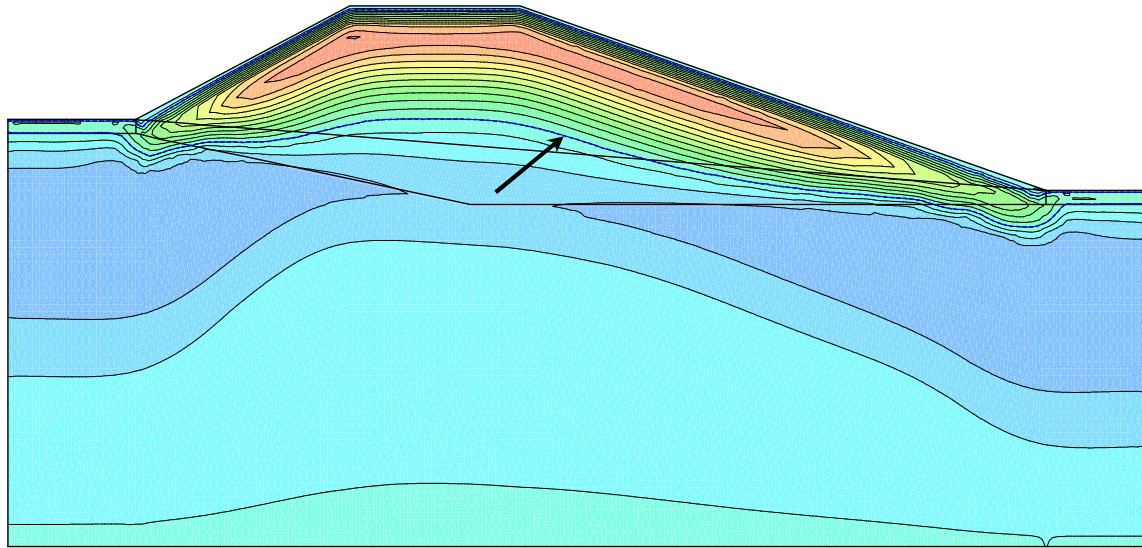
127

Figure G-32. Modeled temperatures for the conduction-only TSW model for September 30. Cold temperatures are represented by shades of blue and warm temperature by shades of red, with T_{min}= -1.90°C and T_{max}= 5.52°C. The temperatures contours are incremented by 0.5°C, and the 0°C isotherm is indicated by the arrow. Screen shot from GEOSTUDIO.
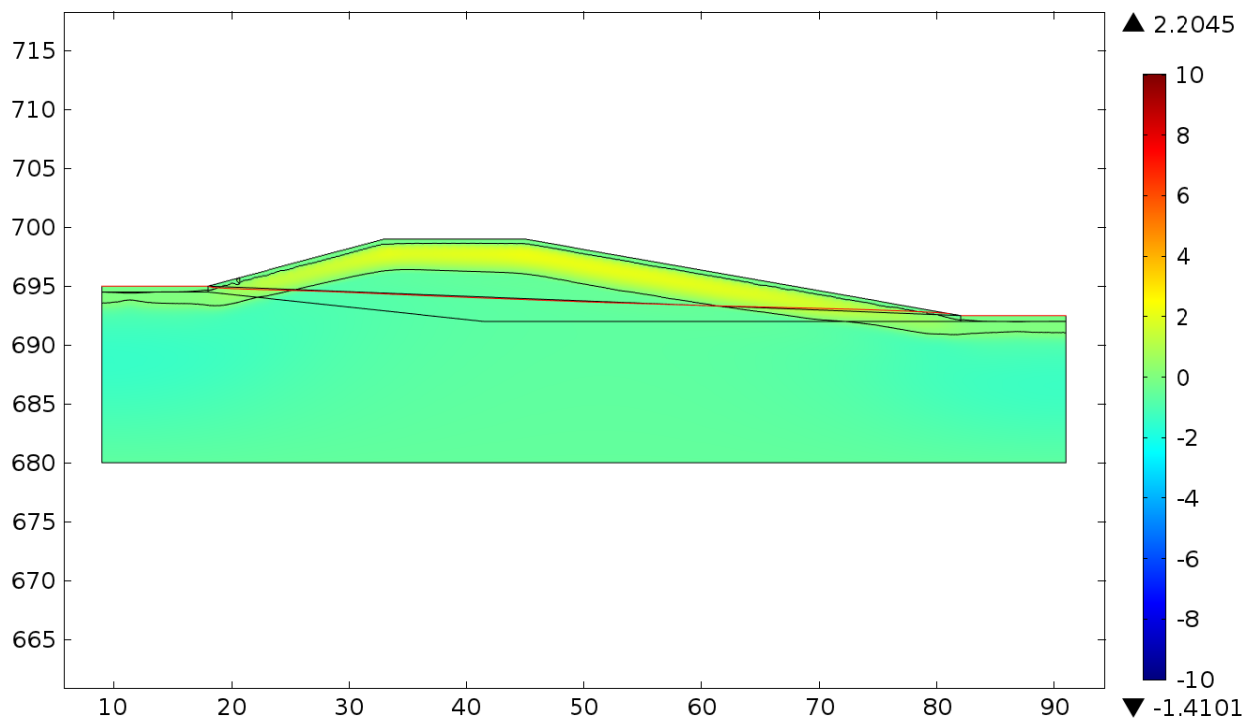

Figure G-33. Modeled temperatures for the conduction-only COMSOL model for September 30. Cold temperatures are represented by shades of blue and warm temperature by shades of red, as indicated by the scale in °C to the right. The 0°C isotherm is indicated by the black line between the shades of yellow and light green. Distances along the x-axis are in meters, and elevations along the y-axis are in meters above sea level. Screen shot from COMSOL.

128